Universität Hamburg
DER FORSCHUNG | DER LEHRE | DER BILDUNG

Tunable Nanocomposite Thin Films: Novel Approaches for Resistive Vapor Sensing Applications

Dissertation

zur Erlangung des Doktorgrades
eingereicht an der Fakultät für Mathematik, Informatik und Naturwissenschaften – Fachbereich Chemie
Universität Hamburg

vorgelegt von
Sophia Caroline Bittinger
Hamburg
2023

Dissertation

Titel: Tunable Nanocomposite Thin Films: Novel Approaches for Resistive Vapor Sensing Applications

Titel (deutsch): Einstellbare Nanohybrid-Dünnschichtfilme: Neuartige Ansätze für Anwendungen als resistive Sensoren für Dämpfe

Eingereicht von: Sophia Caroline Bittinger

Matrikelnummer: 6563027

E-Mail Adresse: sophiabittinger@icloud.com

Arbeitsgruppe: Prof. Dr. Horst Weller

Institut: Institut für Physikalische Chemie

Universität: Universität Hamburg

Datum der Einreichung: 14. Juli 2023

Erstgutachter: Dr. Tobias Vossmeyer

Zweitgutachter: Prof. Dr. Alf Mews

Datum der Disputation: 15. September 2023

Prüfungskommission: Dr. Tobias Vossmeyer
Prof. Dr. Dorota Koziej
Prof. Dr. Tobias Beck

Diese Arbeit wurde im Zeitraum von Juli 2019 bis April 2023 in der Arbeitsgruppe von Prof. Dr. Horst Weller, im Team von Dr. Tobias Vossmeyer, am Institut für Physikalische Chemie im Fachbereich Chemie der Universität Hamburg durchgeführt.

List of Publications

All peer-reviewed research articles that were published within the framework of this thesis are listed below in a chronological order. An equal contribution of authors is denoted by a dagger (†) symbol.

1. H. Schlicke,† S. C. Bittinger,† T. Vossmeyer, "Lithographic Patterning and Selective Functionalization of Metal Nanoparticle Composite Films", *ACS Appl. Electron. Mater.* **2020**, 2, 11, 3741–3748.[1]
2. H. Hartmann, J.-N. Beyer, J. Hansen, S. C. Bittinger, M. Yesilmen, H. Schlicke, T. Vossmeyer, "Transfer Printing of Freestanding Nanoassemblies: A Route to Membrane Resonators with Adjustable Prestress", *ACS Appl. Mater. & Interfaces* **2021**, 13, 34, 40932-40941.[2]
3. H. Schlicke,† S. C. Bittinger,† H. Noei, T. Vossmeyer, "Gold Nanoparticle-Based Chemiresistors: Recognition of Volatile Organic Compounds Using Tunable Response Kinetics", *ACS Appl. Nano Mater.* **2021**, 4, 10, 10399–10408.[3]
4. B. Ketelsen,† H. Schlicke,† V. R. Schulze, S. C. Bittinger, S.-D. Wu, S.-h. Hsu, T. Vossmeyer, "Nanoparticle Based Strain Gauges: Anisotropic Response Characteristics, Multidirectional Strain Sensing, and Novel Approaches to Healthcare Applications", *Adv. Func. Mater.* **2023**, 33, 2210065.[4]
5. S.-D. Wu, S.-h. Hsu, B. Ketelsen, S. C. Bittinger, H. Schlicke, H. Weller, T. Vossmeyer, "Fabrication of Eco-Friendly Wearable Strain Sensor Arrays via Facile Contact Printing for Healthcare Applications", *Small Methods* **2023**, 2300170.[5]

Contents

List of Abbreviations

12A	1-dodecylamine
10DT	1,10-decanedithiol
2D	two-dimensional
4DT	1,4-butanedithiol
6DT	1,6-hexanedithiol
8DT	1,8-octanedithiol
9DT	1,9-nonanedithiol
A	electron acceptor
ADT	α,ω-alkanedithiol
AFM	atomic force microscopy
AG	analyte gas
ANN	artificial neural network
approx.	approximately
FTIR	Fourier-transform infrared
ATR	attenuated total reflectance
brpm	breaths per minute
CB	conduction band
CNT	carbon nanotube
D	electron donor
DEG	diethylene glycol
DI	deionized
DT	dithiol
DUV	deep-UV
e-nose	electronic nose
e-beam	electron beam
e.g.	for example
FFP2	filtering face piece 2
GLY	2,3-dimercaptopropanol
GNP	gold nanoparticle
GO	graphene oxide
HEG	hexa(ethylene glycol) dithiol
HOMO	highest occupied molecular orbital
i.e.	that is
IDE	interdigitated electrode
LbL	layer-by-layer
LDA	linear discriminant analysis

LK	Lerf-Klinowski
LSPR	localized surface plasmon resonance
LUMO	lowest unoccupied molecular orbital
MFC	mass flow controller
MIBK	methyl isobutyl ketone
MOX	metal oxide
NTP	4-nitrothiophenol
OC	organic content
ODE	1-octadecene
OLAC	oleic acid
OLAM	oleylamine
PCA	principal component analysis
PCB	printed circuit board
PDDA	poly(diallyldimethylammonium)
PI	polyimide
PMMA	poly(methyl methacrylate)
ppm	parts-per-million
PTFE	polytetrafluoroethylene
QCM	quartz crystal microbalance
rGO	reduced graphene oxide
XPS	x-ray photoelelectron spectroscopy
r.h.	relative humidity
SAXS	small angle x-ray scattering
SBH	sodium borohydride
SC	spin-coating
SEM	scanning electron microscopy
TBAB	tert-butylamine borane
TEM	transmission electron microscopy
TGA	thermogravimetric analysis
TNC	titania nanocrystal
TND	titania nanodot
TNP	titania nanoplate
TNR	titania nanorod
TOAB	tetraoctylammonium bromide
UV	ultraviolet
VB	valence band
VOC	volatile organic compound
XRD	x-ray diffraction

ZG	zero gas

List of Symbols

α_λ	attenuation coefficient
A_{QCM}	sensitive area of QCM
A	area below sensor signal during exposure
β	tunneling decay constant
c_0	speed of light
c_{v}	gas-phase analyte concetration
δ	interparticle distance
Δf_{s}	resonance frequency shift
$\frac{\Delta G}{G_0}$	relative conductance change
$\left(\frac{\Delta G}{G_0}\right)_{\mathrm{max}}$	maximum relative conductance change
Δm	sorbed analyte mass
e	elementary charge
E_{A}	activation energy
E_{gap}	band gap
ϵ	permittivity
ϵ_0	vacuum permittivity
ϵ_{m}	dielectric constant of surrounding medium
$\epsilon(\omega)$	complex dielectric function of a material
f_0	resonance frequency
$f_{0,\mathrm{f}}$	resonance frequency of coated QCM
Q	flow rate
G	conductance
ΔG^*	free activation energy
I	electrical current
k_B	Boltzmann factor
K_{H}	Henry constant
K_{L}	Langmuir constant
ℓ_{g}	gap length
M_{a}	molar mass
μ	shear modulus
$\mathrm{N_A}$	Avogadro constant
ω	angular frequency
R	electrical resistance
$\left(\frac{\Delta R}{R_0}\right)_{\mathrm{max}}$	maximum relative resistance change
$\left(\frac{\Delta R}{R_0}\right)_{\mathrm{sat}}$	saturation sensor signal

r	particle radius
$\frac{\Delta R}{R_0}$	relative resistance change
R_0	baseline resistance
ρ	density
R_s	shunt resistance
σ_ext	extinction cross-section
σ_P	pre-exponential factor
T	temperature
$t_\mathrm{50,R}$	recovery time to reach 50 % max. response
t_{80}	rise time to reach 80 % max. response
t_{90}	rise time to reach 90 % max. response
t_f	film thickness
t_TNC	thickness of TNC component
V	voltage
V_a	analyte volume
V_p	particle volume
V_s	shunt voltages
w_g	gap width
x_a	analyte fraction

1 Zusammenfassung

In dieser Arbeit wurden hybride Dünnschichten aus (i) organisch vernetzten Goldnanopartikeln (GNPn), sowie aus (ii) Graphenoxid und TiO_2-Nanokristallen (GO/TNCn) hergestellt und hinsichtlich ihrer Anwendung als Chemiresistoren für die Detektion von verschiedenen flüchtigen organischen Substanzen (VOCs) und relative Luftfeuchtigkeit (r.h.) untersucht.

In der ersten vorgestellten Studie wurde eine photolithografische Methode weiterentwickelt und optimiert, um substratgestützte Nonandithiol (9DT)-vernetzte GNP-Filme zu strukturieren, und damit Chemiresistor-Arrays herzustellen. Zur Filmherstellung wurden GNP unterschiedlicher Durchmesser (~4 und ~8 nm) verwendet. Die Methode basiert auf der lithografischen Strukturierung von Polymethylmethacrylat (PMMA) als Opferschicht mittels Tief-UV (DUV)-Strahlung (254 nm), kombiniert mit einem etablierten *Layer-by-layer-Spin-Coating*-Verfahren zur Abscheidung der Hybridfilme. In einem *Lift-Off*-Prozess wird die PMMA-Opferschicht aufgelöst, um strukturierte, voneinander getrennte GNP-Filmbereiche zu erhalten. Die Auflösungsgrenze der *Lift-Off*-Methode wurde untersucht, indem PMMA mittels Elektronenstrahllithografie strukturiert wurde. Es wurde gezeigt, dass intakte GNP/9DT-Filmstrukturen mit Größen von 5 µm auf Silizium-Wafern strukturiert werden konnten. Darüber hinaus wurde die lithographische Methode zur selektiven molekularen Dotierung von vernetzten $GNP_{8.2\ nm}$/9DT-Filmen genutzt, indem bestimmte Filme auf einem 4 × 2-Array mit PMMA selektiv maskiert und freigelegt wurden, um die Filmzusammensetzung durch Einlegen in eine Thiol-/Dithiol-Lösung zu manipulieren, und gleichzeitig die Sensoreigenschaften einzelner Sensoren auf dem Array einzustellen. Die Thiole/Dithiole, die zur Refunktionalisierung der organischen Matrix verwendet wurden waren: Hexaethylenglycol-dithiol (HEG), 2,3-Dimercaptopropanol (GLY) und 4-Nitrothiophenol (NTP), so dass ein Array aus Filmen mit vier unterschiedlichen Zusammensetzungen (inklusive einem unbehandelten GNP/9DT-Film) erhalten wurde. Die resistiven Antworten des Arrays auf Dämpfe von Octan, Heptan, Toluol, 4-Methyl-2-Pentanon (MIBK), Ethanol, 1-Propanol, 1-Butanol und Wasser in einem Konzentrationsbereich von 50—8000 ppm wurden untersucht. Sowohl die molekulare Refunktionalisierung der 9DT/GNP-Filme, als auch die UV-Bestrahlung während der PMMA-Lithografie, führten zu einer Veränderung der Selektivität der Sensoren, die im Vergleich zu den GNP/9DT-Filmen nach den Behandlungen höhere Sensitivitäten für polare Analyten zeigten. Mit Hilfe von Kombinationen der Antworten der unterschiedlichen Sensoren wurden bestimmte Antwortmuster für die verschiedenen Analytklassen erhalten. Dadurch erweist sich diese Methode als sehr vielversprechend zur Herstellung elektronischer Nasen zur Erkennung von Analyten.

In dem zweiten vorgestellten Projekt wurde gezeigt, dass die hybride Nanostruktur organisch vernetzter GNP-Kompositfilme analytabhängige Antwortzeiten induzieren kann, die zur Erkennung und Unterscheidung verschiedener VOCs genutzt werden können. Als erstes wurden die dynamischen Antworten verschiedener α,ω-Alkandithiol (ADT)-vernetzter GNP-Filme untersucht und verglichen, indem sie Dämpfen von Toluol, 1-Butanol, 1-Propanol, 2-Propanol, Ethanol, Wasser, 4M2P und verschiedenen homologen Alkanen ausgesetzt wurden. Aus den Sensorantworten wurden charakteristische Merkmale extrahiert, die mit der Antwortkinetik zusammenhängen, wie die t_{80}-Antwortzeiten und die integrierte Fläche unter den Transienten. Es wurde gezeigt, dass die Antwortzeiten maßgeblich vom Molekülvolumen des Analyten abhängen, im Gegensatz zur maximalen resistiven Signalamplitude, die vor allem von der Polarität und dem Dampfdruck der Analyten bestimmt wird. Dieses Verhalten wurde auf einen diffusionslimitierten Prozess der Analytmoleküle in den Sensorfilm zurückgeführt. In diesem Zusammenhang wurden im Rahmen des Projektes verschiedene Methoden etabliert, um die analytabhängingen Antwortzeiten anzupassen. Zum einen wurden unterschiedlich lange ADT-Vernetzter (4DT – 10DT) zur Filmherstellung verwendet, um den molekularen Transport verschieden großer Analytmoleküle durch die so eingestellten interpartikulären Lücken zu beeinflussen, zum anderen wurde gezeigt, dass die Antwortkinetik auch anhand des GNP-Durchmessers eingestellt werden kann. Des Weiteren wurde gezeigt, dass UV-Bestrahlung von GNP/9DT-Filmen ebenfalls zu einer Verlangsamung der Antwortzeiten führt. Mittels Röntgenphotoelektronenspektroskopie (XPS), optischen und elektrischen Messungen wurde der Einfluss der UV-Strahlung auf die GNP-Filmzusammensetzung und -struktur untersucht, wobei die UV-induzierte Oxidation von primär nicht-vernetzender Dithiole als Hauptursache identifiziert wurde. Mit Hilfe dieser Methoden wurde ein Chemiresistor-Array aus ADT-vernetzten GNP-Filmen mit angepassten Antwortzeiten untersucht, und es konnte gezeigt werden, dass die Anwendung einer linearen Diskriminanzanalyse, basierend auf Kombinationen von resistiven (maximale Signalantwort) und kinetischen Antwortmerkmalen (Fläche, t_{80}), die Erkennung und Unterscheidung sehr ähnlicher Analyten ermöglichte. In einer anschließenden, derzeit noch laufenden Studie, wurde außerdem vorgestellt, dass die einstellbaren, analytabhängigen Antwortzeiten von GNP/6DT-Filmen genutzt werden können, um binäre VOC-Gemische zu unterscheiden und ihre Zusammensetzung bei einer konstanten Gesamtkonzentration zu bestimmen.

Das dritte Projekt dieser Arbeit umfasste GO/TNC-Nanokompositfilme und ihre Anwendung als flexible, resistive VOC- und Luftfeuchte-Sensoren. Zunächste wurde ein *Layer-by-Layer-Spin-Coating*-Verfahren entwickelt, um substratgestützte Schichtsysteme aus eigens hergestelltem GO und photokatalytisch aktiven TNCn auf verschiedenen Substraten aufzubauen, u.a., Silizium, Quarz-Glas und Polyimid (PI). Hierbei wurden organischstabilisierte TiO_2-Nanostäbchen (TNRs, 40 nm Länge, 3 nm Durchmesser) und TiO_2-Nanoplättchen (TNPs, 21 nm Kantenlänge, 10 nm Dicke) zur Filmherstellung eingesetzt, die mittels etablierter Syntheserouten dargestellt wurden. Es wurden weitere Parameter zur Einstellung der Filmzusammensetzung und -dicke angepasst, wie z.B. die Konzentration der Lösungen, sowie die Anzahl der Abscheidungszyklen. Die hergestellten Schichtsysteme wurden mittels spektroskopischer Methoden (Infrarot (IR)-, Raman-, und UV-Vis-Spektroskopie) und mikroskopischer Methoden (Rasterkraftmikroskopie (AFM), Rasterelektronenmikroskopie (REM)) untersucht. Es wurden homogene, geschichtete Hybridfilme mit einstellbaren Schichtdicken zwischen 15-150 nm hergestellt, in denen die TNC homogen verteilt zwischen GO-Lagen inkorporiert waren. Als nächstes wurde mittels UV-aktivierter, photokatalytischer Reduktion (254 nm) von GO zu reduziertem GO (rGO) das GO/rGO-Verhältnis der Hybridmaterialien selektiv angepasst, und ihre Leitfähigkeit gesteuert, so dass die hergestellten Filme elektrisch adressierbar waren. Der Prozess der photokatalytischen Reduktion wurde in Abhängigkeit der UV-Belichtungsdauer (0–7 Stunden), der Filmdicke und der eingesetzten TNC untersucht und mit Hilfe unterschiedlicher Methoden charakterisiert. Es wurden Ladungstransport-Messungen, sowie spektroskopische (UV-Vis-Spektroskopie, IR-Spektroskopie, Raman-Spektroskopie, XPS) und mikroskopische Untersuchungen (AFM, REM) durchgeführt, die zeigen, dass das GO/rGO-Verhältnis und das (GO/rGO)/TNC-Verhältnis mit der UV-Belichtungsdauer eingestellt werden können. Für die TNR-basierten Hybridfilme konnten höhere Leitwerte erzielt werden als für die TNP-basierten Systeme, was mit den unterschiedlichen Größen, exponierten Kristallfacetten und der Oberflächenbeschaffenheit der TNC zusammenhängen kann. Es wird angenommen, dass während der photokatalytischen Reduktion von GO die organischen Liganden an der Oberfläche der TNC (hauptsächlich Oleylamin) oxidiert werden und diese Oxidation eine Triebkraft für die Entstehung von rGO ist. Der allgemein höhere Organikanteil der TNRs verglichen zu den TNPs unterstützt diese Annahme, ebenso wie IR-spektroskopische Untersuchungen, die zeigen, dass mit zunehmender Belichtungszeit die Intensität der Signale, die dem Liganden zugeordnet sind, abnimmt. Die Reduktionsmethode wurde außerdem zur selektiven Reduktion bestimmter Bereiche für die photokatalytisch-lithographische Herstellung von GO/rGO/TNC-Arrays mit angepasster Zusammensetzung eingesetzt. Aufgrund des einstellbaren GO/rGO-Verhältnisses, können die Hydrophilie und allgemein die chemischen Eigenschaften der Hybridfilme eingestellt werden. Der Einfluss dieser Variationen wurde hinsichtlich der Sensitivität von GO/rGO/TNC-Chemiresistoren auf flexiblen Substraten gegenüber Änderungen der r.h. untersucht. Die Kompositfilme zeigten schnelle, reversible Antworten und höhere Sensitivitäten als reine GO/rGO-Filme. Die GO/rGO/TNP-Filme zeigten die schnellsten und höchsten Antworten, wobei mit zunehmendem Reduktionsgrad die Sensitivität gegenüber r.h. abnahm. Die Sensoren konnten auch zur Detektion von Körperluftfeuchtigkeit (Atemfrequenz, Fingerdistanz) verwendet werden. Generell zeigten die Sensoren, je nach r.h. und nach Reduktionsgrad, positive oder negative Widerstandsänderungen. Die Chemiresistor-Messungen von GO/rGO/TNP-Filmen wurden mit mikrogravimetrischen Messungen kombiniert, wobei gezeigt werden konnte, dass die charakteristischen Sensorantworten nicht von der aufgenommenen Analytmenge bestimmt werden, sondern die Film-Analyt-Interaktion, je nach Filmzusammensetzung, unterschiedliche Effekte induziert. Abschließend wurde die chemische Selektivität der GO/rGO/TNC-Filme gegenüber VOCs (Toluol, MIBK, 1-Propanol) und Wasser getestet (50–5000 ppm), wobei auch hier die Filme die höchste Sensitivität für Wasserdampf, gefolgt von MIBK, 1-Propanol und Toluol, aufwiesen und mit zunehmendem Reduktionsgrad die Sensitivität gegenüber polaren Lösungsmitteln abnahm.

2 Abstract

In this work, hybrid thin films consisting of (i) organically cross-linked gold nanoparticles (GNPs) and (ii) graphene oxide and TiO_2 nanocrystals (GO/TNCs) were fabricated and investigated regarding their application as chemiresistor-type sensors for the detection of volatile organic compounds (VOCs) and relative humidity (r.h.).

In the first presented study, a photolithographic method was developed and optimized to pattern substrate-supported 1,9-nonanedithiol (9DT)-cross-linked GNP thin films and to fabricate chemiresistor arrays. GNPs of different diameters (~4 and ~8 nm) were used for film fabrication. The method is based on lithographic patterning of a poly(methyl methacrylate) (PMMA) sacrificial layer using deep ultraviolet (DUV) radiation (254 nm), combined with an established layer-by-layer spin-coating process for the deposition of hybrid GNP/9DT films. In a lift-off process, the PMMA layer is dissolved to obtain patterned, isolated GNP film regions. The resolution limit of the lift-off method was investigated by structuring PMMA using electron beam lithography. It was demonstrated that intact GNP/9DT film structures with sizes down to 5 µm could be patterned on silicon wafers. Furthermore, the lithographic method was used for the selective molecular doping of cross-linked $GNP_{8.2\ nm}$/9DT films by selectively masking and exposing specific film pairs on an 4×2 array with PMMA, in order to manipulate the film composition by immersion in a thiol or dithiol solution. By doping the organic matrix surrounding the GNPs, the sensing properties of individual sensors of the array were adjusted. The thiols/dithiols used for the refunctionalization of the GNP surfaces were hexa(ethylene glycol)-dithiol, 2,3-dimercaptopropanol, and 4-nitrothiophenol, resulting in an array of films with four different compositions (including untreated GNP/9DT films). The resistive responses of the array to vapors of octane, heptane, toluene, methyl isobutyl ketone (MIBK), ethanol, 1-propanol, 1-butanol, and water in a concentration range of 50–8000 ppm were investigated. Both, the refunctionalization of the 9DT/GNP films and the UV irradiation during PMMA lithography led to a change in the selectivity of the sensors. Compared to the GNP/9DT films, the post-treated films showed higher sensitivities to polar analytes, resulting in specific response patterns for different classes of analytes based on combinations of the responses from different sensors. Hence, this method is very promising for the fabrication of electronic noses for analyte recognition.

In the second presented project, it was demonstrated that the hybrid nanostructure of organically cross-linked GNP composite films can induce analyte-dependent response times that can be used for the recognition and discrimination of various VOCs. Firstly, the dynamic responses of α,ω-alkanedithiol (ADT)-cross-linked GNP films were investigated and compared by exposing them to vapors of toluene, 1-butanol, 1-propanol, 2-propanol, ethanol, water, MIBK, and different homologous alkanes. Characteristic features related

to response kinetics, such as t_{80} response times and the integrated area below the transient responses, were extracted. It was shown that the response times mainly depend on the molecular volume of the analyte, unlike the maximum resistive signal amplitude, which is mainly determined by the polarity and vapor pressure of the analytes. This behavior was attributed to a diffusion-limited process of the analyte molecules within the sensor film resulting in significantly retarded responses for larger analytes. In this context, various methods were established to adjust the analyte-dependent response times. On the one hand, different lengths of ADT cross-linkers (4DT to 10DT) were used for film fabrication to influence the molecular transport of analyte molecules through the adjusted interparticle gaps. On the other hand, it was shown that the response kinetics can be influenced by the GNP diameter, which also impacts the film nanogeometry. Furthermore, it was demonstrated that UV irradiation of GNP/9DT films leads to retardations of the response times. The influence of UV radiation on the GNP film composition and structure was investigated using X-ray photoelectron spectroscopy (XPS), optical, and electrical measurements, where UV-induced oxidation of primarily non-cross-linking dithiols was identified as the main effect via XPS measurements. Using these methods, a chemiresistor array of ADT-cross-linked GNP films with adjusted response times was investigated, and it was shown that the application of linear discriminant analysis, based on combinations of resistive (maximum signal response) and kinetic response features (area, t_{80}), enabled the discrimination between very similar VOCs. In a final study, it was also demonstrated that the adjustable, analyte-dependent response times of GNP/6DT films can be used to discriminate binary VOC mixtures and determine their composition at a constant total analyte concentration.

The third project of this thesis involved GO/TNC nanocomposite films and their application as flexible, resistive sensors for humidity and for VOCs. First, a layer-by-layer spin-coating method was developed to fabricate substrate-supported layered systems from colloidal solutions of GO and photocatalytically active TNCs on various substrates such as silicon wafers, quartz glass, and polyimide (PI) foil. Organically-stabilized TiO_2 nanorods (TNRs, 40 nm length, 3 nm diameter) and TiO_2 nanoplates (TNPs, 21 nm edge length, 10 nm thickness) were used for fabrication. GO and TNCs were prepared following established synthesis routes. Additional parameters, such as the concentration of the respective solutions and the number of deposition cycles, were adjusted to tune the hybrid film composition and thickness. The fabricated layered systems were characterized using spectroscopic methods (infrared (IR), Raman, and UV-vis spectroscopy) and microscopic methods (atomic force microscopy (AFM), scanning electron microscopy (SEM)). Homogeneous, layered hybrid films with adjustable thicknesses ranging from 15-150 nm were

prepared, in which the TNCs were uniformly distributed between GO layers, as demonstrated by SEM and UV-vis spectroscopy.

Next, the GO/rGO (reduced GO) ratio of the hybrid materials was selectively adjusted via UV-assisted photocatalytic reduction (254 nm) of GO, thereby controlling their conductivity and enabling electrical addressability. The photocatalytic reduction process was studied by varying the UV exposure time (0-7 hours), film thickness, and the types of incorporated TNCs. The reduction was monitored via charge transport measurements, as well as spectroscopic (UV-vis spectroscopy, IR spectroscopy, and XPS) and microscopic analyses (AFM, SEM). We demonstrated that the GO/rGO ratio and (GO/rGO)/TNC ratio can be controlled by the UV exposure duration. The TNR-based hybrid films exhibited higher conductivity compared to the TNP-based systems, which could be attributed to differences in size, exposed crystal facets, and surface properties of the TNCs. We assume that during the photocatalytic reduction of GO, the organic ligands on the surface of the TNCs (primarily oleylamine) were oxidized, and this oxidation acted as a driving force for rGO formation. The generally higher organic content of TNRs compared to TNPs supported this assumption, as confirmed by IR spectroscopy, which showed a decrease in the intensity of oleylamine-related signals with increasing UV exposure times.

The reduction method was further used for the selective reduction of specific areas to fabricate GO/rGO/TNC arrays with adjusted compositions via photocatalytic lithography, i.e., UV exposure through a photomask. By adjusting the GO/rGO ratio, the hydrophilicity and general chemical composition of the hybrid films was tuned. The influence of varying degrees of reduction on the sensitivity of GO/rGO/TNC chemiresistors on flexible substrates towards r.h. was investigated. The composite films exhibited fast and reversible responses, with overall higher sensitivities compared to pure GO/rGO films. Among the GO/rGO/TNC films, the GO/rGO/TNP films showed the fastest and highest responses, while the sensitivity to r.h. decreased with increasing degree of reduction. The sensors were tested to detect body-related humidity (breathing rate, finger approximation). In general, depending on the r.h. level and the degree of GO reduction, the sensors exhibited positive or negative resistance changes. The chemiresistive measurements of GO/rGO/TNP films were correlated with microgravimetric measurements using hybrid film-coated quartz crystal microbalances, demonstrating that the characteristic responses were not determined by the amount of analyte absorbed but rather by the film-water molecules interaction, which induced different effects depending on the film composition/degree of reduction. Finally, the chemical selectivity of GO/rGO/TNC films was tested for VOCs (toluene, MIBK, 1-propanol) and water (50-5000 ppm). In this concentration range, all films responded with an increase of resistance, and showed the highest sensitivity to water vapor, followed by MIBK, 1-propanol, and toluene. With increasing degree of reduction, the sensitivity to polar solvents decreased.

3 Introduction

With our world becoming increasingly interconnected, sensor technologies, as a key means for gathering information, hold immense potential to be advanced. In 2013, an editorial in the journal *Angewandte Chemie* treated the slow progress in the development of *true* sensors to continuously monitor relevant parameters in environmental or health care applications and ventured a *look into the future*, emphasizing the need for new sensors to become significantly smaller, more reliable and user-friendly, to have adequate lifetimes, and ideally be self-powered.[6] Today, the challenge to fulfill these requirements remains.

With the rise of the *Internet of Things*, aiming at seamlessly integrating multiple devices that interact with our surroundings into a smart network for different applications, the development of novel gas and vapor sensors has been the focus of many recent studies. Whether in air pollution control due to our pressing global environmental crisis, industrial applications, home automation, public safety, or medical diagnosis and personalized health care – the fast and reliable detection of substances in the gas phase is ubiquitous and indispensable.[7]

Among the vast range of target gaseous substances, volatile organic compounds (VOCs) are a particularly significant group of analytes, since they account for a majority of air pollutants and gaseous metabolites. For instance, the analysis of VOCs from exhaled breath or the head-space of bodily fluids can be used for non-invasive retrieval of valuable information on a human's health status.[8] At the same time, monitoring the levels of humidity (i.e., water vapor) has also become increasingly interesting for personal health care, since body-related humidity can be used to monitor respiration, skin moisture, or lung hydration.[9] Furthermore, body-related humidity can be exploited for non-contact switches and speech recognition technologies. The advancement of such remote health monitoring applications is a highly active field of research, not least because the COVID-19 pandemic shed light on the urgency of having efficient, easily scalable systems in place to manage current and future health crises.

In this context, a growing demand for VOC and humidity sensors is their successful implementation in portable, or wearable flexible devices. As the target molecules usually occur in complex and unknown mixtures, their recognition and discrimination in such a "real-life" environment is paramount. Here, a common strategy to achieve a high selectivity is the development of sensor arrays based on cross-sensitive materials to obtain target-specific fingerprints. Further, humidity monitoring finds application in many different settings: For example, relative humidity (r.h.) levels have to be constant around 60 % in hospital operating rooms, but nearly 12 % on airplanes.[10] Thus, sensors with well-adjusted operation ranges for their specific targeted applications are needed. In addition to a good selectivity and linearity, the ideal vapor sensor should have high sensitivities, low response times, great stability and robustness.

Research in nanotechnology, focusing on systems of dimensions ranging from 1–100 nm, significantly contributed to efforts for meeting the aforementioned requirements, with the development of tailored materials with exceptional properties and novel sensing principles for the precise design of advanced gas and vapor sensors.[10–12] In general, the use of nanomaterials comes along with an enhanced sensing performance, e.g., in terms of sensitivity, based on the increased active surface of the materials. They also have tunable physical and chemical properties, depending on their size, shape and composition, and offer the opportunity to fabricate hybrid materials with synergistic effects.[8] Nanomaterials for VOC and humidity sensing can be classified in zero-, one-, two- and three-dimensional materials, and include, among others, metal and metal oxide nanoparticles, carbon-based materials such as graphene-derivatives, carbon black or carbon nanotubes, metal chalcogenides, cellulose paper, and metal organic frameworks.[8,9,12] Overall, it is possible to implement nanostructures as sensitive material in sensor types with different transduction principles. Generally, a sensor consists of the sensing material that responds with a change in a physical property upon interaction with the target molecules, and a transducer that converts the physical change into an electrical or optical signal to be read out.[13] Depending on their operation and transduction principles, VOC and humidity sensors can be classified into different types, such as optical sensors like colorimetric sensors, electromechanical sensors such as quartz crystal microbalances (QCMs) or surface acoustic wave sensors, and electrical sensors, e.g., field-effect transistors, impedance sensors, capacitors and resistors.[8,9,13–15]

This thesis focuses on the development of resistive VOC and humidity sensors and sensor arrays based on tailored hybrid nanomaterials made from (i) organically cross-linked gold nanoparticles and (ii) layered graphene oxide and titania nanocrystals, addressing the aforementioned challenges with novel approaches for enhanced sensor performance.

In the following, a short outline of the structure of this dissertation will be provided. Section 4 aims to establish the theoretical foundation for the research conducted within the framework of the thesis. Section 5 describes in detail the specific goals of the different completed projects, that are subsequently presented and discussed in section 6, which as well provides an outlook for future research possibilities. Finally, all conducted experimental procedures are summarized in section 7.

4 Nanomaterials for Chemiresistive Sensing

A sensor that responds with a change in its electrical resistance to exposure to a chemical compound is commonly referred to as *chemiresistor*. Chemiresistors have been extensively studied and are widely employed for the detection of gases and vapors. Sensing devices with a resistive readout have numerous advantages, such as low power consumption, compact dimensions, re-usability, and simple circuitry, making them attractive for the facile integration in portable or wearable electronics. Figure 4.1a) shows a basic schematic of the chemiresistive measurement principle: The chemiresistor consists of a sensing material deposited onto interdigitated electrodes on an inert substrate, and the material's resistance is continuously measured. Upon exposure to an analyte (green), which interacts with the sensing material, a change in the material's baseline resistance is detected as sensor signal. By using interdigitated electrodes, the sensitive area is maximized, and it further allows for the use of materials with relatively high resistivities. Depending on the nature of the sensing material and the analyte, different chemical or physical interactions between both can trigger the observed response.

Various classes of materials show chemiresistive properties. For example, commercial gas sensors are based on metal oxide (MOX) semiconductors like SnO_2.[16] Here, the sensing principle is based on the oxidation/reduction of gas molecules upon reaction with ionosorbed oxygen species on the MOX surface, which results in a decreasing/increasing width of a space charge layer, and as a consequence, a decrease/increase in resistance.[17] While MOX sensors are highly sensitive, they often lack selectivity, show significant baseline drifts, and have very high operating temperatures.[18] In pursuit of high-performing

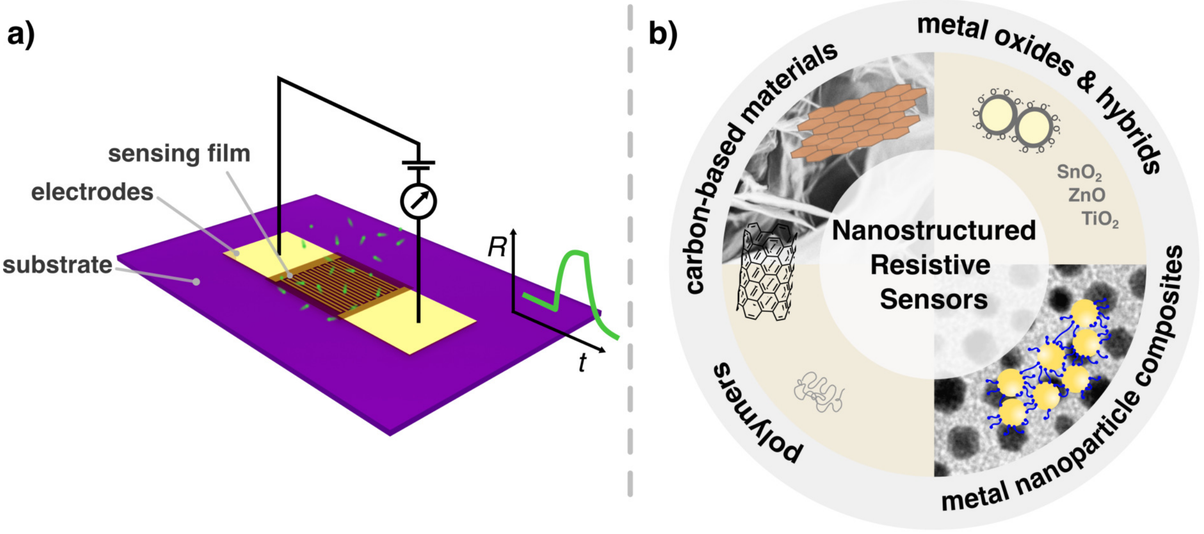

Figure 4.1: a) Schematic depiction of a resistive sensor. b) Overview of various nanostructured materials used for chemiresistive gas and vapor sensing applications.

materials for chemiresistive gas sensors with optimized sensing parameters, various novel nanomaterials of different morphologies and compositions have emerged, often enabling resistive gas sensing at room temperatures.[12] Figure 4.1b) shows a selection of promising nanomaterial classes for gas and vapor sensing applications, including nanostructured MOXs,[17,18] conductive polymers,[19] as well as carbon-based materials,[20] such as graphene, graphene oxide (GO), carbon nanotubes (CNTs), and their composites, and metal nanoparticle assemblies,[21,22] like gold nanoparticle (GNP)-based hybrids.[23] In this regard, even combinations of different classes[24] can be implemented, e.g., as partially selective sensors in a sensor array. In general, the inherently large surface of nanostructured materials can boost the sensing performance by an increased specific surface area for analyte sorption. In addition, their dimensions inherently promote the possibility for sensor miniaturization. Rooted in the hybrid nature of nanocomposite films and of colloidal nanoparticles, and due to sophisticated synthetic methods that enable controlled nanoparticle architectures and complex hybrid systems, the use of nanomaterials allows for the precise design and tunability of a sensitive material. For different classes, the chemiresistive behavior is based on different transduction mechanisms, resulting in special properties, varying affinities, etc., for each class of materials. For instance, the conductivity of composite films comprised of organically stabilized or cross-linked metal nanoparticles is based on highly distance-sensitive tunneling between the metal nanoparticles. Hence, sorption of analyte molecules to the organic matrix, which dictates the interparticular distance, results in pronounced changes in the measured resistivity. Graphene-related materials score with an immense specific surface for analyte sorption, and the chemiresistive responses are generally based on a charge transfer mechanism induced by adsorption of analyte molecules.[21,25]

For the present thesis, the last two listed classes – carbon-based and metal nanoparticle-based chemiresistors – are of special relevance, since it involves different projects about the elaboration and tunability of (i) cross-linked GNP chemiresistor arrays, as well as of (ii) flexible GO/TiO_2-based nanohybrid chemiresistors, for sensing of volatile organic compounds (VOCs) and humidity.

The following sections will give a theory introduction to the unique properties of two different classes of nanomaterials relevant to the present thesis – GNPs and GNP-based composites (sections 4.1 – 4.2) and GO-based materials (section 4.3) – as well as an overview of current research developments through the lens of chemical sensing applications, with special attention to chemiresistive VOC and humidity sensing.

4.1 Gold Nanoparticles

Dating back to antiquity, nicely red- and purple colored glasses and ceramics were handcrafted by adding gold.[26,27] It was not until the 19th century, when Faraday first described the ruby-red color of gold-containing colloidal solutions as arising from *finely-divided gold* – later known as GNPs.[27,28]

With the surging field of nanotechnology, GNPs have gained prominence among different (noble) metal nanoparticles owing to their unique optical properties, high chemical stability, and versatile surface chemistry. These properties made them a paradigm for different fundamental investigations on the nanoscale,[29] and, at the same time, boosted the research on various potential applications of GNPs, e.g., in catalysis, biomedicine, and sensing.[30–32]

4.1.1 Synthesis and Optical Properties

Over the course of the 20th century, several procedures have emerged for the synthesis of GNPs by the reduction of molecular precursors. One of the best-known approaches is the Turkevich method, by which spherical citrate-stabilized GNPs are obtained in aqueous solution via the citrate-mediated reduction of $HAuCl_4$.[33] This method has been continuously adapted and improved in terms of GNP size distribution and uniformity.[32,34] In 1994, the report of the Brust-Schiffrin method entailed a significant breakthrough for GNP syntheses. For the first time, the formation of thiol-stabilized GNPs of controllable size and dispersity with good colloidal stability in an organic solvent was reported. The method is based on a two-phase system of water/toluene, in which a surfactant, tetraoctylammonium bromide (TOAB), is used as phase transfer agent for the gold precursor from the aqueous phase, and the subsequent reduction to gold by sodium borohydride (SBH) in the presence of dodecanethiol as stabilizing ligand.[35] Within the scope of this present work, the use of amine-capped GNPs for sensor fabrication is highly relevant, since it enables a facile ligand exchange with stronger binding thiols and dithiols, allowing for stable GNP film formation.[36,37] In this context, a method derived from the Brust-Schiffrin synthesis, reported by Leff et al., is used for fabrication of amine-stabilized GNPs with diameters that can be adjusted in the range between 2–7 nm, with relatively broad size distributions (σ ~20 %).[38] In this procedure, $HAuCl_4$ is transferred from water to toluene using TOAB, and GNPs are formed upon addition of SBH in the presence of 1-dodecylamine (12A) in ambient conditions. Another synthetic route that yields amine-stabilized GNPs was proposed by Peng et al.[39] Following this method, in which $HAuCl_4$ is reduced by tert-butylamine borane (TBAB) in tetralin in the presence of oleylamine (OLAM), GNPs of controlled diameters between 2.5–10 nm and narrow size distributions are obtained.

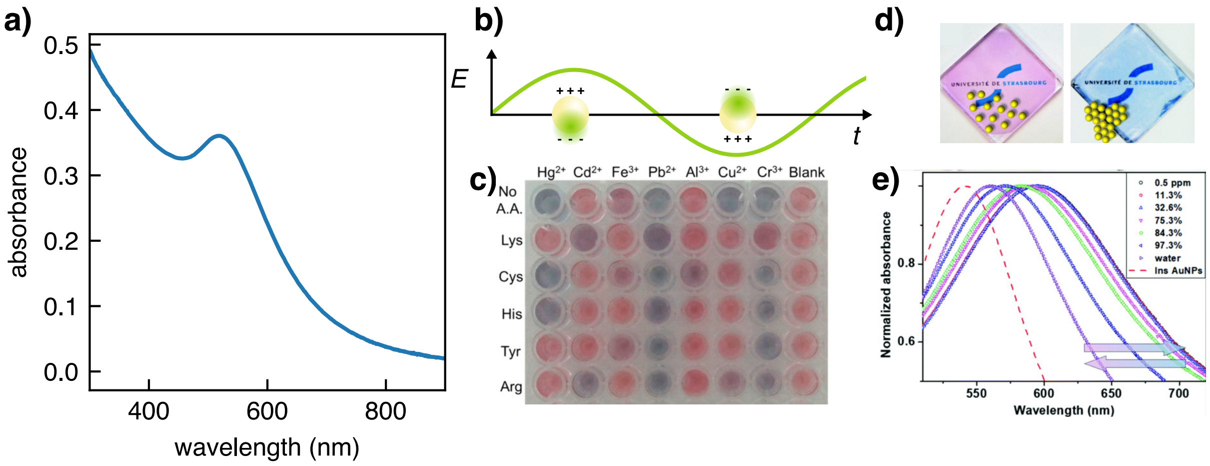

Figure 4.2: a) Typical UV-vis absorbance spectrum of a diluted GNP solution in heptane, showing an absorbance maximum around 515 nm. (GNP size: ~4 nm). b) Schematic of the emergence of LSPR: Interaction of the electric field of incident light with conduction electrons in GNPs (yellow spheres) leads to a charge carrier displacement, inducing a restoring force, and hence, dipole oscillations along the external field. c) Photograph of a colorimetric sensor array based on amino acid-functionalized GNPs for the detection of cations. (Adapted with permission from Ref. [44] ©2014 American Chemical Society). d) Photographs of 2D GNP/PEG networks in humid (left) and dry (right) conditions, and e) corresponding LSPR shifts. (Adapted and reproduced from Ref. [45] with permission from the Royal Society of Chemistry).

Here, the GNP size can be tuned by variations of the temperature (2–40 °C). According to Peng et al., GNPs with larger diameter form at lower reaction temperatures.[39] Interestingly, the opposite trend, namely the formation of larger particles with increasing temperature, was observed in our group after slight modifications, i.e., using a different solvent (hexane) and ligand (12A).

As mentioned previously, GNP dispersions typically exhibit an intense red-pink color – drastically different from the shiny yellow of bulk gold. The distinct red color arises from strong absorption in the visible spectral region. For spherical GNPs, the maximal absorbance typically occurs around ~520 nm, as exemplary shown in figure 4.2a) for ~4 nm sized GNPs synthesized using the Leff method. The strong absorption can be explained by a phenomenon known as localized surface plasmon resonance (LSPR), that also occurs for other noble metal nanoparticles at distinct wavelengths. The phenomenon can be described by the Mie theory which treats the collective oscillations of conduction band electrons when interacting with incident light. When the wavelength of incident light is much larger than a particle of a radius r, ($2r \ll \lambda$, usually $2r < 25$ nm), the electric field can be considered as constant, and the interaction is governed by electrostatics.[40–43] This is referred to as the quasi-static approximation, since wavelength-dependent dielectric functions of the GNP and of the surrounding are taken into account for an electrostatic model.[43]

Figure 4.2b) schematically depicts the interaction of GNPs with an incident wavelength, which results in coherent collective oscillation of the conduction band electrons of the metal with respect to the positively charged cores, resulting in charge separation, causing a restoring force and a dipole oscillation in the direction of the electric field. When the oscillation is in resonance with the frequency of the incident wave, the maximal absorbance can be observed. According to the Mie theory, the total extinction cross-section σ_{ext} for absorption and scattering can be described as the sum of all electric and magnetic multipole oscillations.[46] For GNPs within the quasistatic approximation regime, only the dipolar modes contribute to the cross-section, as described in the following equation 1:

$$\sigma_{\mathrm{ext}} = \frac{9V_{\mathrm{p}}{\epsilon_{\mathrm{m}}}^{3/2}}{c_0}\frac{\omega\epsilon_2(\omega)}{(\epsilon_1(\omega)+2\epsilon_{\mathrm{m}})^2+(\epsilon_2(\omega))^2} \tag{1}$$

where V_{p} is the volume of a spherical particle, c_0 the speed of light, ω the angular frequency of the exciting light, and ϵ_{m} the dielectric constant of the surrounding medium. ϵ_1 and ϵ_2 denote the frequency-dependent, real and imaginary part of the complex dielectric function $\epsilon(\omega)$ of gold, respectively ($\epsilon(\omega) = \epsilon_1 + i\epsilon_2$).[46] Based on equation 1, there is no size dependence for the absorption within the quasi-static approximation, except for intensity variations due to the volume dependence on the particle radius.[42] However, since size-dependent plasmon bandwidths are observed experimentally, a modification to the Mie theory has been introduced which takes into account a size-dependent dielectric function of the nanoparticles.[42] Further, the frequency of the LSPR depends on the GNP's size,[47] shape, dielectric surrounding, and state of aggregation.[40] This results in distinct coloration of GNP solutions or assemblies, that can often be distinguished even by the naked eye. The sensitivity of the change of color on the GNP's distance and chemical surrounding enables the use of GNPs for colorimetric sensing applications.[48,49] For instance, reducing the distance between GNPs compared to the colloidally distributed particles in solution, results in coupling effects and a red-shift of the LSPR band maximum.[50] Figure 4.2c) shows an example for the colorimetric detection of various metal ions using a sensor array of amino acid-functionalized, 11-mercaptoundecanoic acid-capped GNPs.[44] Specific complexations of metal ions by certain amino acids result in the destabilization of the GNPs and aggregation-induced color changes. Based on this array, each substrate produces a distinct pattern enabling naked-eye discrimination between the targeted metal ions. Another example is displayed in figures 4.2d-e), in which a network of GNPs, interconnected by hygroscopic linkers, is used as plasmonic humidity sensor.[45] Part d) shows a photograph of the network in humid (left) and dry (right) environment, where a distinct shift from blue to red is observed, due to a swelling-induced increase of interparticle distances, and changes of LSPR coupling effects. Figure part e) shows the respective normalized absorbance spectra, demonstrating reversible shifts in LSPR maximum with changes in humidity levels.[45]

4.2 Gold Nanoparticle Composite Networks

Functional assemblies of GNP composites have emerged as promising materials for numerous applications owing to their exceptional properties. GNP networks often contain organic ligands or cross-linkers with functional groups, e.g., amines, thiols, phosphines, or carboxylates. One purpose of these molecules is to prevent coalescence of the GNPs; additionally, the hybrid nature of the composite network allows for the adjustment of the material by choice of the organic molecule. Given the strong bond between gold and sulfur,[36] thiols and dithiols have a special status, and dithiols, due to their bifunctionality, render cross-linkage of GNPs possible.

25 years ago, in 1998, Brust et al. investigated the optical and electronic properties of self-assembled films comprised of α,ω-alkanedithiol (ADT)-cross-linked GNPs, finding that they showed non-metallic properties that strongly depended on the cross-linking molecules.[51]

In our group, composites of ADT-cross-linked GNPs have also been studied intensively during the last decades for different applications, like strain sensors,[52,53] micro-/nanoelectromechanical system sensors,[54,55] and resistive chemical sensors.[56–58] In dependence of the desired film properties and the targeted application, GNP thin films can be deposited on a variety of substrates using different methods, including layer-by-layer (LbL) self-assembly,[59] ink-jet printing,[58,60] spray-coating,[61] drop-casting,[62] or LbL spin-coating (SC).[37] In a majority of our own studies, GNP/ADT films were prepared using a LbL SC method established in our group in 2011.[37] Briefly, a GNP stock solution, and a ADT cross-linker solution are alternatively deposited onto a rotating substrate, e.g., a glass slide. The film thickness can be adjusted by the choice of the linker, and the number of SC deposition cycles.[37] By choice of different lengths of ADTs (in our group, commonly varied between 4–10 methylene units), the interparticle distances as well as the related characteristics, like the films' optical, electrical, and mechanical properties, can be well adjusted.[63] The following sections will outline a few concepts regarding the electrical properties and resistive chemical sensing applications of GNP composites, mainly focusing on GNP/ADT films.

4.2.1 Charge Transport Properties

The sensing mechanism of organically stabilized or interlinked GNP composites is rooted in their special charge transport properties. Based on the notion that within such a composite material the organic molecules act as tunneling junctions between the conductive GNP cores, the charge transport can be well described by a model of thermally activated tunneling proposed by Terrill et al. in 1995.[64] According to this model, the conductivity of the composite is defined as in equation 2,[64]

$$\sigma(\delta, T) = \sigma_{\mathrm{P}} \exp\left(-\beta\delta\right) \exp\left(-\frac{E_{\mathrm{A}}}{k_{\mathrm{B}}T}\right) \tag{2}$$

in which σ_{P} is a pre-exponential factor, β the tunneling decay constant, δ denotes the interparticle distance, E_{A} is the activation energy, k_B is the Boltzmann constant, and T the temperature. The first term describes the tunneling process between conductive metal cores. Since tunneling is a distance-dependent process, the conductivity decreases exponentially with increasing interparticular distances. These distances are dictated by the size (chain length) of the insulating molecules that comprise the organic matrix surrounding the nanoparticles. The exponential decrease is reflected in β, which also depends on the nature of the linking/stabilizing molecules.[61] In this thesis, all films used for sensor fabrication, are based on (initially) ADT-cross-linked GNPs. In these hybrids, the Fermi level of GNPs lies between the the highest occupied molecular orbital (HOMO) and lowest unoccupied molecular orbital (LUMO) of the ADT molecule.[65] Electrons tunnel via a super-exchange pathway provided by the side orbitals of the linker.[66] Considering different cross-linking species, such as aromatic linkers, β decreases, due to delocalization of the electrons caused by resonance of the Fermi level with HOMO/LUMO energies of the organic molecules.[61]

Values for β can be estimated from experimental data from a plot of the composite's conductivities $\ln \sigma(\delta, T)$ in dependence of the interparticular distances δ. According to equation 2, the decay constant can be extracted as the slope when neglecting the dependence of the activation energy on the interparticle distance. Furthermore, temperature-dependent transport measurements can be used to extrapolate intercepts from plots of $\ln \sigma(\delta, T)$ vs. $1/T$. The extracted intercept can then be plotted against δ, e.g., as the relative number of methylene units for ADT cross-linked GNPs, to determine β.[65,67] Joseph et al. determined a decay constant $\beta = 0.61 \pm 0.1$ for ADT cross-linked GNPs, with reference to the number of methylene units of the cross-linkers.[68]

The aforementioned thermal activation of the charge transport process is considered in the second exponential term of equation 2. Here, different theories can be considered to describe the related activation energy E_{A}. An electrostatic approach for granular metals was proposed by Abeles et al., after which the conductivity is described using equation 3.[69]

$$\sigma \approx \sigma_{\mathrm{P}} \exp\left(-2\sqrt{\frac{C}{k_{\mathrm{B}}T}}\right) \tag{3}$$

In equation 3, C is equal to $\beta\delta E_{\mathrm{A}}$. The corresponding E_{A} for transferring an electron between two uncharged cores to form a charged pair is defined by equation 4,[69]

$$E_{\mathrm{A}} = \frac{e^2}{8\pi\epsilon\epsilon_0}\left(\frac{1}{r} - \frac{1}{r+\delta}\right) \tag{4}$$

where e is the elementary charge, ϵ the permittivity of the surrounding matrix, ϵ_0 the vacuum permittivity, r the particle radius, and δ the interparticle distance. Based on this theory, a higher conductivity is expected for GNPs of larger sizes. At a certain threshold for small GNPs, the activation barrier becomes too high to be overcome by thermal energy, resulting in a Coulomb blockade.[70] Experimentally determined values for E_{A} in dithiol-cross-linked GNP films were in good agreement with values calculated from equation 4.[51] Another approach to describe the activation is provided by the Marcus theory. Here, the free activation energy ΔG^* is derived from the repolarization of the organic matrix, according to equation 5,[65]

$$\Delta G^* = \frac{\lambda}{4} = \frac{e^2}{16\pi\epsilon_0}\left(\frac{1}{2r_1} + \frac{1}{2r_2} - \frac{1}{r}\right)\left(\frac{1}{\epsilon_{\mathrm{opt}}} - \frac{1}{\epsilon_{\mathrm{s}}}\right) \tag{5}$$

in which λ denotes the outer-sphere reorganization barrier energy, r_1, r_2 the radii of adjacent particles, r the center-to-center interparticle distance, and $\epsilon_{\mathrm{s}}, \epsilon_{\mathrm{opt}}$ the optical and static dielectric constant of the medium, respectively.

4.2.2 Resistive Chemical Sensing

The distance-sensitive charge transport mechanism in GNP composite thin films enables their use for resistive sensing applications that involve changes of the interparticle distances ($\Delta\delta$), for example as strain sensors.[71–73] For a conductive GNP film with a baseline resistance R_0, the sensor response $\frac{\Delta R}{R_0}$ is given by equation 6, which is derived from equation 2.[74,75]

$$\frac{\Delta R}{R_0} = \exp\left(\beta\Delta\delta\right)\exp\left(\frac{\Delta E_A}{k_{\mathrm{B}}T}\right) - 1 \tag{6}$$

In a similar fashion, GNP composites films, such as ADT-cross-linked networks, are suitable platforms for chemical sensing, e.g., for VOCs, gases, and vapors. In principle, the GNPs provide electrical conductivity enabling the resistive signal transduction, and the organic matrix the GNPs are embedded in provides selective binding sites for analyte molecules.[17] The first account of GNP composite chemiresistors was published by Wohltjen and Snow 25 years ago, in which octanethiol-stabilized gold nanoclusters were deposited onto interdigitated electrode structures and exposed to different VOCs and water.[76] To understand the observed response of such materials, two effects that occur during analyte exposure need to be addressed: First, analyte sorption leads to swelling of the film, which, in turn, leads to an increase in interparticle distances.[75,77] According to equation 6, this effect results in an increase of resistance. Secondly, analyte sorption to the film causes changes in the permittivity of the organic matrix of the sensing material. Mostly, VOC exposure results in an increased permittivity of the organic matrix for ADT-cross-linked GNPs. Taking into account equation 4, this effect would result in a smaller activation energy and consequently, a decrease in resistance. ADT/GNP films, however, mostly show positive $\frac{\Delta R}{R_0}$ responses, indicating that swelling of the film is the governing effect in this type of GNP films.

Regarding the ability of films to swell, Joseph et al. compared the sensing behavior of GNPs cross-linked using a flexible linker (1,12-dodecanedithiol) and GNPs cross-linked using a more rigid linker (4-staffane-3,3' "-dithiol). In their study, they found that the films with the rigid linkage exhibited a decrease in resistance for all tested vapors, compared to positive responses for the flexible film, suggesting that swelling might be inhibited by choice of the linker, resulting in a dominant permittivity effect for rigidly-linked films.[78] Further, Zhong and co-workers demonstrated an exponential increase in sensitivity towards vapors of toluene, benzene, and hexane for cross-linked GNP films with increasing cross-linker lengths.[79] Generally, alkanethiol-stabilized GNPs show higher sensitivities than cross-linked GNPs, since the swelling capability is not confined due to GNP interlinkage. However, they also show higher resistivities and lower mechanical stability.

Variations of the amount of sorbed analyte within the film might result in varying response amplitudes. The amount of sorbed analyte is directly linked to the concentration of the analyte in the test atmosphere during exposure, the partition coefficient and vapor pressure of the analyte, as well as the general affinity of the organic matrix towards the target analyte. It is straightforward to assume that matching polarity of the organic matrix and the target analyte result in higher affinities.[61] Additionally, analytes with lower vapor pressures lead to higher partitioning in the composite film, leading to overall higher response signals. Assuming that the change in resistance is proportional to the concentration of sorbed analyte, concentration-dependent measurements can be described using either

Langmuir-[61,77] or Langmuir-Henry[75] sorption isotherms (equations 7–8). Here, the Langmuir-Henry model complements the Langmuir model for selective analyte sorption by a term for non-selective bulk partitioning.[75]

$$\frac{\Delta R}{R_0} = \left(\frac{\Delta R}{R_0}\right)_{\mathrm{sat}} \frac{K_{\mathrm{L}} c_{\mathrm{v}}}{1 + K_{\mathrm{L}} c_{\mathrm{v}}} \tag{7}$$

$$\frac{\Delta R}{R_0} = \left(\frac{\Delta R}{R_0}\right)_{\mathrm{sat}} \frac{K_{\mathrm{L}} c_{\mathrm{v}}}{1 + K_{\mathrm{L}} c_{\mathrm{v}}} + K_{\mathrm{H}} c_{\mathrm{v}} \tag{8}$$

In equations 7–8, $\left(\frac{\Delta R}{R_0}\right)_{\mathrm{sat}}$ denotes the saturation sensor response, K_{L} is the Langmuir constant, K_{H} the Henry constant, and c_{v} is the gas-phase analyte concentration.

4.2.3 Sensor Arrays and Analyte Recognition

Precise analyte recognition and discrimination in complex mixtures remains a major challenge in the development of gas and vapor sensors. The hybrid nature of GNP composite films allows for the tunability of the chemiresistor's affinities and sensitivities, i.e., by adjusting the chemical nature (polarity, functional groups) of the film's organic matrix. This gives rise to the implementation of a variety of hybrid films in sensor arrays, often referred to as *electronic noses* (e-noses).[80] As the name implies, e-nose technology is inspired by the mammalian olfactory system, which relies on a broad variety of non-specific receptor cells in a convergent signaling path. Here, odors can be recognized and assigned by distinct "smell images" or patterns, arising from varying patterns of spatial activity in the olfactory bulb.[81] Similarly, by exploiting the sensors' cross-sensitivities on an array, analytes can be identified by means of a distinct response pattern or fingerprint obtained from

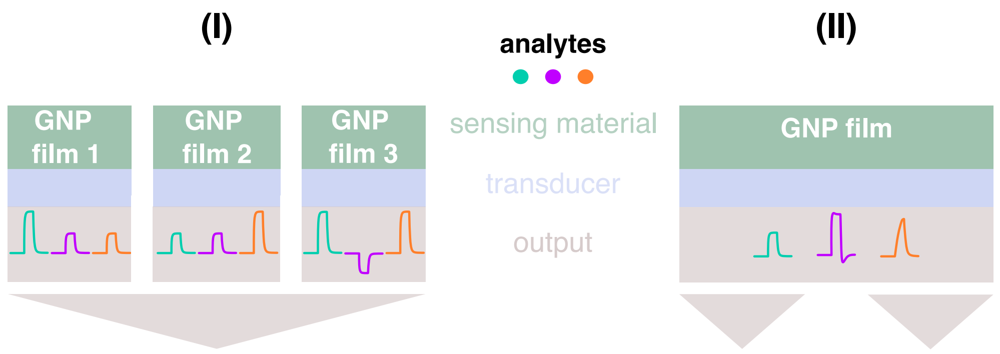

Figure 4.3: Sensing concepts for analyte recognition. (I) Assembly of separate sensors with individual outputs to generate a processed array output. (II) Individual type of sensor with multiparametric, independent response features. Inspired by Ref. [7].

combined responses of single sensors of the array.[21,22] In recent years, a large number of studies have been reported covering the use of GNP-based chemiresistor arrays for detecting, e.g., explosive substances,[82] pollutants,[83] and diagnosing diseases via breath analysis.[24,84] For instance, Haick and co-workers developed a portable chemiresistor array based on differently ligand-stabilized GNP film transducers for the diagnosis of COVID-19 from breath samples.[85] In these referenced works, the obtained patterns are solely based on the varying response amplitudes, i.e., the maximum relative resistance change, of chemiresistors with adjusted affinities, e.g., by variations of the organic ligands/linkers. This common concept to facilitate reliable analyte recognition is schematically outlined in figure 4.3 (I): In principle, each sensor responds to different analytes without being too specific. Usually, a target-specific response pattern is obtained by signal processing using multivariate classification algorithms, such as principal component analysis (PCA), artificial neural networks (ANNs), or linear discriminant analysis (LDA).[86] Among these, LDA is of relevance for this present thesis, since it will be used for sensor array data analysis. LDA is considered a supervised dimensionality reduction and classification algorithm that aims at finding linear combinations to maximize the separation between two or more classes (=analytes). Commonly, a sufficiently large data set is needed for multivariate analysis, since training and test sets are needed, in order to assess the accuracy of the analyte classification.

Another possible concept for this matter is the use of an individual sensor with multivariable or multiparametric sensing principles, that follow different selectivities, in order to combine independent responses for analyte recognition.[21] A related approach is depicted as (II) in figure 4.3, in which this could be accomplished by extracting distinct features of the obtained transient responses, when, e.g., the kinetic and thermodynamic responsive behavior are based on different physical interactions between target analyte and sensing material. These unique response features can then again be fed as input for multivariate algorithms.

In this context, a few studies have addressed the response kinetics of GNP-based chemiresistors, e.g., when operated in water as a so-called electronic tongue (in analogy to the nose).[87] More studies have proposed the potential of using particular kinetic response features for analyte recognition and discrimination.[79,88–91]

In the present thesis, both concepts come to play for the design of well-adjusted ADT/GNP-based chemiresistor arrays for analyte recognition; since methods to control and tune the GNP film composition, as well as independent response features, are elaborated.

4.3 Graphene Oxide-Based Materials

Since its discovery almost 20 years ago,[92] graphene – a 2D single-atom-layered, sp^2-bonded carbon allotrope arranged in a hexagonal lattice[93] – has fascinated the scientific community owing to its unique mechanical and electronic properties, and has sparked excessive research on its potential applications.[94] Based on these efforts, a myriad of graphene derivatives have been investigated, including, i.a., multilayered graphene, graphene quantum dots, and graphene oxide (GO).[95]

Among those, GO is of special interest, not least because of the possibility to produce large quantities of the material as colloidal solutions and as powders, and to structurally convert it to graphene-like reduced GO (rGO).[94–96] Like graphene, GO consists of an atomic layer of carbon arranged in a honeycomb structure. In contrast to pristine graphene, GO exhibits various defects, including oxygenated functional groups and vacancies in the carbon lattice that impart sp^3 hybridization.[97] These defects greatly influence the resulting properties of the material, making GO fundamentally different from graphene. For instance, GO is an electrical insulator, is highly hydrophilic and forms stable colloidal aqueous solutions. Because of its high tunability, e.g., in the sheet size, type and degree of functionalization, GO itself can be considered as a family of materials.[95,98] Due to its large surface area and multiple functional groups as sorption sites for guest molecules, GO is an ideal building block for gas- and humidity sensors. Further, the presence of certain functional groups is highly desirable in terms of chemical re-functionalization of GO or for fabrication of composite materials, where the groups act as reactive or anchoring sites, e.g., for metal organic frameworks,[99] or MOXs.[100,101] The assembly of GO and other nanomaterials or polymers is enabled by bonding interactions due to the chemical activity of GO, and gives rise to the fabrication of multifunctional composites with combined properties.[102,103]

A widely accepted model of a general chemical structure of GO is the Lerf-Klinowski (LK) model that was based on the characterization of the derivatization of graphite to GO via ^{13}C nuclear magnetic resonance- and Fourier-transform infrared (FTIR) spectroscopy.[104] An exemplary structure based on an adapted LK model is shown in figure 4.4a). Accordingly, GO is composed of three regions: aromatic regions, regions of aliphatic six-membered carbon rings, and regions with carbon vacancies.[105] The structure consists of a nearly flat carbon lattice, where hydroxy and epoxide groups are present in the basal plane in close proximity, causing a slight tetrahedral distortion, which results in wrinkling of GO sheets. The sheet edges are predominantly decorated with carboxy- and hydroxy groups, making GO slightly acidic,[106] and carbonyls form at the edges of structural holes.[105] The formation of structural holes can be explained by the release of CO_2 and CO during oxidation. Other proposed defects include radicals and organosulfates.[97]

4.3.1 Graphene Oxide Synthesis

The wet-chemical preparation of GO involves the oxidative exfoliation of graphite flakes. The first synthetic route to obtain multilayered graphite oxide was reported in the mid 19th century by Brodie who treated graphite in a highly oxidizing medium of fuming nitric acid and $KClO_4$ for several days.[97,107] Adaptations to the Brodie method to produce multilayered graphite oxide using $KClO_4$ were later reported by Staudenmaier[108] and Hofmann.[109] These methods, however, have major drawbacks, such as the formation of hazardous gases and long reaction times. The most prominent method to synthesize GO, that is still widely used up to this date, was developed by Hummers and Offeman in 1958.[110] To that time, the method was the safest procedure to produce bulk quantities of GO, in that it circumvented the use of chlorate as oxidizing agent and hence, the formation of explosive by-products. Instead, graphite flakes are oxidized using $KMnO_4$, sulfuric acid, and $NaNO_3$.[110] Still, this method yields toxic nitrous fumes due to the in situ formation of nitric acid during the reaction. In 2010, Tour and co-workers developed an improved, nitrate-free Hummers method in which phosphoric acid was used to assist the oxidative exfoliation of graphite. Following a thorough purification procedure, high yields of GO with a higher degree of oxidation than Hummers' GO, large lateral sizes, and few defects in the graphitic backbone were obtained.[112] In the following years,

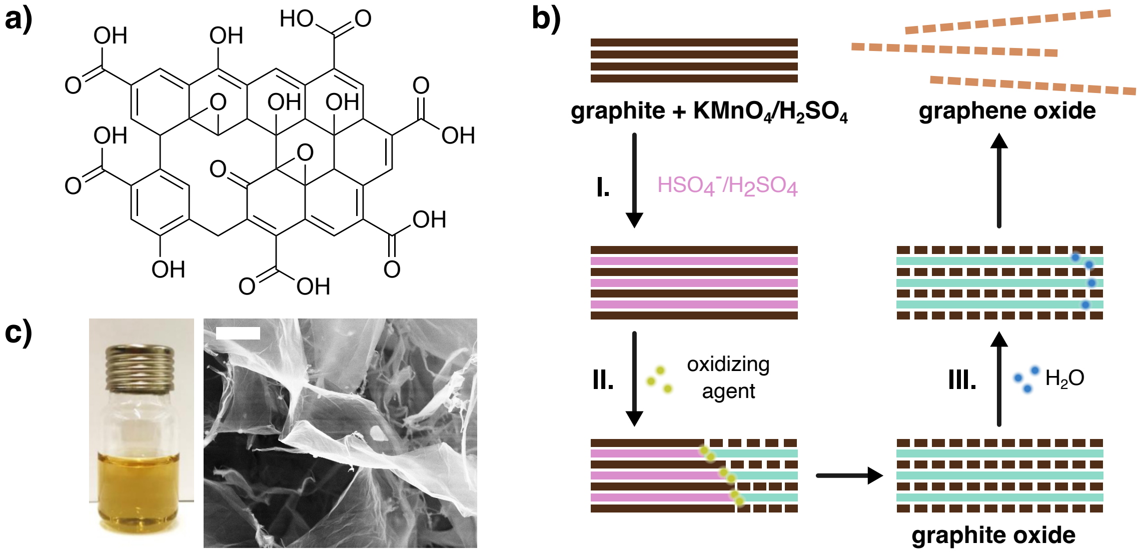

Figure 4.4: a) Chemical structure of GO based on an adapted LK model, with carboxy groups at the edges, and vacancies, epoxide-, and hydroxy groups in the basal plane. b) Schematic depiction of three-step GO formation from the reaction of graphite with potassium permanganate and sulfuric acid. Solid lines represent pristine graphitic monolayers, dashed lines represent GO monolayers. Pink regions depict intercalated sulfuric acid molecules and hydrogen sulfate ions, while green regions represent an intercalated mixture of the reduced oxidizing species and hydrogen sulfate/sulfuric acid. (Adapted from reference [111]). c) Photograph of a honey-colored colloidal aqueous solution of GO prepared by the Chen method, and SEM image of single GO sheets after freeze-drying (scale bar: 2 µm).

other wet-chemical synthetic procedures based on the Hummers method in the absence of $NaNO_3$ were reported. In this present work, GO was synthesized following a route reported by Chen et al., in which graphite flakes are oxidized at elevated temperatures in sulfuric acid by $KMnO_4$ to yield carboxylate-rich GO.[113,114] A three step formation mechanism of single-layer GO in the presence of $KMnO_4$ in sulfuric acid was proposed by Tour and co-workers who identified and characterized intermediate compounds using optical microscopy and Raman spectroscopy.[111] The proposed mechanism is schematically depicted in figure 4.4b). In the first step I., graphite is intercalated by sulfuric acid, making it more accessible for oxidation. The second step II. is the oxidation of this first intermediate in a diffusion-controlled replacement of H_2SO_4/HSO_4^- by oxidant species, resulting in graphite oxide. This step strongly depends on the morphology and size of the utilized graphite flakes, where smaller flakes are oxidized faster. The reduced form of the oxidizing agent remains intercalated within the graphite oxide layers until step III., when graphite oxide is converted to exfoliated GO upon water exposure. During this step, covalently bonded sulfur species are hydrolyzed, and electrostatic interaction and hydrogen bonding between negatively charged GO layers and water yield a colloidal solution, with no remaining order in the *c*-axis of the carbon material.[111] Usually, exfoliation is further promoted mechanically, e.g., via ultrasonic force. Figure 4.4c) shows a photograph of an aqueous colloidal GO solution showing the typical light-brown color. It also shows a scanning electron micrograph of freeze-dried GO with distinct wrinkles on the layers arising from defects. Due to the non-stoichiometric nature of GO, strong batch-to-batch variations are possible, which is why one single batch was used within the frame of this present thesis.

4.3.2 Graphene Oxide Reduction

While uniform thin films of GO can be formed from colloidal solutions using various techniques,[115] which is essential for the use of GO in electronic applications, the obtained films are electrically insulating, since sp^3 hybridization leads to impeded charge carrier percolation, compared to sp^2-hybridized graphene. Here, reduction of GO induces the progressive removal of oxygen-containing functional groups and restoration of the sp^2 system, enabling the formation of a material with properties similar to pristine graphene. The reduction product is commonly referred to as rGO, and can be formed using various methods, either in solution, bulk, or in thin films, such as chemical reduction, heat treatment, UV irradiation, or electrochemical reactions, among others.[116–118] Especially in terms of chemical sensing applications, methods for selectively tuning the degree of reduction, i.e., the C/O ratio, or for removal of specific functional groups, are of great interest to obtain a material with tailored sensing properties.

The degree of reduction can be monitored using different methods. The most straightforward is the optical characterization, since conversion to rGO leads to a color change also discernible with the naked eye. Additionally, due to the increasing hydrophobic nature of rGO, the formed rGO flakes usually precipitate in aqueous environments. Further, the evolution of the electrical conductivity can be used as measure of the progressing partial restoration of the sp^2 system. Ultimately, the C/O ratio can be analyzed using elemental analysis for the obtained bulk, or even surface-sensitive techniques like x-ray photoelectron spectroscopy (XPS).

Chemical Reduction. Chemically rGO can be obtained using, e.g., well-studied reducing agents from organic synthesis such as metal hydrides or hydrohalic acids. A widely used compound for chemical GO reduction is hydrazine, but also alternative "green" reducing agents, e.g., L-ascorbic acid, have been reported.[119] Further, the use of microorganisms, plant extracts, or proteins for rGO formation has been proposed.[118] The chemical reduction can be implemented either in solution, or substrate-deposited GO sheets or films can be exposed to reducing vapors, e.g., hydrazine or HI.[120,121] On the one hand, chemical reduction has the advantage to be completed relatively fast, and that the production of rGO can be scaled up easily. On the other hand, it usually involves the use of toxic substances, it risks the introduction of chemical impurities, and the spatially controlled reduction is not feasible.

Thermal Reduction. Elimination of oxygen-containing functional groups from GO sheets is also possible via thermal treatment. Several reports describe the formation of rGO by heating under different conditions, e.g., in reducing atmospheres, in vacuum, at varying temperatures (typically ≥200 °C), and with variations of heat ramps.[122,123] Many studies suggest that by thermal reduction, structural holes and defects increase inevitably. This is explained by increased pressure between GO layers during heating, and the conversion of the randomly distributed functionalities to gaseous CO and CO_2, leaving structural holes behind.[117,122] Generally, different functional groups are expected to dissociate with increasing temperatures due to varying binding energies. For instance, Gao et al. studied the mechanism of thermal reduction using DFT calculations and found that functional groups attached inside of aromatic domains are eliminated more easily than those present at the edges of an aromatic domain.[124] They also report that at annealing temperatures between 700–1200 °C predominantly hydroxy-, carbonyl-, and carboxy groups are removed while epoxide groups remain unaffected.[124] In contrast, Larciprete et al. reported that precisely the surface coverage of epoxide groups dictates the onset of lattice decomposition, creating precursors for CO/CO_2 during thermal reduction.[125] In

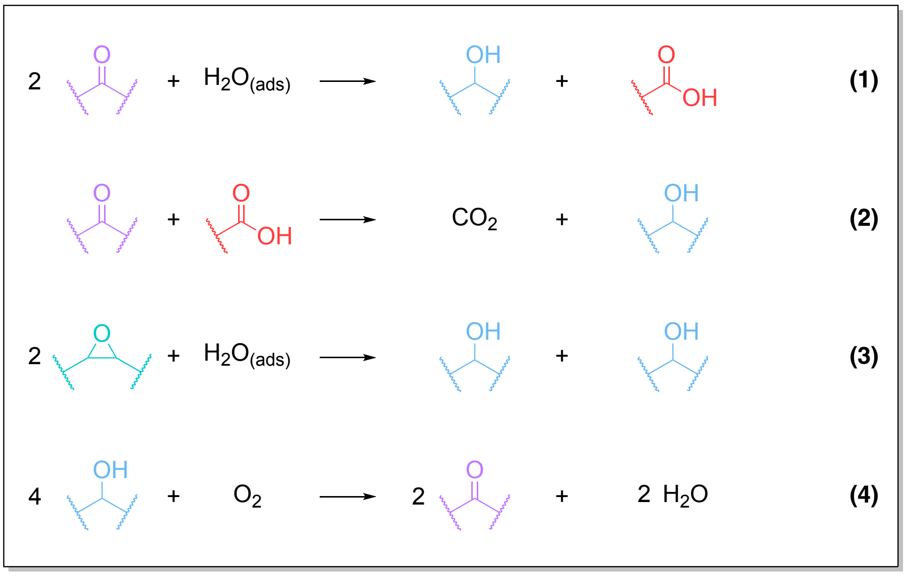

Scheme 4.1: Photoreactions in GO sheets illuminated with UV light, as proposed by Koinuma et al.[128]

summary, despite being a straight-forward, low-cost reduction method, the production of defective rGO sheets is a major disadvantage.

Photoreduction. Reduction of GO can also be induced by photo-activated reactions.[126,127] Matsumoto and co-workers monitored the conversion of GO sheets to rGO under UV illumination (500 W high-pressure Hg lamp) in an oxygen atmosphere with XPS measurements, and proposed different photoreaction pathways, summarized in scheme 4.1.[128] The reactions are based on photogenerated electrons and holes, that are formed in the respective HOMO/LUMO ($\pi \rightarrow \pi*$) when GO, that partly consists of semiconducting sp^2 domains, is exposed to UV light.[128,129] In the first reaction (1), carbonyl groups react with adsorbed water molecules in a disproportionation to a carboxylic and hydroxylic compound. Next (2), the carboxy groups react with carbonyls to CO_2 and a hydroxy compound, resulting in defects in the sheets. Similar to (1), epoxide groups react with adsorbed water to hydroxy groups. The reaction of present and newly produced hydroxy groups with oxygen yield more carbonyl groups and water, in sum, promoting and catalyzing the formation of hydroxy groups and carboxy groups, as experimentally found from XPS data analysis.[128]

TiO_2-Mediated Photoreduction. GO photoreduction is further facilitated when mediated using a photocatalyst, e.g., TiO_2, WO_3,[130] or ZnO.[131] Among photocatalysts, TiO_2 counts to one of the most investigated and employed materials for heterogeneous catalysis.[132] The wide-band gap semiconductor has remarkable chemical stability, is nontoxic, and cost-efficient, and has proven great potential for catalyzing various reactions, such

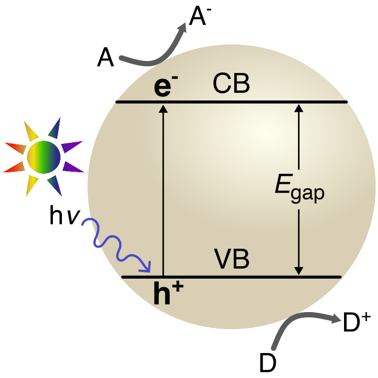

Figure 4.5: Schematic depiction of proposed photocatalytic processes on a TiO_2 catalyst. Upon illumination with light h$\nu \geq E_{gap}$, an electron is excited to the CB, leaving a hole in the VB. The generated charge carriers can partake in chemical reductive and oxidative reactions with electron acceptors (A) and donors (D), respectively. Only charge carriers that migrate to the catalyst surface can drive the photocatalytic reactions.

as water splitting or degradation of pollutants.[132–134] The photocatalytic activity of a semiconductor is dictated by its electronic band structure and its band gap E_{gap}, since it determines the absorption properties and the redox force.[135] In principle, as schematically shown in figure 4.5, in the photocatalytic process, an electron-hole pair is generated upon light exposure, when the photon energy is equal to or exceeding E_{gap}, exciting an electron to the conduction band (CB) and leaving a hole in the valence band (VB). The photogenerated charge carriers can have different fates: They can migrate to the catalyst's surface where they are available for redox reactions with electron acceptors (A) or donors (D).[132,135] The formed holes have a strong oxidation potential of up to 3.0 eV (with reference to a standard hydrogen electrode).[134] Commonly, intermediate reactive radical species are involved in the photocatalytic reactions, when water and oxygen molecules are adsorbed to the TiO_2 surface according to equations 9 – 10.[134] These radical species then act as oxidizing/reducing agents for the specific substrates.

$$h^+ + H_2O \rightarrow {}^{\bullet}OH + H^+ \tag{9}$$

$$e^- + O_2 \rightarrow {}^{\bullet}O_2^{\ -} \tag{10}$$

Other possible fates are the recombination of charge carriers, or their trapping by surface or volume defect sites. Here, the efficient charge separation is the essential process for the photocatalytic activity of the material.[135] Generally, E_{gap} depends on the crystal structure. TiO_2 naturally occurs in three polymorphs: rutile, anatase, or brookite, of which rutile is thermodynamically the most stable. Anatase and rutile both crystallize in the tetragonal crystal system and brookite in the orthorhombic. Rutile has a band gap of 3.02 eV,[134] anatase 3.20 eV,[134] and brookite 3.14 eV.[136]

Especially TiO_2 nanostructures have gained popularity for photocatalytic applications and even photo-activated gas sensing, due to their increased surface-to-volume ratio, and consequently, larger surface photoactivity compared to the bulk material.[134] Although rutile is the thermodynamically stable phase in bulk, TiO_2 nanostructures are predominantly formed in the anatase phase, due to the lower surface energy that carries weight in the formation of colloidal crystals.[137] Regarding the photocatalytic activity, generally higher activity is found for anatase compared to rutile.[135] In this context, many works have focused on the synthesis of anatase TiO_2 nanocrystals (TNCs) with control over the exposed reactive facets, like {101} and {001} facets.[138,139] Further, Kandiel et al. compared the photocatalytic activity of brookite and anatase TNCs, as well as their mixed modifications for methanol oxidation, and reported the highest photocatalytic activity for brookite TNCs.[140] Hence, engineering of the TNCs' size, shape, modification and percentage of exposed facets, is highly relevant for photocatalytic applications, as well as investigations of structure-activity properties.[139] In this context, a surfactant-assisted seeded-growth approach to obtain shape-controlled TNCs with controlled faceting has been reported by Gordon et al.[139] Here, brookite TiO_2 nanorods (TNRs) and anatase nanoplates (TNPs) are synthesized via aminolysis of Ti-carboxylate complexes and oleylamine (OLAM) as co-surfactant. Shape control is achieved by variation of the titanium precursor (TNRs: $TiCl_4$, TNPs: TiF_4). The TNPs have a high percentage of exposed {001} facets that are stabilized by F^-. The percentage of exposed {101} and {001} facets in anatase TNCs was further adjusted by variation of the co-surfactant, and it was found that the TNCs with more exposed {101} facets had the highest photocatalytic activity.[139] However, the brookite TNRs were not further analyzed with regard to their photocatalytic performance.

Due to the high affinity of TiO_2 to carboxylic acids,[145] fabrication of GO/TiO_2 hybrids for GO reduction is especially attractive, since robust networks can easily form. In addition, synergistic properties of such composites can be expected. In 2008, Kamat and co-workers described the first procedure to reduce colloidal solutions of GO using 2–7 nm sized spherical TiO_2 nanoparticles upon UV exposure with a Xe lamp in an ethanolic solution.[141] Figure 4.6a) shows photographs of the colorless, aqueous dispersion of the utilized TiO_2 nanoparticles, of the colloidal mixture of GO and the photocatalyst particles (light brown), and of the resulting rGO-TiO_2 mixture after illumination, indicating the successful (partial) restoration of the aromatic system. Figure 4.6 also summarizes the proposed UV-assisted reaction: Upon excitation with UV light ($h\nu$), an electron-hole pair is generated on the surface of TiO_2. Ethanol functions as hole scavenger, and is oxidized

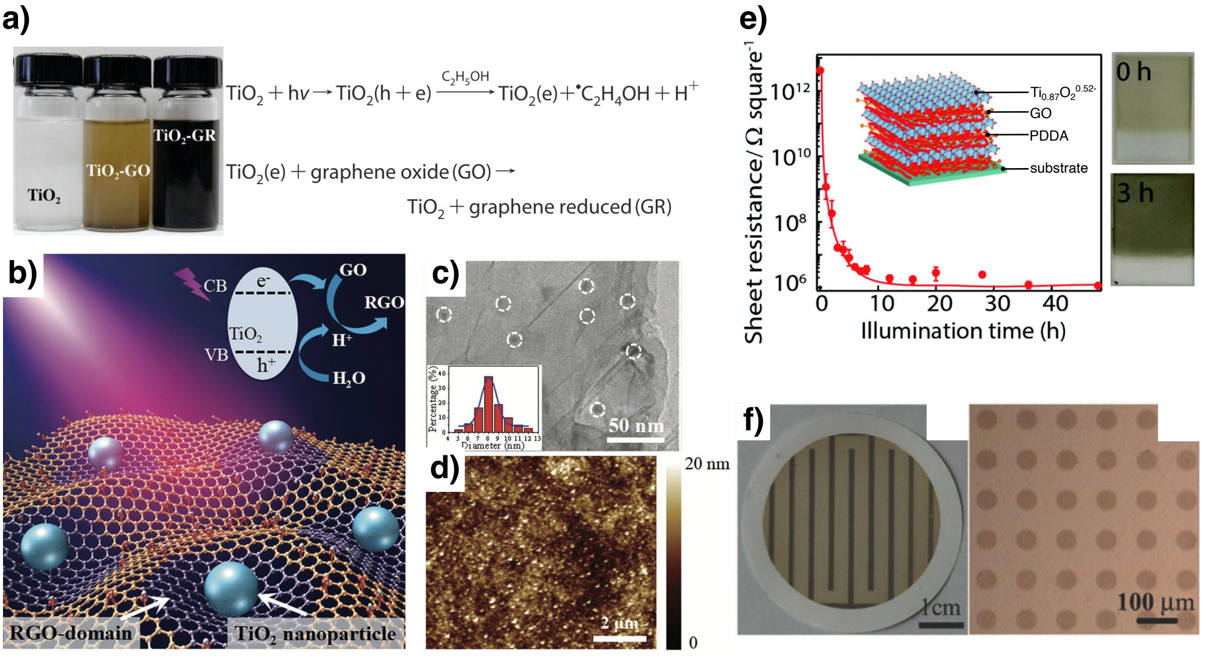

Figure 4.6: a) (Left) Photograph of aqueous dispersions of (colorless) TiO_2 nanoparticles, (light brown) GO-TiO_2 composites, and (black) rGO/TiO_2 composites. (Right) Proposed UV-assisted reduction of GO in presence of ethanol as hole scavenger. Adapted and reprinted with permission from Ref. [141], ©2008 American Chemical Society. b) Schematic of TiO_2 nanoparticle-mediated local formation of rGO domains in composite thin films upon UV exposure in ambient conditions. c) TEM and d) AFM image of corresponding TiO_2 nanoparticle-decorated GO sheets. (b-d) Adapted and reproduced with permission from Ref. [142], ©2018 John Wiley & Sons, Inc. e) Change in sheet resistance during UV illumination of GO/PDDA/$Ti_{0.87}O_2^{0.52-}$ hybrids films, and change of color before (0 h) and after 3 h UV exposure. Adapted and reprinted from Ref. [143] with permission from the Royal Society of Chemistry. f) Photographs of GO/TiO_2–rGO/TiO_2 patterns fabricated via UV exposure using different photomasks. Adapted and reproduced from Ref. [144] with permission from the Royal Society of Chemistry.

to ethoxy radicals, leading to an accumulation of the photogenerated electrons. These electrons will then be injected to adjacent GO sheets, resulting in the reduction of oxygen functional groups.[141] In earlier studies, the same group reported that photo-accumulated electrons in TiO_2 are scavenged by other carbon nanostructures, e.g., fullerenes.[146] Regarding the selectivity of this method, Bell et al. investigated the chemical structure of rGO obtained via TiO_2-assisted photocatalytic reduction in solution via XPS measurements and found that carboxy groups remain widely unaffected.[147] In the following years, the concept has been advanced for the reduction of GO thin films in ambient conditions. For instance, Zhao et al. fabricated resistive-switching memories based on rGO/TiO_2 films obtained via photocatalytic reduction in ambient conditions.[142] As summarized in figure 4.6b), they described the local formation of rGO domains in proximity to evenly distributed TiO_2 nanodots. In ambient conditions, water molecules are adsorbed to the GO surface, presumably acting as hole scavengers in this method.[142] Figures 4.6c-d) depict TEM and AFM images of the employed nanocomposite, showing the distribution of ~8 nm sized TiO_2 nanodots on a GO sheet. Furthermore, Cai et al. described the fabrication and characterization of the UV-assisted reduction of self-assembled superlattices of GO, poly(diallyldimethylammonium) (PDDA), and $Ti_{0.87}O_2^{0.52-}$ nanosheets that are schematically depicted in the inset of figure 4.6e). Using UV illumination at wavelengths ranging between 270–400 nm (irradiance 2.5 mW/cm^2), they monitored the degree of reduction over several hours, e.g., by changes in the sheet resistance of the composite material. They found a decrease in sheet resistance of several orders of magnitude, as plotted in figure 4.6e). According to the evolution of sheet resistance, and the change of color, shown in the inset photographs, the photocatalytic reduction was completed after 3 h. The authors claim that the photocatalytic reduction method is milder compared to, e.g., thermal or chemical reductions, while not further discussing the underlying reduction mechanism.[143] Some studies were dedicated to the structural and chemical differences in rGO obtained via photo- or thermal reduction and addressed mechanistic differences of both methods. Based on time-resolved electron diffraction, -IR spectroscopy, and DFT calculations, Hada et al. proposed a selective removal of epoxide groups in the basal plane of GO upon photoexcitation (in the absence of a photocatalyst), whereas thermal treatment results in the removal of both, hydroxy and epoxide groups.[148] Yao et al. proposed a photothermal mechanism for the reduction of LbL-assembled GO/PDDA/TiO_2 films.[149] A major advantage of the photocatalytic reduction compared to the previously presented methods, apart from the tunability of the degree of reduction via UV exposure times, is that it enables selective patterning of GO films. Reductive patterning can be performed on various substrates and results in spatially controlled conductive areas. Figure 4.6f) shows photographs of patterned GO/rGO paper obtained by photocatalytic reduction via UV illumination through custom-designed photomasks.[144] Here, the darker areas correspond to rGO areas. Hence, this reduction method gives rise to photocatalytic lithography to produce and pattern conductive areas with a defined composition and degree of functionalization, which is highly desirable for the fabrication of functional electronic devices, such as resistive sensors.[150] Another photocatalytic lithography method that is based on the "inverse" effect is the use of a TiO_2 mask to etch pristine graphene sheets: Here, conductive patterns are obtained by exploiting the oxidative properties of the photocatalyst, leading to the site-selective oxidative degradation of graphene.[151]

In the context of this present thesis, the photocatalytic reduction of GO within hybrid films plays a major role as it exploits the hybrid nature of GO/TiO_2 nanoparticle films to selectively tune the material's composition and affinities to solvent vapors by variation of photocatalytic reduction, which is investigated in dependence of precisely shaped TNCs of varying crystal structure and the UV exposure times.

4.3.3 Resistive Chemical Sensing

Composites of GO/rGO- and GO/rGO/TNCs with adjusted composition are interesting for the detection of gases and vapors due to their large amount of sorption sites to interact with target analytes.

Numerous approaches and studies involving GO/rGO and its composites have been published in the past years, especially regarding their humidity sensing applications. Comprehensive accounts of GO/rGO-based humidity sensors can be found in various recent review articles.[20,152–156] This section, however, will focus on GO/rGO-based humidity and gas sensors with a resistive readout and introduce their functioning principles and concepts relevant to this thesis.

As described in the preceding paragraphs of this section, a resistive sensor responds with a change in the measured electrical resistance or current upon exposure to a target analyte. Given the electrically insulating nature of GO, its (gradual) conversion to conductive rGO plays a pivotal role when it comes to its application as resistive sensor.

Functional groups present on the GO/rGO basal plane enable unique interactions with different molecules, which, when sorbed to the sensing material, can generally induce a charge transfer between the carbon network and the analyte, resulting in changes of the electrical conductivity. The sorption ability can be estimated by considering binding energies of molecules on the carbon surface.[25] For example, Guo et al. determined the binding energies of water molecules by first-principal calculations on pristine graphene and hydroxy- and epoxide-functionalized GO, finding significantly higher binding energies for H_2O/hydroxy (0.259 eV/molecule) and H_2O/epoxide (0.201 eV/molecule), compared to H_2O/graphene (0.044 eV/molecule) due to stronger binding via hydrogen bonds compared to van-der-Waals interactions.[157] Even higher binding energies of up to 0.840 eV were calculated by Li and Peng for NH_3 sorption at certain orientations to epoxide- and hydroxy-functionalized GO, which were also much higher than those found for pristine graphene.[127]

Humidity Sensors. The resistive sensing properties of GO and rGO towards humidity are still not fully understood, and the underlying mechanisms are a matter of debate. This is not surprising, considering that, for instance, conversion of the semiconducting properties of thermally rGO from p- to n-type, depending on the thermal annealing temperature, has been discussed.[158] Additionally, despite being an electrical insulator, pristine GO becomes a good ionic conductor in presence of water.[159] Hence, past studies on the influence of water on the electrical conductivity of GO/rGO and on humidity sensors, have found differing trends, i.e., both, humidity-induced increase[160] or decrease[161] in resistance, or a mixed behavior.[162] Recently, Samorì and co-workers investigated chemically modified rGO with adjusted hydrophilicity as resistive humidity sensors. They found that rGO functionalized with hydrophilic moieties shows a better humidity sensing performance compared to pristine rGO, and all sensors exhibited an increase in resistance up to high r.h. levels.[163] Regarding wearble humidity sensors, Wang et al. reported a chemiresistor for respiration and speech monitoring based on GO sorbed onto a non-woven fabric, that responded with a decrease in resistance in the r.h. range of 44–91 %.[164]

The observed sensing behavior – the sign and amplitude of the response, but also response and recovery times – seems to be linked to the level of relative humidity (r.h.), and also to the material's particular chemical and physical structure. For instance, Wee et al. investigated the resistive humidity sensing behavior of single GO sheets in dependence of their sheet sizes (ranging from 0.8 μm – 47 μm), and found that increasing lateral sheet dimensions result in higher sensitivity.[161] The observed increase in conductance was explained taking into account the LK model for the chemical structure of GO: Epoxide and hydroxy groups on the basal plane form aligned exchange sites to enable proton conductivity.[161] However, the GO sheet edges are predominantly decorated with carboxy groups. According to studies by Matsumoto and co-workers on rGO sheets carboxy groups block proton conduction.[128,165] Consequently, with decreasing GO sheet size, the relative amount of carboxy groups increases, resulting in a lower sensitivity due to hindered proton hopping. Wang et al. reported a patterned resistor matrix of ultrathin rGO films on flexible substrates for non-contact humidity sensing, that showed a reversible decrease in resistance in the r.h. range of 4.3–75.7 %.[166] More recently, Haidry and co-workers investigated the direct dependence of humidity sensing properties of GO on the number of hydroxy groups. To this end, they synthesized GO of varying stoichiometry by adapting the amount of $KMnO_4$ and treated the product with ether to modulate the amount of hydroxy groups, as well as the interlayer distances. This was monitored via FTIR spectroscopy and XRD. The material was drop-casted from ethanolic solutions onto electrode structures, and they analyzed the humidity sensing performance in a r.h. range of 6–95 %. Correlation of the sensitivities obtained for the different GO sensors with XRD, FTIR and Raman spectroscopy analysis revealed an enhanced performance of the materials with a higher amount of hydroxy groups.[167] They found a maximum relative change of measured current of $\Delta I_0/I \sim 40$ %, and response and recovery times of 8.5 s, and 13 s, respectively. Interestingly, an increase in resistance was observed for all sensors over the analyzed r.h. range. The same group expanded this study by investigation of the humidity sensing performance depending on the degree of reduction by annealing drop-casted GO films at different temperatures, demonstrating a switching from n-type to p-type behavior for rGO annealed at higher temperatures (> 150 °C).[168] Different phenomena need to be addressed to elucidate the “switching” behavior. As previously introduced, the chemiresistive properties of highly rGO (and pristine graphene) are based on a charge transfer mechanism.[169] Here, rGO functions as charge donor or acceptor when exposed to an analyte, resulting in n- or p-type responses, depending on the chemical nature of the analyte molecules.[169] In general, the conductivity of rGO is governed by holes as charge carriers.[168–170] In this case, water molecules act as electron donors, leading to a decrease of hole density, and as a consequence, an increase in resistance.[167,169] On the other hand, GO with a lower degree of reduction exhibits both, more polar functional groups to act as water sorption sites, and a lower baseline conductivity due to less developed sp^2 domains. In this case, at higher r.h. levels, sorbed water can easily form a continuous network, resulting in a decrease in resistance due to proton conductivity of water via the Grotthus mechanism.[162] For other film structures, e.g., hybrid materials with (conductive) interlayer fillers, water-induced swelling can also contribute to an increase in resistance.[171]

The interplay of these competing effects is determined by the GO/rGO ratio, film structure, r.h. level, and can be exploited to fabricate chemiresistors for specific humidity sensing applications with tunable and complementary linear detection ranges and sensitivities, when GO can be gradually converted from a hydrophilic to hydrophobic material, e.g., via controlled reduction.

Other Gas and VOC Sensors. Apart from humidity, graphene and GO/rGO-based films can interact with other chemical compounds, such as various VOCs and gases. In analogy to the mechanism proposed for water molecules, mainly charge transfer interactions are expected to determine the sensing behavior of GO/rGO chemiresistors. The pioneering work for the detection of molecules with graphene chemiresistors was done by Novoselov and co-workers in 2007, in which mechanically cleaved graphene sheets of several micrometers in lateral size, equipped with metal electrodes, were exposed to CO, NH_3, H_2O, and NO_2 molecules.[172] Positive (CO, NH_3) and negative (H_2O, NO_2) changes in resistivity were recorded, depending on the electron (positive) or hole (negative) doping ability of the analytes, i.e., here, water acted as electron acceptor, as determined via Hall measurements.[172] Regarding GO/rGO, Robinson et al. studied the chemiresistive responses of chemically rGO sheets with varying degree of reduction towards dinitrotoluene and other chemical warfare agents at part-per-billion concentrations, finding positive values for $\frac{\Delta R}{R_0}$ with faster response times and higher response amplitudes for rGO with higher degree of reduction.[173] Remarkably, Park et al. studied the ethanol vapor sensing behavior of thermally rGO films (200 °C in Ar atmosphere) and their untreated counterparts and reported switching responses from n-type (GO) to p-type responses (rGO), proposing the combination of GO/rGO films in a sensor array for improved selectivity.[174] As explanation for the n- to p-type transition, they claim a change of the dominant charge carriers from electrons to holes, without further discussion.[a] With regard to sensor arrays based on GO/rGO, a recent study investigated the performance of a sensor array based on holey GO films with an adjusted degree of carboxylation towards acetone, NH_3, and alcohol vapors with concentrations up to 1600 parts-per-million (ppm), finding positive $\frac{\Delta R}{R_0}$ for all analytes, except for a mixture of ammonia/humidity, with the highest sensitivity towards water, followed by methanol, ethanol, and ammonia.[175] For all VOC exposures in humid carrier gas (r.h. 28 %), a drastic decrease of $\frac{\Delta R}{R_0}$ was measured, to the degree of a negative response for the ammonia exposure under humidity.[175] The use of this sensor array enabled the discrimination of analytes using LDA.[175] One study by Lee et al. addressed the gas sensing properties of photocatalytically rGO/TiO_2 composites towards NH_3, acetone, methanol, and ethanol.[176] The composites were obtained upon UV illumination of an aqueous GO/TiO_2 mixture in the presence of ethanol, and then drop-casted onto electrode structures. Comparison of untreated and photocatalytically rGO-hybrids showed a transition from n-type to p-type sensing behavior, reportedly caused by the UV-induced change from an n-n- to a p-n heterojunction. The composites showed higher sensitivities and faster response times than a pristine GO sensor, however, they exhibited poor long-term stability.[176]

---

[a] Note from the author: Possibly, due to its good selectivity towards water and humidity, the non-reduced GO film responds to a certain amount of water content in ethanol, based on the mechanisms discussed in the preceding paragraph.

5 Goal

The aim of this thesis was to elaborate and investigate novel tunable inorganic-organic nanocomposite films for resistive vapor sensing applications. Various projects were accomplished focusing on two different classes of materials: **(I)** organically cross-linked gold nanoparticles (GNPs), and **(II)** graphene oxide/TiO_2 nanocrystal composites (GO/TNC), with the ultimate goal of developing highly sensitive chemiresistors for the detection and identification of several volatile organic compounds (VOCs), and for relative humidity (r.h.) sensing applications.

A general overview of the accomplished projects, that will be presented and discussed in the next section, is provided in figure 5.1.

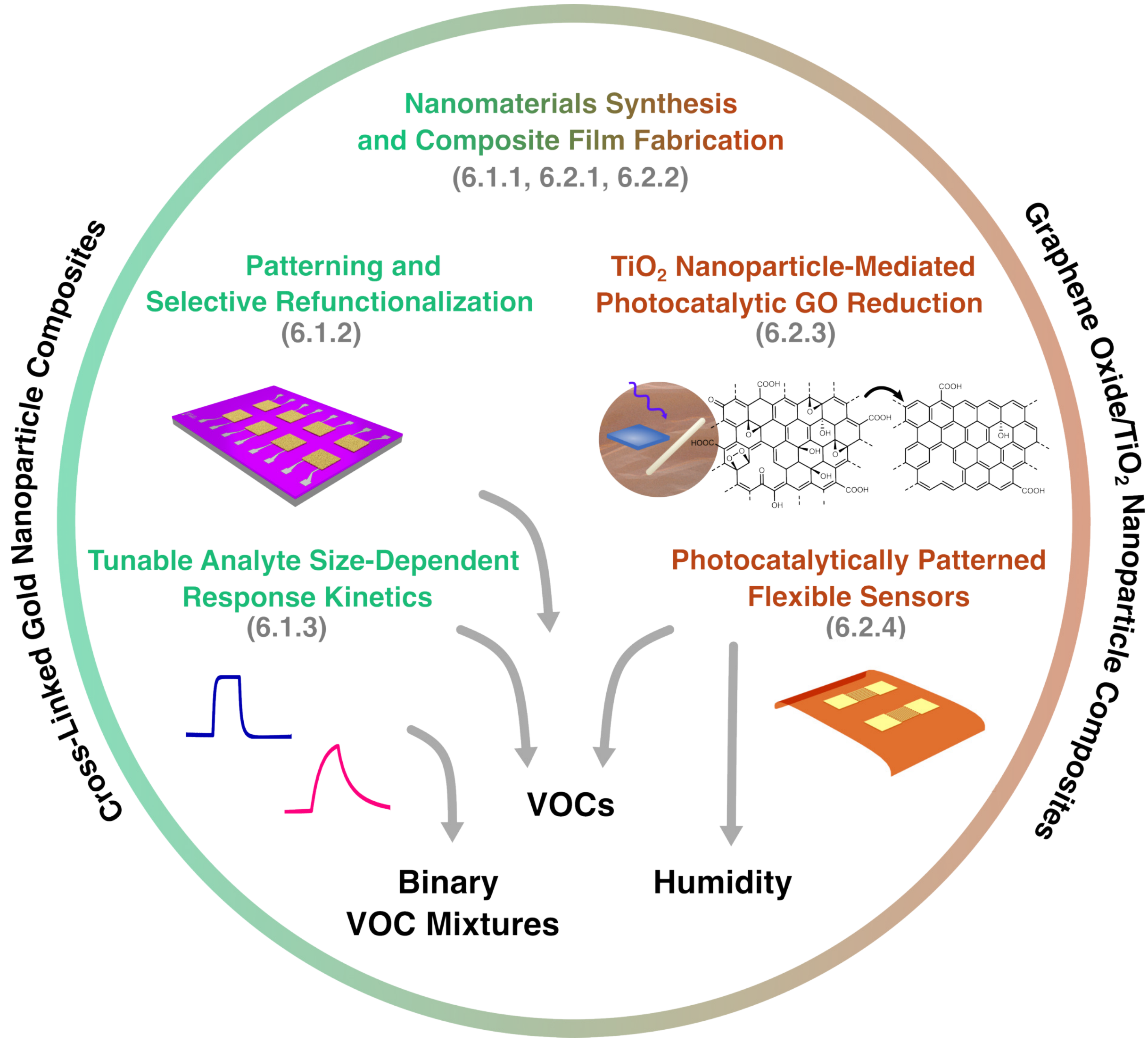

Figure 5.1: Graphical table of contents for the projects presented in this thesis.

(I) One project focused on the investigation of cross-linked GNP thin films and their implementation in chemiresistor arrays for the detection and recognition of VOCs and water. General aspects regarding sensor fabrication and operation will be introduced in section 6.1.1. The first objective was the characterization and optimization of lithographically patterned GNP film arrays, fabricated via a facile poly(methyl methacrylate) (PMMA)-based lift-off method, and the fabrication of multifunctionalized GNP film arrays using this technique to increase the chemical variety, and hence, the cross-sensitivity on the array. This study is summarized in section 6.1.2.

The second objective was the investigation of the sensor response kinetics of α,ω-alkanedithiol (ADT) cross-linked GNP films in order to establish a novel approach for VOC discrimination. Here, the main question was to investigate the relation between the films' nanostructure and the analyte-dependent dynamic sensor responses, and to identify different methods for the deliberate adjustment of sensor response times. Further, the performance of sensor arrays based on GNP films with tuned response times during exposures to water, VOCs, and binary VOC mixtures was to be studied and evaluated using linear discriminant analysis (LDA). These results are summarized in section 6.1.3.

(II) The second project addressed the r.h. and VOC sensing properties of GO/TNC thin films. To this end, shape-controlled titania nanorods (TNRs) and titania nanoplates (TNPs), and GO were synthesized (section 6.2.1). The first goal was to develop a method for the fabrication of tunable homogeneous nanohybrid thin films using differently shaped TNCs (section 6.2.2). Since the incorporated TNCs are photocatalytically active, the next step was to study the impact of ultraviolet (UV) illumination on the electrical, optical, structural, and chemical properties of the composites, and to monitor UV-induced formation of rGO under variation of different parameters, such as the embedded TNC catalyst, film thickness, and UV illumination times (section 6.2.3). Last, this selective reduction approach was investigated for the fabrication of photocatalytically patterned sensor arrays. Here, the goal was to develop composites with adjusted GO/rGO areas on flexible substrates and to analyze them with regard to their r.h. and VOC sensing properties, in dependence of the degree of GO reduction (section 6.2.4).

6 Results and Discussion

6.1 Gold Nanoparticle Film Chemiresistors

The studies presented in the following sections focused on thin films comprised of dithiol (DT) cross-linked GNPs which are well-known for their chemiresistive sensing properties.[58,75,77,177] First, a general introduction to the sensing principle will be provided (section 6.1.1), followed by the presentation of different projects (sections 6.1.2 – 6.1.3) involving the elaboration of sensor arrays for the discrimination of volatile organic compounds (VOCs) and their binary mixtures.

6.1.1 Principle of Thin Film Fabrication and Vapor Sensing

Cross-linked GNP films were fabricated using a facile and time-efficient spin-assisted layer-by-layer (LbL) deposition technique established in our group in 2011.[37] In this work, amine-stabilized GNPs with diameters ranging between ~3–9 nm were used for composite film fabrication. GNPs of varying sizes were prepared following synthetic procedures reported by Leff et al.[38] and Peng et al.,[39] with slight modifications. Figures 6.1a-b) show representative transmission electron microscopy (TEM) images of 9.0 nm sized GNPs (Peng method), and 3.5 nm sized GNPs (Leff method), respectively. Commonly, GNP batches fabricated by the Leff method have a relatively high polydispersity of ~20 %.[38] A scheme of the general film deposition process is depicted in figure 6.1c). First (I.), the desired substrate, e.g., a glass slide, silicon wafer equipped with electrodes, or

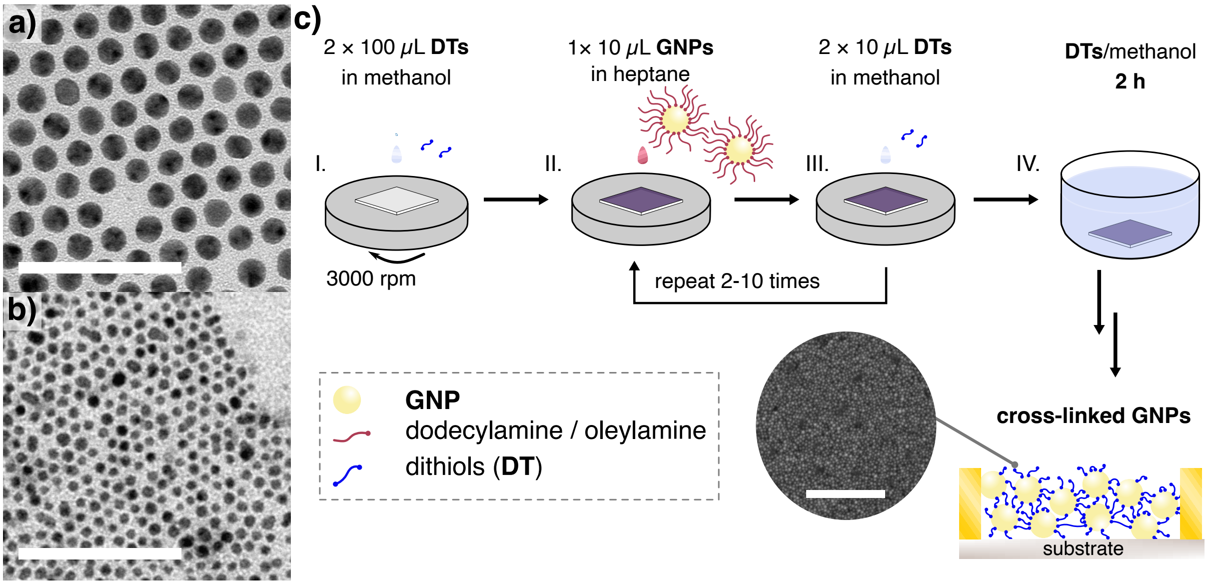

Figure 6.1: Representative TEM images of GNPs synthesized by the a) Peng method (GNP diameter 9.0 nm) and the b) Leff method (GNP diameter: 3.5 nm). Scale bars: 50 nm. c) Schematic representation of the LbL SC method for the preparation of cross-linked GNPs from colloidal GNP solutions and organic DTs. The inset shows a representative SEM image of the GNP film structure. Scale bar: 200 nm.

a polymeric substrate, is rotated at a constant speed using a spin-coater, and coated twice with a methanolic solution (7.4 mM) of a molecular cross-linker, e.g., α,ω-alkanedithiols (ADTs). After ~20 s dwell time for solvent evaporation, the colloidal amine-stabilized GNPs in heptane are deposited on the rotating substrate (II.), followed again by two deposition steps of the cross-linking agent (III.). Each coating step is spaced by ~20 s. During film deposition, the amine ligands, e.g., dodecylamine (12A) or oleylamine (OLAM), are stripped from the GNP surface and exchanged with the introduced DTs,[37,52,68] due to the high binding affinity of DTs to gold, leading to the formation of Au-S thiolates,[36] and GNP cross-linkage. By increasing the number of deposition cycles (steps II.-III.), composite films of adjusted film thickness can be obtained. Here, films of thicknesses ranging between 40–80 nm were typically chosen for chemiresistor fabrication. Finally, (IV.) the substrate-supported GNP films are submerged in the DT-cross-linker solution for 2 h, to enhance the degree of cross-linkage of the resulting material. The inset in figure 6.1b) shows a scanning electron microscopy (SEM) image revealing the granular, disordered structure of a representative ADT-cross-linked GNP film (cross-linker: 1,9-nonanedithiol (9DT), GNP diameter: 7.3 nm) obtained using the LbL spin-coating (SC) method. This method allows for the simple and efficient adjustment of the desired film composition, e.g., by using different types of molecular cross-linkers or the nanoparticles' size, shape, and material, offering a versatile toolbox for the fabrication of hybrid films with tailored optical, electrical, and ultimately, sensing properties. To probe the chemiresistive behavior of as-deposited GNP/DT films, or arrays composed thereof, the films were typically deposited on electrode structures, or were equipped with metal electrodes shortly after fabrication enabling electrical contact and continuous measurement of the sensors' resis-

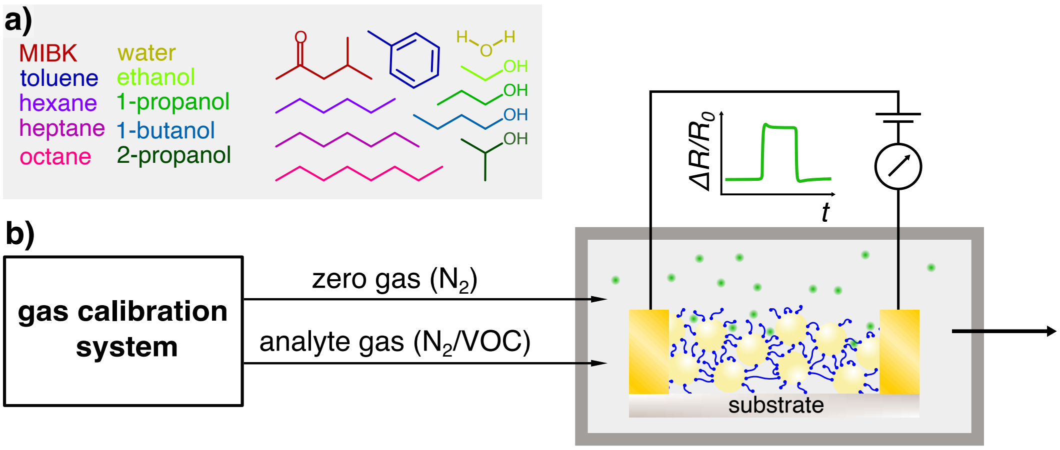

Figure 6.2: a) Overview of components employed as target analyte vapors for GNP film chemiresistors. b) Schematic of the measurement setup used for the characterization of the transient responses of GNP film chemiresistors to different analyte vapors. Adapted and reprinted with permission from Ref. [3], ©2021 American Chemical Society. (DOI: 10.1021/acsanm.1c01892)

tance during analyte exposures. In this project, several substances were employed as target analytes. These analytes and their chemical structures are summarized in figure 6.2a): a set of alkanes, alcohols, methyl isobutyl ketone (MIBK), toluene, and water. In a typical measurement, schematically depicted in figure 6.2b), the sensors were placed in a test cell connected to a commercial gas calibration system equipped with a vapor pressure saturator (CGM 2000, MCZ Umwelttechnik), and a flow controller providing a constant flow of 0.5 L/min through the test cell. Here, the gas calibration system provided nitrogen (5.0) as zero gas (ZG). The sensors were then transiently exposed to analyte vapor-enriched nitrogen with varying analyte concentrations (AG), alternated with ZG exposures. Typical exposure periods were 12–20 minutes, e.g., 4 min AG exposure, followed by 8 or 16 min ZG exposure. The sensors were operated at a constant voltage (2.5–5 V), and the sensors' resistive responses were continuously recorded. As indicated in the sketch shown in figure 6.2b), the relative resistance change ($\frac{\Delta R}{R_0}$) was computed from the recorded time-trace, according to equation 11:

$$\frac{\Delta R}{R_0}(t) = \frac{R(t)}{R_0} - 1 \tag{11}$$

where R is the measured electrical resistance, and R_0 the sensor's baseline resistance during ZG exposure. R_0 was typically determined for each exposure period by fitting linear functions considering 30 s interval resistance data recorded up to 5 s before the onset of AG transients, and 30 s intervals at the end of ZG exposure, 5 s before the next transient onset. The maximal sensor response $\left(\frac{\Delta R}{R_0}\right)_{\text{max}}$ was determined as the average $\frac{\Delta R}{R_0}$ over 10 s at the end of each AG exposure, 5 s before the onset of ZG exposure.

6.1.2 Lithographically Patterned and Refunctionalized Chemiresistor Arrays

This section contains key findings that were summarized and published in the following journal article: H. Schlicke,† S. C. Bittinger,† T. Vossmeyer, "Lithographic Patterning and Selective Functionalization of Metal Nanoparticle Composite Films", *ACS Appl. Electron. Mater.* **2020**, 2, 11, 3741–3748.[1]

The basic procedure to pattern cross-linked GNP films using PMMA deep UV (DUV) photolithography was established in a preceding study within the framework of the author's (S.C.B) Master's thesis under supervision of Dr. Hendrik Schlicke (H.S.), where the idea of using it for GNP film refunctionalization was also explored in preliminary experiments.[178] Within the scope of the present work, the resolution limits of the patterning method, as well as its use for the fabrication of tailored GNP film arrays, e.g., using varying GNP sizes, were investigated. Furthermore, the method was optimized and implemented for the fabrication of chemiresistor arrays with adjusted sensitivities based on the refunctionalization of the films' organic matrix. Regarding the author contributions of the cited publication, H.S. and S.C.B. contributed equally to the study. S.C.B. co-planned the research idea and experimental design, acquired and evaluated all experimental data, and co-wrote the manuscript.

Lithographic Patterning

Defined patterning of GNP films is essential for their implementation in various advanced sensing applications. With regard to the fabrication of sensor arrays for vapor sensing applications, controlled deposition of the GNP film transducers is indispensable to prevent cross-talk between sensitive areas and to increase the number of individual transducers on a device. Different deposition techniques, such as ink-jet printing[57,58,85] or drop-casting[24,179,180] have been reported to produce GNP-based vapor sensing devices and arrays. Generally, lithographic patterning methods are highly desirable, e.g., in terms of time-efficient production of arrays. Conventional optical lithography procedures, however, cannot be easily implemented for patterning of organically-stabilized nanomaterials, due to the use of unsuitable water-based compounds, such as alkaline developers. A lithographic method based on PMMA as photoresist was established for patterning GNP/ADT films in our group earlier.[178] PMMA lithography is compatible with these nanocomposites, since it is fully processed in organic solvents. PMMA is commonly used as positive-tone photoresist in electron beam (e-beam) lithography,[181] but is also known to degrade under exposure to DUV radiation.[182]

In this study, patterned GNP films were obtained via UV exposure of PMMA using a home-built DUV light source with a main emission peak at 254 nm and an irradiance of 520 mW/cm^2. A detailed description of the radiation source is provided in the Appendix, section A.1.1. Figure 6.3a) shows the lift-off procedure for the fabrication of patterned GNP film arrays. First (I.), a PMMA layer (~200 nm) is deposited on the substrate via spin-coating and exposed to UV light through a quartz mask, yielding a pre-patterned mask after development in a MIBK/2-propanol mixture. Next (II.), a 1,9-nonanedithiol (9DT) cross-linked GNP film is deposited onto the PMMA mask via LbL SC, as described in section 6.1, figure 6.1. By dissolving the underlying PMMA layer in acetone, patterned GNP films are obtained (III.). This method was applied to fabricate GNP film arrays based on differently sized GNPs (3.8 nm and 7.3 nm). The larger GNPs were kindly provided by Svenja Kunze and Karen Schäfer (University of Hamburg). The electrical properties of the patterned films were investigated and compared, as shown in figure 6.3b). Here, the *IV* curves of eight $\mathrm{GNP}_{3.8\ \mathrm{nm}}$/9DT, and of seven $\mathrm{GNP}_{7.3\ \mathrm{nm}}$/9DT film sections are shown. All measured film sections exhibit similar *IV* characteristics, indicating that controlled and reproducible GNP film sections are obtained using the lift-off method. An average conductivity of ~6.4×10^{-3} S/cm was determined for the $\mathrm{GNP}_{3.8\ \mathrm{nm}}$/9DT films, which is in good agreement with values reported in the literature.[52,75] An overall higher conductivity (~4.5×10^{-2} S/cm) was determined for $\mathrm{GNP}_{7.3\ \mathrm{nm}}$/9DT films, due to the lower activation energies expected for the tunneling-based charge transport in films made from larger GNPs.[69,183] A photograph of a representative GNP/9DT array is displayed as inset

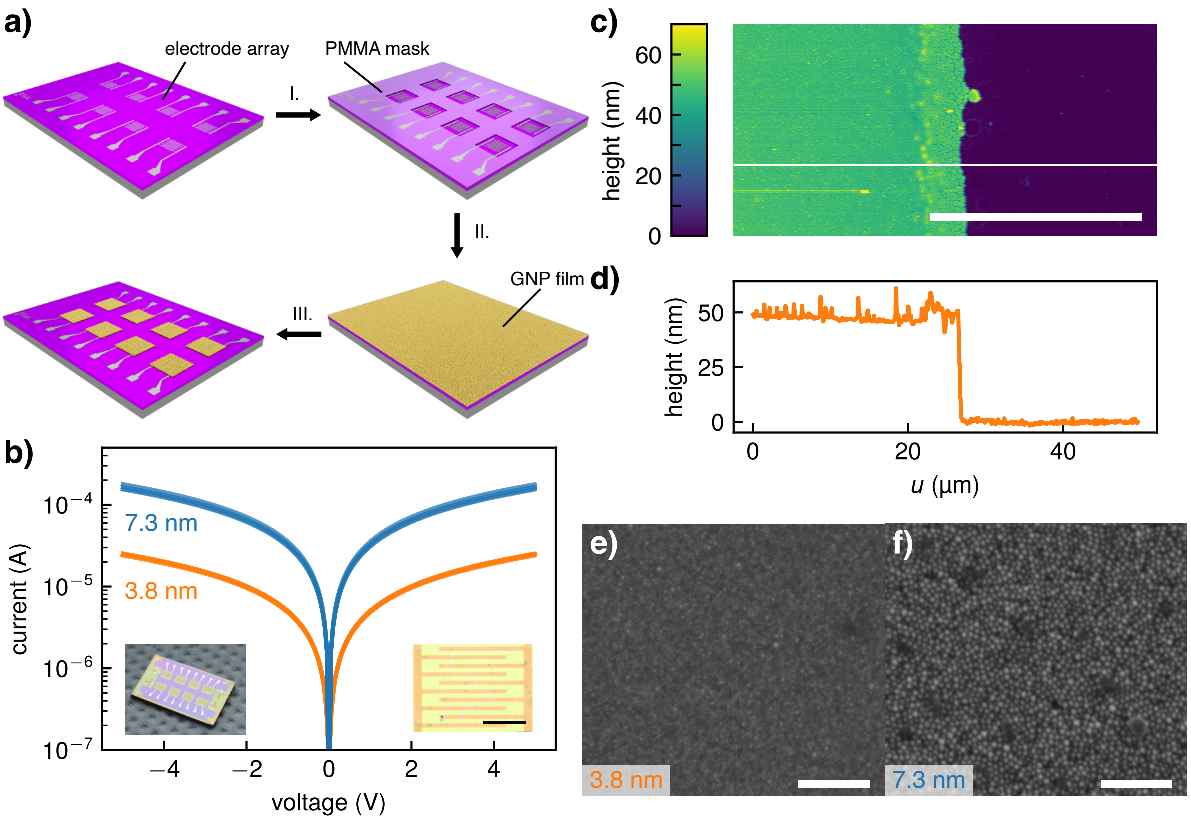

Figure 6.3: a) Schematic of the lift-off procedure used for patterning cross-linked GNP films. (I) Deposition and patterning of the PMMA mask layer, (II) deposition of the GNP film, and (III) patterning of the GNP film via PMMA lift-off. b) *IV* characteristics of patterned GNP film sections on IDEs fabricated using differently sized GNPs (diameter: 7.3 nm and 3.8 nm). The shown curves are *IV* data of seven and eight GNP film sections, respectively. The inset shows a photograph of a representative chip consisting of eight GNP film resistors and an optical micrograph of a GNP film-coated IDE structure (scale bar: 500 µm). c) AFM image (scale bar: 25 µm) and d) corresponding height line profile recorded along the white line drawn in c), at the edge of a GNP film section (GNP diameter: 3.8 nm). e, f) High-resolution SEM images of patterned GNP films fabricated using GNPs with diameters of e) 3.8 and f) 7.3 nm (scale bars: 100 nm). Reprinted with permission from Ref. [1], ©2020 American Chemical Society. (DOI: 10.1021/acsaelm.0c00770)

in 6.3b), consisting of eight GNP film sections (1.8 mm × 2.2 mm) deposited onto interdigitated electrode (IDE) structures (Ti/Pt, thickness: 10 nm/40 nm) on a SiO_2/Si wafer. An optical micrograph of a GNP film-covered IDE structure is shown as inset, too. The patterned GNP films were analyzed via atomic force microscopy (AFM). Figures 6.3c-d) show an exemplary AFM scan recorded at the edge of a patterned GNP/9DT film, and a corresponding height profile, recorded along the thin white line, revealing a film thickness of ~49 nm. Slight structural inhomogeneities are visible at the edge of the patterned film, possibly caused by partial film detachment at the edges during lift-off due to variations in thickness of the PMMA mask. Figures 6.3e-f) show scanning electron microscopy (SEM) images of inner areas of patterned $GNP_{3.8\ nm}$/9DT and $GNP_{7.3\ nm}$/9DT, respectively, showing the disordered, granular structure typically obtained for GNP/ADT films deposited via LbL SC.[63] In order to investigate whether microscaled GNP film structures

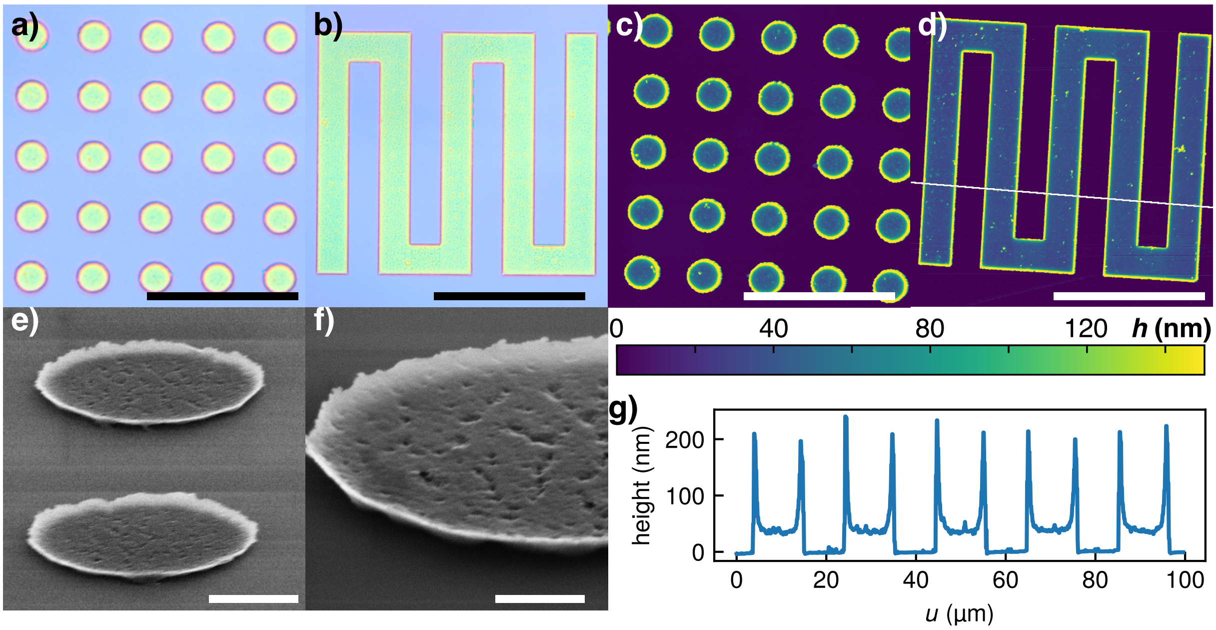

Figure 6.4: a, b) Optical micrographs (scale bars: 25 µm, 50 µm), c, d) AFM images (scale bars: 25 µm, 50 µm), and e, f) SEM images (scale bars: 2 µm, 800 nm) of a patterned GNP film (GNP diameter: 3.8 nm) using e-beam PMMA lithography. The structures are (a, c, e, f) circles of a diameter of ~5 µm and b, d) meander structures of a width of ~10 µm. g) Height line profile corresponding to the meander structure measured along the white line in shown d). Adapted and reprinted with permission from Ref. [1], ©2020 American Chemical Society. (DOI: 10.1021/acsaelm.0c00770)

can be fabricated using the lift-off patterning process, PMMA was processed via e-beam lithography, due to the limited resolution of the home-built DUV source. Here, miscellaneous microstructures were patterned into the PMMA layer and $GNP_{3.8\ nm}$/9DT films were deposited via LbL SC on the e-beam-structured mask. Optical microscopy images of GNP film circles (diameter: 5 µm) and a GNP film meander (width: 10 µm) obtained after PMMA dissolution are shown in figures 6.4a,b), respectively. Well-defined GNP film structures (yellow) with the targeted dimensions are visible on the wafer substrate (blue). AFM images corresponding to equivalent structures are shown in figures 6.4c-d). A height profile, measured along the thin white line drawn in figure 6.4d), is depicted in figure 6.4g). A thickness of ~42 nm was determined for the inner film sections, however, pronounced edge beads of up to 200 nm, corresponding to the PMMA layer thickness, can be observed. Since the GNP films are deposited into troughs in the PMMA mask, the formation of edge beads is expected. Figures 6.4e-f) show tilted SEM images of respective circular GNP film sections, clearly showing the differing film morphology at the edges. With regard to GNP films fabricated using the custom-built UV source for PMMA exposure, no pronounced edge beads were observed (cf. figure 6.3c). This is presumably caused by varying resolutions of the PMMA masks obtained using the custom-built UV source and an e-beam: High resolution-, sharp and steep PMMA edges are obtained using e-beam exposure, while using the low-resolution home-built UV source, a gradient-like

PMMA profile is probably obtained at the structure's edges, leading to less pronounced edge beads. In general, the facile and straight-forward patterning method has proven as versatile and useful, and its application has been expanded to other research activities in our group. For instance, it enabled the fabrication of photolithographically patterned (2.4 mm×400 μm) rectangular GNP/9DT films for multi-directional strain sensing applications[4] and for well-defined square 1,6-hexanedithiol (6DT) cross-linked freestanding GNP membranes.[2]

Selective Refunctionalization and Sensing

For the development of chemiresistor arrays based on GNP composites, the presented patterning method was implemented not only for defining and separating the sensitive areas on an array, but also for refunctionalization of the composite films' organic matrix by selectively unmasking certain film sections. The affinity of the composite films towards VOCs can be selectively adjusted by choice of the molecules comprising the films' organic matrix, since analyte sorption is widely dependent on interactions with the organic matrix. Consequently, a wide variety of functional groups is highly desirable for fabricating sensor arrays to combine and exploit the sensors' cross-sensitivities. On the one hand, the presented patterning method could be used by successively spin-coating differently cross-linked or ligand-stabilized GNPs onto respective PMMA masks. On the other hand, the composition of as-fabricated cross-linked film can be doped using molecular ligands. In this study, GNP/9DT$_{8.2\ \mathrm{nm}}$ arrays were fabricated following the procedure described in figure 6.3a). GNPs were kindly provided by Dr. Bendix Ketelsen (University of Hamburg).

The general refunctionalization process is schematically described in figure 6.5a). Three refunctionalization agents with different functionalities, two dithiols and a monothiol, were selected: hexa(ethylene glycol) dithiol (HEG), 2,3-dimercaptopropanol (GLY), and 4-nitrothiophenol (NTP). After preparation of the initial array, a PMMA layer was deposited onto the patterned GNP/9DT film sections via spin-coating. For the first refunctionalization step (I.), PMMA was lithographically structured as described in the previous paragraph. A custom-designed quartz mask was used exposing the PMMA layer covering 2/8 GNP film areas of the array structure. After development, the structure was immersed in a methanolic solution of the first refunctionalization agent (HEG) for 2 hours. Here, the exposed GNP/9DT films were exposed to the dithiol, while 6/8 films were protected with the PMMA mask. After dissolution of the PMMA mask in acetone, the process was repeated twice with different doping agents, resulting in (III.) a chemiresistor array with four different types of GNP films (one pair, each). Here, diffusion of the (di)thiol molecules into the film is expected, and binding of the thiol groups to the GNPs in a ligand-exchange type reaction. It is to note that using this process, each GNP film sec-

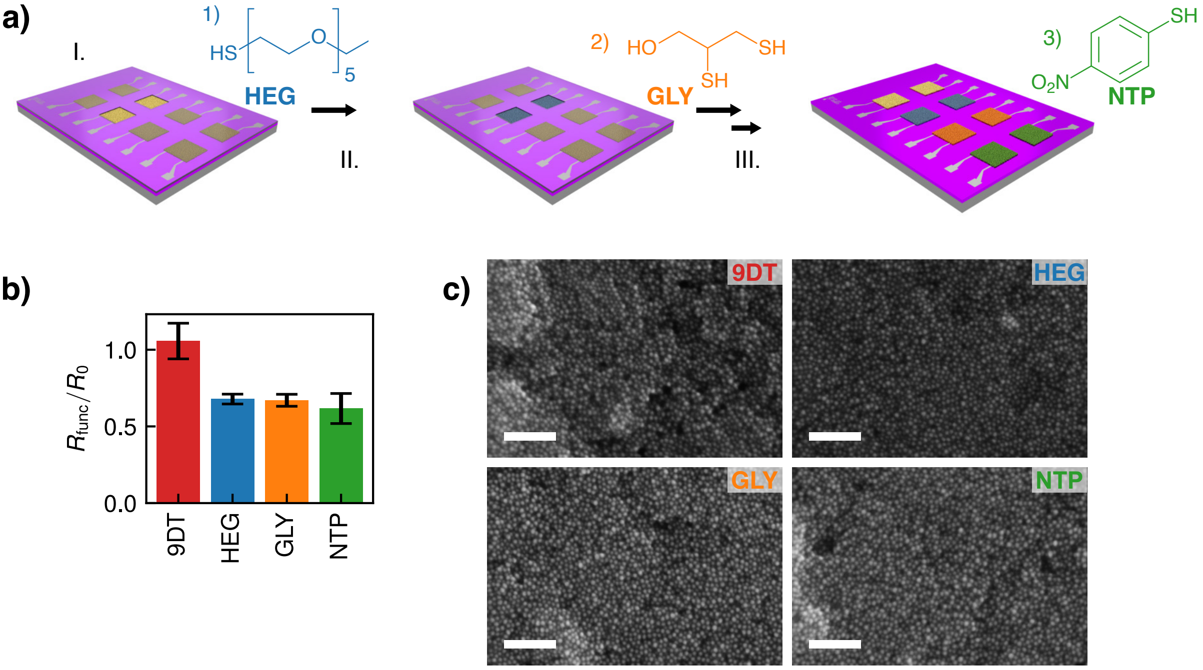

Figure 6.5: a) Schematic of the procedure for GNP film chemiresistor refunctionalization. (I) One GNP/9DT sensor pair is unmasked using a patterned PMMA layer. (II) Molecular doping the GNP film by immersion in a refunctionalization agent solution. (III) Repetition of steps (I-II) for subsequent refunctionalization of other sensor pairs. b) Resistance change of chemiresistors measured after the refunctionalization process with respect to the GNP/9DT sensors. Error bars represent deviations between the resistance changes of two film sections on the array. c) SEM images showing sections of an untreated GNP/9DT film section, and of GNP/9DT films refunctionalized using HEG, GLY and NTP. (scale bar: 100 nm). Rearranged and reprinted with permission from Ref. [1], ©2020 American Chemical Society. (DOI: 10.1021/acsaelm.0c00770)

tion to be molecularly doped was exposed to UV light during PMMA exposure. This step led to an increase in conductivity for all films. The influence of UV exposure on the properties of GNP/ADT films will be addressed in detail in a paragraph in the following section 6.1.3.[a] After refunctionalization was completed, the electrical charge transport properties of all film areas were characterized and compared to an untreated GNP/9DT film. Figure 6.5b) shows the relative resistance of the differently refunctionalized films with respect to their initial state. After the refunctionalization treatment, all films exhibited lower resistances, which, as mentioned before, is mainly attributed to UV exposure. To assess the impact of UV exposure and refunctionalization treatment on the composite film structure and morphology, the sensor array was analyzed via SEM. Figure 6.5c) depicts an overview of respective micrographs for all film sections, showing no differences between the refunctionalized (HEG, GLY, NTP), and the untreated (9DT) GNP films. All films exhibit a comparable film structure, where well-defined spherical nanoparticles are discernible. As a consequence, the observed changes, e.g., in conductivity, can be mainly attributed to a modification of the organic matrix, and other effects, e.g., UV-

---

[a] Note, that, in case UV exposure of the GNP film areas is not desired or feasible, it can be easily avoided by applying the successive, purely lift-off based film deposition process.

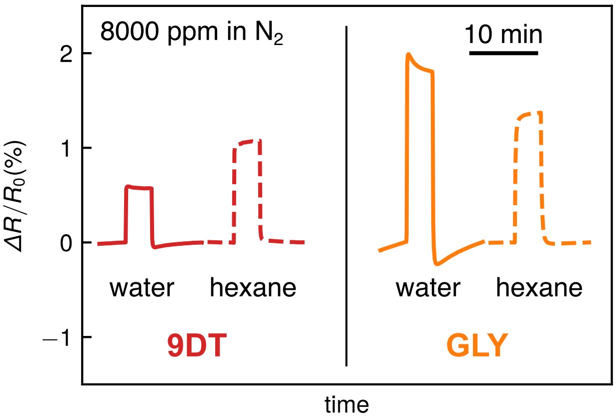

Figure 6.6: Exemplary baseline-corrected response transients of an unmodified GNP/9DT sensor, and a sensor refunctionalized using GLY to vapors of water and hexane at an analyte concentration of 8000 ppm. Nitrogen was used as ZG and carrier gas. Reprinted with permission from Ref. [1], ©2020 American Chemical Society. (DOI: 10.1021/acsaelm.0c00770)

induced GNP fusion should be further investigated. Finally, the sensing properties of the array were analyzed. To this end, the chip was mounted to a custom-designed printed circuit board (PCB), contacted via wire-bonding, placed in a test cell and exposed to a set of eight different analytes (1-butanol, 1-propanol, ethanol, water, toluene, MIBK, hexane, heptane) at varying concentrations between 50–8000 parts-per-million (ppm). Each transient AG exposure was 4 minutes, followed by 8 minutes ZG exposure. Details of the measurement setup and readout principle can be found in the Experimental Section, 7.7.2. Exemplary baseline-corrected response transients of two sensors of the array – an untreated GNP/9DT sensor, and a GNP/9DT/GLY sensor – to water and hexane vapor at 8000 ppm are shown in figure 6.6. The refunctionalized GNP/9DT/GLY chemiresistor shows an increased sensitivity to both analytes. Moreover, both chemiresistors differ in selectivity: While the GNP/9DT film had a higher response amplitude for hexane, the refunctionalized film had a higher response amplitude to water. This observed change in selectivity supports the notion of a successful post-fabrication modification of the GNP films' organic matrix, where the purely (hydrophobic) 9DT-based film has a higher affinity towards alkanes, while the 9DT/GLY-based sensors act more hydrophilic. This behavior might also be caused by UV-induced reactions of the cross-linkers, e.g., oxidation of thiols (cf. the next section 6.1.3), and by the introduction of polar ligands, such as GLY, providing more hydrophilic sorption sites, e.g., for water molecules. All measured timetraces are provided in the Appendix, section A.1.2. As described in section 6.1.1, the maximal relative resistance change $\left(\frac{\Delta R}{R_0}\right)_{\mathrm{max}}$ of all chemiresistors was extracted as sensor signal for all transient exposures. Figure 6.7 summarizes the obtained response patterns for eight analytes at two different concentrations (400 ppm and 8000 ppm). By combining the sensor responses of the four types of GNP films, distinct response patterns can be seen for different analyte classes, e.g., for the homologous series of alcohols and water (6.7a-d).

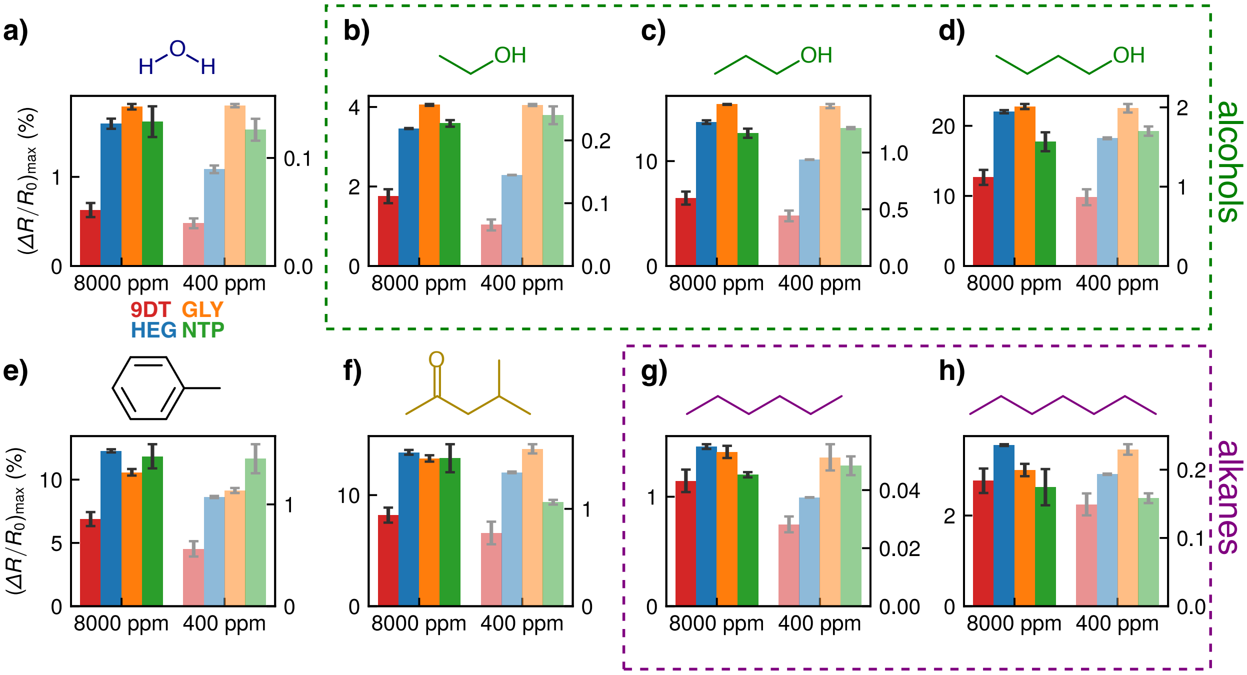

Figure 6.7: Maximum relative resistance changes of unmodified (9DT) GNP film chemiresistors and GNP film chemiresistors refunctionalized using HEG, GLY, and NTP when exposed to vapors of a) water, b) ethanol, c) 1-propanol, d) 1-butanol, e) toluene, f) MIBK, g) hexane, and h) heptane for 4 min at concentrations of 8000 and 400 ppm. Error bars indicate the standard deviation of maximum relative resistance changes of two sensors on the array. Reprinted with permission from Ref. [1], ©2020 American Chemical Society, (DOI: 10.1021/acsaelm.0c00770).

Particular response patterns were also obtained for MIBK and toluene, especially at lower concentrations. Generally, the response amplitude depends on the applied analyte concentration, and the analyte vapor pressure, where analytes with lower vapor pressures, e.g., 1-butanol, partition into the film to a higher degree,[75] causing a stronger response. The selectivity of the GNP/9DT sensors is in good agreement with data reported in the literature.[58,75] Comparing the response patterns obtained for the alcohols and alkanes, the ratio of the HEG/NTP responses seems to increase with increasing alkyl chain length. This might be caused by increasing response times for the NTP-treated sensor for these analytes, effectively yielding lower values $\left(\frac{\Delta R}{R_0}\right)_{\mathrm{max}}$. This aspect will be discussed in detail in the next section 6.1.3.

In conclusion, these results demonstrate that the PMMA-based lithography can be used to yield spatially well-defined chemical sensor arrays, and to selectively refunctionalize the composite films' organic matrix. The method can be further implemented and optimized for the fabrication of GNP film arrays with a larger set of compositions for VOC discrimination.

6.1.3 Tunable Response Kinetics for Analyte Recognition

This section contains results that were summarized and published in the following journal article: H. Schlicke,† S. C. Bittinger,† H. Noei, T. Vossmeyer, "Gold Nanoparticle-Based Chemiresistors: Recognition of Volatile Organic Compounds Using Tunable Response Kinetics", *ACS Appl. Nano Mater.* **2021**, 4, 10, 10399–10408.[3]

The notion to utilize GNP transducers' analyte-dependent response times for VOC discrimination was proposed and addressed in previous works of our group.[178,184] Based on these preliminary results, this study aimed at a thorough understanding of the origin of analyte-dependent response times of cross-linked GNP chemiresistors, and the elaboration of methods to deliberately adjust their dynamic responses, e.g., by variation of the cross-linker, GNP size, and UV treatment. Using this toolbox for tuning the GNP films' sensing behavior, chemiresistor arrays with adjusted response kinetics were fabricated and employed for the discrimination between VOCs and binary VOC mixtures. Parts of these results were collected in close collaboration with Jan-Niklas Beyer, B.Sc., (University of Hamburg), who contributed results regarding the binary VOC mixtures sensing, and contributed to GNP syntheses within the framework of his Master's thesis project. Regarding the author contributions of the cited publication, H.S. and S.C.B. contributed equally to the study. S.C.B. co-planned the research idea and experimental design, acquired and evaluated all experimental data, and co-wrote the manuscript.

Extraction of Response Features

As mentioned in the previous section 6.1.2 on chemiresistor arrays based on GNP composites for VOC discrimination, significant efforts have been undertaken to develop devices with diversified chemical compositions, in order to combine the resistive response amplitudes of multiple sensors with, at best, orthogonal selectivity, to obtain an analyte-specific fingerprint.[58,60,185] The results presented so far (cf. 6.1.2) focused on the combination of resistive response features to obtain analyte-specific signatures, as well. Novel approaches, however, not only focus on the extraction of the response amplitudes, but also on the use of several response features to enable accurate analyte identification, commonly aided by advanced signal processing algorithms.[86,186,187] On the one hand, common requirements considered for assessment of the performance of gas and vapor sensors are a fast response- and recovery time, usually quantified by, e.g., t_{90}, i.e., the time needed to reach 90 % of the saturated response amplitude. On the other hand, valuable information and singular response features can be extracted from a sensor's delayed dynamic response during transient exposure to a target analyte. In the context of GNP-based chemiresistors, several studies have addressed their response kinetics, and proposed their use for enhanced analyte identification.[87–90] In prior studies in our group, analyte-dependent response times have been observed for GNP/6DT composite films (GNP diameters: 3–4 nm). However, a comprehensive investigation regarding (i) the underlying mechanism for varying response times, and (ii) the selective adjustment of response kinetics for analyte recognition has not been reported so far. Figures 6.8a-c) show exemplary baseline-corrected response transients of a GNP/6DT chemiresistor to 4 minute exposures to water, toluene, and heptane vapor (8000 ppm), respectively.

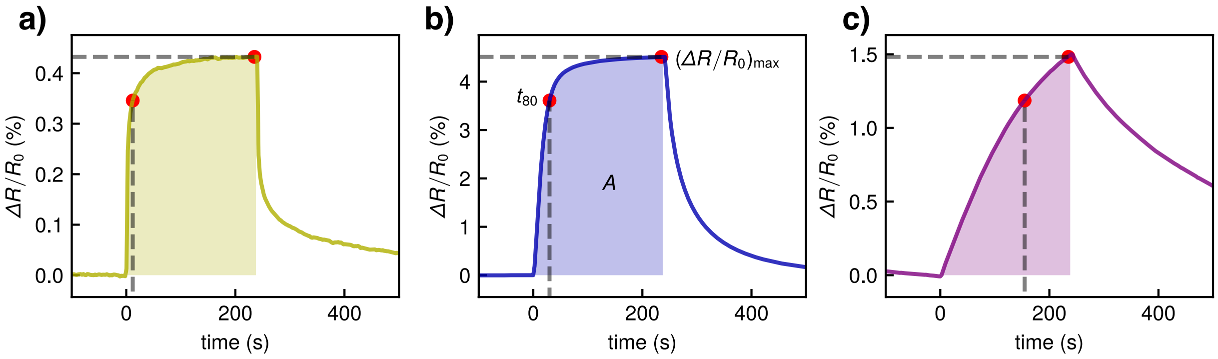

Figure 6.8: Exemplary baseline-corrected response transients of a GNP/6DT chemiresistor (GNP diameter: 3.4 nm, film thickness: 68 nm) to a) water, b) toluene, and c) heptane, at 8000 ppm.[178] The transients are annotated with specific response features: the integrated area A below the transient (shaded), t_{80} response times, and $\left(\frac{\Delta R}{R_0}\right)_{\mathrm{max}}$ (red circles). Adapted and reprinted with permission from Ref. [3], ©2021 American Chemical Society. (DOI: 10.1021/acsanm.1c01892)

The transients clearly differ in their shapes, giving rise to the extraction of specific response features, as indicated by the red circles and annotations in figure part b). For detailed analysis, comparison, and for the use of the sensors' response kinetics, distinct response features, that also reflect the particular transient shapes, were extracted from the measured timetraces:

I $\left(\frac{\Delta R}{R_0}\right)_{\max}$ as resistive response feature was extracted (as described in section 6.1.1)

II t_{80}, as the response time to obtain 80 % of $\left(\frac{\Delta R}{R_0}\right)_{\max}$

III A, as the integrated area below the sensor signal, normalized to $\left(\frac{\Delta R}{R_0}\right)_{\max}$

Interestingly, while the extracted resistive response features for the GNP/6DT sensor follow the expected sequence (toluene>heptane>water), where the response amplitude is mainly affected by the analytes' polarity and vapor pressures, the kinetic response features, e.g., A, show a deviating trend (water>toluene>heptane), appearing to depend on the molecular size of the target analytes, allowing for their combination to achieve accurate analyte recognition. This observation gave rise to an in-depth analysis of analyte-dependent response kinetics of GNP/ADT-based chemiresistors, and their selective tunability for the fabrication of chemiresistor arrays.

Tunability of Response Times via Cross-Linker Length

The correlation between analyte-dependent response kinetics and GNP/ADT films' composition and nanogeometry was explored in this study. Preliminary experiments suggested that the observed analyte-dependent response times are caused by diffusion-limited analyte sorption in the nanocomposites. To test this assumption, GNP films comprised of different ADT cross-linkers were fabricated via LbL SC on glass substrates. A previous study in our group demonstrated that variation of cross-linker lengths between 4- and 10 methylene units resulted in adjusted interparticular spacings. For composite films fabricated using 3.2 nm sized GNPs, distances ranging from 0.5–1.1 nm were estimated via small angle x-ray scattering measurements (SAXS) assuming an fcc arrangement within the films.[63] For this investigation, thin films were fabricated from GNPs with a core diameter of ~3.6 nm. A TEM image and the particle size distribution histogram of the employed GNPs are depicted in figures 6.9a-b). Figure 6.9c) shows the molecular structure of cross-linkers used: 1,4-butanedithiol (4DT), 6DT, 1,8-octanedithiol (8DT), and 1,10-decanedithiol (10DT). Prior to chemiresistor measurements, the as-prepared films were characterized via UV-vis absorption spectroscopy, AFM, and *IV* measurements. Film sections were equipped with Au electrodes (thickness: 100 nm, electrode spacing ~400 µm) for electrical and sensing measurements. Figure 6.9d) shows absorbance spectra of the

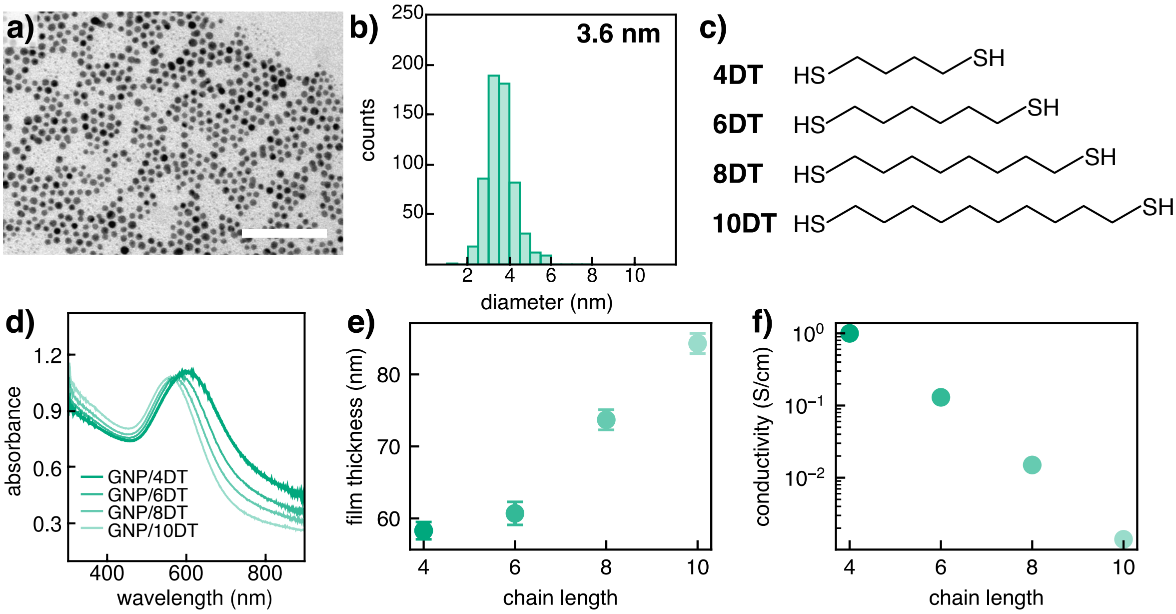

Figure 6.9: a) TEM image (scale bar: 50 nm) and corresponding b) size distribution histogram of 3.6 nm sized GNPs used for composite film fabrication with different cross-linkers shown in c). d) UV-vis absorbance spectra of GNP/ADT films. e) Film thicknesses determined via AFM analysis for GNP/ADT films fabricated using 4DT–10DT cross-linkers. The error bars correspond to deviations from 10 extracted height profile lines. f) Conductivities of GNP/ADT films. Subplots a,b,d) were adapted and reprinted with permission from Ref. [3], ©2021 American Chemical Society. (DOI: 10.1021/acsanm.1c01892)

films fabricated using different cross-linkers. A red-shift of the LSPR maximum is visible for shorter cross-linkers, due to increased coupling between adjacent GNPs with reduced interparticle distances.[37,63,188] AFM analysis revealed average film thicknesses ranging from 60 – 85 nm (figure 6.9e). The film conductivities were calculated from the linear *IV* curves under consideration of the film thickness and the electrode geometry and are plotted in figure 6.9f). Depending on the alkyl chain length of the cross-linkers, the conductivity can be tuned over several orders of magnitude, while the conductivity decreases with increasing cross-linker length. The values determined in this study are in good agreement with conductivities reported in the literature for similar films.[63] In order to study the impact of varying interparticle distances on the chemiresistors' response times, the as-fabricated sensors were transiently exposed to vapors of various analytes (ethanol, 1-propanol, 2-propanol, 1-butanol, hexane, heptane, octane, toluene, and MIBK) with concentrations ranging from 100–4000 ppm for 4 minutes, followed by 16 minutes ZG exposure. The measurements were conducted over the course of ~2 weeks. Exemplary response transients of chemiresistors fabricated using different cross-linkers to toluene and MIBK vapors of 100 and 800 ppm are displayed in figure 6.10. All GNP/ADT films show comparable response amplitudes at the given concentrations due to the similar chemical nature of the used cross-linkers, which dictates the affinity of the organic matrix to the target analytes and mainly governs the resulting relative resistance changes. However, pronounced differences can be seen regarding the response and recovery times of the selected sensors. Most notably, the GNP/4DT and GNP/6DT chemiresistors show analyte-dependent dynamic responses, with higher response times for MIBK than toluene. The GNP/10DT and GNP/8DT films, on the other hand, show fast responses (similar transient

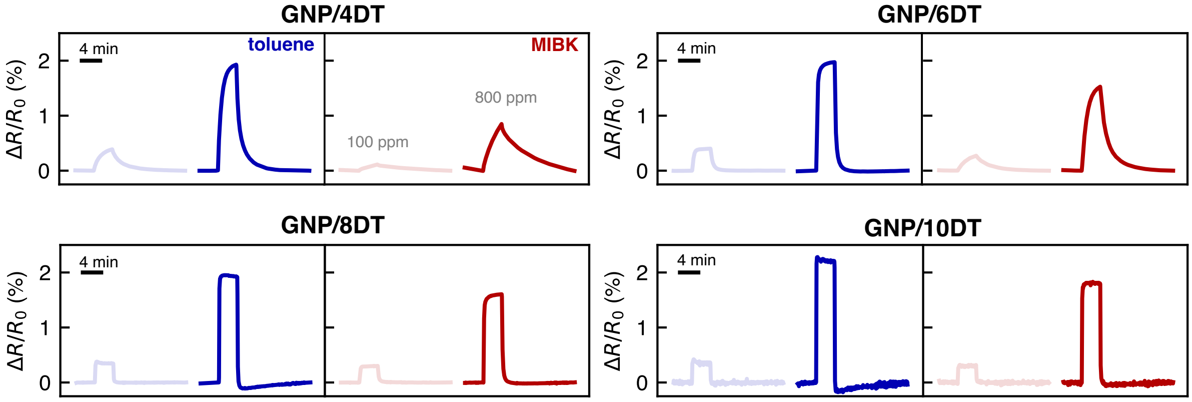

Figure 6.10: Exemplary baseline-corrected transient responses of GNP/ADT chemiresistors with comparable film thicknesses fabricated using 3.6 nm GNPs and varying cross-linker lengths to vapors of toluene (blue) and MIBK (red) at concentrations of 100 and 800 ppm, indicated by the color intensity. Adapted and reprinted with permission from Ref. [3], ©2021 American Chemical Society. (DOI: 10.1021/acsanm.1c01892)

shapes) for both analytes. As described in the previous paragraph, t_{80} was extracted from the chemiresistors' responses to 800 ppm toluene, MIBK, and 1-propanol. The dependence of the extracted response time on the cross-linker chain length is shown in figure 6.11a). Supporting the observed transient shapes shown in figure 6.10, significantly higher t_{80} response times were obtained from the chemiresistors comprising shorter cross-linkers (4DT and 6DT), with pronounced differences for all three analytes. In order to correlate the observed response times with the analyte size, first, the analytes' molecular volumes V_a in liquid phase were estimated using the following equation 12:

$$V_\mathrm{a} = \frac{M_\mathrm{a}}{\mathrm{N_A} \rho_\mathrm{a}} \tag{12}$$

where $\mathrm{N_A}$ is the Avogadro constant (6.022×10^{23} mol^{-1}), and M_a and ρ_a are the molar mass and density of the analyte, respectively. The cubic root of this calculated volume was considered as a measure of the analyte size having the same dimension as the edge-to-edge interparticle distances estimated via SAXS.[63] Figure 6.11b) shows the correlation of t_{80}, extracted for 800 ppm exposures, and this estimated size measure for the set of probed analytes for (top plot) GNP/4DT and (bottom plot) GNP/6DT chemiresistors. Clearly, t_{80} increases with increasing analyte volume. The trend is more pronounced for the GNP/4DT sensor compared to the GNP/6DT sensor, and is most prominent for analytes with sizes $\leqslant 0.55$ nm. Despite having almost identical calculated molecular volumes,

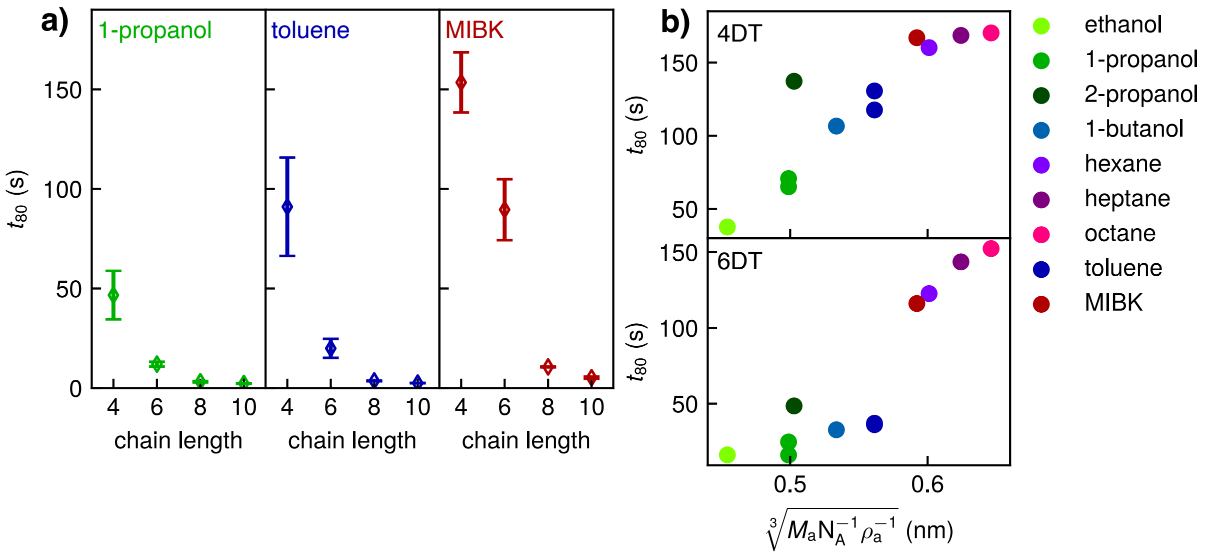

Figure 6.11: a) Response times t_{80} of GNP/ADT chemiresistors fabricated using 3.6 nm GNPs and ADTs of varying chain lengths (4DT–10DT) for transient exposure to 800 ppm of 1-propanol, toluene, and MIBK. The error bars represent the deviations of measurements of two sensors fabricated from the same GNP/ADT film. b) Response times t_{80} in dependence of $\sqrt[3]{M_\mathrm{a}\mathrm{N_A^{-1}}\rho_\mathrm{a}^{-1}}$ of a GNP/4DT (top) and a GNP/6DT (bottom) chemiresistor for different analytes at 800 ppm. Rearranged and reprinted with permission from Ref. [3], ©2021 American Chemical Society. (DOI: 10.1021/acsanm.1c01892)

significantly different response times are obtained for 1-propanol and 2-propanol exposures, especially for the GNP/4DT sensor. A possible dependence of the observed response times with the analytes' vapor pressure, which vary for 1-propanol and 2-propanol, was ruled out, as shown in the Appendix A.1.4.
In summary, these results demonstrate a strong correlation of the nanocomposite films' nanogeometry and their dynamic responses to VOCs of different molecular size. Controlling the mesh size of the films by choice of the molecular cross-linker, the chemiresistors' response times can be selectively tuned and utilized for size-selective analyte recognition.

Tunability of Response Times via Nanoparticle Size

Another possibility to tune the analyte transport within thin films is by varying the GNP sizes and shapes. For instance, Haick and co-workers showed that differently shaped ligand-stabilized metal nanoparticles (spheres vs. cubes) provide different interparticle voids impeding/facilitating analyte diffusion, resulting in distinct response times.[62] The use of GNPs of different core diameters for film fabrication, while keeping the cross-linker type and concentration constant, is expected to impact both, the degree of cross-linkage within the films,[53] as well as the interparticle distances. For instance, in a previous study from our group, Olichwer et al. investigated the cavity sizes in superlattices of ligand-stabilized GNPs of different sizes.[189] From SAXS measurements, the derived interparticle distance increased with the GNP size for systems comprising the same organic ligand.[189] Regarding cross-linked GNPs, a similar trend can be expected, possibly allowing for the adjustment of size-dependent response kinetics by variations of the GNP size.

Therefore, 6DT-cross-linked GNP chemiresistors were fabricated using GNPs of different sizes (3.5 ± 0.6 nm and 9.0 ± 0.5 nm), synthesized via the Leff[38] and Peng method,[39] respectively. The sensors were exposed to vapors of heptane, toluene, and 1-propanol at a concentration of 800 ppm. Based on the results shown in the previous paragraph, pronounced size-dependent response retardations are expected from GNP/6DT films fabricated using 3–4 nm sized GNPs. Figures 6.12b-c) show exemplary baseline-corrected transient responses to 800 ppm heptane, toluene, and 1-propanol for $\mathrm{GNP}_{9.0\ \mathrm{nm}}$/6DT and $\mathrm{GNP}_{3.5\ \mathrm{nm}}$/6DT, respectively. Obviously, distinct transient shapes were obtained for both film systems. The $\mathrm{GNP}_{3.5\ \mathrm{nm}}$/6DT sensor shows relatively slow responses with analyte-dependent differences, in agreement to the data shown in the previous paragraph. However, overall fast responses can be observed for the $\mathrm{GNP}_{9.0\ \mathrm{nm}}$/6DT sensor for all analytes. It is to note that the sensing signal recorded for heptane using the $\mathrm{GNP}_{3.5\ \mathrm{nm}}$/6DT sensor shows a comparably low signal-to-noise ratio, due to the overall low response amplitude. Still, it was possible to extract t_{80} response times from all transients, as summarized in figure 6.12a). Clearly, chemiresistors fabricated from smaller GNPs show pronounced

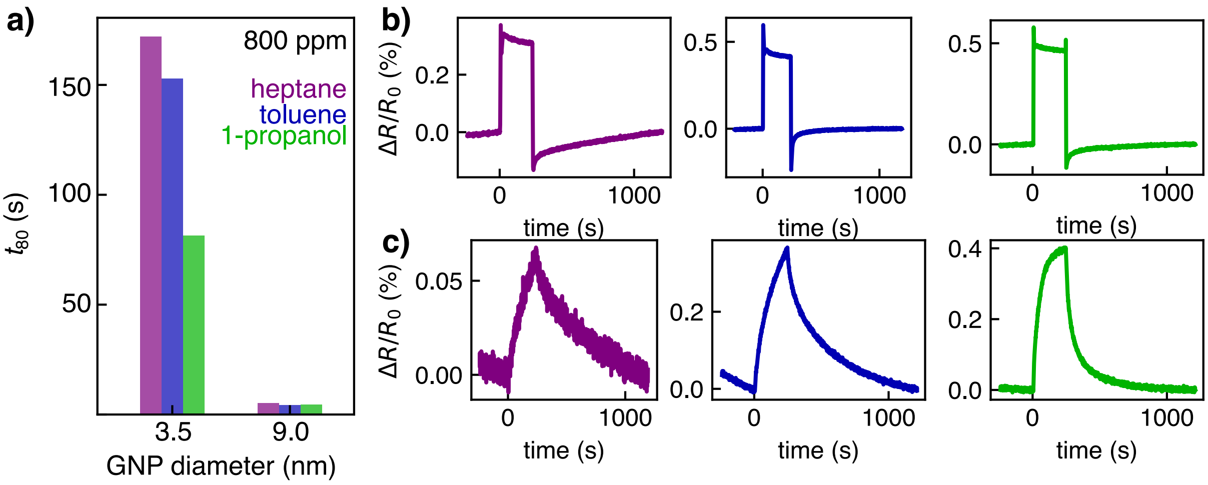

Figure 6.12: a) Response times t_{80} extracted from transient responses to heptane, toluene and 1-propanol at 800 ppm of GNP/6DT sensors made from differently sized GNPs. b-c) Exemplary baseline-corrected transient responses to 800 ppm heptane (purple), toluene (blue), and 1-propanol (green) corresponding to the b) GNP$_{9.0\text{ nm}}$/6DT and c) GNP$_{3.5\text{ nm}}$/6DT sensor.

analyte size-dependent response retardations, while fast responses (< 10 s) are obtained from the GNP$_{9.0\text{ nm}}$/6DT sensor for all analytes. These preliminary findings suggest that, aside from adjustment of response times via choice of ADTs, the void sizes and the concomitant diffusion-controlled response times, can be modulated by varying the GNP size. Note that in our published experiments, a strong dependence of the GNP batch used for film fabrication on the observed response kinetics was described, as well as partly inconclusive trends, especially when comparing GNPs of similar sizes (3–4 nm).[3] Still, the overall trend that chemiresistors fabricated from larger GNPs show faster responses was reported.[3] However, other parameters, e.g., the GNP shape, size- and shape distributions, the degree of order within the films, and the organic-inorganic content ratio might play significant roles concerning analyte-dependent response times.

Tunability of Response Times via UV Exposure

The aforementioned methods for tuning the response times of GNP/ADT chemiresistors rely on adjusting the film composition before or during film fabrication, such as by choice of the cross-linker or the GNP size. Using these methods, individual films or film sections on an array can be fabricated sequentially. However, strategies to remotely and gradually adjust the response characteristics of GNP/ADT films in post-fabrication steps are also of interest regarding, e.g., directed chemical modifications of a certain organic matrix surrounding the GNPs, or time- and material-efficient array fabrication. In this study, a UV-based procedure to selectively tune the response times of GNP/ADT films with initially non-selective response times was developed. Cross-linked films, fabricated using 9DT and 3.2 nm sized GNPs, were exposed to UV radiation for varying durations using a custom-built DUV source (254 nm, 520 mW/cm^2, cf. the Appendix, section A.1.1). The GNP batch was kindly provided by Dr. Bendix Ketelsen (University of Hamburg). To ensure the films' stability after UV exposure, they were re-immersed into a 9DT/methanol solution (7.4 mM) for 2 hours. For electrical and resistive sensing experiments, the film sections were equipped with gold electrodes (thickness: 100 nm). The sensor responses towards toluene, hexane, heptane, and octane were investigated using these films, as described in the previous paragraph. Figure 6.13 shows exemplary response transients for toluene and heptane exposures at 800 ppm for the unexposed GNP/9DT film (left panel), and for the GNP/9DT$_{60\mathrm{min\ UV}}$ film (right panel). Based on the observed transient shapes, UV treatment results in pronounced response retardations. On the one hand, almost rectangular, i.e., fast responses, that only differ in their amplitudes for both analytes, can be observed for the unexposed GNP/9DT film. On the other hand, the UV-treated film exhibits slowed responses compared to the untreated films, and also analyte-dependent response retardations, with a slower response to heptane compared to toluene. It is to note, that the sensitivity is also affected, since slightly lower response amplitudes are obtained within the transient exposure times when delayed responses occur. Resistive and kinetic response features, $\left(\frac{\Delta R}{R_0}\right)_{\mathrm{max}}$ and t_{80}, were extracted, as described previously. Figure 6.14 shows scatter plots of the combined response features for analyte concentrations ranging from 100–8000 ppm, indicated by the color intensity of the data. Accordingly, using the extracted response features of the unexposed GNP/9DT sensor (figure part 6.14a), the alkanes and toluene cannot be discriminated, due to overall fast responses (<15 s) for all analytes. However, well-distinguishable patterns are obtained for the GNP/9DT$_{60\mathrm{min\ UV}}$ sensor due to the UV-induced analyte-dependent response retardation. As described in the previous paragraphs, (cf. figure 6.11), the extracted t_{80} response times for this sensor

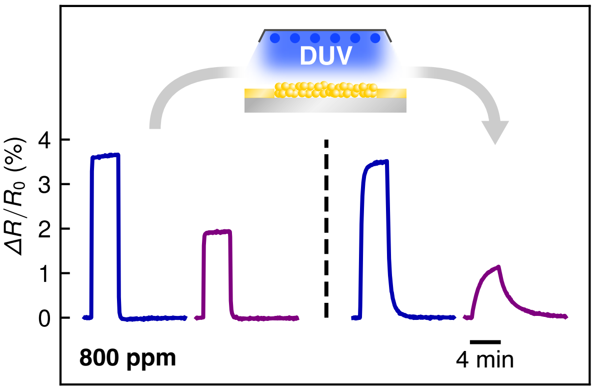

Figure 6.13: Comparison of the response of GNP/9DT chemiresistors to transient exposure to 800 ppm toluene (blue) and heptane (violet) for an untreated sensor and a sensor exposed to UV radiation for 60 minutes. Reprinted with permission from Ref. [3], ©2021 American Chemical Society. (DOI: 10.1021/acsanm.1c01892)

increase with increasing analyte molecular size (octane > heptane > hexane > toluene). Additionally, a concentration-dependence of t_{80} can be observed, with overall faster responses at higher concentrations. Based on these results, UV exposure can be employed as post-fabrication treatment of initially non-selective GNP/ADT chemiresistors to achieve discrimination between chemically similar analytes based on their molecular sizes.

The influence of UV exposure on the composite films' properties was further analyzed via UV-vis spectroscopy, electrical measurements, and x-ray photoelectron spectroscopy (XPS). The evaluation of the optical and *IV* measurements can be found in detail in the Appendix, section A.1.5. Optical measurements revealed a red-shift (~7 nm) of the LSPR maximum, suggesting decreased interparticle distances, possibly due to UV-induced cross-linker degradation. In addition, *IV* measurements of (re)-stabilized sections of a GNP/9DT film, illuminated for 0 min and 60 min, respectively, demonstrate that UV treatment leads to a slightly increased conductivity. However, further *IV* measurements conducted at cryogenic temperatures showed no pronounced differences in charge transport activation energies, calculated according to an Arrhenius activation model, between DUV-treated and untreated reference films. The impact of UV exposure on the chemical composition of selected films was investigated using XPS based on the assumption that UV-induced alterations of the cross-linkers comprising the organic matrix might occur. To this end, a cross-linked GNP/9DT film was deposited on an unoxidized silicon wafer via LbL SC. One section of the film was exposed to UV radiation for 120 minutes through a quartz slide. After UV exposure, the film was immersed in the 9DT/methanolic cross-linker solution for 2 hours, in analogy to the chemiresistor samples. Another section of the film was left untreated as the reference. The measurements and data fitting were conducted by Dr. Heshmat Noei (DESY Hamburg). XPS spectra of the S 2p energy

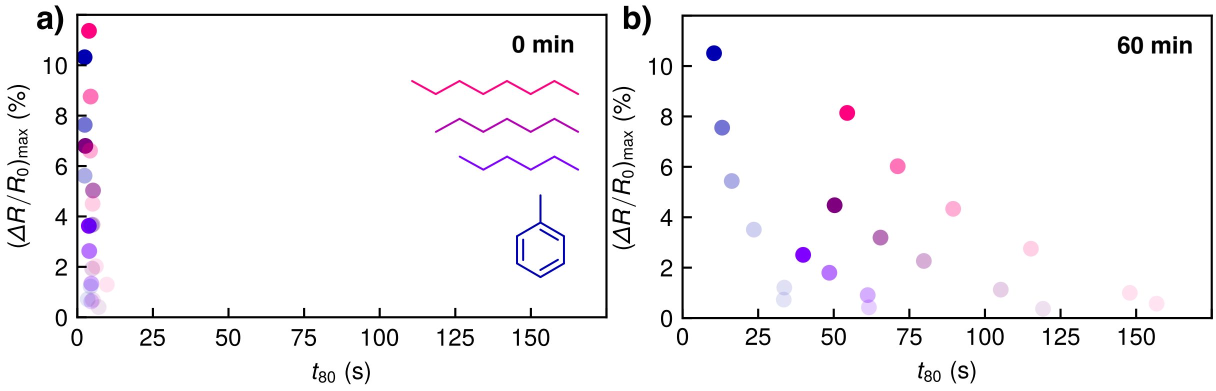

Figure 6.14: Scatter plots of the maximum relative resistance change vs. t_{80} for a) an untreated and b) UV-treated sensor for toluene, hexane, heptane, and octane at varying concentrations ranging from 100 to 8000 ppm. Sensor responses with $\left(\frac{\Delta R}{R_0}\right)_{max}$ below 0.25 % were excluded. Rearranged and reprinted with permission from Ref. [3], ©2021 American Chemical Society. (DOI: 10.1021/acsanm.1c01892)

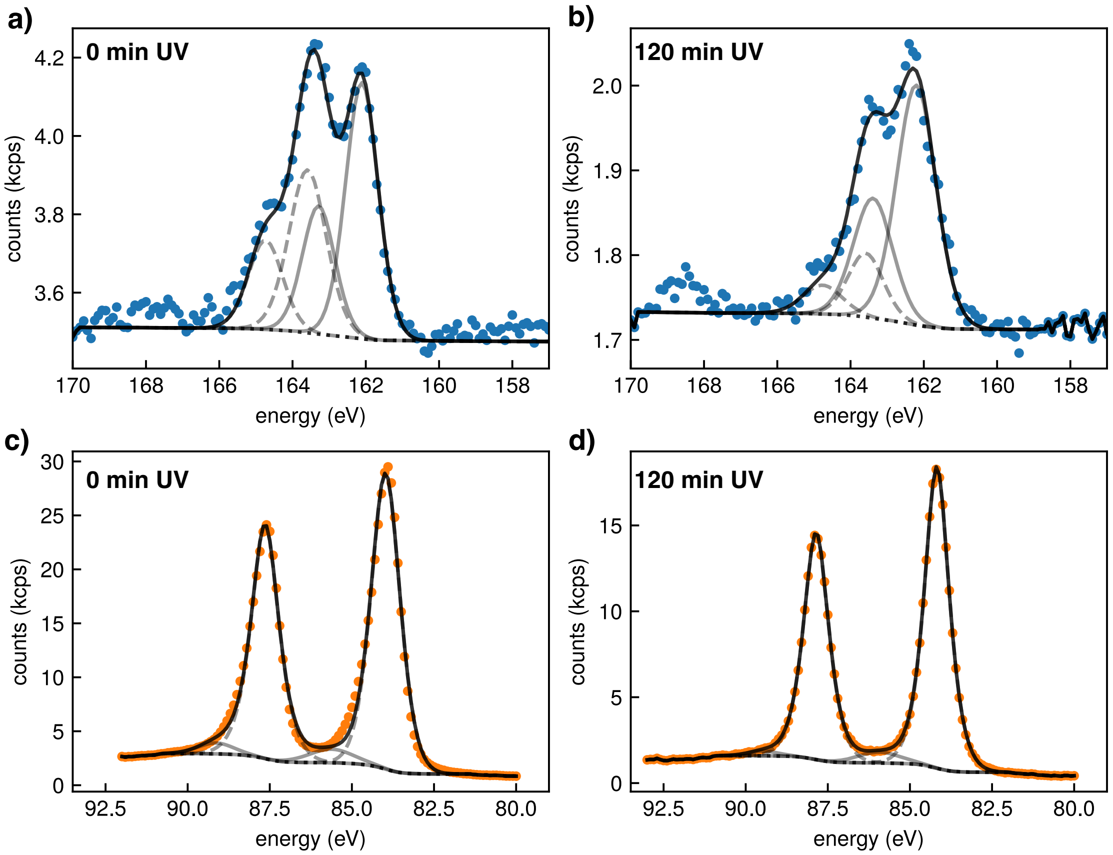

Figure 6.15: Deconvoluted XPS spectra of the (a,b) S 2p and (c,d) Au 4f energy ranges of an (a,c) untreated GNP/9DT film and (b,d) a UV-treated GNP/9DT film (120 minutes). Adapted and reprinted with permission from Ref. [3], ©2021 American Chemical Society. (DOI: 10.1021/acsanm.1c01892)

range of the untreated GNP/9DT film and the GNP/9DT$_{120\ \mathrm{min\ UV}}$ film are displayed in figures 6.15a) and 6.15b), respectively. The peaks were fitted using two doublets of Gaussian functions, corresponding to the $2p_{3/2}$ and $2p_{1/2}$ orbitals of thiols. The $2p_{3/2}$ peaks, centered at ~164 eV and at ~162 eV, correspond to S-H bonds and to S-Au bonds, respectively.[63] The obtained fit functions are shown in figure 6.15 as dashed (S-H) and solid (S-Au) gray lines. The black line corresponds to the resulting envelope function. Figures 6.31c) and 6.31d) show the fitted spectra of the Au 4f energy range for both films. Atomic ratios were calculated from the integrals of the signals and are summarized in table 6.1. While the ratio of gold-bound sulfur to gold is nearly unchanged after UV treatment, the fraction of hydrogen-bound sulfur, i.e., the amount of free thiols groups, decreases drastically in relation to gold-bound sulfur. In addition, the UV-treated film had a higher ratio of total gold to sulfur (detected in the 160–166 eV range) compared to the untreated film.

Table 6.1: Ratios of gold-bound sulfur to hydrogen-bound sulfur, of gold to sulfur, and of gold-bound sulfur to gold within the GNP/9DT films.[3]

GNP film	N(S-Au)/N(S-H)	N(Au)/N(S)	N(S-Au)/N(Au)
GNP/9DT$_{\text{0min UV}}$	1.37	3.39	0.17
GNP/9DT$_{\text{120min UV}}$	4.16	5.01	0.16

These results can be attributed to the favored oxidation of thiol groups of non-bridging 9DT molecules, suggesting that UV treatment does not cause significant de-linkage of the cross-linked films. Furthermore, a small signal at ~169 eV arises in the spectrum for the UV-treated film (figure 6.15b) which can be assigned to oxygen-containing sulfur species, e.g., sulfonates.[190] The oxidative formation of disulfides is also conceivable. It should be noted that, compared to earlier studies, the untreated GNP/9DT film shows a lower amount of free thiol groups,[63] possibly due to the shorter immersion (2 h) of the films in the cross-linker solutions after film deposition compared to earlier works.[37] In an earlier study of our group, XPS measurements were used to monitor artificial aging experiments of GNP/9DT films. Similar trends, i.e., a decrease in S-H content and an increased content of oxidized sulfur species, were observed for artificially aged GNP/9DT films (GNP core diameter ~3–4 nm) stored at 65 °C and 65 % r.h. in a climate chamber for 7 days,[53] further indicating that UV exposure might induce accelerated aging. As additional explanation for the increasing S-Au/S-H ratio, Ketelsen proposed the catalytic oxidation of cross-linking thiol groups on the GNP's surface, and their subsequent replacement by non-bridging thiols.[53] Further, evaporation of cross-linker molecules from the organic matrix is also possible, as proposed by Joseph et al. for long-term aged and ozone-treated interlinked GNP films.[191,192]

In general, the proposed processes would lead to a densification of the composite films, possibly causing hindered analyte diffusion and the observed response retardations. According to the presumed formation of oxygen-containing sulfur species, a UV-directed tunability of the sensor's selectivity can be expected and will be addressed in the next paragraph.

VOC Discrimination

In light of the results presented in the preceding paragraphs, the strategies to selectively adjust the dynamic responses of GNP/ADT films towards different analytes were used for the fabrication of a chemiresistor array for VOC discrimination. The sensor array consisted of GNP/ADT films fabricated using 3.6 nm sized GNPs and cross-linkers of varying lengths (4DT, 6DT, 8DT, 9DT) (cf. figure 6.9a-c), as well as GNP/9DT films exposed to UV radiation for varying duration, as schematically depicted in figure 6.16a). Using the same setup as described in the previous sections, the array was exposed to transients (4 minutes) of ten analyte vapors: octane, heptane, hexane, 1-butanol, 2-propanol, 1-propanol, ethanol, water, toluene, and MIBK. The analyte concentrations ranged between 100-4000 ppm. The recorded timetraces for all sensors on the array can be found in the Appendix, section A.1.3. For each sensor, distinct response features were extracted from the obtained sensor signals for each transient exposure, namely the maximum relative resistance change $\left(\frac{\Delta R}{R_0}\right)_{\max}$ as resistive feature and the integrated area A below the transient as kinetic feature. For representation, the resistive features of each sensor were normalized to the maximum response observed for the entire set of analytes (denoted as R^*). Similarly, the integrated areas A were rescaled between 120 s and the maximum area observed for every sensor for all analytes (denoted as A^*). Figures 6.16b-d) show radar plots of these response features for different analyte groups for exposures of 2000 ppm, revealing distinct patterns for the respective sets of analytes. Considering, for instance, the homologous series of alkanes (figure 6.16d), the resistive features of all sensors produce a similar shape for all alkanes and vary mostly in their magnitude due to the varying vapor pressures of the analytes. The kinetic features, however, mainly depend on the analyte size and are nearly

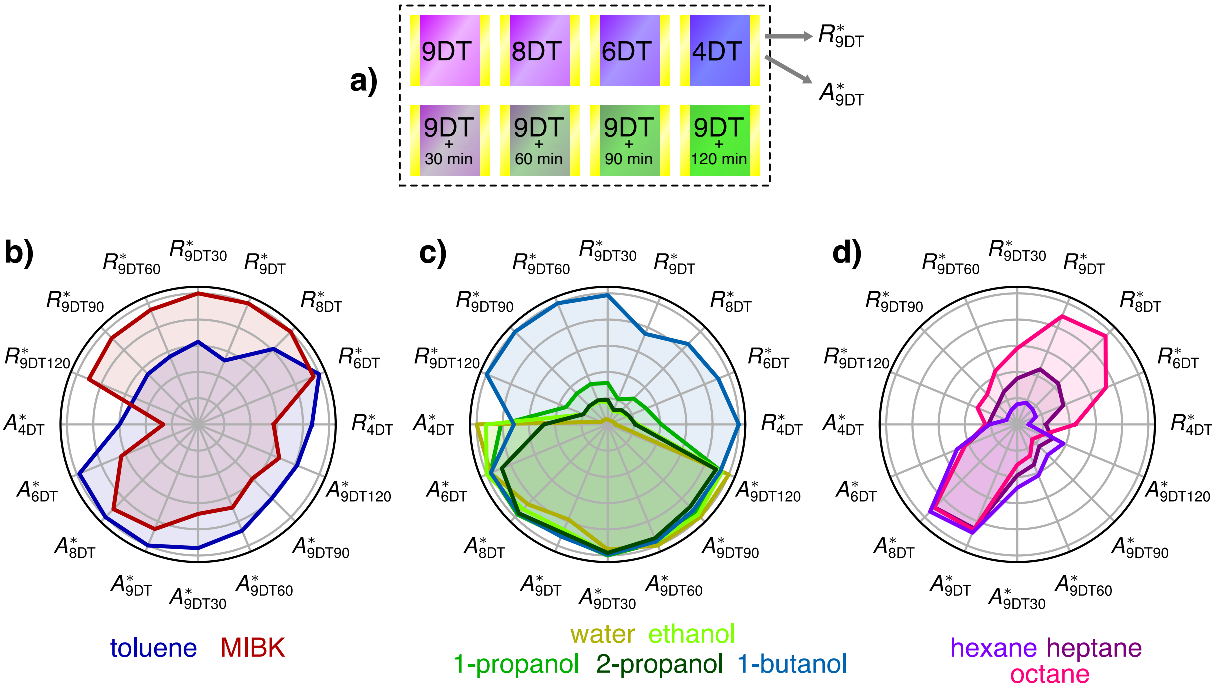

Figure 6.16: a) Schematic showing the composition of the GNP/ADT sensor array used for VOC discrimination based on the annotated resistive and kinetic response features. b-d) Radar plots of A^* and R^* of 8 sensors, extracted from transient responses to 2000 ppm b) toluene and MIBK, c) water, ethanol, 1-propanol, 2-propanol, 1-butanol, and d) hexane, heptane and octane. Adapted and reprinted with permission from Ref. [3], ©2021 American Chemical Society. (DOI: 10.1021/acsanm.1c01892).

identical for all alkanes for the sensors GNP/9DT and GNP/8DT, but vary according to the analyte size for the close-meshed- and UV-treated films, as discussed in the previous paragraphs (cf. figure 6.11). With regard to the chemiresistors' selectivity, the UV-treated GNP/9DT films exhibit an increased sensitivity towards polar analytes (figure 6.16b) compared to their untreated GNP/9DT counterpart. The increased sensitivity might be caused by the UV-induced formation of oxidized thiol species, e.g., sulfonates, imparting higher affinities towards polar solvents. This assumption is consistent with XPS analysis of UV-treated films, that suggests UV-induced oxidation of non-bridging thiol groups present in the films' organic matrix (cf. figure 6.15). Similar changes in sensitivity were described by Joseph and co-workers after ozone-treatment of bisthiocarbamate cross-linked GNPs.[192]

Drawing from the distinct patterns obtained from the extracted response features of the chemiresistor array, $\left(\frac{\Delta R}{R_0}\right)_{\text{max}}$ and $A/\left(\frac{\Delta R}{R_0}\right)_{\text{max}}$ were used as input for linear discriminant analysis (LDA). LDA was conducted by implementation of the `discriminant_analysis.LinearDiscriminantAnalysis` class from the scikit-learn (version 0.24.2) python library using the eigen-solver algorithm. The resulting LDA plot is presented in figure 6.17 and shows clear clustering of the particular analytes, except for MIBK that cannot be clearly separated from the adjacent heptane and hexane groups. Notably, well-separated clusters are obtained despite the input/training data (colored circles) corresponding to analyte exposures of varying concentrations (100–4000 ppm). For some analytes, e.g., octane, the clusters appear slightly elongated accordingly, as indicated by the intensity of the colors, possibly due to the more pronounced concen-

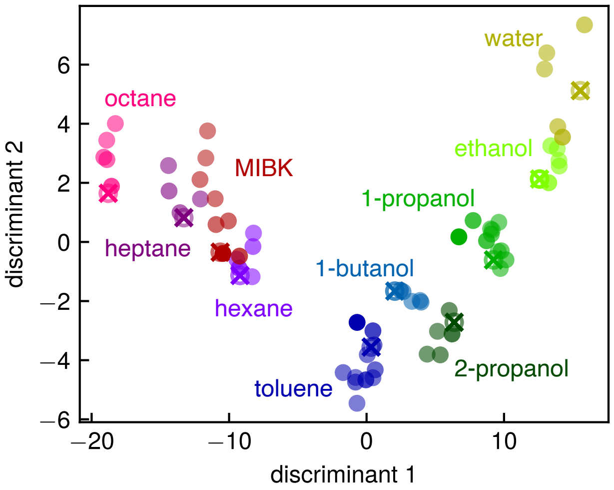

Figure 6.17: LDA of data sets for 10 VOCs collected using the GNP/ADT chemiresistor array, based on kinetic and resistive features as input. The colored circles correspond to the training set showing the class separation attained using LDA. The intensity of the color corresponds to varying concentrations (100-4000 ppm). The empty circles are projections of test exposures (2000 ppm) on the LDs. The crosses correspond to the analytes predicted by the LDA algorithm for the test exposures. Reprinted with permission from Ref. [3], ©2021 American Chemical Society. (DOI: 10.1021/acsanm.1c01892)

tration dependency of the response times for some analytes. Furthermore, the trained LDA was used to predict unlabeled test exposures at a given concentration (2000 ppm), shown as white circles in figure 6.17. As can be seen from the outline color, these test exposures were projected correctly onto their respective clusters, and using the `discriminant_analysis.LinearDiscriminantAnalysis` prediction function, the exposures were classified correctly with an accuracy of 100 %, as indicated by the color of the crosses plotted onto the outlined circles. Additional test exposures corresponding to higher and lower concentrations were probed (effectively also changing the training data set) and resulted in partly inaccurate predictions. These results are provided in the Appendix, section A.1.6. However, we assume that implementing an LDA using a larger input data set will enhance its accuracy, allowing for its reliable use for analyte prediction over a wide concentration range.

To highlight the benefit of using adjusted, analyte-dependent response kinetics for analyte discrimination, LDA was performed based solely on the resistive responses of the GNP/ADT sensor array. Here, LDA did not generate well-separated analyte clusters and provided partly inaccurate predictions (cf. the Appendix, section A.1.6). These results clearly demonstrate the advantage of using tunable analyte-dependent response times for VOC recognition.

Outlook: Binary VOC Mixtures Sensing

Although the identification of VOCs in their pure states was enabled by the use of adjusted response kinetics of cross-linked GNP films, the reliable recognition of target analytes in mixtures of unknown composition is of special relevance from an application point of view.[8] Therefore, it is of interest to investigate how exposure to VOC mixtures would reflect in GNP/ADT chemiresistors' response times, and whether they can be utilized for discrimination of VOCs in mixtures. For this purpose, chemiresistor arrays were fabricated using GNPs with a diameter of 3.5 nm and 6DT as cross-linker, since we demonstrated that analyte-dependent response retardations are observed for this system. A TEM image of the GNPs used for array fabrication is shown in figure 6.18a). Patterned GNP films were fabricated on silicon wafers equipped with 8 IDEs (Ti/Au, thickness: 10 nm/40 nm), following the lift-off process presented in detail in section 6.1.2, figure 6.3. Figure 6.18b) depicts a photograph of a representative device used for mixtures sensing measurements. The device consists of two patterned GNP/6DT sensor arrays. The array chips were connected via wire-bonding to a custom-designed PCB used to interface the sensors inside the test cell. Overlayed *IV* curves of 15 GNP/6DT films on the array are plotted in figure 6.18c), demonstrating that GNP films with highly reproducible electrical properties are obtained by the lift-off-based patterning method. Note, that 1/16

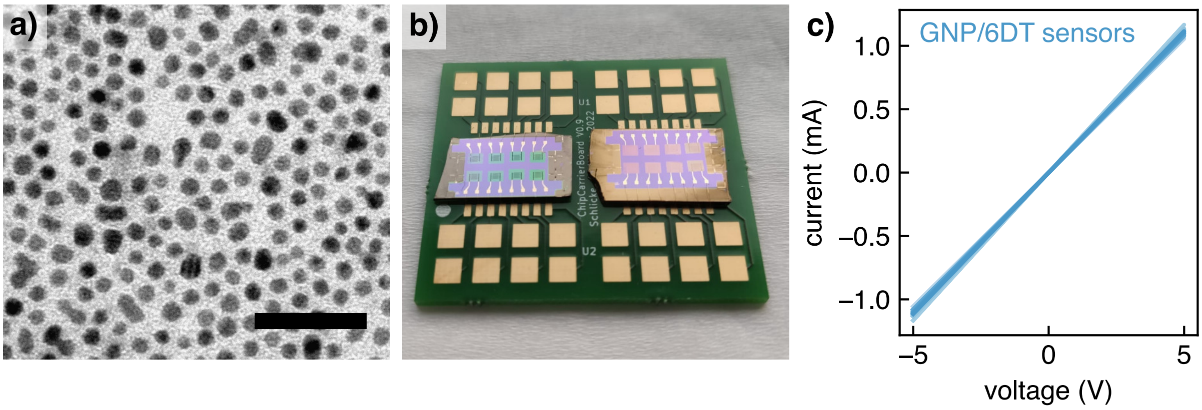

Figure 6.18: a) Exemplary TEM image of GNPs (diameter: 3.5±0.6 nm) used for chemiresistor array fabrication (scale bar: 20 nm). b) Photograph of a representative sensing device consisting of two lithographically patterned GNP/ADT arrays (2 × 8 sensor areas) on silicon wafers, supported on a custom-designed printed circuit board (green) for electrical contact. c) *IV* curves of 15 patterned GNP/6DT films on the array.

sensors was excluded from the measurements due to a damaged IDE on the array. The chemiresistive responses of the array towards four binary VOC mixtures of varying analyte fractions were investigated. To this end, the sensor array was placed in a custom-built test cell and contacted using spring-loaded pin connectors. A home-built measurement device was used to provide a constant bias of 2.5 V and to measure the sensor signal of 13 sensors in parallel at a sampling rate of ~2 Hz. The circuitry of the employed readout system was designed by Dr. Hendrik Schlicke (Fraunhofer Center of Applied Nanotechnology). Two gas calibration systems (CGM 2000, MCZ Umwelttechnik) were used to provide binary VOC mixtures where each system generated certain concentrations of one component (AG). Nitrogen (5.0) was used as the carrier gas and as ZG, and the total concentration was set to 400 ppm. The valves for switching between AG and ZG of both systems were triggered simultaneously at programmed intervals using an Arduino-controlled switching device. The outlet flows of each system were merged using a T-connector. From this mixed flow, 0.5 L/min were constantly purged through the test cell using a flow controller. A schematic depiction of the setup is given in the Experimental Section, section 7.7.

An overview of the investigated binary mixtures of “analyte a” and “analyte b”, along with the set analyte fractions, is listed in table 6.2. At a constant total concentration of 400 ppm, the fraction x_a of “analyte a” was varied between 0 – 1, in 0.1 steps. The fraction of “analyte b” was set accordingly as $1{-}x_a$. Each VOC composition was measured twice in a random sequence, as listed in table 6.2. The measurements were conducted over the course of ~2 weeks. All timetraces are provided in the Appendix, section A.1.8.

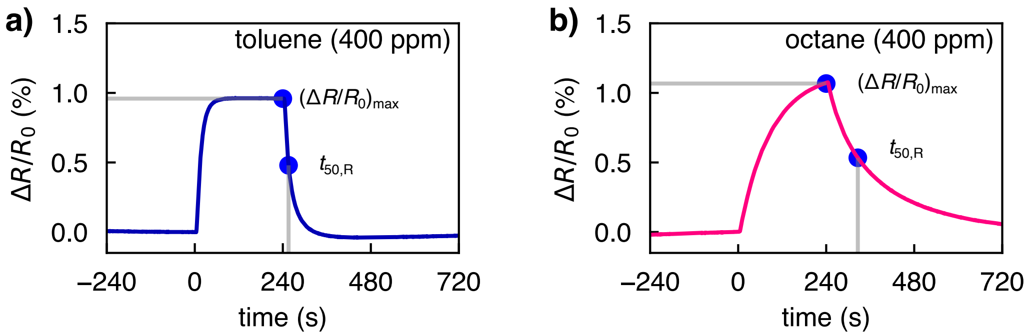

Figure 6.19: Exemplary response transients of a GNP/6DT chemiresistor on an array to exposures of pure a) toluene and b) octane vapors at a concentration of 400 ppm (4 minutes). As indicated by the blue circles, $\left(\frac{\Delta R}{R_0}\right)_{max}$ and $t_{50,R}$ were extracted as resistive and kinetic response features from the signals.

Table 6.2: Binary VOC mixtures at a total vapor concentration of 400 ppm and targeted analyte fractions.

	analyte a	analyte b	analyte fraction x_a
1[a]	hexane	octane	0, 0.8, 0.4, 0.6, 0.7, 1, 0.5, 0.1, 0.9, 0.3, 0.2 0.9, 0.4, 0.5, 0.6, 1, 0.3, 0.1, 0, 0.2, 0.8, 0.7
2[ab]	toluene	octane	0, 0.8, 0.4, 0.6, 0.7, 1, 0.5, 0.1, 0.9, 0.3, 0.2 0.9, 0.4, 0.5, 0.6, 1, 0.3, 0.1, 0, 0.2, 0.8
3[ab]	1-propanol	octane	0, 0.8, 0.4, 0.6, 0.7, 1, 0.5, 0.1, 0.9, 0.3, 0.2 0.9, 0.4, 0.5, 0.6, 1, 0.3, 0.1, 0, 0.2, 0.8
4	1-propanol	MIBK	0, 0.8, 0.4, 0.6, 0.7, 1, 0.5, 0.1, 0.9, 0.3, 0.2 0.9, 0.4, 0.5, 0.6, 1, 0.3, 0.1, 0, 0.2, 0.8, 0.7

For all 13 GNP/6DT sensors, various response features were extracted for each VOC mixture exposure. Figures 6.19a-b) show exemplary response transients of one chemiresistor to pure toluene and octane exposures at 400 ppm, respectively. As indicated by the blue circles, $\left(\frac{\Delta R}{R_0}\right)_{max}$ was determined, as described in the preceding paragraphs, to extract $t_{50,R}$ as kinetic feature, corresponding to the time during ZG exposure needed to reach $0.5 \cdot \left(\frac{\Delta R}{R_0}\right)_{max}$. Commonly, slow response rise times also result in delayed recovery times, as clearly visible, e.g., for the GNP/6DT sensor response to octane. The AG exposure time (240 s) was subtracted from the raw recovery times to obtain corrected values. The observed transient shapes and extracted $t_{50,R}$ recovery times for toluene and octane ($t_{50,R\text{-octane}} > t_{50,R\text{-toluene}}$) are consistent with the results discussed in the preceding section for GNP/6DT chemiresistors. In order to evaluate the evolution of the response kinetics with variations of the VOC mixture composition, $t_{50,R}$ was plotted against the set analyte

---

The second x_a=0.1 exposure was excluded from evaluation due to a systematically faulty flow setting for the octane component. [b] The second x_a=0.7 exposure is missing due to a premature interruption of the measurement.

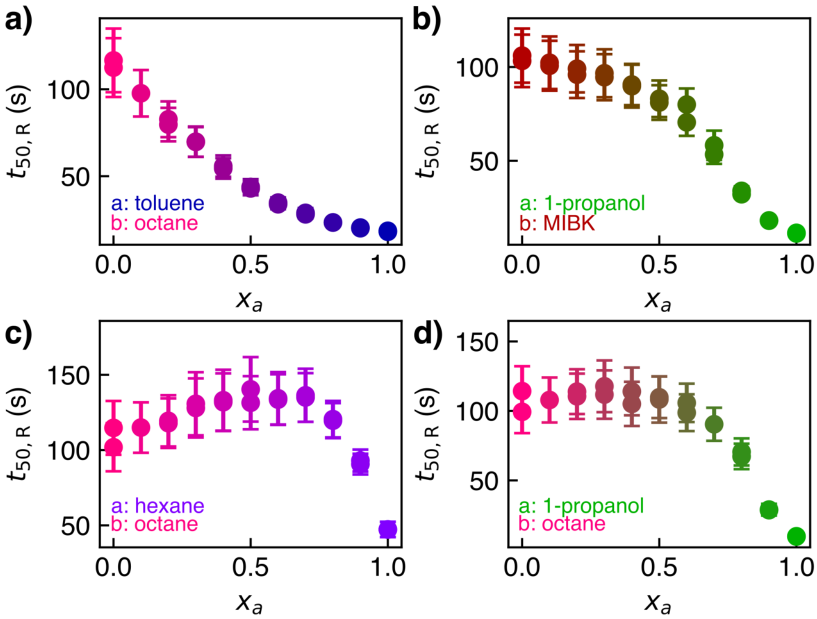

Figure 6.20: Correlation of $t_{50,R}$ and the set analyte fraction x_a in binary VOC mixtures of a) toluene and octane, b) 1-propanol and MIBK, c) hexane and octane, d) 1-propanol and octane. The total vapor concentration was constant at 400 ppm. All mixing ratios were measured twice. The error bars correspond to the standard deviation of values extracted for 13 GNP/6DT chemiresistors.

fraction x_a, as displayed in figures 6.20a-d) for four binary mixtures. First of all, with regard to the pure analyte exposures (x_a=0 and x_a=1), analyte-size dependent $t_{50,R}$ times can be seen, as expected. The fastest recovery times correspond to 1-propanol exposures. Interestingly, gradual changes in $t_{50,R}$ for different VOC compositions are visible, suggesting the superposition of both, the faster and slower response, depending on the mixing ratio. While for the mixtures of toluene/octane and 1-propanol/MIBK (figures 6.20a-b) distinct intermediate values are obtained, the mixtures of hexane/octane and 1-propanol/octane, shown in figure parts 6.20c-d), show almost constant $t_{50,R}$ values for relative octane fractions between 0–0.5. For the hexane/octane mixture, a slight increase of $t_{50,R}$ is visible for increasing hexane content, even though overall faster responses are expected for hexane vapor. This can be explained by the pronounced concentration dependence of the response/recovery times for octane vapors,[3] as visible e.g., in figure 6.14 for UV-treated GNP films. Apparently, the chemiresistors are more sensitive to variations of the relative octane content, which is reflected in the kinetic features of the responses. Presumably, this effect is caused by the large differences in vapor pressures between both analytes. It is expected that octane, which has a lower vapor pressure, partitions predominantly into the organic matrix of the film,[75] dominating the observed signal response, even though (less) hexane molecules diffuse faster into the film.

The evolution of the resistive responses for the binary mixtures are provided in the Appendix, section A.1.7. For octane/hexane and 1-propanol/octane mixtures, the responses spread over a range of ~ Δ0.8 %, and ~ Δ0.2–0.4 % for toluene/octane and 1-propanol/MIBK, indicating that similar response amplitudes might result in a better resolution of the analyte-dependent response kinetics using a GNP/6DT-based sensor array. In view of the results suggesting that varying VOC mixtures compositions result in superimposed transient shapes that reflect analyte-specific signatures, the composed sensor signals were tentatively fitted according to a linear combination model described by equation 13. According to this model, the composed response transient $\frac{\Delta R}{R_0}_{\mathrm{A,B}}(t)$ can be described as the weighted sum of the pure components' transient responses, where the weighting factors A and B ideally correspond to the respective relative analyte fractions.

$$\frac{\Delta R}{R_0}_{\mathrm{A,B}}(t) = A \cdot \frac{\Delta R}{R_0}_{\mathrm{A}}(t) + B \cdot \frac{\Delta R}{R_0}_{\mathrm{B}}(t) \tag{13}$$

The gray curve in 6.21a) depicts an exemplary composed transient for a toluene/octane mixture with relative analyte fractions of 0.5. The pink and blue curve correspond to pure octane and toluene exposures at 400 ppm, respectively, that were used as input data. Based on equation 13, A and B were derived from fit parameters determined using the `optimize.curve_fit` function from the SciPy (version 1.10.1) python library. Figure 6.21b) shows the fitted composed transient (dotted red line), as well as the weighted input data. The calculated fit function describes the measured composed transient very well, and the determined relative weighting factors (0.48/0.52) are almost identical to the set vapor composition of 0.5/0.5. This procedure was conducted for all measured transient responses for all tested binary mixtures. The calculated relative weighting factors were plotted against the set analyte fractions, and are shown in figure 6.22. The composed transients for toluene/octane and 1-propanol/MIBK mixtures are well-described by the linear model used, as the calculated analyte fractions correlate almost linearly with the set mixing ratios. This indicates that the particular transient shapes and analyte-dependent

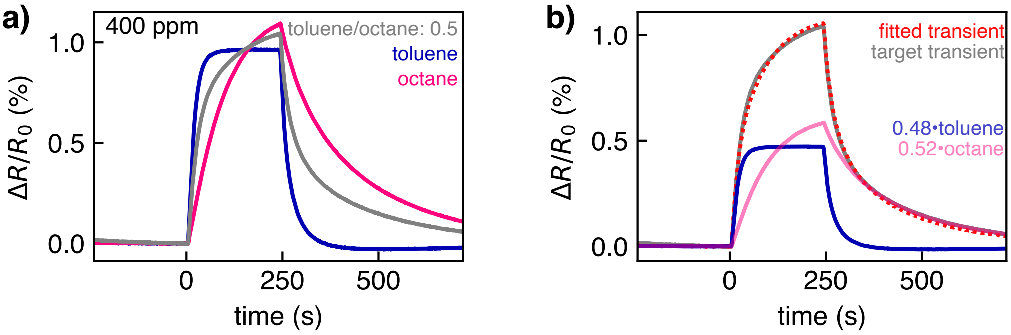

Figure 6.21: a) Measured transient responses of a GNP/6DT chemiresistor to vapors of toluene (blue), octane (pink) and toluene/octane (0.5/0.5) (gray) at a vapor concentration of 400 ppm. b) Output of a modeled transient response (dotted red line) to a toluene/octane mixture (0.5/0.5) using a linear combination of transient responses to toluene (light blue) and octane (light pink).

response kinetics can be utilized to predict the composition of binary mixtures. In the case of the 1-propanol/MIBK mixture (figure 6.22b), the calculated MIBK fraction is slightly overestimated for x_a=0.3–0.7. As expected from the indistinguishable response times extracted for hexane/octane and 1-propanol/octane exposures, the composed transients could not be described as linear combinations of the pure components, as the octane content is largely overestimated in both cases.

In conclusion, the use of analyte-dependent response kinetics is promising for VOC recognition in analyte mixtures, and will be further explored in future studies. Here, it was demonstrated that a single sensor type with adjusted dynamic responses yields distinct response signatures to certain binary VOC mixtures that can be deconvoluted to determine the relative amount of each component at a given concentration. The limitations observed for some mixtures, e.g., the concentration dependence of response times, will be further investigated and could be overcome by using various chemiresistors with different selectivities and response kinetics. Data acquisition will be optimized to train an artificial neural network with response transients for VOC recognition. Further, the underlying mechanism for mixtures sensing will be studied. For instance, the influence of vapor interactions and possible phenomena of cosolvency/cononsolvency, that are known polymer-based sensors,[193,194] should be considered. The measurements will be expanded

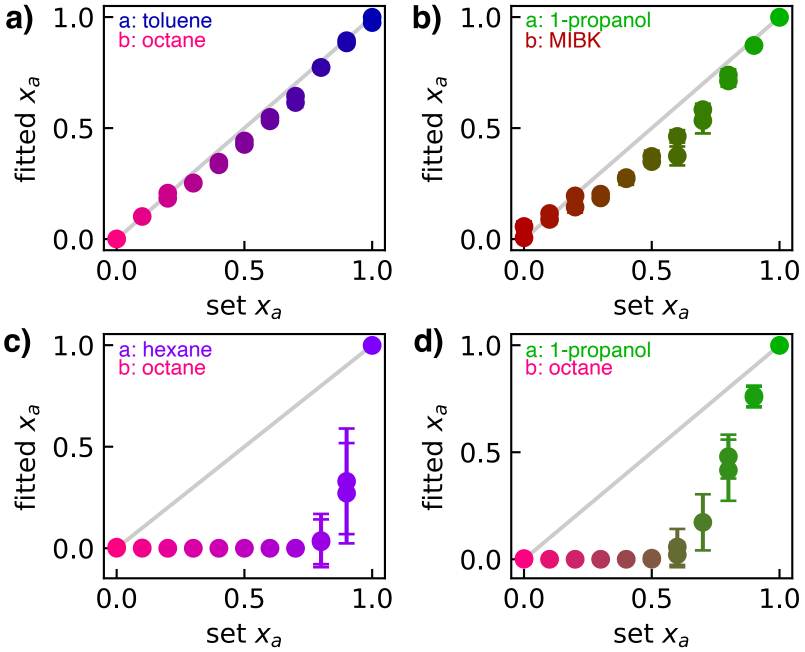

Figure 6.22: Relation of fitted analyte fractions vs. set analyte fractions in binary VOC mixtures of a) toluene/octane, b) 1-propanol/MIBK, c) hexane/octane, and d) 1-propanol/octane. All mixing ratios were measured twice. The error bars correspond to the standard deviation of values fitted for transients of 13 GNP/6DT chemiresistors.

to analyze ternary mixtures, and mixtures in humid environment to advance the use of these sensors in real-life conditions.

6.2 Graphene Oxide-TiO_2 Nanocomposites

This chapter focuses on the development of nanocomposite films comprised of TNCs and GO/rGO for resistive humidity and VOC sensing applications. GO and rGO are highly interesting materials for gas and vapor sensing applications due to their large surface area and anchoring groups for target molecules.[195] The combination of GO/rGO and TNCs in hybrid films results in versatile nanocomposites as potential sensors, since TNCs offer additional analyte sorption sites, and can be utilized to modulate the chemical composition of the hybrid film. Herein, a method to selectively tune the properties of such films was established which exploits the photocatalytic activity of TNCs to gradually reduce GO by exposure to UV light. First, the influence of the TNC shape, film thickness and composition, and UV exposure times on the photocatalytic reduction was studied. The obtained hybrid GO/rGO/TNC films were characterized using electrical measurements, spectroscopy and microscopy techniques regarding their electrical, optical and structural properties. Furthermore, this method was used to pattern GO/rGO areas on flexible substrates, allowing for the tunability of the chemical composition, and hence, the sensitivity and selectivity of the hybrid materials to r.h. and VOCs.

Parts of the results presented in this chapter were collected within the framework of Bachelor's and Master's theses under supervision of the author. Jana Struck, M.Sc., (University of Hamburg) optimized the GO/TNC thin film fabrication method, synthesized TNRs, and contributed major parts to the spectroscopic and electrical characterization of GO/rGO/TNR films.[196] Sophie Benthien, B.Sc., (University of Hamburg) contributed to the fabrication and characterization of flexible photocatalytically patterned GO/rGO/TNC chemiresistors.[197]

6.2.1 Synthesis and Characterization of Nanomaterials

Graphene Oxide

GO was synthesized for thin film fabrication according to a modified Hummer's method reported by Chen et al. in 2015.[113] Briefly, the synthesis involves the reaction of graphite flakes in a highly oxidizing medium, and the subsequent mechanical exfoliation to obtain colloidal solutions of monolayered GO. Figure 6.23a) displays an SEM image of freeze-dried GO which exhibits a porous and sponge-like structure. Additionally, figure parts b)-c) show an AFM image of individual GO sheets, deposited on a substrate, and a corresponding extracted height profile, respectively. AFM analysis revealed lateral dimensions of GO sheets of up to 5 µm, and a sheet thickness of ~1.1 nm, which is in good agreement with values reported in the literature for an atomic layer of GO.[112,113] Figure 6.23d) shows a UV-vis absorbance spectrum of an aqueous dilution of exfoliated GO, showing the characteristic bands at ~235 nm and ~300 nm, corresponding to the $\pi - \pi*$ transition of the graphitic structure, and the n-$\pi*$ transitions, arising from the sp^3 hybridized areas in GO, respectively.[113] Figure 6.23e) shows an attenuated total reflectance (ATR)-Fourier-transform infrared (FTIR) transmittance spectrum of freeze-dried GO which con-

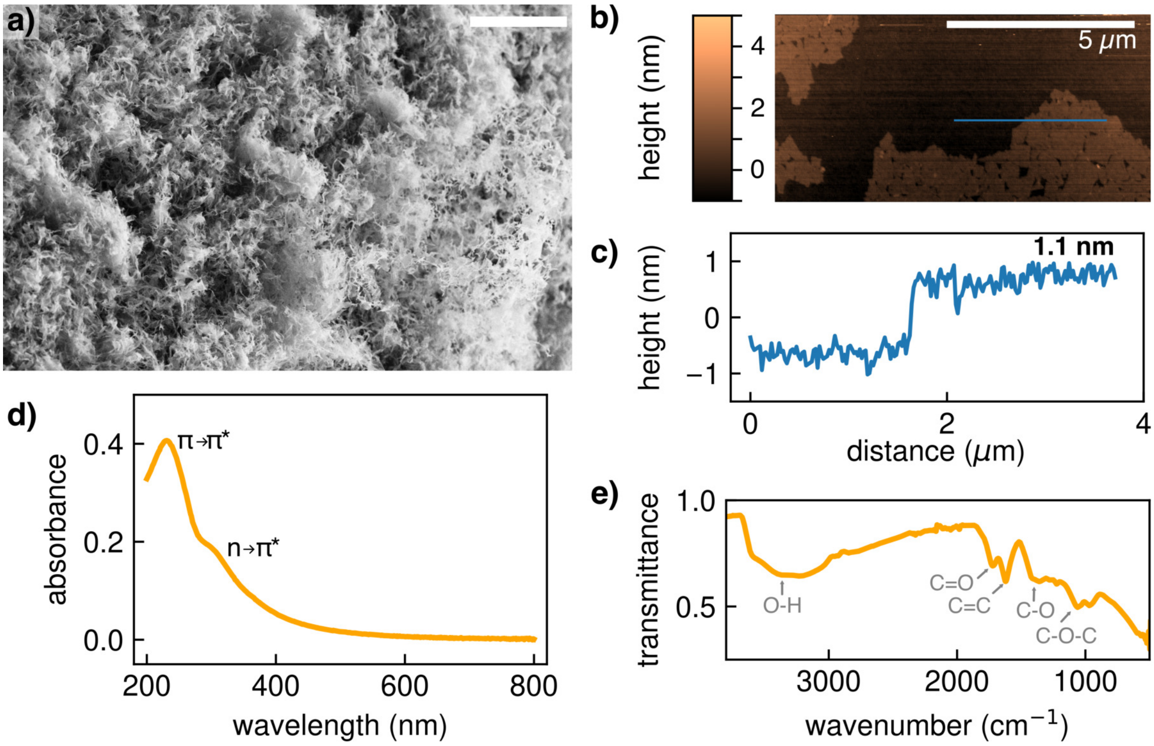

Figure 6.23: Characterization of GO synthesized for hybrid film fabrication. a) SEM image of freeze-dried GO flakes (scale bar: 80 µm). b) Topographic AFM image (10 µm×5 µm) of GO flakes drop-casted from an aqueous stock solution (0.5 mg/mL) onto a silicon wafer. c) Height line profile corresponding to the flake edge along the thin line drawn in b). d) UV-vis absorbance spectrum of a 0.01 mg/mL aqueous GO solution. e) ATR-FTIR transmittance spectrum of the freeze-dried GO.

firms the presence of oxygen-containing functional groups, showing characteristic bands at 3400-3200 cm^{-1} (O-H stretching), at 1720 cm^{-1} (C=O stretching), 1625 cm^{-1} (graphitic C=C), 1284 cm^{-1} and 1218 cm^{-1} (C-O bonds) and 1054 cm^{-1} (asymmetric C-O-C stretching).[112,198] GO was also characterized by combustion (CHS) and pyrolysis (O) elemental analysis. The relative atomic percentages are summarized in table 6.3. Based on the results, an empirical sum formula can be derived as $C_6H_{4.9}O_{4.8}S_{0.05}$, referring to a ring unit of 6 carbon atoms. The obtained C/O ratio of 1.25 is lower than the ratio reported by Chen et al. based on XPS analysis (C/O = 2.83),[113] however, this value should be considered with caution, since it is prone to error due to the difficulty to completely dehydrate GO.[112,199]

Table 6.3: CHSO-Elemental analysis of GO.

element	atomic %
C	38.3
H	31.0
S	0.29
O	30.4

TiO_2 Nanocrystals

TNCs of varying shapes were synthesized for their use as photocatalysts in composite GO/TNC films. Due to their varying sizes and shapes, differences in photocatalytic activities can be expected, e.g., due to variations of exposed facets with different photocatalytic activities.[139] TNRs and titania nanoplates (TNPs) were synthesized in a seeded-growth method reported by Gordon et al.[139] Here, shape control was achieved by variation of the titanium salt precursor and the choice of the co-surfactant (here: OLAM).

Figure 6.24 shows an overview of the characterization of the a) TNRs and b) TNPs used for thin film fabrication. Figure parts i) show exemplary TEM images of the different TNCs. The TNRs had an average length of 40 ± 7 nm and a thickness of ~3 nm, and the TNPs an average edge length of 22±3 nm. The insets show photographs of the TNC stock solutions in chloroform with a mass concentration of approx. 20 mg/mL, as determined via thermogravimetric analysis (TGA, cf. section A.1.9 in the Appendix). While the TNR solution (figure part a) appears slightly yellow, the TNP solution (figure part b) exhibits a characteristic blue color which arises from oxygen vacancies that are formed in the presence of fluorine that is provided by the TiF_4 precursor.[139] This results in n-doping of the material, and hence, low-energy transitions that can be excited by visible (red) light, leading to the observed blue color.[139] Figure parts ii) show the x-ray diffraction (XRD) patterns of

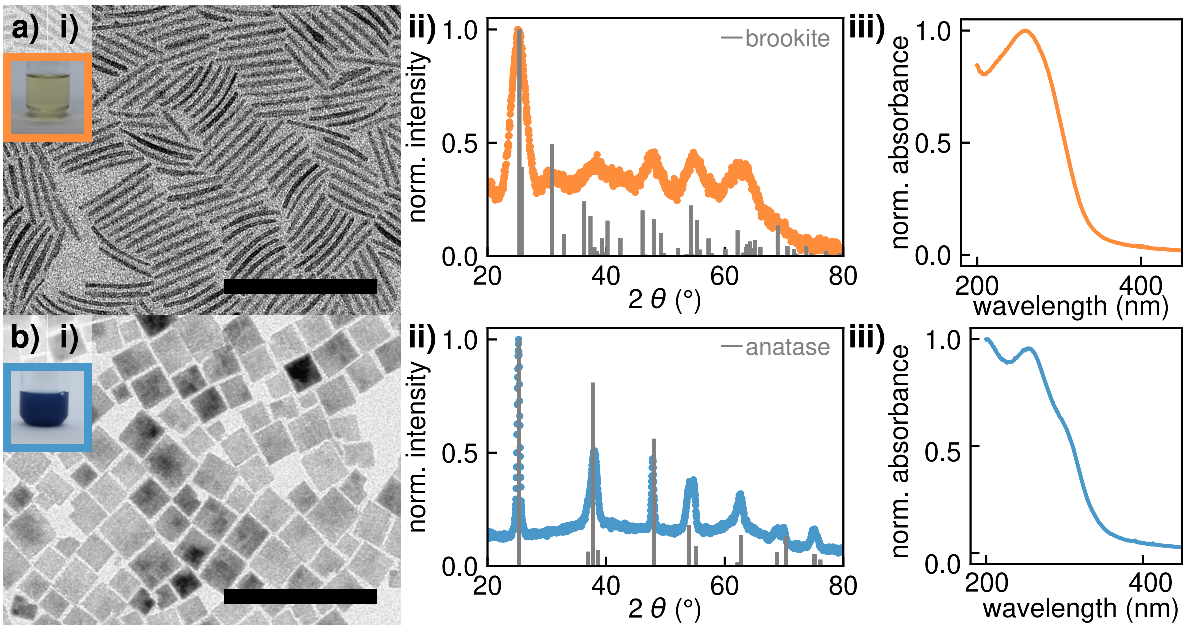

Figure 6.24: Overview of a) TNRs and b) TNPs used for hybrid film fabrication. i) Exemplary TEM images of the respective TNCs (scale bars: 100 nm). The inset shows photographs of the stock solutions in chloroform. ii) Normalized XRD diffractograms with the corresponding reference peaks for brookite[200] (TNRs) and anatase[201] (TNPs). iii) Normalized UV-vis absorbance spectra of the TNC solution spin-coated on a quartz slide.

the respective TNCs. Here, the TNPs show reflexes that correspond to the anatase crystal phase, and the TNRs show additional reflexes that can be assigned to the brookite crystal phase and presumably have an anatase-brookite mixed phase. The formation of brookite TNRs is described in the literature and occurs in a self-regulated seed-catalyzed phase transformation of anatase seeds to brookite during nanorod growth.[202] Figure parts iii) of figure 6.24 show the normalized UV-vis absorbance spectra of both types of TNCs. Both exhibit an absorbance maximum in the UV region related to the band gap energy of the TNCs. The maximum is located at ~260 nm, and the TNPs show a shoulder around 305 nm. This feature was observed in the literature for organically cross-linked TNP films[203] and nanocrystalline TiO_2 thin films deposited via chemical vapor deposition, and can be explained by quantization of the band structure of the nanocrystals.[204] Due to the maximal absorbance of all samples in the deep UV (DUV) range, a DUV source (emission wavelength of 254 nm) was used for the TNC-mediated photocatalytic reduction of GO (for detailed characterization of the lamp, see section A.1.1 in the Appendix).

6.2.2 Thin Film Fabrication and Characterization

Film Deposition via Layer-by-Layer Spin-Coating

The first part of this project involved the fabrication and characterization of hybrid films composed of TNCs and GO on various substrates. For this purpose, a LbL SC method was

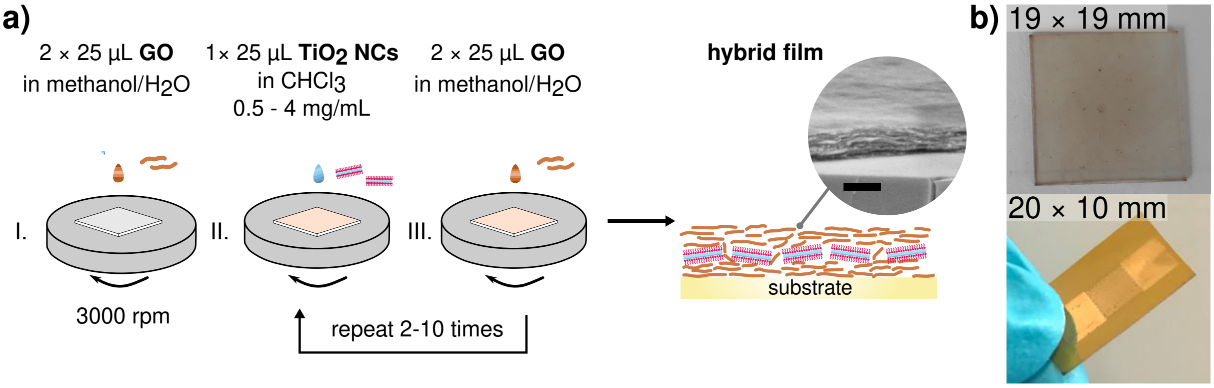

Figure 6.25: a) Schematic depiction of the LbL SC process used for GO/TNC film fabrication. (I.) An aqueous/methanolic GO solution (0.05–0.1 *wt*%) is applied to the rotating substrate (3000 rpm) to cover the substrate, and next (II.) the OLAM-capped (pink) TNCs in chloroform (0.5–4 mg/mL) are deposited, followed by GO deposition, yielding a sandwiched GO/TNC hybrid film. The inset shows an SEM image of the cross-section of a GO/TNR film after 10 deposition cycles (scale bar: 200 nm). b) Photographs of exemplary films deposited on a transparent quartz substrate (top) and on a flexible PI substrate equipped with an IDE (bottom). The inset numbers indicate the sizes of the respective substrates.

developed for the reproducible and time-efficient fabrication of layered hybrid films. The method was adapted from a procedure established in our group for the fabrication of organically cross-linked TNC membranes, in which layered films are formed by alternating deposition of TNCs from a colloidal solution, and a molecular cross-linker (e.g., dicarboxylic acids) from a solution.[203] Since GO is functionalized with carboxy groups, it was used to replace the low molecular weight organic cross-linker, assuming that the TNCs attach to the GO sheets due to the high affinity of carboxy groups to titania surfaces.[145]

Figure 6.25a) schematically shows the procedure for GO/TNC composite film fabrication. Hybrid films were deposited onto a variety of substrates, e.g., quartz slides, Si/SiO_2 wafers and polyimide (PI) substrates equipped with IDEs (Au, thickness: 50 nm). First, (I.), 2 × 25 µL of a methanolic/aqueous GO solution (0.05 – 0.1 *wt*%) was applied to the rotating substrate, with each deposition step spaced by 30 s (I.). Due to its high surface tension, water is not an ideal solvent for spin-coating onto a rotating substrate. However, GO exfoliation in organic solvents is challenging.[205] To achieve a uniform film deposition, GO was first suspended in water and exfoliated by sonication, and this solution was diluted using methanol according to the desired concentration. In the next step (II.), 25 µL of the respective TNC solution in chloroform (0.5 – 4 mg/mL, depending on the desired film composition) were applied. After 30 s, the deposition step of GO was repeated (III.). Depending on the desired film thickness and composition, the number of deposition cycles and the concentrations of the respective solutions were varied. It was possible to achieve homogeneous films with thicknesses ranging from ~15–150 nm. The film deposition was monitored by UV-vis absorbance spectroscopy of thin films deposited on quartz substrates. Figure 6.25b) shows an exemplary GO/TNR film deposited on a quartz slide

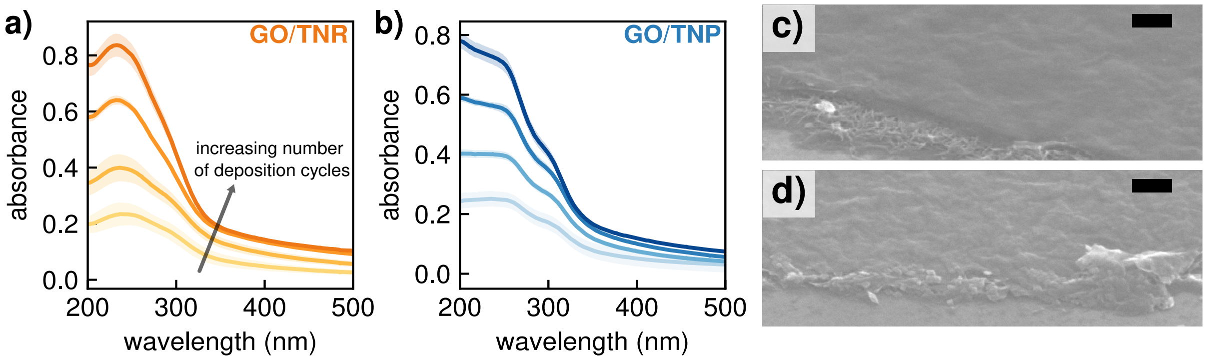

Figure 6.26: UV-vis absorbance spectra of a) GO/TNR and b) GO/TNP hybrid films fabricated applying 1 – 4 SC deposition cycles. The shaded area indicates the standard deviation from measurements at four different position of the quartz-glass-supported films. c-d) SEM images of edges of a GO/TNR and GO/TNP film, respectively (scale bars: 100 nm).

(10 SC deposition cycles). The obtained films revealed a light brown color, arising from the incorporated GO. Figures 6.26a-b) show the evolution of UV-vis absorbance spectra with increasing LbL SC deposition cycles for GO/TNR and GO/TNP films, respectively. Spectra were recorded at four different positions of each film and averaged. The shaded areas correspond to the standard deviation of four measurements, indicating a homogeneous film deposition on the substrates. The absorbance features of the single components are well visible (cf. figures 6.25iii and 6.23d). Since the films fabricated using different TNCs show a comparable absorbance after four SC deposition cycles, a comparable thickness and film layer formation can be assumed. Figures 6.26c-d) show SEM cross-sections of GO/TNR- and GO/TNP-films, fabricated using 4 SC deposition cycles, respectively. The images were recorded at film edges that were manually scratched using a cannula. The layered structure of the films, consisting of GO-covered TNCs is well visible. The film thickness after one SC deposition cycle was determined via AFM analysis and was ~17 nm and ~18 nm for the GO/TNP- and GO/TNR hybrid films, respectively. The corresponding AFM scans can be found in the Appendix, section A.1.10.

An approximation of the relative content of GO and TNCs within a thin film after one SC deposition cycle, based on the UV-vis absorbance of the films, can be found in the Appendix, section A.1.10, and revealed an estimated volume fraction of 39 % and 44 % TNPs and TNRs within the films, respectively.

6.2.3 TiO_2-Mediated Photocatalytic Reduction of Graphene Oxide

The sensing and electrical properties of the as-prepared hybrid films were adjusted via TNC-mediated photocatalytic reduction of GO to rGO. Figure 6.27a) schematically shows the photocatalytic reduction experiment. Here, the composite films were illuminated using a custom-built DUV source with a main emission wavelength of 254 nm and an irradiance of 520 mW/cm^2 in ambient conditions (cf. Appendix, section A.1.1). To

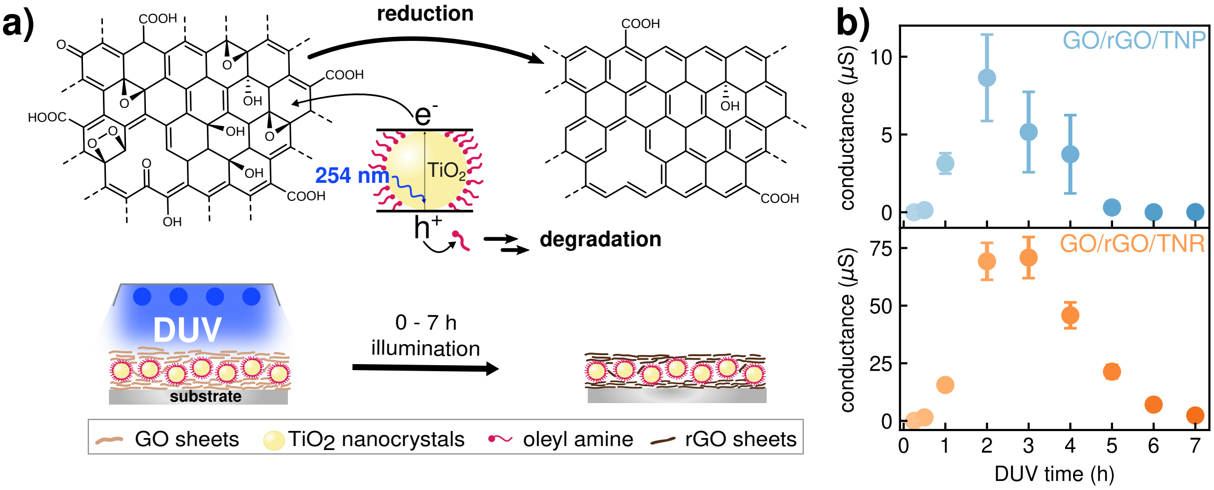

Figure 6.27: TNC-mediated photocatalytic reduction of GO. a) Sketch of a GO/TNC hybrid film on a substrate, consisting of GO sheets and OLAM-stabilized TNCs before (left) and after (right) UV illumination. (Top, left) Generalized chemical structure of GO functionalized with different oxygen containing functional groups. UV illumination (254 nm) leads to the excitation of an electron from the valence band to the conduction band of the TNCs. The photo-excited electrons are scavenged by the GO, resulting in the reduction of functional groups and the formation of rGO, while the organic ligands on the TNC surface are oxidized/degraded. b) Evolution of the film conductance with increasing UV exposure time for (blue) GO/TNP and (orange) GO/TNR films. The error bars represent the standard deviation based on film areas on two IDEs on one substrate.

avoid heating of the samples during UV exposure, the apparatus was constantly ventilated using fans. Figure 6.27a) shows an arbitrary chemical structure of GO with aromatic regions and regions decorated with different oxygen containing functional groups, e.g., epoxide and hydroxy groups in the basal plane, and carboxy groups predominantly present on the edges, inspired by the Lerf-Klinowski model proposed for the chemical structure of graphite oxide.[104] Upon UV excitation, an electron-hole pair is generated in the TNCs. The generated electron then is available for reduction of the adjacent GO, leading to the partial restoration of the aromatic system. In similar experiments reported in the literature, the photocatalytic reduction of GO and GO/TiO_2 thin films is carried out in the presence of ethanol as hole scavenger, leading to the accumulation of the photo-generated electrons on the titania surface for GO reduction.[206] Since the photocatalytic reduction experiments done in this work took place in ambient conditions, we assume that the amine ligands (OLAM) are oxidized[207] and degraded in the process, as has been previously reported for other OLAM-stabilized nanocomposites used in photocatalysis.[208] Furthermore, reactive oxygen species, such as hydroxy- and superoxide radicals, are likely to form upon excitation in ambient conditions in the presence of water and oxygen, and to partake in the reductive and oxidative processes.[133,209] However, investigations of the catalytically active species and the reaction mechanism of the GO reduction were not addressed within the scope of this project.

The evolution of the electrical, optical, and structural properties of the hybrid films with variation of the UV exposure time, TNC shape and film thickness/compositions was investigated. First, GO/TNR- and GO/TNP films deposited on Si/SiO_2 wafers equipped with two IDEs, fabricated using one SC deposition cycle, i.e., one sandwiched layer of the TNCs, were exposed to UV radiation for up to 7 h. *IV* measurements were recorded in certain time intervals (0.25, 0.5, 1, 2, 3, 4, 5, 6, 7 h) in a nitrogen atmosphere. Voltages were swept between ±1 V and the resulting current was measured using a Keithley 2601A sourcemeter. Before each measurement, the test cell containing the hybrid films was purged with nitrogen for approximately 1 min to remove adsorbed water molecules and to obtain a stable baseline resistance. In a nitrogen atmosphere, all films exhibited Ohmic behavior. The film conductance G was extracted as the slope from the respective *IV*-curves. Figure 6.27b) shows the evolution of the conductance for GO/rGO/TNP (blue) and GO/rGO/TNR films (orange) with increasing UV exposure time. For both types of films, a drastic increase in conductance can be observed with the onset of UV exposure, indicating the formation of rGO and the restoration of conductive sp^2 hybridized areas.

In both cases, a maximum in conductance can be observed, followed by a steady decrease with increasing UV illumination time. The observed decreasing conductance could indicate a re-oxidation or photocatalytic degradation of the carbon network itself with prolonged UV exposure, as was reported in the literature for the reduction of GO sheets attached to titania nanoparticles in ethanol.[210] Radich et al. reported that illumination of aqueous suspensions of GO and titania nanoparticles with UV light (Xe lamp, 250 mW/cm^2) first leads to the formation of rGO, which is then further degraded to smaller fragments and ultimately, to CO_2.[211] For the films shown in figure 6.27b), the maximal conductance was reached after 2 h for the GO/rGO/TNP films, and after

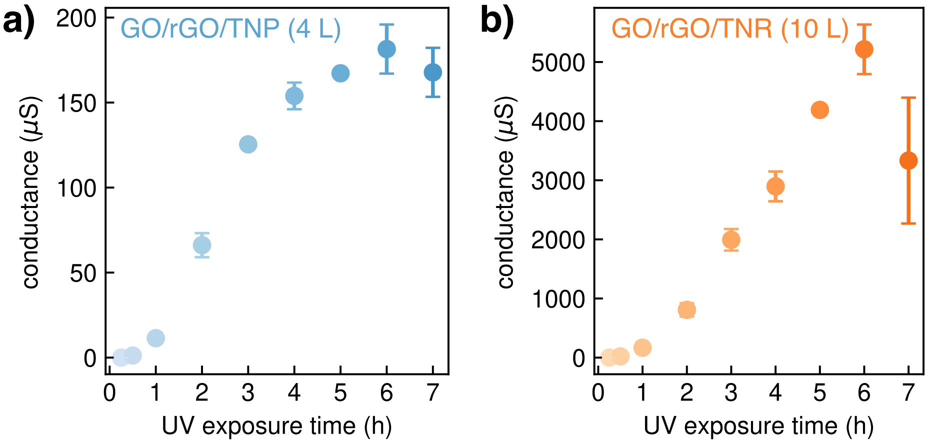

Figure 6.28: Evolution of conductance during continuous UV exposure for a) GO/rGO/TNP- and b) GO/rGO/TNR films fabricated using a) 4 SC deposition cycles (4 L), and b) 10 SC deposition cycles (10 L) on silicon wafers. The error bars correspond to the deviation of two films measured on one substrate equipped with two IDE structures. The conductance was extracted as the slope from the respective *IV*-curves.

3 h for the GO/rGO/TNR films. Notably, the conductance of the GO/rGO/TNR films was up to 8 times higher than that of the GO/rGO/TNP films. Additionally, the onset of decreasing conductance is delayed compared to the GO/rGO/TNP films. Plots of the conductance G vs. the UV exposure time corresponding to multilayered (4 and 10 SC deposition cycles) GO/rGO/TNP- and GO/rGO/TNR films are shown in figure 6.28). For these films, the resulting conductance is overall higher and it saturates for a longer period of time compared to the thinner films, but also appears to slowly decrease after several hours of UV exposure. However, the onset of GO degradation is clearly delayed in comparison to the thinner films. The overall higher conductance can be explained by the higher film thickness. Additionally, due to more layers within the film, the reduction process might take longer to be completed. In summary, these results demonstrate that the electric conductivity of GO/TNC thin films can be enhanced and tuned over several orders of magnitude by UV illumination.

The differences between the TNR- and TNP-based films might arise due to the different nature of the incorporated TNCs: For instance, the TNPs have larger lateral dimensions than the TNRs, possibly leading to an advantage of the TNRs in their photocatalytic efficiency due to their higher surface-to-volume ratio providing more interfacial contact sites for the formation of rGO to occur evenly throughout the extended film.[212] The distinct shapes and sizes might also cause differences within the layered structure and interactions between GO and the TNCs. Furthermore, the amount of OLAM ligands is higher on the TNRs' surface, as determined via TGA (cf. the Appendix, section A.1.9). As stated in the previous paragraph, we assume that the driving force of the reduction might be the oxidative degradation of the OLAM molecules on the TNC surface. Consequently, the lower amount of OLAM for the GO/rGO/TNP films might be a limiting factor for the formation of rGO, resulting in a premature re-oxidation/degradation of GO after the consumption of OLAM is completed. Experiments with varying TNC concentration were conducted (cf. the Appendix, section A.1.11), which revealed a) increased rates of reduction and b) higher overall conductances for higher TNC content. This might be due to the overall higher amount of sacrificial OLAM ligands within the films, allowing for an extended rGO formation instead of premature GO degradation. Further, as described in section 6.2.1, the TNCs also differ in their crystal structures and exposed facets with different photocatalytic activity. However, while the anatase phase and its exposed {101} and {001} facets are often described as exhibiting the highest photocatalytic activity in the literature,[139,213] there are studies reporting that brookite TNCs show superior photocatalytic activity for certain applications,[140,209] leaving this aspect regarding the GO reduction inconclusive.

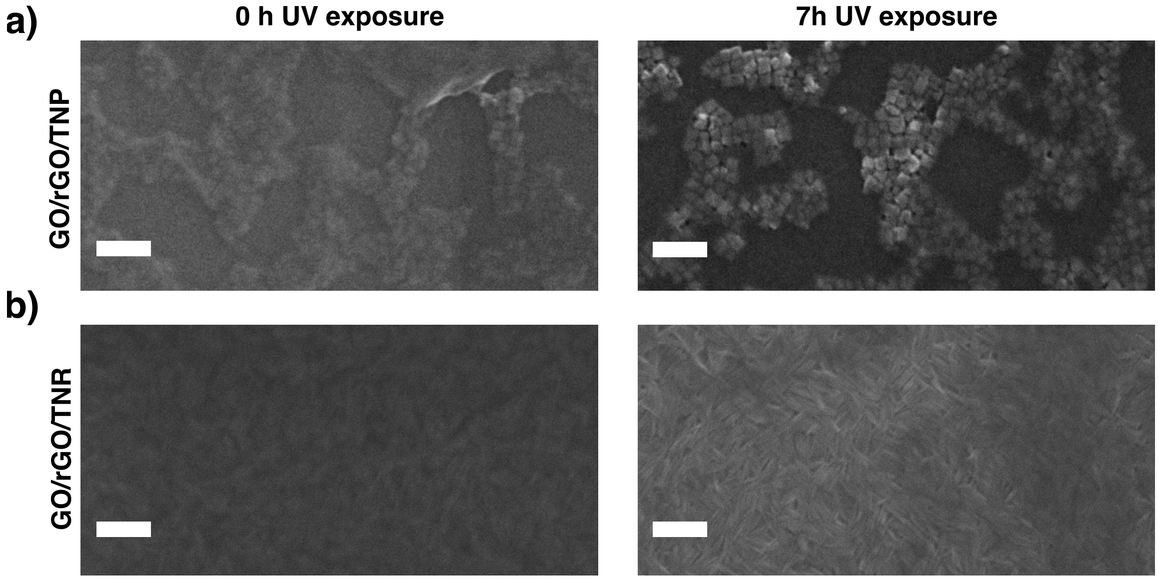

Figure 6.29: SEM images of a) GO/TNP thin films (1 SC deposition cycle) before (left) and after (right) 7 h UV exposure. b) GO/TNR thin films (1 SC deposition cycle) before (left) and after (right) 7 h UV exposure. Scale bars: 100 nm.

SEM analysis of analogous thin films deposited on Si substrates, before (0 h) and after prolonged UV exposure (7 h) are shown in figure 6.29a-b) for GO/rGO/TNP and GO/rGO/TNR films, respectively. Different TNC distribution on the substrate can be observed for TNP- and TNR-based films, which might also lead to the observed differences in the evolution of conductance. The images clearly demonstrate the evolution of film composition and GO/TNC ratio with increasing UV exposure times. After 7 h of UV exposure, large areas of TNRs and TNPs become more visible and are only partially covered by GO/rGO sheets (dark areas), supporting the assumption that the carbon network degrades over time.

To further monitor the progressing reduction and to analyze the structural and chemical changes within the GO/rGO/TNC films, UV-vis absorbance spectroscopy, ATR-FTIR spectroscopy and x-ray photoelectron spectroscopy (XPS) measurements were conducted. Figure 6.30a) shows stacked FTIR spectra of drop-casted GO/TNP- (blue) and GO/TNR- (orange) films on silicon wafers before (0 h) and after UV illumination for selected times, as well as the spectra of the respective pure TNCs drop-casted onto a substrate, and of OLAM (gray). Due to the low resolution of ATR-FTIR spectroscopy for thin films, the samples were prepared via drop-casting. The measurements were done to qualitatively analyze changes of functional groups in GO/TNC hybrid films and the reduction times cannot be compared to those prepared via LbL SC, since the drop-casted films were thicker and less homogeneous. The recorded spectra of the initial GO/TNC films all show the GO-specific bands (cf. figure 6.23e), as well as pronounced bands around 2900 cm^{-1} corresponding to

CH_2 stretch vibrations arising from OLAM ligands, confirming the presence of OLAM-stabilized TNCs in the deposited material. The GO/TNR films also show a pronounced band below 800 cm^{-1} that corresponds to Ti-O-Ti vibrations.[214] This band is neither present in the spectrum of pure TNPs, nor in the spectrum of the GO/TNP composite. With increasing UV exposure time, a relative decrease of the CH_2 band can be observed, confirming the degradation of OLAM during illumination. Control experiments in which pure OLAM-stabilized TNCs films were treated with UV light were performed, and FTIR spectra show the complete disappearance of the OLAM-CH_2 band in less than 5 min (cf. the Appendix, section A.1.12). Further, the band around 1625 cm^{-1}, that can be assigned to C=C vibrations, shifts to lower energies, as expected from aromatic systems, confirming the restoration of the graphene-like structure. Both, the band around 1050 cm^{-1} which can be assigned to C-O-C stretching modes of epoxide groups, and the broad signal between 3000–3500 cm^{-1}, arising from O-H bonds and water, decrease with increasing UV exposure times, suggesting the partial removal of hydroxy- and epoxide group, while the signal corresponding to C=O bonds (1720 cm^{-1}) seems unaffected in its relative amplitude. Figures 6.30b-c) show UV-vis absorbance spectra of GO/rGO/TNP (blue) and GO/rGO/TNR (orange) films (spin-coated on quartz substrate, 1 SC deposition cycle), respectively, after different UV exposure times. Again, the shaded area represents the

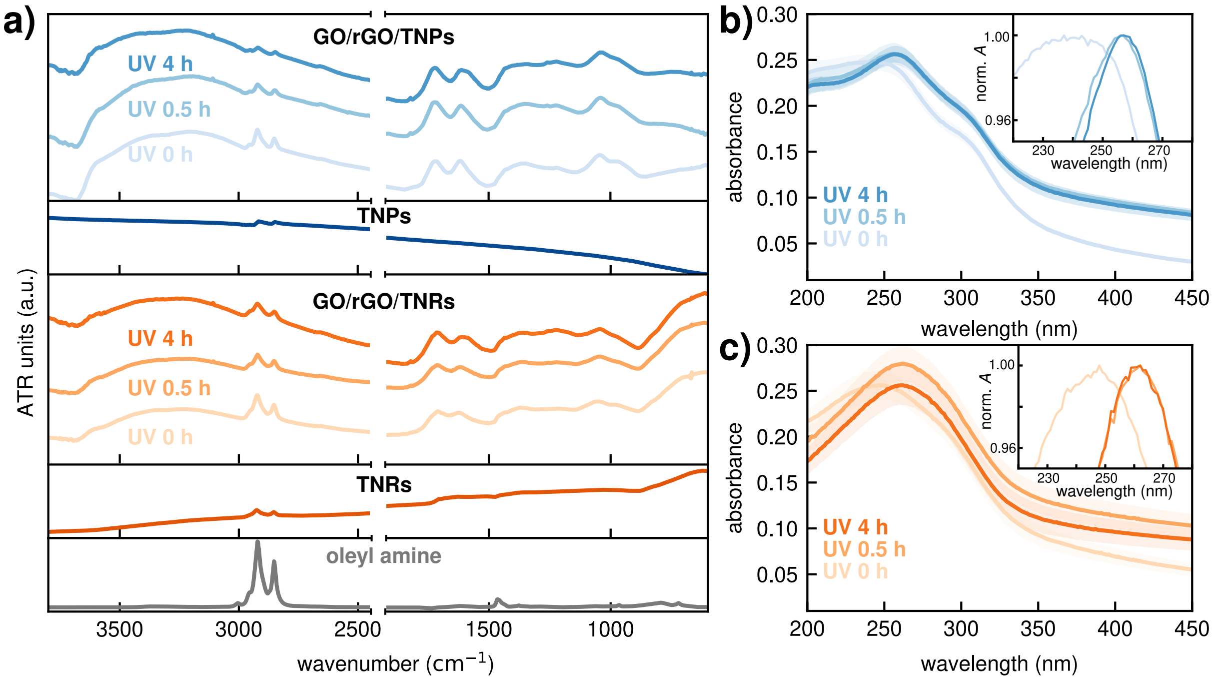

Figure 6.30: a) Stacked plots of normalized FTIR-ATR spectra of drop-casted GO/rGO/TNP (blue) and GO/rGO/TNR (orange) films with increasing UV exposure times (0 h, 0.5 h, 4 h), and reference spectra of the pure TNPs (dark blue) and TNRs (dark orange), as well as oleylamine (gray). b) Evolution of the UV-vis absorbance spectra of GO/rGO/TNP and c) GO/rGO/TNR thin films (one SC deposition cycle). The shaded areas represent the standard deviation of four measurements recorded at four different film spots. The insets show a magnified area of the absorbance, normalized to the maximum.

deviation from four measurements at different film positions. Here, a red-shift of the maximum of up to 25 nm can be observed, as well as generally an increased absorbance, which is in agreement with the formation of rGO.[113] With increasing exposure times, the features corresponding to the TNCs (best visible for the TNP-based samples) appear more pronounced, confirming the tunability of GO/TNC ratio within the films and the possible degradation of GO. Optically, a change in color from light-brown to dark-brown/black was observed with increasing exposure times. Reference experiments of pure GO films, deposited onto substrates via LbL SC, were performed and revealed UV-induced changes of the material. However, the formation of rGO, assessed by the increase in conductance, was drastically slower in the absence of the TNC photocatalyst. The control experiments are summarized in the Appendix, section A.1.12.

For an in-depth analysis of the chemical changes during UV illumination, XPS measurements were performed for thin films of GO/rGO/TNPs and GO/rGO/TNRs treated with UV light for 0, 0.5, and 4 h. These times correspond to the initial state of the hybrid films before reduction, a state during rGO formation, before reaching the conductance maximum, and a state of advanced UV exposure and possible GO/rGO degradation. Figures 6.31a-d) show XPS spectra for the C 1s, O 1s, Ti 2p and N 1s spectral region for both film types at different UV exposure times, respectively. The measurements were performed by Dr. Mona Kohantorabi and Dr. Heshmat Noei at DESY (Prof. A. Stierle group). Note, that the plots shown represent the raw measurement data that has not been calibrated and hence, slight shifts are visible comparing the GO/rGO/TNR- and GO/rGO/TNP spectra. In addition, the quantitative analysis could not be performed within the time frame of this thesis, however, the obtained data will be discussed qualitatively. Generally, the TNP- and TNR-based hybrid films show similar trends, regardless of the incorporated TNC

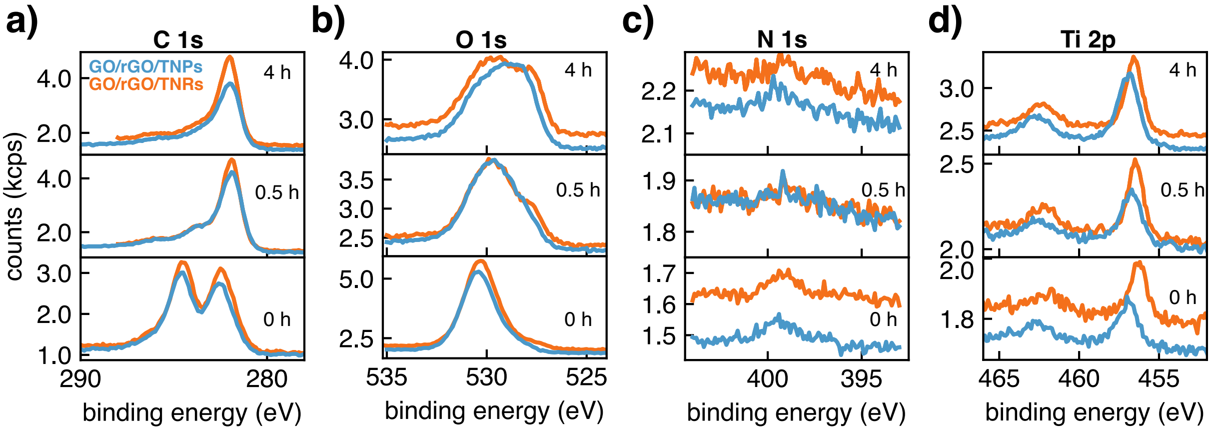

Figure 6.31: XPS spectra of the a) C 1s, b) O 1s, c) N 1s, and d) Ti 2p energy ranges of GO/rGO/TNC films treated with UV radiation for (top-to-down) 4 h, 0.5 h, and 0 h, made using (blue) TNPs and (orange) TNRs.

species. The C 1s spectra (figure 6.31a) clearly show the conversion from GO to rGO. For the initial films two peaks of similar intensity can be seen at ~284 eV and >286 eV, corresponding to C=C bonds and to oxidized carbon species, respectively.[112] With increasing UV exposure times, the peak corresponding to the oxidized carbon drastically decreases, and the main peak at lower energies, corresponding to C=C bonds, remains. Similarly, the O 1s spectra show an evolution of the predominant species with increasing UV exposure times. For the initial films, the main peak is visible around 530 eV, that can be assigned to the organic C-O and C=O bonds of GO. With increasing UV exposure time, a second peak appears at lower energies, that can be assigned to the metal oxide bond.[203] Since with prolonged UV illumination, the rGO layer becomes thinner, and starts to decompose, the film character shifts from organic to inorganic, so that the metal oxide peak becomes more visible, as the TNC surfaces are more exposed than in the initial film. Because of the low information depth of XPS, due to the short mean free path length of photoelectrons, this signal is not well visible for the initial films, in which multilayered GO covered the TNCs. This observation is confirmed considering the Ti 2p spectra: All spectra show the characteristic Ti $2p_{3/2}$ and $2p_{1/2}$ peaks at 458 eV and 464 eV, which exhibit less noise with increasing UV exposure time, i.e., are better resolved due to the higher exposure of TNCs within the films. Finally, N 1s spectra were measured to assess the fate of the OLAM ligands. For the initial films, a low intensity peak can be discerned at ~400 eV, that can be assigned to the amine ligand,[203] while the signal intensity decreases with increasing illumination time, which is in agreement with the measured ATR-FTIR spectra of drop-casted hybrid films.

In conclusion, TNC-assisted GO reduction allows for controlled and tunable composite films with well-adjusted optical and electrical properties. It is possible to adjust the ratio of TNC to carbon by variations of the UV exposure times, and possibly the concentration of the respective nanomaterials. To further elucidate the photocatalytic reduction process in these films, the experiments could be carried out under inert gas atmosphere, or in the presence of reducing vapors, such as ethanol.

6.2.4 Photocatalytically Patterned Resistive Sensors

The implementation of graphene-based materials in functional electronic devices demands for strategies to precisely control their spatial position. A promising approach to pattern graphene/GO is the use of photocatalytic lithography which circumvents the use of photoresists and solvents as potential contaminants.[150] A few studies have reported strategies for the photocatalytic patterning of graphene and GO, by utilizing, e.g., TiO_2 nanoparticles,[149] TiO_2 photomasks,[151] or ZnO nanoparticles[215] as photoactive agents for either oxidation (graphene) or reduction (GO) processes.[150] The method established in this work for remote GO reduction within hybrid thin films, mediated by the photocatalytic activity of incorporated TNCs upon UV exposure, was implemented for photocatalytic lithography for the fabrication of tailored, patterned films. The tunability of the materials' composition (tunable number of polar functional groups) gave rise to the investigation and optimization of chemiresistor arrays with regard to their selectivity and sensitivity towards r.h. and VOCs in dependence of the GO/rGO ratio and the nature of incorporated TNCs. For this purpose, hybrid films, fabricated by the procedure described in detail in section 6.2.2, were exposed to UV light through quartz photomasks.

Photocatalytic Lithography

Figures 6.32a,b) show microscopy images of different magnifications of a GO/rGO/TNR thin film after UV exposure (1 h) through a photomask with miscellaneous structures for 1 h. Since the custom-built UV light source might limit the resolution of the obtained patterns, these films were illuminated using a UV lamp (Osram HBO 200 W/DC, Hg lamp, multiline spectrum) from a mask aligner (Karl Suss MJB-3).

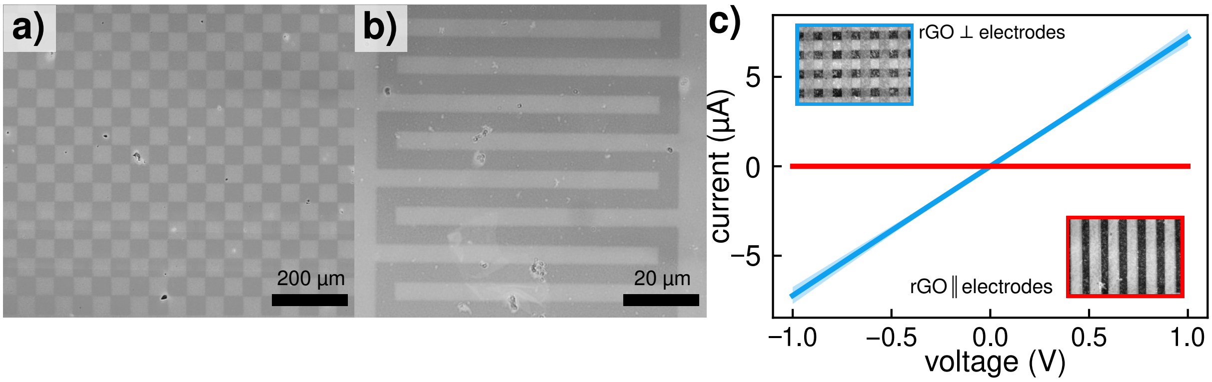

Figure 6.32: a-b) Optical micrographs of GO/rGO/TNR hybrid films deposited on SiO_2/Si wafers after UV illumination for 1 h through a photomask (scale bars: 200 µm and 20 µm). c) *IV*-curves of GO/TNR films after UV illumination for 1 h through a photomask either perpendicular (⊥) to the IDEs, connecting the IDEs with the resulting rGO (blue), or parallel (∥) to the IDEs (red). The shaded area represents the standard deviation from two sensors each.

The checkerboard and meander structures are clearly visible, indicating the selective reduction of GO at the exposed areas. To verify the selective reduction, and that the material's properties are reflected in the formed patterns, two IDE structure-supported thin films were illuminated through a photomask with stripes (20 µm) aligned perpendicular to the IDEs and parallel to the IDEs, respectively. Figure 6.32c) shows the resulting *IV*-curves, clearly demonstrating that UV exposure perpendicular to the IDEs leads to a significant increase in conductivity, indicating the formation of rGO connecting the IDE fingers, as shown in the inset microscopy image in the top left (blue). For UV exposure parallel to the IDEs, no significant increase in conductivity was observed, confirming the selective reduction of GO only on the exposed areas. However, experiments regarding the resolution limit of this method, as well as long-term illumination, should be conducted in the future, since it is conceivable that with prolonged UV exposure, reactive species might migrate and diffuse through the GO network, resulting in a loss of resolution, as reported by Zhang et al. in 2011 for photocatalytically patterned graphene using different types of TiO_2 photomasks.[151] Further experiments to investigate the transition from GO to rGO at a pattern interface with regard to the electronic properties could be performed using Kelvin-probe force microscopy.

Humidity Sensors

The r.h. sensing properties of photocatalytically patterned, multilayered GO/TNC hybrid films were investigated. With special regard to the use of GO-based r.h. sensors in personal health applications, e.g., in respiration[164] or epidermal humidity monitoring,[9] transducers on flexible substrates to be implemented in wearable devices are highly desirable. Hence, hybrid GO films containing TNPs or TNRs were fabricated according to the procedure shown in figure 6.25 on flexible PI foil. Since the multilayered films enabled the adjustment of overall higher conductivities and further provided a longer GO/rGO functionalization window (cf. figure 6.28), thin films with an estimated film thicknesses of ~50 nm were prepared. Figure 6.33a) schematically depicts the fabrication of GO/rGO/TNC humidity sensors with variable degrees of reduction on flexible PI substrates via photocatalytic patterning. First (i), GO/TNC films were deposited onto plasma-treated PI substrates equipped with two IDE structures (50 nm Au), and were then (ii) exposed to UV light through a quartz mask, exposing one IDE area for a certain time, depending on the desired degree of reduction and electrical conductivity. The mask was rotated by 180°, and the second IDE area was exposed to UV light, yielding a sensor array with two films of varying GO/rGO ratios. Table 6.4 summarizes the sensors' compositions and the applied UV exposure times for reduction. Depending on the incorporated TNCs, the UV exposure times were varied to obtain comparable conductivities as a measure of

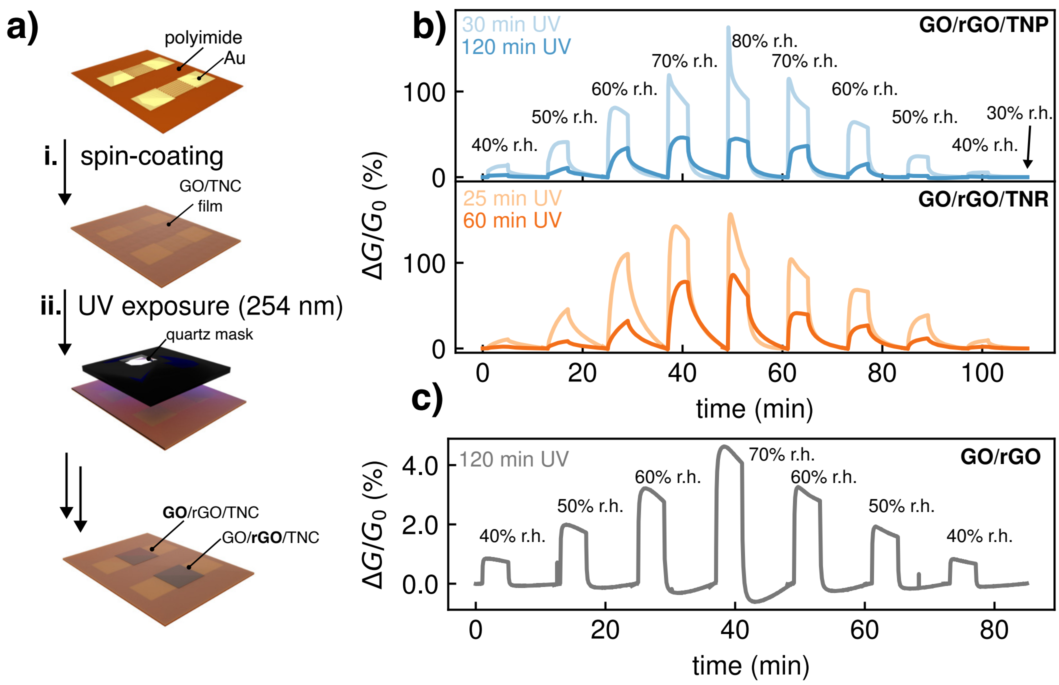

Figure 6.33: a) Fabrication process of photocatalytically patterned GO/rGO/TNC sensors on flexible PI substrates equipped with IDE structures. (i) GO/TNC film deposition via LbL SC on PI substrates. (ii) UV exposure through a custom-patterned quartz mask for selective GO reduction, yielding hybrid films of varying GO/rGO ratios depending on the UV exposure times. b) Baseline-corrected relative conductance change of GO/rGO/TNP- (blue) and GO/rGO/TNR (orange) films of adjusted degrees of reduction to transient (4 min) variations in r.h. (40-80 %, baseline: 30 % r.h.) c) Baseline-corrected relative conductance change to variations in r.h. (40-70 %, baseline: 30 % r.h.) of a GO/rGO reference film. All measurements were conducted at room temperature.

degree of reduction. A film of pristine GO, fabricated using the same amount of GO as in 4 SC deposition cycles for GO/TNC composite films (10×25 µL), was illuminated for 2 h with UV light for rGO formation and investigated as a reference.

Table 6.4: Hybrid films fabricated for resistive r.h. sensing experiments.

sensor name	composition	UV exposure (min)
TNP-30	GO/rGO/TNP	30
TNP-120	GO/rGO/TNP	120
TNR-25	GO/rGO/TNR	25
TNR-60	GO/rGO/TNR	60
GO-120	GO/rGO	120

To probe the sensors' resistive sensing properties, the films were placed into a custom-built test cell, connected to a gas calibration system (CGM 2000, MCZ Umwelttechnik) equipped with a zero gas system (NGA 600-25 MD, MCZ Umwelttechnik) to provide purified air (quality 5.0) and two humidification units to provide humidified ZG and humidified AG. A constant voltage (1 V) and the resulting currents were measured using a

Keithley 2601A sourcemeter or an Agilent 4156C parameter analyzer. Purified air with a baseline humidity of 30 % r.h. (at room temperature) was used as ZG to mimic ambient conditions. The sensors were then exposed to transients of increasing r.h. (40-50-60-70-80 %, and back) for 4 minutes each, followed by 8 minutes of ZG exposure. The control measurement with the GO/rGO film was conducted for the r.h. range of 40-70 %. A commercial gas sensor (BME680 Bosch Sensortec) was read out in parallel to determine the r.h. levels during the measurement. The corresponding timetrace can be found in the Appendix, section A.1.13. For all films, the relative conductance change $\frac{\Delta G}{G_0}$ was extracted as sensor signal from the recorded $I\ (t)$ traces, with $G = I/V$, according to equation 14,

$$\frac{\Delta G}{G_0} = \left[\frac{G(t)}{G_{\text{base}}(t)} - 1\right] \times 100\ \% \tag{14}$$

where G_{base} is the baseline conductance that was determined by applying linear fits to each transient, taking a ~30 s interval ~5 s before r.h. exposure onset, and a ~30 s interval after ~7.4 min of ZG exposure, into account as linear fitting range. Figures 6.33b-c) display baseline-corrected sensor response signals for the three types of sensors. All sensors show an increase in conductance upon humidity exposure. An increase in conductance is known from the literature for graphene[216] and GO[161] at high r.h., and is explained by sorption of water molecules on the hydrophilic functional groups, forming chains of ionic conductivity.[162] In the case of GO, it is assumed that the epoxide and hydroxy groups provide proton hopping sites for a percolation path according to the Grotthus mechanism:[217] $H_2O + H_3O^+ \rightarrow H_3O^+ + H_2O$.[161,165,218] A more detailed description of the sensing mechanism can be found in the next paragraph.

Figure 6.34 summarizes and compares the sensing characteristics of the investigated films. Figure parts 6.34a-c) show the maximum relative conductance change for each r.h. transient for the GO/rGO/TNP, GO/rGO/TNR, and GO/rGO composites, respectively. Since all films exhibit fairly linear behavior in the analyzed r.h. range, linear functions were fitted to the data. The sensitivities were determined as the respective slopes and are summarized in figure part d). While the GO/rGO reference sensor (figure 6.34c) exhibits low hysteresis and good linearity in the analyzed r.h. range, the sensitivity was boosted by a factor of up to 20 for the GO/rGO/TNC hybrid films, emphasizing synergistic effects in the hybrid material. Here, the films with lower degree of reduction have the highest sensitivities, which is related to the higher number of polar functional groups present, providing sorption sites for water molecules.[157,167] Furthermore, the TNCs might provide additional sorption sites for water molecules, and the intercalation of TNCs between GO sheets might result in a structure with a larger surface area and improved sorption site accessibility, compared to pristine multilayered GO films.[157] The highest sensitivity

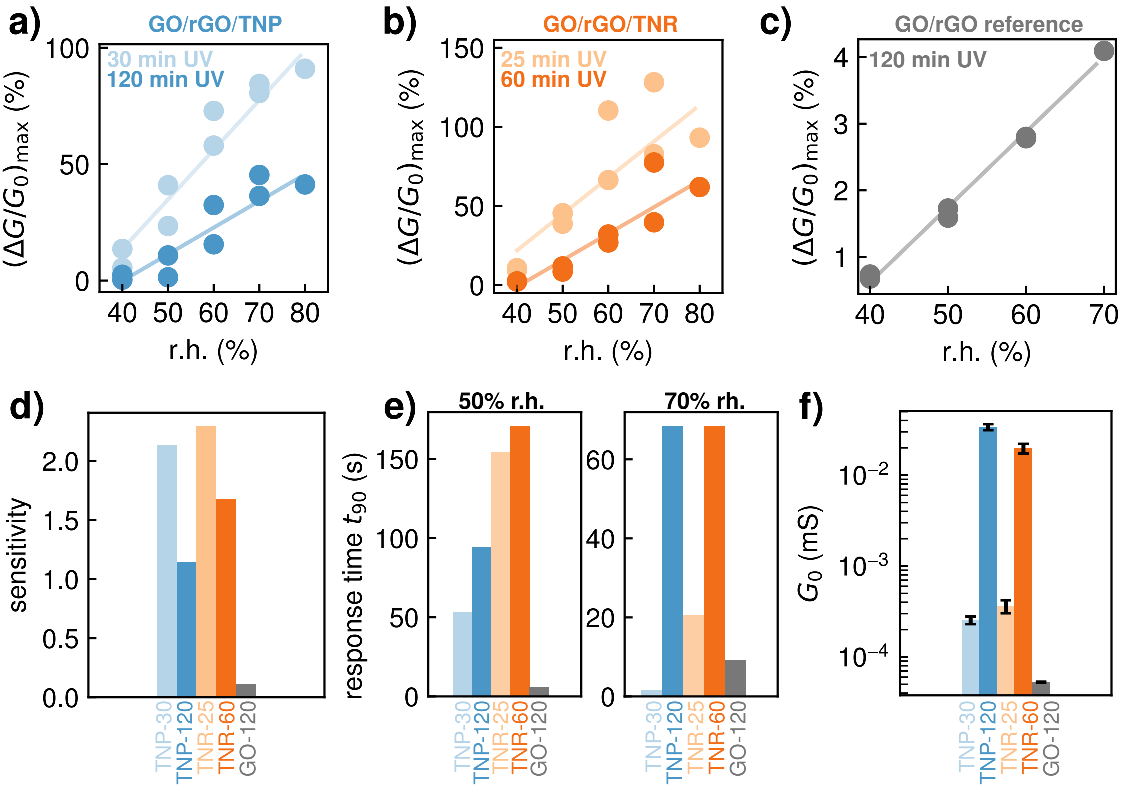

Figure 6.34: Sensor characteristics for GO/rGO/TNC sensors for high r.h. measurements. a-c) R.h. response isotherms for GO/rGO/TNP, GO/rGO/TNR, and GO/rGO films, respectively. The lines represent linear functions fitted to the data to extract the sensitivities shown in d). e) Response times for the 5 sensors for 50 % and 70 % r.h. transients. f) Baseline conductances (30 % r.h.) for all sensors, averaged for the entire measurement, as indicated by the error bars.

was extracted for the TNR-based films, however, they also suffer from more pronounced hysteresis than the TNP-based films, as can also be seen in the timetraces in figure 6.33b). Additionally, exemplary response times t_{90}, corresponding to the time needed to reach $0.9\times\left(\frac{\Delta G}{G_0}\right)_{\max}$, were extracted for 50 % and 70 % r.h. transients, as depicted in figure 6.34e). The obtained response times depend on both, the degree of reduction and the incorporated TNCs: For both types of hybrid films, the response times increase with increasing degree of reduction (TNR-60 and TNP-120), while overall higher response times can be observed for the TNR-based films. The GO-120 sensor shows relatively fast response (and recovery) times, as can be seen in the timetraces, as well. At 70 % r.h., the TNP-30 sensor shows the fastest response of all sensors, with t_{90} = 1.5 s, averaged for both 70 % r.h. transients. However, it is to note that the transient shapes, i.e., the extracted response times, for the GO/rGO/TNC films, especially for the TNR-based films, showed large variations for the same r.h. level, as can be seen in the timetraces. Finally, figure 6.33f) compares the baseline conductances for all five sensors, showing conductances in a similar range for the TNR-60 and TNP-120, as well as the TNR-25 and TNP-30 sensors. In the absence of a TNC catalyst, UV exposure of the spin-coated GO film results in a significantly slower rGO formation, as indicated by the low conductance obtained for the GO-120 reference film. Although the GO-120 film demonstrated fast and reproducible responses to r.h., probably due to its relatively high GO content, the hybrid films, especially GO/rGO/TNP films, surpassed pure GO films in terms of significantly enhanced sensitivity, faster response times at high r.h., and greater efficiency regarding time and use of GO material during sensor fabrication. While the sensitivity of GO films could possibly be improved by optimizing their thickness and GO content, the low conductance, resulting from the low degree of reduction, is not favorable for implementation as resistive sensors. In contrast, the TNC-mediated photocatalytic reduction allows for short UV exposure times to achieve reasonable film conductivities and adequate GO/rGO ratios, making it an efficient method for r.h. sensor fabrication.

Based on its high sensitivity and low response times, the performance of the GO/rGO/TNP (30 min UV) sensor was further explored in body-related humidity sensing experiments at ambient conditions. For this purpose, the PI-supported sensor was contacted using small crocodile clips and wires. A constant voltage of 1 V was provided by a Keithley 2601A sourcemeter, and the current was continuously recorded. From the measured current, the relative conductance change was computed as sensor signal, as described in equation 14. Measurements regarding respiration monitoring, as well as skin moisture-based proximity

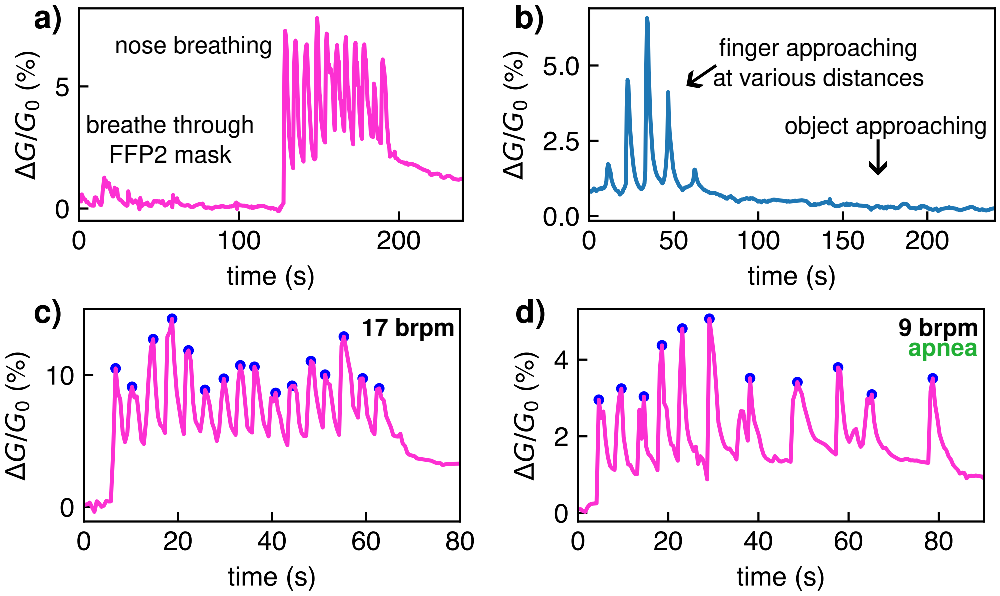

Figure 6.35: Real-time body-related humidity sensing using a GO/rGO/TNP chemiresistor (TNP-30). Relative conductance change of the sensor a) during breathing in proximity of the film through a FFP2 mask, and during nose breathing after removing the mask, as indicated; b) while approaching a human finger at varying distance to the film, and while approaching an inanimate plastic object, as indicated, c) during mouth breathing in proximity of the sensor to determine a healthy breathing rate, and d) during nose breathing with interruptions to detect apnea. The blue markers in c) and d) indicate found peaks that were used for breathing rate determination.

detection, were performed. Figure 6.35a) displays the relative conductance change of the sensor for the detection of human breath. According to a study from 2020, the humidity levels of exhaled human breath can vary between 42 – 91 % and has a temperature between 31.4 – 34.8 °C.[219] During the first ~60 s, the test person was breathing in close proximity (~5-10 cm) to the sensor wearing a filtering facepiece 2 (FFP2) mask. After ~100 s, the mask was removed and the test person continued breathing normally through the nose. This resulted in a pronounced increase in conductance with response amplitudes of up to 5 %. It is notable that the sensor does not immediately recover to its baseline current after breathing in proximity of the sensor was stopped, however, the response and recovery times are sufficiently fast to resolve the breathing rate, as is visible from the particular signal peaks. In addition, the breathing rate of mouth breathing was extracted, as shown in figure 6.35b). For mouth breathing, overall higher responses were measured. The rate of 17 breaths per minute (brpm) was determined using the `scipy.signal.find_peaks` function of the SciPy (version 1.10.1) python library, by finding the local maxima, as indicated by the blue points in the plot. Further, the sensor was used to monitor an interrupted breathing pattern, to assess its potential use for apnea detection, as shown in figure 6.35d). Here, obvious interruptions are visible in the sensor response, and a low breathing rate of 9 brpm was extracted. Finally, figure 6.35b) depicts the relative conductance change of the sensor upon finger approximation at varying distances during the first ~60 s, showing clear differences in amplitude for varying finger distances. From ~180 s, a finger-shaped plastic object was approximated to the film surface, showing no discernible sensor response.

Based on these preliminary experiments, the fabricated hybrid GO/rGO/TNP sensors show a promising performance for body-related humidity sensing applications in wearable sensors. Further investigations regarding the influence of, e.g., temperature, strain, or movements on the sensor performance should be addressed in the future.

Sensing Mechanism

To further study the r.h. sensing behavior of GO/rGO/TNP flexible sensors, the resistive responses of composite films of varying GO/rGO ratios (degrees of reduction) to a wider r.h. range (0.95–79 %), related to dry, purified air as ZG, were investigated. In addition, quartz crystal microbalances (QCMs) (f_0~10 MHz, AT-cut, Au electrodes) were coated on one side with analogous hybrid films via the LbL SC procedure, and treated with UV light for the same duration as the chemiresistors. These GO/rGO/TNP-coated QCMs were operated in parallel to the resistive measurements in order to determine the amount of sorbed water molecules in the hybrid materials, and to correlate the observed resistive responses with the relative mass uptake. The samples fabricated for these measurements are summarized in table 6.5. It is to note, that the obtained film thickness might vary for the different substrates and AFM measurements were not possible for PI-supported films, due to the roughness of the substrate. However, both sets of samples cover gradually increasing degrees of reduction and can be compared qualitatively. As described in the previous paragraph, purified air (0 % r.h.) was provided as ZG using a zero gas system (NGA 600-25 MD, MCZ Umwelttechnik). R.h. levels of up to 27 % were provided using a gas calibration system (CGM 2000, MCZ Umwelttechnik) with a vapor saturation unit, while higher r.h. levels (>40 %) were provided using a humidification module (MCZ Umwelttechnik). The sensors were transiently exposed to the desired r.h. for 4 min, followed by 8 min ZG exposure. The r.h. values of the sequence set by the gas calibration system were determined by placing a commercial BME680 sensor in a test cell connected in series to the measurement cell. The dosed humidity levels were ~ 0.95, 2.2, 4.0, 8.3, 16, 27, 42, 61, 79 %. The respective timetrace can be found in the Appendix, section A.1.13. The chemiresistors were operated at a constant bias of 1 V, and the resulting current was measured using a Keithley 2601A sourcemeter or an Agilent 4156C parameter analyzer, depending on the sensors' baseline resistance. The QCM resonant frequency was read out using an Agilent E5100A network analyzer.

Table 6.5: GO/rGO/TNP films fabricated for resistive and microgravimetric r.h. sensing experiments.

UV exposure times for QCM samples (min)	UV exposure times for chemiresistors (min)
5	20[a]
25	25
120	120
240	240

Figure 6.36a-c) shows baseline-corrected response transients to distinct r.h. levels for all four chemiresistors. At low r.h. (2 %, figure part a), the GO/rGO/TNP-20 film shows, as was seen in the r.h. measurements presented in the preceding paragraph, a positive maximum relative conductance change of ~10 %. The films with higher degrees of reduction (increasing from left to right), however, exhibit negative $\frac{\Delta G}{G_0}$ of down to -5 %. This behavior, i.e., an increase in resistance upon r.h. exposure, has been described in the literature for rGO-based sensors, and is caused by perturbations of the p-type conductivity of rGO in the presence of electron donors, such as water, leading to a decrease of charge carrier density.[156,168,170] With increasing r.h. levels (figure 6.36b), the sign of the observed negative sensor signals inverts, and the r.h. value at which this inversion can

---

[a] A chemiresistor measurement with a film exposed to UV light for 5 minutes was performed but could not be evaluated due to high noise arising from the film's high baseline resistance.

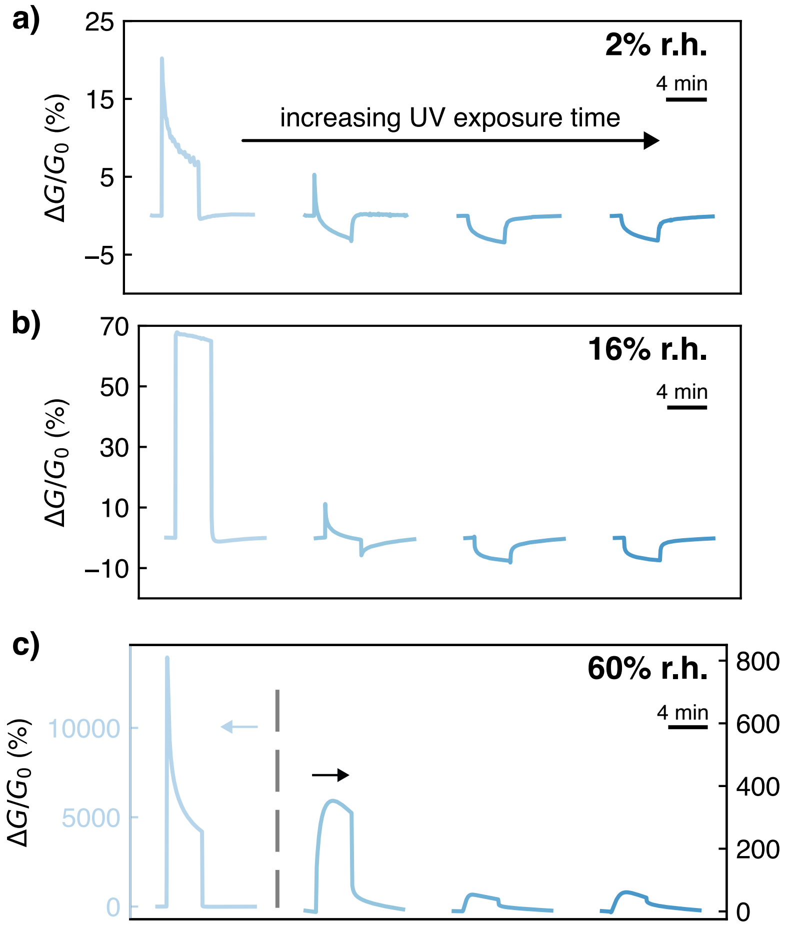

Figure 6.36: Selected baseline-corrected response transients of GO/rGO/TNP films of (from left to right) increasing rGO content adjusted via increasing UV exposure times to a) 2 %, b) 16 %, and c) 60 % r.h. changes at room temperature. Dry purified air was used as ZG.

be observed, depends on the degree of reduction of the films: While at 16 % r.h. the GO/rGO/TNP-25 film shows a positive relative conductance change of up to ~5 %, the GO/rGO/TNP-120 and -240 films still exhibit negative $\frac{\Delta G}{G_0}$ of approx. -7 %, each. At even higher r.h., all sensors exhibit positive sensor responses, as depicted in figure 6.36c) for 60 % r.h. Figure 6.37 shows the response isotherms of the four chemiresistors for a low r.h. range, up to ~30 %, clearly demonstrating inflection points of the sensor signal's sign at lower r.h., for shorter UV illumination times, e.g., higher GO/rGO ratios, with the GO/rGO/TNP-240 sensor exhibiting only negative responses in the considered range. Strikingly, the GO/rGO/TNP-120 and -240 films show very similar response amplitudes and transient shapes up to 16 % r.h., and also had comparable baseline resistances, with the -240 film even exhibiting a slightly higher baseline resistance, possibly indicating that the maximum conductance attainable via photocatalytic reduction was reached, and the onset of rGO degradation began (cf. section 6.2.2, figure 6.27).

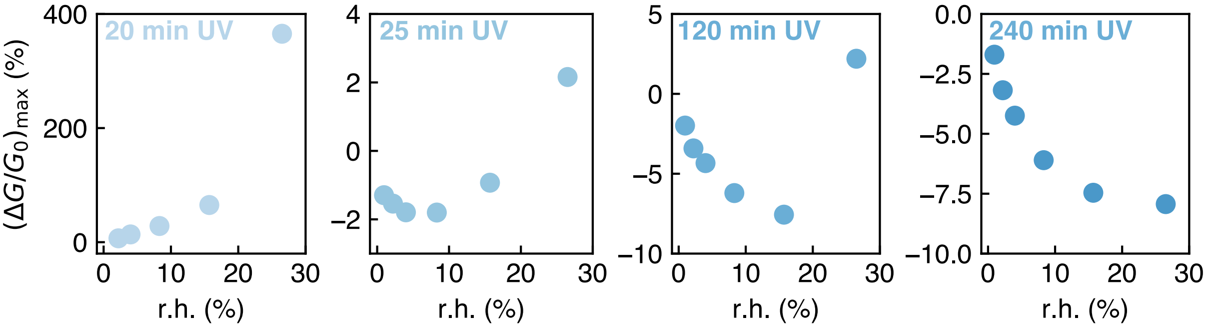

Figure 6.37: Response isotherms of GO/rGO/TNP chemiresistors of varying degrees of reduction to low Δr.h. up to 27 %.

The chemiresistor response isotherms for the entire measured r.h. range is shown in figure 6.38. With decreasing GO/rGO ratio, the sensor responses for large Δr.h., e.g., ~80 % r.h., are less reliable, which is primarily due to baseline shifts, probably due to sudden water condensation on the hybrid films at high r.h., indicating that, depending on the degree of reduction, the films demonstrate optimal r.h. sensing ranges. The respective timetraces can be found in the Appendix, section A.1.15. Using the TNP-induced photocatalytic GO reduction to tune the GO/rGO ratio of the hybrid films, the humidity sensing behavior and response isotherms of the hybrid films can be tuned for r.h. detection in different ranges for certain applications.

The GO/rGO/TNP-20 film with the highest GO/rGO ratio shows the overall highest sensitivity, where water sorption leads to an increased conductance over several orders of magnitude, resulting in very high relative responses, with respect to the very low baseline conductance in dry conditions. Additionally, its high baseline resistance makes its use less practical for a simple resistive readout, however, for applications where Δr.h. need to be monitored at overall higher baseline r.h., this type of GO-rich composite is very promising. Films with increasing rGO content have higher overall conductivities, and show

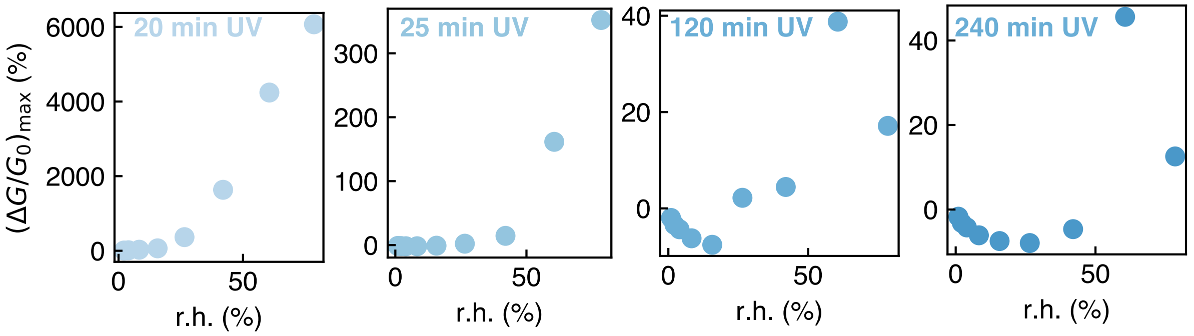

Figure 6.38: Response isotherms of GO/rGO/TNP chemiresistors of varying degrees of reduction to low Δr.h. up to 79 %.

concentration-dependent relative resistance changes in a low r.h. range, still exhibiting high affinities to water molecules. Based on combinations of two or more sensors with adjusted GO/rGO ratios, precise r.h. sensing could be accomplished over a wide range.

As stated earlier, microgravimetric measurements were performed in parallel to the resistive measurements to determine the amount of sorbed analyte for varying GO/rGO ratios within GO/rGO/TNP films, and to compare these results to the chemiresistive responses and sensitivities. Due to the different transduction mechanisms, QCM measurements enabled the analysis of hybrid films of very large GO/rGO ratios, i.e., of virtually electrically insulating materials that were not suited for resistive sensing. From the shift in frequency Δf_s of the film-coated QCM, the change of mass Δm due to analyte sorption can be calculated using the Sauerbrey equation.[220]

$$\Delta m = -\Delta f_s \frac{\sqrt{\mu \rho}}{2 f_{0,f}^2} A_{QCM} \tag{15}$$

In equation 15, μ and ρ are the shear modulus (29.47 GPa) and the density (2.65 g/cm^3) of quartz, $f_{0,f}$ the resonant frequency of the hybrid-film coated QCMs, and A_{QCM} the sensitive area of the QCM (0.2043×10^{-4} m^2). First, the mass of the respective hybrid film was determined from the observed frequency shifts with respect to the QCM resonant frequency f_0 after film deposition and photocatalytic reduction, which ranged between

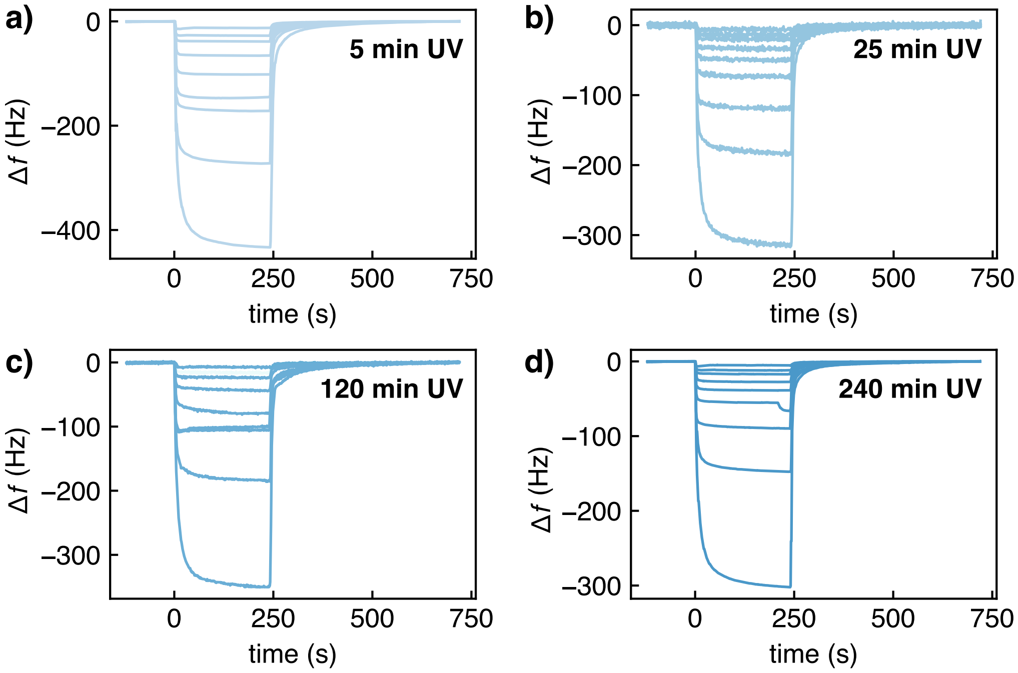

Figure 6.39: Resonance frequency shifts of GO/rGO/TNP-coated QCMs to Δr.h. between 0.95–79 %. The coated QCMs were exposed to UV light for different times ranging from 5–240 minutes to adjust the coatings' degrees of reduction.

-1.8– -2.5 kHz. The largest frequency shift and consequently, the highest mass, was estimated for the GO/rGO/TNP-5 film (~2.3 µg), while the films of lower GO/rGO ratio had masses of ~1.7 – 1.9 µg, with no clear trend regarding mass differences depending on their UV exposure times. The overall lower masses in comparison to the GO-rich film, could be due to the gradual decomposition of the organic ligands and removal of functional groups from GO with increasing UV exposure times. Here, in-situ UV illumination of hybrid film-coated QCMs would be interesting to monitor the change of mass of the films during the UV treatment.

Figure 6.39 shows the baseline corrected relative frequency shifts of the four samples during 4 min r.h. exposure (0.95 – 79 % r.h.). During r.h. exposure, a decrease of the resonance frequency down to -300 – -400 Hz is visible for all samples, independent of the degree of reduction. As the QCMs were only coated with the hybrid films from one side, it is to note, that water molecules are also sorbed to the bare QCM, however, reference measurements have demonstrated that the resulting frequency shifts are much lower (<2 %) compared to the obtained shifts shown here. Hence, the contribution of this effect to the obtained signals can be neglected. For all samples, sorption- and desorption of water molecules is fast and reversible, based on the response- and recovery times of the transients. The transients corresponding to 27 and 42 % r.h. for the GO/rGO/TNP-120 sample (figure 6.39c), are identical and seem to be cut-off, which was presumably caused by an artifact during the measurement. The transient corresponding to 27 % r.h. for the GO/rGO/TNP-240 sample (figure 6.39d) shows a sudden downshift during the end of the exposure time, which might be due to a sporadic condensation event within the tubing system or in the test cell. From these data, the mass of sorbed water was calculated using the Sauerbrey equation 15. The relative mass uptake $\Delta m/m$ of the films is displayed in figure 6.40 in dependence of increasing r.h. levels for all films. (The gray

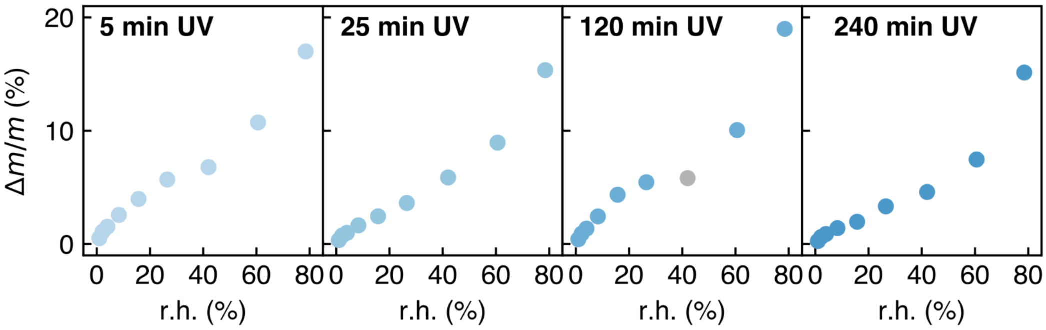

Figure 6.40: Sorption isotherms of four QCM samples coated with GO/rGO/TNP films with varying degree of reductions for r.h. levels ranging from 0.95 – 79 %. The gray data point in c) corresponds to the cut-off frequency shift shown in figure 6.39c).

data point for the GO/rGO/TNP-120 sample corresponds to the cut-off frequency shift shown in figure 6.39c.) The resulting sorption isotherms show no clear differences for films of varying GO/rGO ratios, and can be described as type II isotherms[221] that are obtained for non-porous or macroporous materials, and result from unrestricted monolayer-multilayer sorption of analyte up to high analyte concentrations (here: r.h.). These observed isotherms support the assumption, that secondary water sorption occurs at higher r.h. levels (>40 %), forming multilayered, physisorbed water films. A maximal relative mass uptake of 16-18 % can be seen for the films. Also, at lower r.h., in the monolayer-sorption region, similar relative mass uptakes can be seen for all samples, regardless of their adjusted GO/rGO ratio, demonstrating that all films still exhibit comparable affinities to water. These results indicate that the observed distinct chemiresistive responses of films with varying GO/rGO ratios are not caused by varying amounts of sorbed analyte, but are governed by the differing host-guest interactions that depend on the tuned chemical structure and composition of the hybrid materials, and the different charge transport properties of the films.

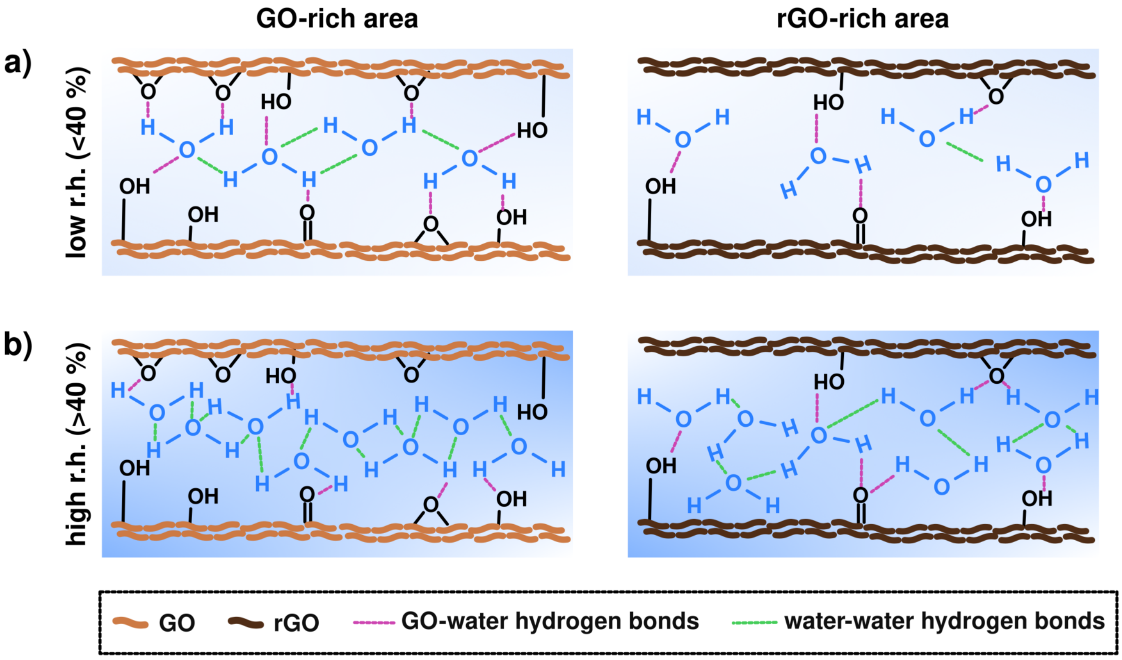

Figure 6.41: Humidity sensing mechanism proposed for sensors with adjusted GO/rGO ratios. a) At low r.h. levels (<40 %), GO-rich areas (left), provide a high density of polar functional groups as sorption sites for water molecules that can interact via hydrogen bonds, contributing proton hopping sites additionally to intermolecular water hydrogen bonds (green dashed lines), facilitating the formation of paths of ionic conductivity. In rGO-rich areas (right), sorbed water molecules cannot form ionic conductive chains, and act as electron donor, disrupting the hole-based rGO conductivity. b) At higher r.h. levels (>40 %), secondary water sorption leads to intermolecular hydrogen bonds and predominant ionic conductivity for both compositions.

Figure 6.41 shows a schematic of the proposed interactions between water molecules and (left) GO- and (right) rGO-rich areas of the hybrid materials at a) low and b) high r.h. levels, resulting in different signs of the chemiresistor sensor signals. GO-rich areas have a high density of polar functional groups, e.g., hydroxy and epoxide groups, providing water sorption sites and enabling analyte sorption via hydrogen bonds (pink dashed lines). Due to the even distribution of chemisorbed water molecules, these can form a percolation path of ionic conductivity according to the Grotthus mechanism, as described in the previous paragraph, where the present functional groups of GO can act as additional proton hopping sites. This results in an increased conductivity. RGO-rich areas, however, have a lower density of polar functional groups for chemisorption of water molecules. The increasing rGO content entails a significantly higher electrical conductivity due to the restored graphitic structure of rGO, that is described as p-doped in the literature. As a consequence of the decreased number of available sorption sites, water molecules might preferably interact with other water molecules present, so no continuous, extended water network can be formed for ionic conductivity. In this case, the sorbed water molecules, that act as free electron donors, interfere in the hole-governed conductivity of rGO, leading to an observed increase in resistance.[156] Additionally, even though some ionic conductivity might be present also at lower r.h. levels in these types of films, the resulting increase of conductance might be superimposed by the overall higher conductance of the films. At higher r.h. levels, with a threshold of approx. 40 % r.h., a secondary physisorbed layer of water molecules can be formed in both types of materials, and becomes the predominant interaction, leading to switching of the sign of the sensor signal, even in the more conductive, rGO-rich films.

Comparative measurements were performed using TNR-based GO/rGO films, as well as thinner GO/rGO/TNP films. These results are briefly provided in the Appendix, section A.1.14.

In summary, TNC-assisted photocatalytically reduced GO films show promising and tunable r.h. sensing properties, with adjustable linear detection ranges and sensitivities, depending on the UV illumination times. Future studies will involve further characterization of the sensing mechanism by impedance measurements to investigate and differentiate the occurring charge transport mechanism within the films (electronic vs. ionic conductivity).

Outlook: VOC Sensors

To evaluate and extend the potential resistive sensing applications of GO/rGO/TNC composites, the chemiresistive responses of GO/rGO/TNR hybrid films with photocatalytically adjusted GO/rGO ratios towards a set of VOCs and water were probed, to screen their selectivity in dependence of their degree of reduction. For this purpose, a GO/rGO/TNR

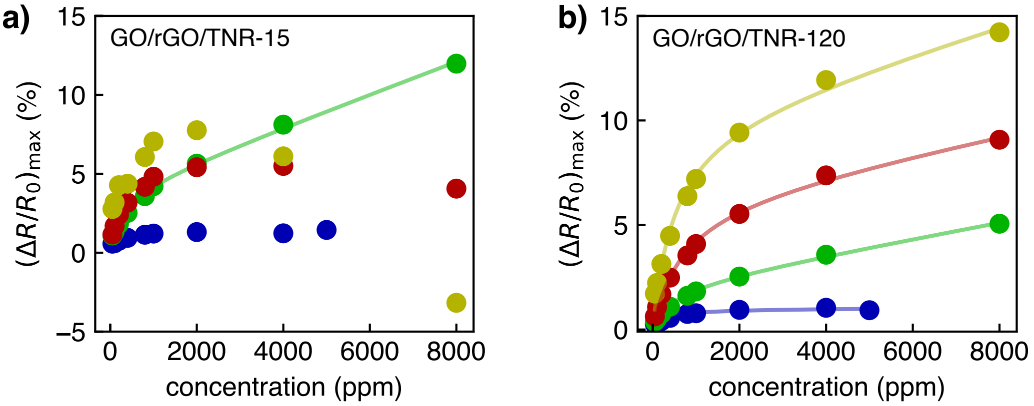

Figure 6.42: Response isotherms of the a) rGO/TNR-15 and b) rGO/TNR-120 sensors for MIBK (red), water (yellow), 1-propanol (green), and toluene (blue) exposures in a nitrogen atmosphere. The lines represent functions fitted to the isotherms according to a Langmuir-Henry sorption model (cf. equation 8).

film (estimated t_f ~ 40 nm) was deposited onto PI equipped with two IDEs via LbL SC, and different film sections were illuminated to UV light for 15 and 120 min, respectively. The films were exposed to varying concentrations (50–8000 ppm) of 1-propanol, MIBK, water, and (50–5000 ppm) toluene for 4 minutes, followed by 8 minutes ZG exposure. In these measurements, nitrogen (5.0) was used as carrier gas and as ZG. The sensors were operated at a constant voltage of 1 V and the current was continuously measured. The relative resistance change was computed as sensor signal, and $\left(\frac{\Delta R}{R_0}\right)_\mathrm{max}$ was extracted, as described in previous sections. The response isotherms for both chemiresistors for all analytes are summarized in figure 6.42. Figure 6.43a-d) show the baseline-corrected response transients of the GO/rGO/TNR-120 film for 1-propanol, MIBK, toluene, and water. The rGO/TNR-120 film shows positive relative resistance changes for all vapors in the analyzed concentration range, exhibiting the highest sensitivity to water, followed by MIBK, 1-propanol, and toluene. Here, all VOCs act as electron donors, disturbing the p-type conductivity of the rGO network, resulting in the observed increase of resistance. It was found that the response isotherms of the GO/rGO/TNR-120 sensor can be described well using a Langmuir-Henry model, according to equation 8.

As described in section 4.2.2, $\left(\frac{\Delta R}{R_0}\right)_\mathrm{sat}$ is the sensor's saturation response, K_L is the Langmuir binding constant, c is the analyte concentration, and K_H the Henry constant. This model describes the sorption isotherms well qualitatively. Studies to experimentally evaluate the proportionality of the sensor response amplitude to the amount of sorbed analytes for all VOCs will be addressed in the future with gravimetric QCM measurements. In general, both sensors are more selective for water and analytes with polar functional groups, as can be seen from the comparatively low responses to toluene. Up to concentrations of 2000 ppm, the GO/rGO/TNR-15 sensor shows the highest sensitivities for water vapor, and similar responses to MIBK and 1-propanol. In agreement with the results shown in

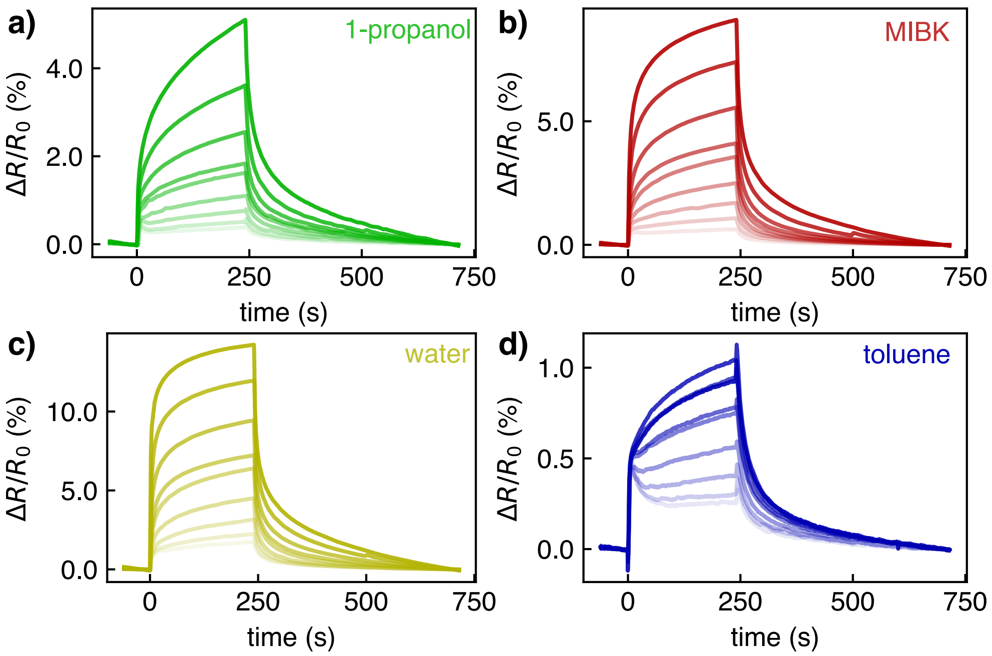

Figure 6.43: Response transients of a GO/rGO/TNR film (UV illumination time: 120 min) to a) 1-propanol, b) MIBK, c) water, and d) toluene vapor at varying concentrations, as indicated by the intensity of the color.

the preceding section about the r.h. sensing properties of GO/rGO/TNP sensors, an inversion of the sensor signal sign for higher water vapor concentrations (>4000 ppm) is observed for this sensor. The response towards MIBK seems to saturate for concentrations >2000 ppm. Significantly higher responses towards 1-propanol were obtained for the GO/rGO/TNR-15 sensor. Presumably, the selectivity of the sensors is based on the ability of the target analytes to interact via hydrogen bonding with the functionalized GO areas, and on their electron-donating properties.[222] Here, 1-propanol and water can act both, as electron pair donor and acceptor for hydrogen bonding, while MIBK is only an acceptor, and toluene cannot interact via hydrogen bonds. Here, $\pi-\pi$-interactions could occur with the graphitic structure of rGO.[223] For the GO/rGO/TNR-15 sensor, it was only possible to fit a Langmuir-Henry function to the response isotherm for 1-propanol. On the one hand, the adjustment of the response isotherms with the degree of reduction might be of advantage for the combination of two or more sensors for analyte recognition and concentration determination, on the other hand, e.g., the higher conductivity and more stable sensing signals, make the rGO-rich sensors investigated in this work more attractive for VOC sensing. The respective stacked response transients for the less reduced GO/rGO/TNR-15 film, which showed a significantly higher level of noise due to its higher baseline resistance, are provided in the Appendix, section A.1.16. Reversible responses were observed for all four analytes with fast response and recovery times for water and MIBK vapor, while the response and recovery to 1-propanol vapor are slower.

To explore the VOC sensing and recognition abilities of photocatalytically reduced GO/TNC hybrid films, more analytes should be probed in the future. In addition, GO/rGO/TNC films of even higher rGO content could be analyzed to evaluate whether selectivity shifts towards more non-polar solvents occur with increasing degree of reduction. Additionally, VOC sensor arrays combining GO/rGO/TNC films, and the GNP-based chemiresistors described in section 6.1 are highly promising, since implementation of GO/rGO/TNC resistive sensors would impart cross-sensitivity to polar solvents and could reliably detect r.h. variations during VOC exposure. Current studies in our group also address the VOC sensing properties of purely TNC-based films towards reducing and oxidizing gases and vapors.

7 Experimental Section

All experimental procedures – syntheses and characterization of nanomaterials, thin film fabrication and characterization, as well as analysis and measurement procedures – will be described in detail in the following sections.

7.1 Synthesis of Gold Nanoparticles

Dodecylamine (12A)-stabilized gold nanoparticles (GNPs) of varying sizes were synthesized by two different methods. GNPs with an average diameter between 3–4 nm were synthesized following a procedure reported by Leff et al.,[38] while larger particles with a diameter around 9 nm were obtained following a procedure reported by Peng et al.[39]

Chemicals and Apparatus. (*Chemicals*) 1-Dodecylamine (12A, 98 %), tert-butylamine borane (TBAB, 97 %), gold(III)-chloride trihydrate, tetraoctylammonium bromide (TOAB), sodium borohydride (SBH, 98 %), and oleylamine (OLAM, 98 %) were purchased from Merck. 2-Propanol (99.7 %), ethanol (≥99.9 %), hexane (≥99 %), and toluene (99.5 %) were purchased from VWR Chemicals. Heptane (99 %) was purchased from Grüssing GmbH. Deionized (DI) water (resistivity 18.2 MΩcm) was purified using an ELGA LabWater purification system. (*Apparatus*) Centrifuge (Sigma 3-18K, Sigma 1-15K).

Leff method. In a typical synthesis, 225 mg (0.570 mmol) gold(III)-chloride trihydrate were dissolved in 20 mL DI water. 645 mg (1.18 mmol) TOAB were dissolved in 20 mL toluene, and this solution was added to the yellow aqueous gold salt solution under vigorous stirring for phase transfer of the precursor. After the phase transfer was completed (i.e., the complete discoloration of the aqueous phase), a solution of 1.18 g (6.37 mmol) 12A in 30 mL toluene was added. The mixture immediately turned beige and opaque. Next, a freshly prepared solution of 230 mg (6.08 mmol) SBH in 15 mL DI water was quickly added to the mixture, resulting in an instant color change to dark purple. After ~18 hours, the reaction was stopped. The aqueous phase was separated using a syringe and discarded. Next, ~80 mL ethanol were added and the mixture was vigorously shaken for precipitation of the GNPs. Subsequently, the suspension was stored at −18 °C for ~1 day. Most of the supernatant (~50 mL) was discarded, and the residual suspension was centrifuged for 10 min (4393 g, −6 °C). The supernatant was discarded, and the precipitated GNPs were dried in ambient conditions. Finally, the GNPs were dispersed in 4 mL heptane, and filtered using a syringe filter (PTFE, 200 μm), yielding a ruby red solution.

Peng method. The synthesis was carried out in a 3-neck-flask in ambient conditions. First, 22.6 g (122 mmol) 12A were added to 40 mL hexane at 40 °C. After 12A was completely dissolved, the mixture was cooled down to 32 °C, and 406 mg (1.03 mmol) gold(III)-chloride trihydrate were added to the solution under vigorous stirring (850 rpm). The mixture was kept stirring for ~30 min, until a bright orange suspension was formed. Then, 136 mg (1.56 mmol) of the reducing agent TBAB were added to a solution of 2.28 g (12.3 mmol) 12A in 4 mL hexane. After TBAB was completely dissolved, this solution was rapidly added to the reaction mixture. After 1 hour, the reaction was stopped. Next, 200 mL ethanol were added to the red mixture for precipitation of the GNPs. After vigorous shaking, the suspension was stored at 4 °C for 3 hours. The suspension was centrifuged for 5 min (4000 g, 0 °C), the supernatant was discarded, and the pellet was redispersed in 4 mL heptane. The GNPs were precipitated with 2-propanol (1/3, *v*/*v*) and centrifuged again for 10 min (8000 g, 0 °C). This washing step was repeated, and finally, the GNPs were dispersed in 4 mL heptane, and the dispersion was filtered using a syringe filter (PTFE, 200 µm).

Ligand Exchange and TEM Analysis. A ligand exchange was conducted for transmission electron microscopy (TEM) analysis since 12A-stabilized GNPs are prone to fuse under TEM conditions.[37] For this purpose, 25 µL OLAM were dissolved in 500 µL heptane, and 25 µL of the respective GNP stock solution were added. This mixture was incubated for 30 min on a shaking tray. Next, 1 mL ethanol was added for precipitation, and the suspension was centrifuged for 10 min (6000 g, room temperature). In case the supernatant was not completely discolored, the centrifugation time was increased in 5 min increments. The colorless supernatant was discarded and the GNPs were dried in ambient conditions. For TEM analysis, the GNPs were redispersed in an adequate volume of toluene, yielding a clear-pink mixture. Next, 10 µL of the diluted GNPs were drop-casted onto a carbon-coated copper TEM grid, and the solvent was allowed to evaporate in ambient conditions. TEM measurements were conducted in the Department for Electron Microscopy of the Institute of Physical Chemistry by Stefan Werner using a JEOL JEM-1011 microscope (LaB_6, 100 kV). Particle size statistics were evaluated using the software *ImageJ*.

UV-vis Spectroscopy and Concentration Determination. Depending on the concentration of the stock solution, a 600- or 300-fold dilution was prepared in heptane. Optical spectroscopy measurements were performed using a Varian Cary50 spectrophotometer over a range of 300–900 nm in a quartz cuvette (optical path: 10.00 mm). All spectra were corrected for heptane background absorbance. The molar concentration of the stock solutions were estimated using the Haiss equation,[224] taking into account the absorbance at 450 nm, the dilution factor, and the GNP diameter determined via TEM analysis.

7.2 Synthesis of Shape-Controlled Titania Nanocrystals

Titania nanocrystals (TNCs) of different shapes were used for thin film fabrication. Titania nanorods (TNRs) of varying sizes and titania nanoplates (TNPs) were synthesized in a seeded-growth approach following the Gordon method[139] with slight modifications.[203] For control experiments, titania nanodots (TNDs) were synthesized by a method by Fraunhofer Center of Applied Nanotechnology. All reactions were carried out in a nitrogen atmosphere using standard Schlenk technique.

Chemicals and Apparatus. (*Chemicals*) 1-octadecene (ODE, 90 %), oleic acid (OLAC, 90 %), oleylamine (OLAM, 98 %), diethylene glycol (DEG, 99 %), and titanium(IV) chloride (99 %) were purchased from Merck. Titanium(IV) fluoride (99 %) was purchased from Alfa Aesar. Chloroform (99 %), 2-propanol (IPA, 99.7 %), and toluene (99.5 %) were purchased from VWR Chemicals. DI water (resistivity 18.2 MΩcm) was purified using an ELGA LabWater purification system. (*Apparatus*) Syringe pump (KDS Legacy 100, KD Scientific), centrifuge (Sigma 3-18K).

TNR Synthesis. In a typical synthesis for TNRs with an average length of ~40 nm, a precursor solution of 20 mL ODE and 6.8 mL OLAC was prepared. At the same time, a reaction solution of 60 mL ODE, 60 mL OLAM and 3.6 mL OLAC was prepared and both solutions were degassed in vacuum at 120 °C. After 2 hours, both solutions were cooled down to 60 °C, and 0.5 mL $TiCl_4$ were added to the precursor solution which was stirred for 15 min to complete the formation of the brown titanium oleate complex. Next, 2.5 mL of the precursor solution were added to the reaction solution and the mixture was heated to 290 °C under vigorous stirring and under reflux, and was kept stirring for 15 min for seed formation. For the subsequent growth of the nanorods, 10 mL of the precursor solution were continuously added to the reaction solution via syringe pump at a constant rate of 9 mL/h. During the course of the synthesis, the solution turned yellow indicating TNR formation. After the precursor addition was completed, the mixture was stirred for 10 min, and was then cooled down to ambient temperature swiftly. The suspension was precipitated with IPA (1/1, v/v) and centrifuged for 15 min (8000 g, 15 °C). The solid was redispersed in toluene, and precipitated with IPA (1/1, v/v) or, in some cases, a mixture of IPA/acetone (0.66/0.33/1, $v/v/v$), and centrifuged again as described above. The resulting solid was redispersed in 15 mL chloroform, resulting in a clear-yellow solution.

Depending on the desired TNR length, the amount of added precursor solution for both, seed formation and growth, was varied, as well as the concentration of the precursor solution and addition rates, as briefly summarized in table 7.1.

Table 7.1: Variation of reaction parameters to tune the TNR length.

TNR length	precursor solution $TiCl_4$/OLAC/ODE (mmol/mmol/mL)	V_{seeds} (mL)	V_{growth} (mL)	addition rate (mL/h)
25 nm	9.2/43/40	5	10	18
50 nm	8.2/8/40	1	15	9
90 nm	8.2/8/40	1	25	9

TNP Synthesis. TNPs with an average edge length of ~22 nm were fabricated by the same procedure as described in the previous paragraph with the following modifications. Instead of $TiCl_4$, 0.45 g TiF_4 were dissolved in the precursor solution consisting of 16 mL ODE and 5.4 mL OLAC. To fully dissolve the precursor, the solution was heated up to 100 °C. For the seed formation, 1 mL of the precursor solution was added to the reaction solution. For the growth, 18 mL of the precursor solution were continuously added at a constant rate of 9 mL/h via syringe pump. During the continuous addition, the reaction mixture turned pale-green first and finally, deep blue, indicating the formation of TNPs. For purification, the suspension was precipitated with IPA (1/1, v/v) and centrifuged for 15 min (6000 g, 15 °C). The precipitate was redispersed in chloroform and the washing and precipitation step were repeated twice. The resulting blue solid was dispersed in 15 mL chloroform. Due to the formation of a colorless precipitate, the solution was filtrated using a syringe filter (PTFE, 200 µm), yielding a dark-blue, clear solution.

TND Synthesis. For the synthesis of TNDs with an estimated diameter between 5–10 nm, 120 mL DEG were degassed in vacuum for 1 hour at 60 °C. Next, 8 mL $TiCl_4$ were added to the DEG under vigorous stirring, and kept for 10 min. Afterwards, 4 mL DI water were added to the reaction solution, and the mixture was heated to 160 °C. After 4 h, the mixture was allowed to cool down to ambient temperature. Then the reaction mixture was added to 500 mL acetone and a colorless solid precipitated. Most of the colorless supernatant was carefully discarded, and the TNDs were centrifuged for 15 min (8000 g, 15 °C). The precipitate was then dried under vacuum, yielding a brownish crystalline solid.

Surface Modification and Phase Transfer. The surface of the as-synthesized TNDs was modified with OLAM as ligand in order to prepare a TND solution in organic solvents for subsequent film deposition via spin-coating. The procedure was conducted based on the method by Hensel et al.[203] First, 1 g of the dried TNDs was dissolved in a mixture of 5 mL OLAM, 5 mL IPA and 15 mL toluene, yielding a clear-yellow solution. The mixture was stirred for approx. 19 hours. Afterwards, the solution was washed and precipitated with acetone (1/1, *v*/*v*) to remove an excess of OLAM, and centrifuged for 15 min (8000 g, 15 °C). The precipitate was redispersed in 30 mL chloroform, yielding a clear, yellowish solution.

TEM Analysis. TEM analysis was performed to determine the size and shape of the as-synthesized, as well as of surface-modified TNCs. For sample preparation, 5-10 µL of the stock solution were dissolved in 1.5 mL toluene, and 10 µL of this dilution were drop-casted onto a carbon-coated copper TEM grid. The measurements were performed in the Department for Electron Microscopy of the Institute of Physical Chemistry by Stefan Werner using a JEOL JEM-1011 microscope (LaB_6, 100 kV). Particle size statistics for the TNR and TNP samples were evaluated using the software *ImageJ*.

TG Analysis. The mass concentration and the organic content of the TNCs were determined by thermogravimetric analysis (TGA) using a thermomicrobalance (NETZSCH TG209 F1 Iris System). Depending on the concentration of the respective stock solution, 400-600 µL of the solution were dried in a ceramic crucible by solvent evaporation at ~60 °C. The samples were then heated in a nitrogen atmosphere as follows: First, the temperature was increased to 120 °C (10 K/min), and kept for 20 min. Then the sample was heated to 800 °C (10 K/min) and kept for 20 min. In a final step, air was purged to the test cell at 800 °C for 20 min.

XRD Analysis. For XRD measurements to characterize the TNC crystal structure, the stock solution was drop-casted (50-100 µL) on XRD wafers and dried under ambient conditions. The measurements were conducted from 20-90°, using a Philips X'Pert PRO MPD powder diffractometer with a Cu-K_α source (0.154 nm). The obtained diffractograms were compared with reference diffractograms from the ICSD database.[200,201]

7.3 Synthesis of Graphene Oxide

Chemicals and Apparatus. (*Chemicals*) Graphite (-325 mesh 99.8 %) and potassium permanganate (99.0 %) were purchased from Alfa Aesar. Hydrochloric acid (37 %) was purchased from VWR Chemicals, hydrogen peroxide (30 %) from Merck, and sulfuric acid (95 %) from Chemsolute. DI water (resistivity 18.2 MΩcm) was purified using an ELGA LabWater purification system. (*Apparatus*) Centrifuge (Sigma 3-18K), ultrasonic bath (Bandelin Sonorex RK 255H).

Synthesis. Graphene oxide (GO) was synthesized according to a procedure reported by Chen et al.[113] with slight modifications. First, 1.0 g graphite flakes were suspended in 23 mL sulfuric acid and the mixture was cooled down in an ice bath. Under vigorous stirring, 3.0 g $KMnO_4$ were carefully added portion-wise to the mixture. The ice bath was removed, and the reaction solution was heated to 40 °C and kept for 30 min. Next, 50 mL (DI) water were added to the dark-green mixture, and it was heated to 95 °C. After 15 min, 150 mL DI water were added, followed by a stepwise addition of 20 mL of hydrogen peroxide solution (30 *wt*%) until the color of the mixture changed from brown to yellow. After cooling down, the mixture was centrifuged for 20 min (4000 g, 20 °C) and the supernatant was discarded. The precipitate was washed with approx. 50 mL of a mixture of HCl/water (1/9, *v*/*v*) to remove metal ions and centrifuged for 1 hour (8000 g, 10 °C). This washing step was repeated twice. The precipitate was suspended in 300 mL DI water and purified via dialysis tubing (molecular cut-off: 3.5 kDa) to remove excess of acid and metal ions. After dialysis was completed, the suspension was sonicated for 30 min. To remove un-exfoliated GO flakes, the suspension was centrifuged for 30 min (3000 g, 20 °C). The black precipitate was discarded, and the supernatant was filtered using a Büchner funnel, yielding a clear, light-brown solution. Finally, the GO was freeze-dried, and the aerogel was used for further analysis. For thin film fabrication, the freeze-dried GO was resuspended in DI water, depending on the desired concentration, and sonicated for 5 min.

AFM Analysis. The thickness and lateral sizes of a GO monolayer were analyzed via atomic force microscopy (AFM) analysis. An aqueous GO solution (0.5 mg/mL) was prepared and sonicated for GO exfoliation. A few drops of this solution were drop-casted onto a SiO_2/Si wafer and dried in ambient conditions. Height maps were recorded for selected areas of the substrate using a Digital Instruments AFM with a Nanoscope IV controller, using the tapping mode. The AFM images were processed using the software Gwyddion 2.62 to level the data and to extract height profiles.

UV-vis Spectroscopy. For UV-vis spectroscopy measurements, a diluted aqueous GO solution (0.01 mg/mL) was prepared. Spectra were recorded for the range of 200 – 800 nm with a Varian Cary50 spectrophotometer in a quartz cuvette (optical path: 10.00 mm). All data were corrected for DI water background absorbance.

FTIR-ATR Spectroscopy. Fourier-transform infrared (FTIR) spectra of freeze-dried GO were measured using a Bruker Invenio R FTIR spectrometer (RT-DLaTGS detector, KBr beam splitter), equipped with a Golden Gate attenuated total reflectance (ATR) unit (Specac). Spectra were recorded between 4000 – 400 cm^{-1}. All spectra were corrected for ambient air background.

Element Analysis. Element analysis for the elements CHSO was conducted to determine the composition and degree of oxidation of as-synthesized GO. The measurements were carried out by the Central Element Analysis staff of the Department of Chemistry at University of Hamburg. 20 mg of freeze-dried GO were analyzed via combustion/pyrolysis analysis using a EuroEA element analyzer equipped with an oxygen analyzer (Hekatech). All measurements were repeated at least once, and the resulting mass percentages were averaged.

7.4 Lithographic Fabrication of Electrode Microstructures and Photomasks

Custom-designed electrode structures on oxidized silicon wafers and polyimide (PI) substrates, as well as quartz photomasks for DUV lithography were fabricated using standard photolithography.

Materials and Apparatus. (*Materials*) Chromium-coated glass photomask blanks (MB Whitaker Nanofilm, 2.5 × 2.5 × 0.06 in^3, SL LRC 10M 1518), thermally oxidized silicon wafers (orientation <100>, 500 nm SiO_2, Si-Mat), quartz cover slides (Science Services, (25×25×1 mm^3 or 50×50×1 mm^3), polyimide (PI, RS, Kapton™, ~50×50×0.05 mm^3). (*Chemicals*) Hydrogen peroxide (30 %, Chemsolute), potassium iodide (99.5 %, Merck), triammonium citrate (99.5 %, Merck), DI water. (*Apparatus*) Micro writer (Durham Magneto Optics Ltd. MicroWriter ML-3), mask aligner (Karl Suss MJB-3, equipped with a Hg lamp), spin-coater (Suss MicroTec LabSpin 6 TT), hot plate (Präzitherm), vacuum evaporation plant system (œrlikon Leybold Vacuum, UNIVEX 350G), sputtering instrument (Gatan PECSTMModel 682 Ar ion beam system).

Photomask Fabrication

For the preparation of interdigitated electrode (IDE) structures on PI, photomasks were fabricated on a chromium-coated glass blank plate. The patterns were designed using the software *Klayout* (versions >0.25.9). The photoresist-coated blank plates (AZ 1518) were selectively irradiated using a micro writer with a light dose of 90 mJ/cm^2 (λ = 385 nm, with a resolution of 1 µm). After irradiation, the photoresist was developed in the AZ726 MIF developer for 60 s under gentle agitation. Development was stopped by immersion

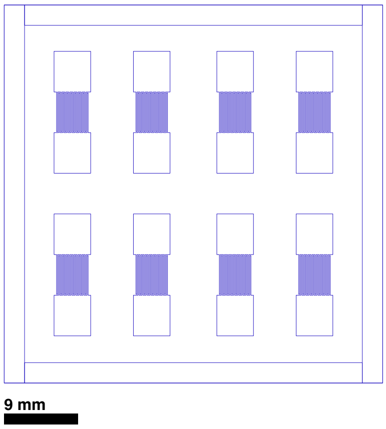

Figure 7.1: Design of the photomask used for the fabrication of 8 IDE structures on PI substrates consisting of 16 fingers of 125 µm width, spaced by 125 µm, with an overlap of 4750 µm.

and rinsing in DI water. Next, the substrate was immersed in a commercially available chromium etchant solution (TechniEtch Cr01) for 60 s, and then thoroughly rinsed with DI water. Finally, the photoresist was removed with acetone, and the mask was cleaned in 2-propanol and water, and then dried in a stream of nitrogen. The used mask design, as exported from the software *Klayout 0.27.4*, are shown in figure 7.1.

Fabrication of Electrodes on Polyimide

A layer of gold (thickness: 50 nm) was deposited onto PI via thermal evaporation. The substrates were then coated with the negative-tone photoresist AZ nLOF 2020 via spin-coating (3000 rpm, 60 s), and then soft-baked for 60 s at 110 °C. Next, the resist-coated PI substrates were exposed through a photomask (cf. figure 7.1) for 12 s using a mask aligner. A post-exposure bake was conducted for 60 s at 110 °C. The photoresist was developed for 60 s by immersion in the AZ 726 MIF developer, and rinsed with DI water and dried in a stream of nitrogen. Then, the exposed gold areas were removed by immersion in a gold etchant solution ($KI/I_2/H_2O$, 4/1/400, $m/m/m$) for approximately 2 minutes. The substrates were then rinsed with DI water. The photoresist was removed by immersion in TechniStrip NI155 for 30 minutes at 65 °C, yielding the gold IDEs on PI. The substrates were cleaned in a final step by subsequent immersion in acetone, 2-propanol, and water, and dried in a gentle stream of nitrogen.

Fabrication of IDEs on Silicon Wafers

Various IDE arrays were fabricated on oxidized silicon wafers in the course of this work, for GNP film deposition, as well as GO/rGO/TNC film deposition.

Ti/Pt Electrodes. Oxidized silicon wafers (~18×21 mm^2) were coated with the the negative-tone photoresist AZ nLOF 2020 via spin-coating (3000 rpm, 60 s). The substrates were soft-baked at 110 °C for 60 s, and exposed through a custom-designed photomask (featuring the design of 2×8 IDEs, 10 fingers, 50 µm width, an overlap of 800 µm, and an interdigital gap of 50 µm), using a mask aligner for 12 s. The substrates were baked at 110 °C for 60 s. The resist was developed in the AZ 726 MIF resist for 60 s, then rinsed with DI water and dried in a stream of nitrogen. The substrates were treated in an air plasma for 2 minutes. Next, Ti/Au were deposited (thickness: 10 nm/40 nm), via sputtering. To obtain the IDEs, a lift-off was conducted, in which the substrates were immersed in TechniStrip NI555 at 60 °C for approximately 1 hour.

Ti/Au Electrodes. For later projects, similar electrode arrays featuring Ti/Au electrodes were fabricated. Here, the oxidized silicon wafers were coated with Ti/Au (thickness:

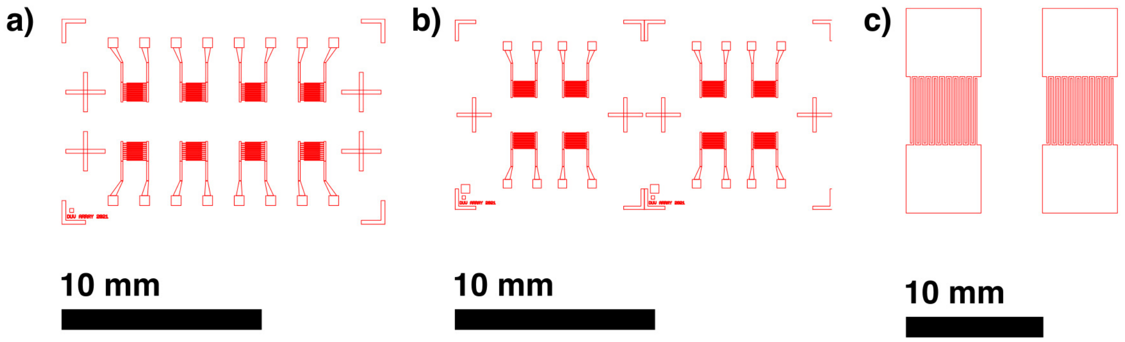

Figure 7.2: Designs of IDEs fabricated on oxidized silicon wafers. a) Array of 8 IDEs used for GNP film array fabrication for binary mixtures sensing (20 fingers, 25 µm width, 25 µm interdigital gap, and 800 µm overlap) b) Array of 2×4 IDEs used for GO/rGO/TNC film characterization and patterning (20 fingers, 25 µm width, 25 µm interdigital gap, and 1180 µm overlap), c) IDEs used for GO/rGO/TNC film deposition and characterization (20 fingers, 125 µm width, 125 µm interdigital gap, and 4750 µm overlap).

10 nm/40 nm) via thermal evaporation, and coated with the AZ nLOF 2020 resist as described in the previous paragraphs. The resist was exposed directly using the micro writer to obtain the desired electrode structures (typically 400 mJ/cm^2, λ = 385 nm, with a resolution of 1 µm). An overview of the electrode geometry designs used for the different investigations is summarized in figure 7.2. Depending on the size of the substrate, the number of IDEs/wafer were varied and adjusted. The photoresist was processed as described in the previous paragraphs. The gold layer and photoresist were removed as described in the previous paragraph for photomask fabrication. The titanium layer was etched by immersion in a 5 *wt*% triammonium citrate solution in hydrogen peroxide for 4 minutes at 35 °C. Afterwards, the substrates were thoroughly rinsed with water and dried in a stream of nitrogen.

Fabrication of Quartz Photomasks

Custom-designed photomasks were fabricated on quartz substrates for DUV lithography for GNP film patterning, and for photocatalytic lithography of GO/rGO/TNC films. Different patterns were designed using the software *Klayout* (versions >0.25.9). First, the quartz glass slides were treated in a solution of water/ammonia/hydrogen peroxide (5/1/1, *v*/*v*/*v*) for 20 minutes at 65 °C to remove contaminations. The substrates were then coated with Ti/Au (thickness: 10 nm/90 nm) via thermal evaporation. Afterward, the substrates were coated with the photoresist AZ nLOF 2020 via spin-coating (3000 rpm, 60 s), and baked for 60 s at 110 °C. The resist was then exposed using the micro writer (typically 400 mJ/cm^2, λ = 385 nm, with a resolution of 1 µm) according to the designed patterns. Figure 7.3 shows different patterns used for quartz photomask fabrication, as exported from *Klayout*. The substrates were baked for 60 s at 110 °C after exposure, and the

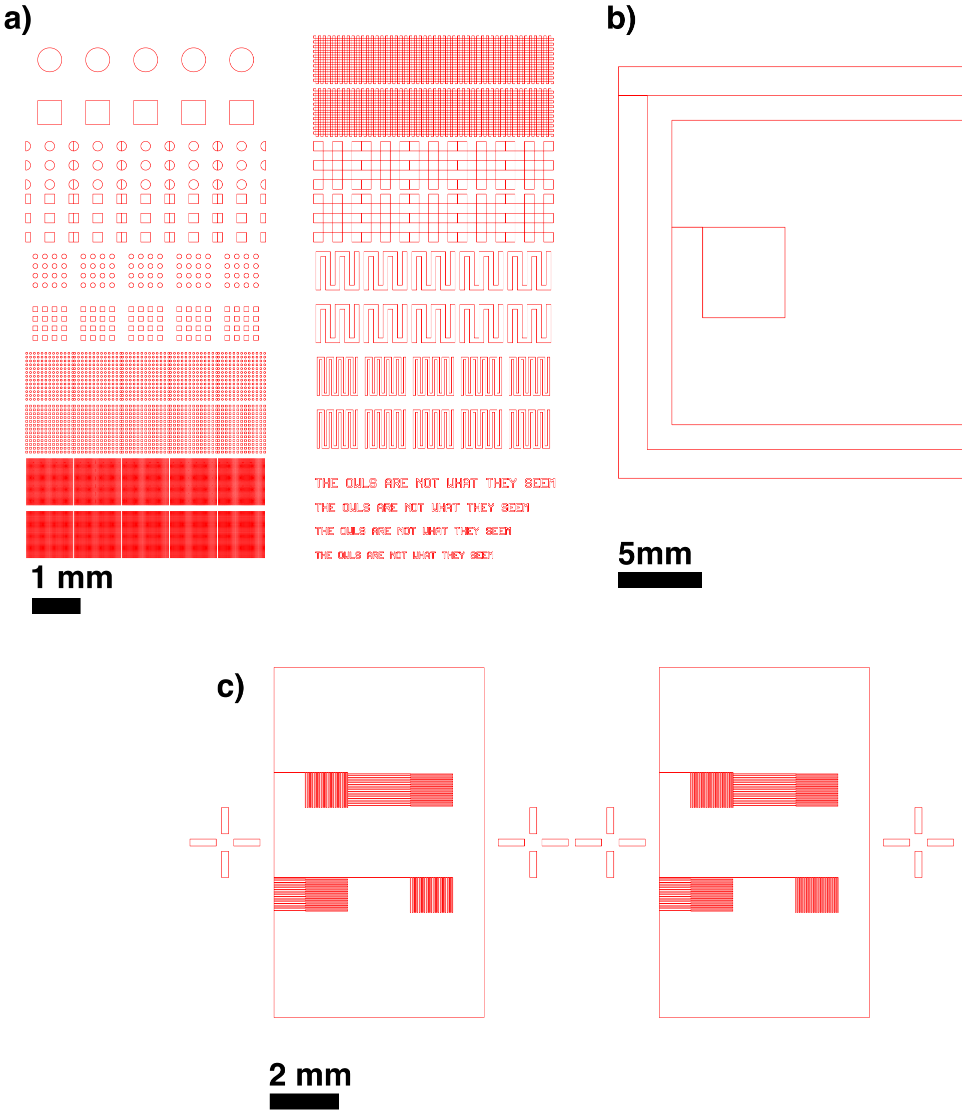

Figure 7.3: Schematic designs for quartz photomasks used for a) testing the resolution of photocatalytic lithography of GO/rGO/TNC films with miscellaneous patterns, b) selective illumination of GO/rGO/TNC films on IDEs for adjustment of the GO/rGO ratio, and c) selective illumination of GO/rGO/films on IDE arrays (cf. figure 7.2b) with 20 µm stripe patterns perpendicular or parallel to the IDE fingers.

photoresist was developed by immersion in the AZ 726 MIF developer for 60 s. After development, the substrates were thoroughly rinsed with DI water and dried in a stream of nitrogen. Subsequently, the gold layer, titanium layer, and finally, the photoresist, were removed as described in the previous paragraph.

7.5 Fabrication and Characterization of GNP Films

Cross-linked GNP films were fabricated using a layer-by-layer spin-coating (LbL SC) procedure.[37] Thin films were deposited directly onto glass substrates (22×22 mm^2) or, for the fabrication of GNP/ADT sensor arrays, on poly(methyl methacrylate) (PMMA)-coated IDEs on thermally oxidized silicon wafers (~ 20×11 mm^2). Differently sized GNPs and various cross-linkers, e.g., α,ω-alkanedithiols (ADTs), as well as different monothiols, were used for chemiresistor (array) fabrication.

Materials and Apparatus. (*Materials and Chemicals*) GNPs/heptane (as-synthesized). 1-Butanol (99 %), 1,6-hexanedithiol (6DT, ≥97 %), 1,9-nonanedithiol (9DT, ≥97 %), and 1,10-decanedithiol (10DT, ≥95 %) were purchased from Alfa Aesar. Acetone (≥99.8 %), methanol (≥99.8 %), and 2-propanol (≥99.5 %) were purchased from VWR Chemicals. Poly(methyl methacrylate) (PMMA, average molecular weight: ~996 kDa), 1,4-butanedithiol (4DT, ≥97 %), hexa(ethylene glycol) dithiol (HEG, ≥97 %), methylisobutyl ketone (MIBK, >98.5 %), and 1,8-octanedithiol (8DT, ≥97 %) were purchased from Merck. Chlorobenzene (≥99 %) was purchased from Honeywell. 2,3-Dimercapto-1-propanol (GLY, ≥98 %) and 4-nitrothiophenol (NTP, 80 %) were purchased from Fluka. SiO_2/Si wafers (<100> orientation, 500 nm SiO_2, diameter: 200 mm, thickness: 725±10 μm, 8-25 Ωcm, p-doped, Si-Mat). Si wafers (<100> orientation, diameter: 76.2 mm, thickness: 380±20 μm, 8-25 Ωcm, Si-Mat), DI water (purified with an ELGA LabWater purification system (18.2 MΩcm)). Glass cover slides (Carl Roth, LH24.1, ($22 \times 22 \times 0.2$ mm^3). (*Apparatus*) Plasma cleaner (Harrick Plasma PDC-002), spin-coater (Suss MicroTec, LabSpin 6 TT), ultrasonic bath (Bandelin Sonorex RK 255H).

Glass-Supported GNP Film Chemiresistors

Preparation of Glass Substrates. Before film deposition, the glass slides were cleaned under sonication in acetone for 15 min to remove contaminations. Next, the substrates were treated in an air plasma for 2 min, yielding hydrophilic glass surfaces.

GNP Film Deposition. The desired ADT cross-linker was dissolved in methanol (7.4 mM). The substrates were placed on a spin-coater and constantly rotated at 3000 rpm. First, 100 μL of the cross-linker solution were deposited two times, spaced by a 20 s between each deposition step for solvent evaporation. Next, 10 μL of the GNP stock solution were deposited onto the rotating substrate, followed by two depositions of 10 μL of the cross-linker solution. Each deposition step was spaced by delays of 20 s. The alternating deposition cycles were repeated 4–6 times. The coated substrates were immersed into approx. 8 mL of the methanolic cross-linker solution for approx. 2 hours. Then, the substrate-supported films were washed with acetone and dried in a stream of nitrogen.

Lithographically Patterned GNP Films

Patterned GNP films were fabricated based on a lift-off method developed using PMMA as photoresist. SiO_2/Si wafers equipped with 8 photolithographically structured IDE structures, were used as substrates. The IDE fabrication process is described in section 7.4.

PMMA Lithography and Lift-Off. First, a PMMA/chlorobenzene solution (33 mg/mL) was deposited on the IDE structure via spin-coating (4000 rpm, 60 s). Then, the substrate was baked for 10 min at 60 s. Next, the PMMA layer was irradiated through a custom-designed quartz photomask using a home-built UV lamp (cf. section A.1.5) for 130 min. The photomask was fixated directly onto the PMMA-coated substrate using small magnets. For the fabrication of smaller micro-sized GNP film areas, the PMMA layer was processed as electron beam resist and exposed using a FEI Quanta 3D FEG scanning electron microscope with an area dose of 120 mC/cm^2 (10 kV acceleration voltage). After irradiation, PMMA was developed for 70 s in a 3:1 (*v*/*v*) mixture of 2-propanol and MIBK, and the substrate was rinsed with 2-propanol for at least 30 s. Next, GNP/ADT films were deposited via LbL SC on the patterned PMMA layer, as described in the previous paragraph. Finally, a lift-off was conducted to yield patterned GNP films, where the PMMA layer was dissolved in acetone under vigorous agitation.
For the arrays that were fabricated for binary analyte mixtures sensing, 100 µL of both, the GNP solution and of the 6DT cross-linker solution were applied for film deposition, aiming at achieving a more homogeneous film thickness distribution on the arrays.

Selective GNP Film Refunctionalization. Different thiol and dithiol species were selectively introduced into the organic matrix of patterned GNP/9DT films. Here, a patterned GNP/9DT array was coated with a PMMA layer as described in the previous paragraph, and the PMMA was processed by the described UV lithography steps, where the PMMA layer covering 2/8 GNP film areas was exposed. After development, the substrate was immersed in a methanolic molecular dopant solution (HEG, 200 mM) for 2 h. Next, the PMMA layer was dissolved in acetone. This process was repeated twice, each time exposing a new GNP/9DT pair and using a different molecular dopant solution: GLY/methanol (200 mM), and NTP/methanol (~20 mM), yielding a sensor array with 4 pairs of differently functionalized GNP films.

GNP Film Characterization

Charge Transport Measurements. Glass-supported GNP films were separated into quarters of ~1×1 cm^2. For electrical characterization and chemiresistor measurements, these segments were equipped with gold electrodes (thickness: 100 nm) via thermal evaporation using a cannula as shadow mask, resulting in a conductive GNP film channel of a length ℓ_g of ~400 μm and width w_g of ~1 cm. Current-voltage measurements of all as-fabricated films were conducted under ambient conditions using a custom-built probe station using either an Agilent 4156C semiconductor parameter analyzer, or a Keithley 2601A sourcemeter. Voltages swept between ±5 V in 0.05 V steps were applied while the current was recorded. The conductivity σ of the films was calculated according to equation 16,

$$\sigma = G\frac{\ell_g}{w_g t_f} \tag{16}$$

where G is the conductance, extracted as the slope from the recorded IV curves, and t_f the film thickness, estimated via AFM, as described in the next paragraph.

Film Thickness Determination. The film thickness of GNP films was determined via AFM analysis. For glass-supported films, another ~1×1 cm^2 sized film segment was fixated onto a magnetic plate using tape. Multiple scratches were introduced into the film using a cannula. The GNP film was thoroughly cleared from residues caused from scratching with a strong stream of nitrogen. Height maps (typically, 20×5 μm^2) were recorded at the scratch edges at two different film positions using a Digital Instruments AFM with a Nanoscope IV controller in the tapping mode. For lithographically patterned GNP films, scans were recorded at the patterned film edges, using a JPK Nanowizard AFM. Height profiles were extracted using the software *Gwyddion*. Typically, ten step functions (five per scan) were fitted to the extracted profile, and averaged as the film thickness.

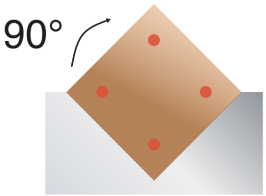

Figure 7.4: Schematic depiction of a glass-supported film mounted to a custom-built sample holder for UV-vis spectroscopy. The red markers correspond to the area which is measured. Four spots were measured after subsequent rotation of the sample, as indicated.

UV-vis Spectroscopy. Absorbance spectra of glass-supported GNP films were recorded using a Varian Cary50 spectrophotometer in a wavelength range of 300–900 nm. After film deposition, the glass-supported films were mounted to a custom-designed sample holder, and its backside was carefully cleaned mechanically using a wipe and acetone. Four spectra were recorded at four different positions, as shown in figure 7.4. All spectra were corrected for background absorbance from bare glass slides.

XPS Measurements. The impact of UV light on the chemical composition of GNP/9DT films was analyzed using X-ray photoelectron spectroscopy (XPS) measurements. For this purpose, 9DT/GNP films were deposited onto silicon wafers via LbL SC, and exposed to UV radiation for 2 h. Spectra acquisition and evaluation were conducted by Dr. Heshmat Noei at DESY. The measurements were done using a high-resolution two-dimensional delay line detector. Incident radiation was provided using a monochromatic Al K_α X-ray source (photon energy 1486.6 eV; anode operating at 15 kV). Spectra acquisition was performed in fixed transmission mode. A pass energy of 25 eV was chosen, resulting in a resolution >0.4 eV. A flood gun was used to compensate charging effects. Binding energies were calibrated based on the Au $4f_{7/2}$ peak at 84.0 eV.

7.6 Fabrication and Characterization of TNC/GO/rGO Films

Hybrid films of GO and TNCs were fabricated on various substrates using a LbL SC process. The procedure was inspired by a method by Hensel et al.[203] and Schlicke et al.[37] The films were deposited directly onto different types of substrates (quartz slides, Si and SiO_2/Si wafers, and polyimide (PI), quartz crystal microbalances (QCMs), depending on the targeted measurements.

Materials and Apparatus. (*Materials and Chemicals*) TNCs/chloroform (0.5–4 mg/mL), GO/water/methanol (0.05–0.1 *wt*%). Methanol (99.8 % VWR Chemicals), DI water (18.2 MΩcm, purified with an ELGA LabWater purification system). Quartz slides (Won Ik Quartz Europe, 20 × 20 × 0.5 mm^3), PI (RS, Kapton™~20×10×0.05 mm^3), SiO_2/Si wafers (<100> orientation, 500 nm SiO_2, diameter: 200 mm, thickness: 725±10 µm, 8-25 Ωcm, p-doped, Si-Mat). Si wafers (<100> orientation, diameter: 76.2 mm, thickness: 380±20 µm, 8-25 Ωcm, Si-Mat), QCMs (resonant frequency: 10.00 MHz, diameter: 14 mm, Ti/Au electrodes, QuartzPro). (*Apparatus*) Mask Aligner (Karl Suss MJB-3), Plasma cleaner (Harrick Plasma PDC-002), spin-coater (Suss MicroTec LabSpin 6 TT).

Preparation of Substrates. Before film deposition, the desired substrates were treated in an air plasma for 2 min, yielding hydrophilic surfaces.

GO/TNC Film Deposition. The desired substrate was placed on the spin-coater and constantly rotated at 3000 rpm. First, 25 µL of a methanolic/aqueous GO solution were applied to the rotating substrate. After 30 s for solvent evaporation, the deposition step was repeated. After 30 s, 25 µL of the desired TNC/chloroform solution were deposited onto the rotating substrate, followed by the deposition of 2×25 µL GO solution, again each deposition step spaced by 30 s delay time. This sequence was repeated 3 – 10 times, depending on the desired film thickness. The concentration of the TNC and GO solutions was varied, depending on the desired composition.
For film deposition on QCMs, the substrates were placed slightly off-center of the spin-coater, to avoid accumulation of the material in the central active area of the sensor. The QCMs were coated on one side.

Photocatalytic Reduction and Patterning of GO/rGO/TNC Films

Photoreduction and Patterning. For the photocatalytic reduction of GO to reduced GO (rGO), the substrate-supported GO/rGO/TNC films were exposed to UV radiation for varying times using a home-built DUV source (main emission: 254 nm) in ambient conditions. A detailed characterization of the radiation source is provided in the Appendix, section A.1.1. Exposure times were varied between 15 min for up to 7 h, depending on the targeted measurements. In order to prevent heating of the samples during prolonged illumination, the setup was continuously ventilated using 2 fans. For photocatalytic lithography experiments, the films were exposed through custom-designed quartz masks, shown in figure 7.3. To pattern smaller microstructures, the films were exposed through a quartz mask using a Mask Aligner equipped with a Hg UV lamp.

GO/rGO/TNC Film Characterization

The herein described experimental methods were applied to both, composite films during and after completed film deposition to characterize the formation of the hybrid system, as well as after UV exposure to investigate the effects of photocatalytic reduction.

Film Thickness Determination. The film thickness of GO/TNC and GO/rGO/TNC films deposited on (oxidized) Si wafers was determined via AFM analysis using a Digital Instruments microscope equipped with a Nanoscope IV Controller. ~1×1 cm^2 sections of the substrate-supported films were fixated on a metallic plate using tape. The film was scratched several times using a cannula, and subsequently purged with a strong stream of nitrogen to remove residues caused by scratching. Height maps (20×5 µm^2 or 2.5 µm^2) were recorded at the edge of a scratched film and the underlying substrate at, at least, two different film positions using the tapping mode. The obtained data were analyzed using the software *Gwyddion*. Ten height profiles (5 per scan) were extracted and averaged to determine the film thickness.

UV-vis Spectroscopy. GO/rGO/TNC films deposited on quartz glass substrates were characterized via optical spectroscopy using a Varian Cary50 spectrophotometer. To this end, the substrate-supported films were mounted to a custom-built sample holder, shown in the previous section, in figure 7.4. Before spectra acquisition, the backside of the quartz substrates was carefully cleaned mechanically using a wipe and acetone. Absorbance spectra were recorded in the wavelength range of 200–600 nm at four different film positions by rotation of the substrate in the sample holder. All data were corrected for background absorbance by recording a baseline absorbance spectrum of a quartz glass slide.

Scanning Electron Microscopy. The film morphology before and after UV exposure was investigated via SEM analysis. To this end, GO/TNC films were deposited onto unoxidized Si wafers and exposed to UV light for 0–7 h. The measurements were conducted in the Department of Electron Microscopy of the Institute of Physical Chemistry at University of Hamburg by Robert Schön and Dr. Charlotte Ruhmlieb, using a Zeiss LEO 155 Gemini microscope (acceleration voltage: 30 kV).

FTIR Spectroscopy. To analyze the GO reduction, GO/rGO/TNC thick films were analyzed using FTIR spectroscopy measurements. To this end, composite films were fabricated by alternatively drop-casting (10 μL) the respective colloidal solutions onto an unoxidized Si wafer. Spectra were recorded using a Bruker Invenio R spectrometer equipped with a Specac Golden Gate ATR unit. Spectra were recorded in a range of 4000–400 cm^{-1} (scan rate: 128). Baseline measurements were recorded from the ambient surrounding.

Charge Transport Measurements. To monitor the progressing GO reduction, GO/TNC films were deposited onto oxidized Si wafers equipped with IDE structures, and exposed to UV radiation for varying times. The substrate-supported films were placed in a custom-built polytetrafluoroethylene (PTFE) test cell (volume ~20 mL) and purged with nitrogen (Linde 5.0) for ~1 min to remove sorbed water molecules. The films were contacted using spring-loaded pin connectors. Current-voltage curves were measured using a Keithley 2601A sourcemeter or an Agilent 4165C semiconductor parameter analyzer. Voltages swept between ±1 V were applied (in 0.02 V steps), and the resulting current was recorded.

XPS Measurements. Selected GO/rGO/TNC films were analyzed by XPS measurements. For this purpose, hybrid films using TNRs and TNPs (2 mg/mL in $CHCl_3$) were deposited on Ti/Au-coated silicon wafers ((2×2) cm^2, Ti/Au thickness: 10 nm/100 nm) by LbL SC (1 deposition cycle). After deposition, the substrate was divided into four equally sized sections. The different sections were exposed to UV light for 30 minutes and 240 minutes for GO reduction. One section was left untreated as reference film, and one was used for AFM analysis. XPS measurements were conducted by Dr. Mona Kohantorabi and Dr. Heshmat Noei at DESY. The measurements were done using a high-resolution two-dimensional delay line detector. Incident radiation was provided using a monochromatic Al K_α X-ray source (photon energy 1486.6 eV; anode operating at 15 kV). Spectra acquisition was performed in fixed transmission mode. A pass energy of 25 eV was chosen, resulting in a resolution >0.4 eV. A flood gun was used to compensate charging effects. Binding energies were calibrated based on the C 1s peak at 284.8 eV.

7.7 Sensing Measurements

7.7.1 General Setup

Different vapor sensing experiments were conducted within the framework of this thesis. Depending on the project and the investigated sensing materials, different setups were used and adapted. In general, analyte vapors were provided using commercial gas calibration systems (CGM2000, MCZ Umwelttechnik). Figure 7.5 shows the general

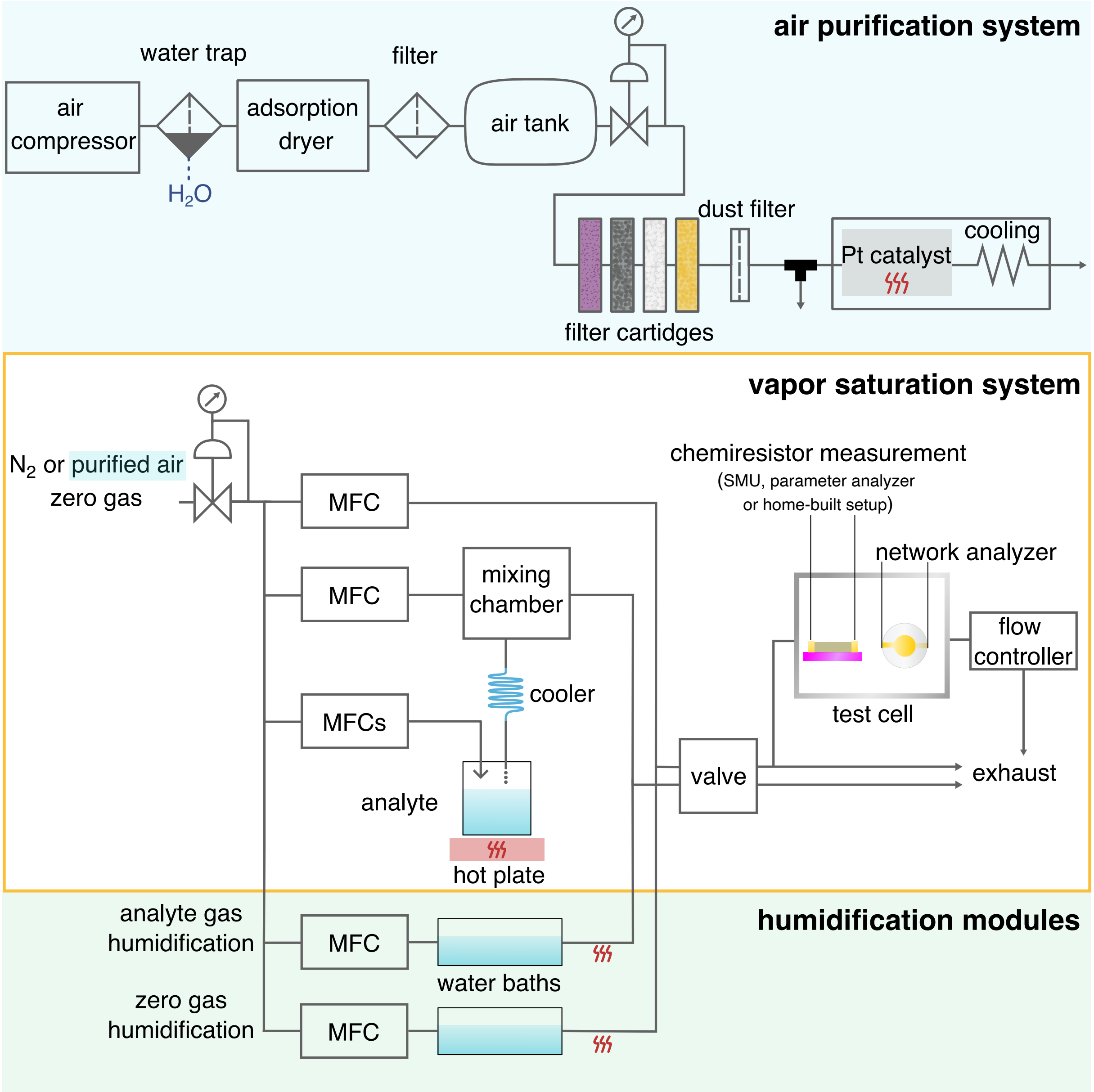

Figure 7.5: Schematic depiction of the flow chart of the setup used for different vapor sensing experiments. The basic setup consists of a vapor saturation system (yellow unit) to provide analyte mixtures at defined concentrations. For humidity sensing, the setup can be extended by a humidification unit (green unit). Zero gas can be set to nitrogen (in-house line) or to purified dry air, which is obtained by an air purification system (blue unit).

flow plan of the modular experimental setup used to provide analyte vapors with defined concentrations. The basic setup consists of a vapor saturation system (yellow unit) in which the gas flow is regulated using mass flow controllers (MFCs). Generally, zero gas (ZG) is continuously provided by either using the in-house nitrogen supply, or a zero gas purification system (blue unit). The ZG line is split into two different lines: The first line is pure ZG, and is regulated by an MFC, typically set to 1 L/min. The second line generates the analyte gas (AG), i.e., analyte-enriched ZG with defined analyte concentrations. For this purpose, ZG is guided through the liquid analyte compound in a saturator vessel (typically set to 30 °C) at a certain flow rate Q, and a condenser, that is set to a certain temperature, to generate a saturated vapor of the analyte, which is then guided to a mixing chamber where it is mixed and diluted with ZG to obtain the desired concentration at a desired total flow rate (typically $Q = 1$ L/min). Finally, the ZG and AG can be alternatingly fed to the test cell by switching between both lines using an externally controlled valve. The flow through the test cell is regulated using a flow controller and was set to 500 mL/min for all experiments.

For relative humidity (r.h.) sensing experiments with GO/rGO/TNC films, the setup was expanded by two humidification modules (green unit) for the AG and ZG lines, respectively. Here, saturated water vapor is generated by feeding ZG through tempered water baths at a desired flow rate regulated by two MFCs. This water vapor is guided through heated tubings (60 °C) and then then mixed with ZG at a T-piece according to the desired r.h. level. In these experiments, purified air was used as ZG, that was generated using a commercial zero gas system (NGA 600-25 MD, MCZ Umwelttechnik). The general setup of the zero gas system is shown as the blue unit of figure 7.5. Purified air is generated in multiple steps from ambient air. First, ambient air is pressurized by an oil-free compressor, dried using an adsorption dryer, and collected in a pressure tank. Next, the dried air is guided through several filtering materials: (i) $KMnO_4/Al_2O_3$ for the removal of SO_2, SO_3, NH_3, NOx, H_2S, i.a., (ii) activated carbon for O_3, NO_2 and higher-boiling hydrocarbons removal, (iii) molecular sieve (10 Å) for adsorption of H_2O, CO_2, H_2S, CO, i.a., and (iv) silica gel with an indicator to remove and indicate residual humidity. As final purification step, the air stream is guided through a catalytic purification unit consisting of a Pt catalyst (485 °C) and a subsequent cooling coil, to obtain methane- and CO-free purified, dry air, that can be used as ZG in the vapor saturation system. Table 7.2 gives a general overview of the used systems, ZG, and test cell volumes and types, depending on the target analytes and investigated material.

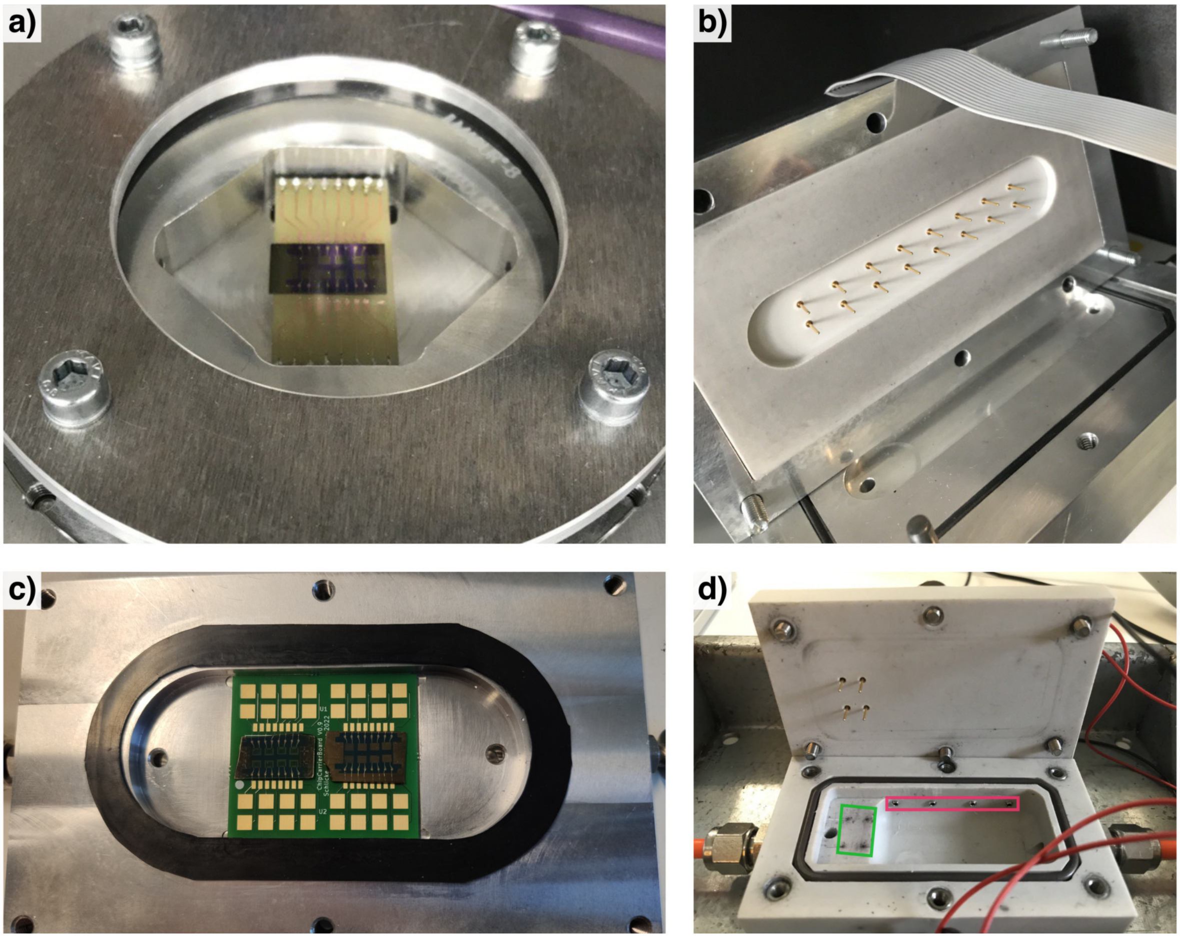

Figure 7.6: Photographs of test cells used for sensing measurements. a) Aluminum test cell for PCB-supported GNP film arrays (8 sensors), contacted via socket pins and a ribbon cable. The test cell is sealed by an optical glass and a O-ring. Cell volume: ~16 mL. An exemplary GNP film array, contacted via wire-bonding to the PCB, is placed inside of the test cell. b) Aluminum test cell for placement of 8 chemiresistors with approximately 0.6–1 cm electrode pad distances, contacted via the 8 pairs of spring-loaded pin connectors. Cell volume: ~10 mL. c) Exemplary PCB carrying two GNP film arrays (16 sensors) inside of an Al-test cell used for VOC mixtures sensing. The films on the wafer were contacted via wire-bonding to the PCB, which is contacted using spring-loaded pin connectors. Cell volume: ~16 mL. d) PTFE test cell used for simultaneous chemiresistor (placed in the green area) and QCM (placed in pink area) measurements. The chemiresistors were contacted via spring-loaded pin connectors, the QCM wire holders were pushed into the metal-encased apertures. Cell volume: ~20 mL.

Table 7.2: Overview of the measurement settings for different projects.

Sensing Material	AG	ZG	Test cell volume	Test cell type (figure 7.6)
GNP film arrays$_{\text{patterned}}$	VOCs and water	N_2	16 mL	a)
GNP films$_{\text{glass supported}}$	VOCs and water	N_2	10 mL	b)
GNP film arrays$_{\text{patterned}}$	binary VOC mixtures	N_2	16 mL	c)
GO/rGO/TNC films	r.h.	purified air	20 mL	d)
GO/rGO/TNC films	VOCs and water	N_2	20 mL	d)

7.7.2 Gold Nanoparticle Film Chemiresistors

Chemicals. Ethanol (≥99.9 %), 1-propanol (99.5 %), 2-propanol (≥99.5%), heptane (99 %), toluene (99.5 %), and hexane (99 %) were purchased from Grüssing GmbH. Octane (>99 % was purchased from Acros Organics), methylisobutyl ketone (MIBK, >98.5 %) from Merck, and 1-butanol (99 %) from Alfa Aesar. DI water was purified with an ELGA water purification system (18.2 MΩcm). Nitrogen 5.0 (Linde).

VOC and Water Vapor Sensing.

The resistive sensing properties of GNP films and GNP film arrays towards various analyte vapors were investigated. Depending on the resistor type (8 single glass-supported resistors or lithographically patterned sensor arrays), different aluminum test cells, shown in figure 7.6a-b), were used. Usually, the GNP film array structures were first glued onto suitable printed circuit boards (PCBs) and contacted via wire-bonding to enable electrical readout, while the glass-supported resistors were directly contacted using spring-loaded pin connectors. All measurements were conducted using a custom-built setup for read-out of eight resistors. A constant voltage (5 V) was provided using a Keithley 2601A sourcemeter. The voltage drop at shunt resistors R_s that were connected in series to each GNP film (typically, around 5 % of the respective GNP resistor's baseline resistance) was measured using a Keithley 2002 multimeter. The measured voltages (V_s) at 8 shunts were successively forwarded to the multimeter using a custom-built multiplexer based on reed relays. The sensor resistances were computed from the resulting current and the applied voltage under consideration of the respective burden voltages according to equation 17. The sensors were dosed with AG (typical concentration range: 50–8000 ppm) for 4 minutes, spaced by 8 or 16 minutes nitrogen exposure.

$$R = R_s(5\ \mathrm{V} - V_s)/V_s \tag{17}$$

Binary VOC Mixtures Sensing.

The chemiresistive responses of GNP/6DT sensor arrays (2×8 films) towards binary VOC mixtures were probed. The photolithographically patterned GNP film arrays were glued onto a PCB and contacted via wire-bonding. The PCB carrying two arrays was mounted to a custom-built aluminum test cell (cell volume ~16 mL), as shown in figure 7.6c). Binary VOC mixtures were provided by combining two commercial vapor saturation systems (CGM 2000, MCZ Umwelttechnik), as depicted in figure 7.5 as the yellow unit. A schematic depiction of the setup used for binary mixtures sensing is shown in figure 7.7. Each unit generated AG with a certain analyte, and the valves of both systems were

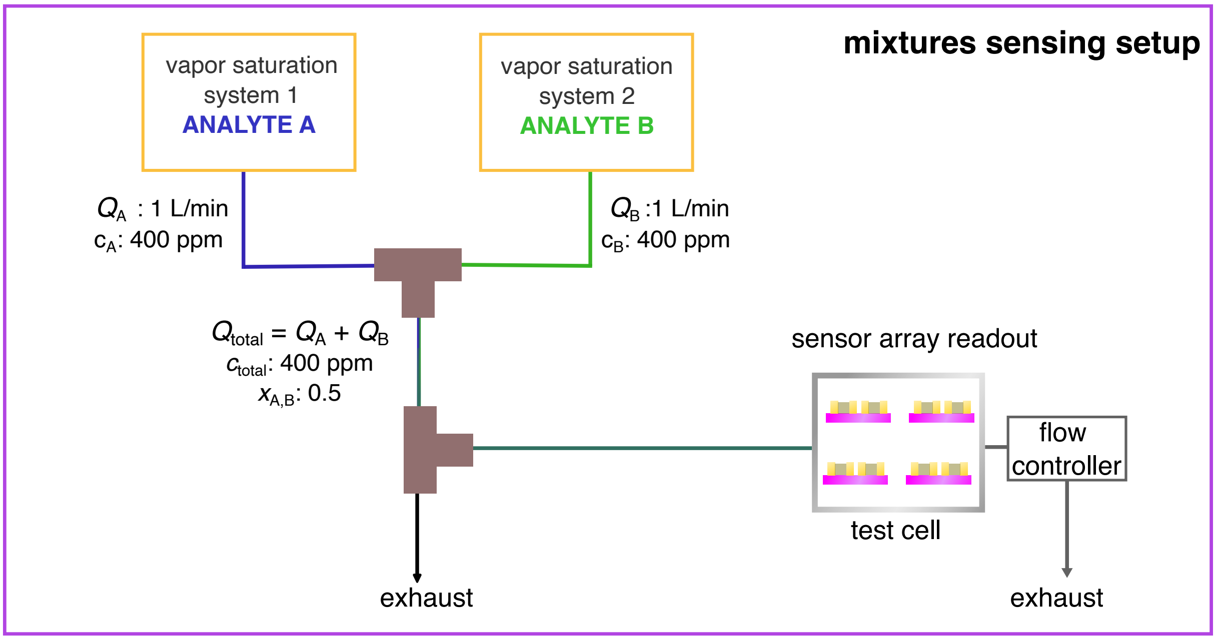

Figure 7.7: General depiction of the setup used to provide binary vapor mixtures. The setup consists of two separate vapor saturation systems (yellow units, cf. figure 7.5) whose outlets are mixed using a T-connection.

triggered simultaneously using an Arduino-controlled switching device. Both units were set to a total flow rate Q of 1 L/min. The respective AG streams were then united and mixed in a T-piece, resulting in a total flow of 2 L/min. Using a MFC-controlled pump, a fraction of the mixed AG was fed through the test cell at a rate of 500 mL/min. To adjust the analyte fractions (0–1, in 0.1 steps), the concentrations of each component were adjusted by the flow rates through the respective saturator/condenser system, while the total analyte concentration was kept at 400 ppm for all mixtures. A custom-built electrical readout device was used for the measurement of 16 sensors, based on shunt voltages measured at shunt resistors connected in series to the resistors, at an applied reference voltage of 2.5 V. The circuitry was designed by Dr. Hendrik Schlicke (Fraunhofer Center of Applied Nanotechnology).

7.7.3 GO/rGO/TNC Film Chemiresistors

Chemicals. 1-Propanol (99.5 % Grüssing GmbH), MIBK (>98.5 % Aldrich), toluene (99.5 % Grüssing GmbH), water, purified with an ELGA water purification system (18.2 MΩcm), Nitrogen 5.0 (Linde), Purified air (air purification system).

Resistive Humidity Sensing.

The resistive response of GO/rGO/TNC films of varying degree of GO reduction towards changes in relative humidity (r.h.) at ambient temperature were probed. To this end, hybrid films deposited on a PI substrate equipped with 2 IDEs were illuminated with UV light for different durations through a quartz mask. After UV exposure of both film areas, the PI substrate was cut to obtain two separate PI-supported sensors to place them in the test cell.

Depending on the analyzed r.h. range, the setup was adapted. In these measurements, purified air (cf. figure 7.5) was used as ZG. For measurements in the range of 0–80 % r.h., water vapor of up to 10000 ppm (~30 % r.h.) was generated using the standard vapor saturation unit (cf. figure 7.5, yellow unit), and for r.h. levels of 40–80 %, the humidification module for the AG line was used. For the investigation of r.h. changes from a baseline humidity of 30 %, the measurement was conducted using the humidification modules for both, ZG and AG. Purified air with a constant r.h. level of 30 % was used as ZG, while the r.h. level of AG was increased to up to 80 %. Optionally, a commercial humidity sensor (BME680, Bosch SensorTec) was placed into the same test cell and read-out using a Raspberry Pi. The sensors were exposed to AG for 4 minutes, followed by 8 minutes ZG. The PI-supported films were placed in a PTFE test cell (volume ~20 mL), shown in figure 7.6d), where up to two sensors were read out in parallel. The sensors were operated at a bias voltage of 1 V, that was applied using either a a Keithley 2601A sourcemeter of an Agilent 4156C semiconductor parameter analyzer, and the resulting current was constantly measured.

QCM Measurements.

The resistive r.h. measurements were combined with gravimetric measurements of GO/rGO/TNC film-coated QCMs to determine the amount of sorbed water molecules. The measurements were conducted using dry purified air as ZG and the sensors were exposed to a r.h. range of 0–80 % using the combined saturator/humidification system. Both, the resistors and film-coated QCMs were placed in a test cell shown in figure 7.6d). The QCMs were contacted using wired sample holders. The baseline resonance frequency of the QCMs was recorded using an Agilent E5100A Network Analyzer for

100 s in ZG atmosphere prior to film deposition, and after film deposition and reduction, to estimate the mass of the deposited hybrid films. During the r.h. measurements, the resonance frequency of the QCM was continuously monitored using using an Agilent E5100A Network analyzer, that was interfaced via GPIB and controlled with a custom-scripted python program provided by Dr. Hendrik Schlicke (Fraunhofer CAN), using the `OUTPRESO?` command[225] to record the (anti)-resonance impedances and (anti)-resonance frequencies.

Resistive VOC Sensing.

For the analysis of the chemiresistive responses towards different analytes, the PI-supported films were placed in the same test cell used for the r.h. measurements (cf. figure 7.6d). The sensors were exposed to vapors of 1-propanol, water, toluene, and MIBK in a concentration range of typically 50–8000 ppm. Nitrogen was used as ZG and carrier gas. AG and ZG times were set to 4 minutes and 8 minutes, respectively. A bias voltage of 1 V was applied using either a Keithley 2601A sourcemeter of an Agilent 4156C semiconductor parameter analyzer, and the resulting current was constantly recorded.

8 Bibliography

[1] H. Schlicke, S. C. Bittinger, T. Vossmeyer, *ACS Appl. Electron. Mater.* **2020**, *2*, 3741–3748.

[2] H. Hartmann, J.-N. Beyer, J. Hansen, S. C. Bittinger, M. Yesilmen, H. Schlicke, T. Vossmeyer, *ACS Appl. Mater. Interfaces* **2021**, *13*, 40932–40941.

[3] H. Schlicke, S. C. Bittinger, H. Noei, T. Vossmeyer, *ACS Appl. Nano Mater.* **2021**, *4*, 10399–10408.

[4] B. Ketelsen, H. Schlicke, V. R. Schulze, S. C. Bittinger, S.-D. Wu, S.-h. Hsu, T. Vossmeyer, *Adv. Funct. Mater.* **2023**, *33*, 2210065.

[5] S.-D. Wu, S.-h. Hsu, B. Ketelsen, S. C. Bittinger, H. Schlicke, H. Weller, T. Vossmeyer, *Small Methods* **2023**, 2300170.

[6] O. S. Wolfbeis, *Angew. Chem. Int. Ed.* **2013**, *52*, 9864–9865.

[7] R. A. Potyrailo, *Chem. Rev.* **2016**, *116*, 11877–11923.

[8] M. Khatib, H. Haick, *ACS Nano* **2022**, *16*, 7080–7115.

[9] Z. Duan, Y. Jiang, H. Tai, *J. Mater. Chem. C* **2021**, *9*, 14963–14980.

[10] V. Montes-García, P. Samorì, *Adv. Mater.* **2023**, 2208766.

[11] Y. Y. Broza, R. Vishinkin, O. Barash, M. K. Nakhleh, H. Haick, *Chem. Soc. Rev.* **2018**, *47*, 4781–4859.

[12] T. Zhou, T. Zhang, *Small Methods* **2021**, *5*, 2100515.

[13] J. Dai, O. Ogbeide, N. Macadam, Q. Sun, W. Yu, Y. Li, B.-L. Su, T. Hasan, X. Huang, W. Huang, *Chem. Soc. Rev.* **2020**, *49*, 1756–1789.

[14] R. Malik, V. K. Tomer, Y. K. Mishra, L. Lin, *Appl. Phys. Rev.* **2020**, *7*, 021301.

[15] T. Delipinar, A. Shafique, M. S. Gohar, M. K. Yapici, *ACS Omega* **2021**, *6*, 8744–8753.

[16] N. Taguchi, *pat.*, 45-38200, **1962**.

[17] M. E. Franke, T. J. Koplin, U. Simon, *Small* **2006**, *2*, 36–50.

[18] Z. Wang, L. Zhu, J. Wang, R. Zhuang, P. Mu, J. Wang, W. Yan, *RSC Adv.* **2022**, *12*, 24614–24632.

[19] J. Janata, M. Josowicz, *Nature Mater.* **2003**, *2*, 19–24.

[20] J.-M. Tulliani, B. Inserra, D. Ziegler, *Micromachines* **2019**, *10*, 232.

[21] R. A. Potyrailo, *Chem. Soc. Rev.* **2017**, *46*, 5311–5346.

[22] V. Montes-García, M. A. Squillaci, M. Diez-Castellnou, Q. K. Ong, F. Stellacci, P. Samorì, *Chem. Soc. Rev.* **2021**, *50*, 1269–1304.

[23] J. Yi, Y. Xianyu, *Adv. Funct. Mater.* **2022**, *32*, 2113012.

[24] M. K. Nakhleh, H. Amal, R. Jeries, Y. Y. Broza, M. Aboud, A. Gharra, H. Ivgi, S. Khatib, S. Badarneh, L. Har-Shai, L. Glass-Marmor, I. Lejbkowicz, A. Miller, S. Badarny, R. Winer, J. Finberg, S. Cohen-Kaminsky, F. Perros, D. Montani, B.

Girerd, G. Garcia, G. Simonneau, F. Nakhoul, S. Baram, R. Salim, M. Hakim, M. Gruber, O. Ronen, T. Marshak, I. Doweck, O. Nativ, Z. Bahouth, D.-y. Shi, W. Zhang, Q.-l. Hua, Y.-y. Pan, L. Tao, H. Liu, A. Karban, E. Koifman, T. Rainis, R. Skapars, A. Sivins, G. Ancans, I. Liepniece-Karele, I. Kikuste, I. Lasina, I. Tolmanis, D. Johnson, S. Z. Millstone, J. Fulton, J. W. Wells, L. H. Wilf, M. Humbert, M. Leja, N. Peled, H. Haick, *ACS Nano* **2016**, *11*, 112–125.

[25] K. Toda, R. Furue, S. Hayami, *Anal. Chim. Acta* **2015**, *878*, 43–53.

[26] M.-C. Daniel, D. Astruc, *Chem. Rev.* **2004**, *104*, 293–346.

[27] S. Eustis, M. A. El-Sayed, *Chem. Soc. Rev.* **2006**, *35*, 209–217.

[28] M. Faraday, *Phil. Trans. R. Soc. Lon.* **1857**, *147*, 145–181.

[29] R. Sardar, A. M. Funston, P. Mulvaney, R. W. Murray, *Langmuir* **2009**, *25*, 13840–13851.

[30] A. Corma, H. Garcia, *Chem. Soc. Rev.* **2008**, *37*, 2096.

[31] Y.-C. Yeh, B. Creran, V. M. Rotello, *Nanoscale* **2012**, *4*, 1871–1880.

[32] K. Saha, S. S. Agasti, C. Kim, X. Li, V. M. Rotello, *Chem. Rev.* **2012**, *112*, 2739–2779.

[33] J. Turkevich, P. C. Stevenson, J. Hillier, *Discuss. Faraday Soc.* **1951**, *11*, 55.

[34] F. Schulz, T. Homolka, N. G. Bastús, V. Puntes, H. Weller, T. Vossmeyer, *Langmuir* **2014**, *30*, 10779–10784.

[35] M. Brust, M. Walker, D. Bethell, D. J. Schiffrin, R. Whyman, *J. Chem. Soc. Chem. Commun.* **1994**, 801–802.

[36] R. G. Nuzzo, B. R. Zegarski, L. H. Dubois, *J. Am. Chem. Soc.* **1987**, *109*, 733–740.

[37] H. Schlicke, J. H. Schröder, M. Trebbin, A. Petrov, M. Ijeh, H. Weller, T. Vossmeyer, *Nanotechnology* **2011**, *22*, 305303.

[38] D. V. Leff, L. Brandt, J. R. Heath, *Langmuir* **1996**, *12*, 4723–4730.

[39] S. Peng, Y. Lee, C. Wang, H. Yin, S. Dai, S. Sun, *Nano Res.* **2008**, *1*, 229–234.

[40] S. K. Ghosh, T. Pal, *Chem. Rev.* **2007**, *107*, 4797–4862.

[41] G. Mie, *Ann. Phys.* **1908**, *330*, 377–445.

[42] S. Link, M. A. El-Sayed, *J. Phys. Chem. B* **1999**, *103*, 4212–4217.

[43] K. L. Kelly, E. Coronado, L. L. Zhao, G. C. Schatz, *J. Phys. Chem. B* **2003**, *107*, 668–677.

[44] G. Sener, L. Uzun, A. Denizli, *ACS Appl. Mater. Interfaces* **2014**, *6*, 18395–18400.

[45] M. A. Squillaci, X. Zhong, L. Peyruchat, C. Genet, T. W. Ebbesen, P. Samorì, *Nanoscale* **2019**, *11*, 19315–19318.

[46] S. Link, M. A. El-Sayed, *J. Phys. Chem. B* **1999**, *103*, 8410–8426.

[47] U. Kreibig, L. Genzel, *Surf. Sci.* **1985**, *156*, 678–700.

[48] N. L. Rosi, C. A. Mirkin, *Chem. Rev.* **2005**, *105*, 1547–1562.

[49] Y. Lu, Y. Liu, S. Zhang, S. Wang, S. Zhang, X. Zhang, *Anal. Chem.* **2013**, *85*, 6571–6574.

[50] P. K. Jain, W. Huang, M. A. El-Sayed, *Nano Lett.* **2007**, *7*, 2080–2088.

[51] M. Brust, D. Bethell, C. J. Kiely, D. J. Schiffrin, *Langmuir* **1998**, *14*, 5425–5429.

[52] B. Ketelsen, M. Yesilmen, H. Schlicke, H. Noei, C.-H. Su, Y.-C. Liao, T. Vossmeyer, *ACS Appl. Mater. Interfaces* **2018**, *10*, 37374–37385.

[53] B. Ketelsen, PhD thesis, University of Hamburg, **2022**.

[54] H. Schlicke, S. Kunze, M. Rebber, N. Schulz, S. Riekeberg, H. K. Trieu, T. Vossmeyer, *Adv. Funct. Mater.*, *20*, 2003381.

[55] H. Schlicke, M. Behrens, C. J. Schröter, G. T. Dahl, H. Hartmann, T. Vossmeyer, *ACS Sens.* **2017**, *2*, 540–546.

[56] N. Olichwer, A. Meyer, M. Yesilmen, T. Vossmeyer, *J. Mater. Chem. C* **2016**, *4*, 8214–8225.

[57] C.-H. Su, H.-L. Chiu, Y.-C. Chen, M. Yesilmen, F. Schulz, B. Ketelsen, T. Vossmeyer, Y.-C. Liao, *Langmuir* **2019**, *35*, 3256–3264.

[58] B. Ketelsen, P. P. Tjarks, H. Schlicke, Y.-C. Liao, T. Vossmeyer, *Chemosensors* **2020**, *8*, 116.

[59] D. Bethell, M. Brust, D. J. Schiffrin, C. Kiely, *J. Electroanal. Chem.* **1996**, *409*, 137–143.

[60] Y. Milyutin, M. Abud-Hawa, V. Kloper-Weidenfeld, E. Mansour, Y. Y. Broza, G. Shani, H. Haick, *Nat. Protoc.* **2021**, *16*, 2968–2990.

[61] F. J. Ibañez, F. P. Zamborini, *Small* **2012**, *8*, 174–202.

[62] E. Dovgolevsky, U. Tisch, H. Haick, *Small* **2009**, *5*, 1158–1161.

[63] H. Schlicke, S. Kunze, M. Finsel, E. W. Leib, C. J. Schröter, M. Blankenburg, H. Noei, T. Vossmeyer, *J. Phys. Chem. C* **2019**, *123*, 19165–19174.

[64] R. H. Terrill, T. A. Postlethwaite, C.-h. Chen, C.-D. Poon, A. Terzis, A. Chen, J. E. Hutchison, M. R. Clark, G. Wignall, J. D. Londono, R. Superfine, M. Falvo, C. S. Johnson, E. T. Samulski, R. W. Murray, *J. Am. Chem. Soc.* **1995**, *117*, 12537–12548.

[65] J. M. Wessels, H.-G. Nothofer, W. E. Ford, F. von Wrochem, F. Scholz, T. Vossmeyer, A. Schroedter, H. Weller, A. Yasuda, *J. Am. Chem. Soc.* **2004**, *126*, 3349–3356.

[66] M. A. Ratner, B. Davis, M. Kemp, V. Mujica, A. Roitberg, S. Yaliraki, *Annals N.Y. Acad. Sci.* **1998**, *852*, 22–37.

[67] W. P. Wuelfing, R. W. Murray, *J. Phys. Chem. B* **2002**, *106*, 3139–3145.

[68] Y. Joseph, I. Besnard, M. Rosenberger, B. Guse, H.-G. Nothofer, J. M. Wessels, U. Wild, A. Knop-Gericke, D. Su, R. Schlögl, A. Yasuda, T. Vossmeyer, *J. Phys. Chem. B* **2003**, *107*, 7406–7413.

[69] B. Abeles, P. Sheng, M. Coutts, Y. Arie, *Adv. Phys.* **1975**, *24*, 407–461.

[70] K. Likharev, *Proc. IEEE* **1999**, *87*, 606–632.

[71] J. Herrmann, K.-H. Müller, T. Reda, G. R. Baxter, B. Raguse, G. J. J. B. de Groot, R. Chai, M. Roberts, L. Wieczorek, *Appl. Phys. Lett.* **2007**, *91*, 183105.

[72] T. Vossmeyer, C. Stolte, M. Ijeh, A. Kornowski, H. Weller, *Adv. Funct. Mater.* **2008**, *18*, 1611–1616.

[73] L. Yi, W. Jiao, C. Zhu, K. Wu, C. Zhang, L. Qian, S. Wang, Y. Jiang, S. Yuan, *Nano Res.* **2016**, *9*, 1346–1357.

[74] N. Krasteva, Y. Fogel, R. E. Bauer, K. Müllen, Y. Joseph, N. Matsuzawa, A. Yasuda, T. Vossmeyer, *Adv. Funct. Mater.* **2007**, *17*, 881–888.

[75] N. Olichwer, E. W. Leib, A. H. Halfar, A. Petrov, T. Vossmeyer, *ACS Appl. Mater. Interfaces* **2012**, *4*, 6151–6161.

[76] H. Wohltjen, A. W. Snow, *Anal. Chem.* **1998**, *70*, 2856–2859.

[77] T. Vossmeyer, Y. Joseph, I. Besnard, O. Harnack, N. Krasteva, B. Guse, H.-G. Nothofer, A. Yasuda, *SPIE Proc.* **2004**, 202–212.

[78] Y. Joseph, A. Peic, X. Chen, J. Michl, T. Vossmeyer, A. Yasuda, *J. Phys. Chem. C* **2007**, *114*, 12855–12859.

[79] Wang, X. Shi, N. N. Kariuki, M. Schadt, G. R. Wang, Q. Rendeng, J. Choi, J. Luo, S. Lu, C.-J. Zhong, *J. Am. Chem. Soc.* **2007**, *129*, 2161–2170.

[80] L. J. Hubble, J. S. Cooper, A. Sosa-Pintos, H. Kiiveri, E. Chow, M. S. Webster, L. Wieczorek, B. Raguse, *ACS Comb. Sci.* **2015**, *17*, 120–129.

[81] G. M. Shepherd, *Nature* **2006**, *444*, 316–321.

[82] W. R. Collin, G. Serrano, L. K. Wright, H. Chang, N. Nuñovero, E. T. Zellers, *Anal. Chem.* **2014**, *86*, 655–663.

[83] S. K. Kim, H. Chang, E. T. Zellers, *Anal. Chem.* **2011**, *83*, 7198–7206.

[84] M. K. Nakhleh, Y. Y. Broza, H. Haick, *Nanomedicine* **2014**, *9*, 1991–2002.

[85] B. Shan, Y. Y. Broza, W. Li, Y. Wang, S. Wu, Z. Liu, J. Wang, S. Gui, L. Wang, Z. Zhang, W. Liu, S. Zhou, W. Jin, Q. Zhang, D. Hu, L. Lin, Q. Zhang, W. Li, J. Wang, H. Liu, Y. Pan, H. Haick, *ACS Nano* **2020**, *14*, 12125–12132.

[86] W. Hu, L. Wan, Y. Jian, C. Ren, K. Jin, X. Su, X. Bai, H. Haick, M. Yao, W. Wu, *Adv. Mater. Technol.* **2018**, 1800488.

[87] K.-H. Müller, E. Chow, L. Wieczorek, B. Raguse, J. S. Cooper, L. J. Hubble, *Phys. Chem. Chem. Phys.* **2011**, *13*, 18208–18216.

[88] M. Ancona, A. Snow, F. Perkins, B. Pate, D. Park, *Sens. Actuator B Chem.* **2013**, *177*, 936–946.

[89] W. Zhao, L. F. Al-Nasser, S. Shan, J. Li, Z. Skeete, N. Kang, J. Luo, S. Lu, C.-J. Zhong, C. J. Grausgruber, R. Harris, *Sens. Actuator B Chem.* **2016**, *232*, 292–299.

[90] X. Shi, S. Lu, L. Wang, J. Luo, C.-J. Zhong in IIE Annual Conference Proceedings, **2006**, pp. 1–6.

[91] J. Luo, J. Luo, L. Wang, X. Shi, J. Yin, E. Crew, S. Lu, L. M. Lesperance, C.-J. Zhong, *Sens. Actuator. B Chem.* **2012**, *161*, 845–854.

[92] K. S. Novoselov, A. K. Geim, S. V. Morozov, D. Jiang, Y. Zhang, S. V. Dubonos, I. V. Grigorieva, A. A. Firsov, *Science* **2004**, *306*, 666–669.

[93] A. K. Geim, K. S. Novoselov, *Nature Mater.* **2007**, *6*, 183–191.

[94] O. C. Compton, S. T. Nguyen, *Small* **2010**, *6*, 711–723.

[95] C. Cheng, S. Li, A. Thomas, N. A. Kotov, R. Haag, *Chem. Rev.* **2017**, *117*, 1826–1914.

[96] Y. Zhu, S. Murali, W. Cai, X. Li, J. W. Suk, J. R. Potts, R. S. Ruoff, *Adv. Mater.* **2010**, *22*, 3906–3924.

[97] P. P. Brisebois, M. Siaj, *J. Mater. Chem. C* **2020**, *8*, 1517–1547.

[98] S. Eigler, A. Hirsch, *Angew. Chem. Int. Ed.* **2014**, *53*, 7720–7738.

[99] C. Petit, J. Burress, T. J. Bandosz, *Carbon* **2011**, *49*, 563–572.

[100] X. Li, W. Qi, D. Mei, M. L. Sushko, I. Aksay, J. Liu, *Adv. Mater.* **2012**, *24*, 5136–5141.

[101] Y. Xia, R. Li, R. Chen, J. Wang, L. Xiang, *Sensors* **2018**, *18*, 1456.

[102] H.-P. Cong, J.-F. Chen, S.-H. Yu, *Chem. Soc. Rev.* **2014**, *43*, 7295–7325.

[103] T. Lee, S. H. Min, M. Gu, Y. K. Jung, W. Lee, J. U. Lee, D. G. Seong, B.-S. Kim, *Chem. Mater.* **2015**, *27*, 3785–3796.

[104] A. Lerf, H. He, M. Forster, J. Klinowski, *J. Phys. Chem. B* **1998**, *102*, 4477–4482.

[105] K. Erickson, R. Erni, Z. Lee, N. Alem, W. Gannett, A. Zettl, *Adv. Mater.* **2010**, *22*, 4467–4472.

[106] A. M. Dimiev, L. B. Alemany, J. M. Tour, *ACS Nano* **2013**, *7*, 576–588.

[107] B. C. Brodie, *Phil. Trans. R. Soc.* **1859**, *149*, 249–259.

[108] L. Staudenmaier, *Ber. Dtsch. Chem. Ges.* **1898**, *31*, 1481–1487.

[109] U. Hofmann, E. König, *Z. Anorg. Allg. Chem.* **1937**, *234*, 311–336.

[110] W. S. Hummers, R. E. Offeman, *J. Am. Chem. Soc.* **1958**, *80*, 1339–1339.

[111] A. M. Dimiev, J. M. Tour, *ACS Nano* **2014**, *8*, 3060–3068.

[112] D. C. Marcano, D. V. Kosynkin, J. M. Berlin, A. Sinitskii, Z. Sun, A. Slesarev, L. B. Alemany, W. Lu, J. M. Tour, *ACS Nano* **2010**, *4*, 4806–4814.

[113] J. Chen, Y. Li, L. Huang, C. Li, G. Shi, *Carbon* **2015**, *81*, 826–834.

[114] J. Chen, Y. Zhang, M. Zhang, B. Yao, Y. Li, L. Huang, C. Li, G. Shi, *Chem. Sci.* **2016**, *7*, 1874–1881.

[115] J.-J. Shao, W. Lv, Q.-H. Yang, *Adv. Mater.* **2014**, *26*, 5586–5612.

[116] I. Jung, D. A. Dikin, R. D. Piner, R. S. Ruoff, *Nano Lett.* **2008**, *8*, 4283–4287.

[117] S. Pei, H.-M. Cheng, *Carbon* **2012**, *50*, 3210–3228.

[118] C. Kiang Chua, M. Pumera, *Chem. Soc. Rev.* **2014**, *43*, 291–312.

[119] M. J. Fernández-Merino, L. Guardia, J. I. Paredes, S. Villar-Rodil, P. Solís-Fernández, A. Martínez-Alonso, J. M. D. Tascón, *J. Phys. Chem. C* **2010**, *114*, 6426–6432.

[120] D. D. Kulkarni, S. Kim, M. Chyasnavichyus, K. Hu, A. G. Fedorov, V. V. Tsukruk, *J. Am. Chem. Soc.* **2014**, *136*, 6546–6549.

[121] S. Pei, J. Zhao, J. Du, W. Ren, H.-M. Cheng, *Carbon* **2010**, *48*, 4466–4474.

[122] M. Acik, G. Lee, C. Mattevi, A. Pirkle, R. M. Wallace, M. Chhowalla, K. Cho, Y. Chabal, *J. Phys. Chem. C* **2011**, *115*, 19761–19781.

[123] A. V. Dolbin, M. V. Khlistyuck, V. B. Esel'son, V. G. Gavrilko, N. A. Vinnikov, R. M. Basnukaeva, I. Maluenda, W. K. Maser, A. M. Benito, *Applied Surface Science* **2016**, *361*, 213–220.

[124] X. Gao, J. Jang, S. Nagase, *J. Phys. Chem. C* **2010**, *114*, 832–842.

[125] R. Larciprete, S. Fabris, T. Sun, P. Lacovig, A. Baraldi, S. Lizzit, *J. Am. Chem. Soc.* **2011**, *133*, 17315–17321.

[126] Y. H. Ding, P. Zhang, Q. Zhuo, H. M. Ren, Z. M. Yang, Y. Jiang, *Nanotechnology* **2011**, *22*, 215601.

[127] H. Li, C. Bubeck, *Macromol. Res.* **2013**, *21*, 290–297.

[128] M. Koinuma, C. Ogata, Y. Kamei, K. Hatakeyama, H. Tateishi, Y. Watanabe, T. Taniguchi, K. Gezuhara, S. Hayami, A. Funatsu, M. Sakata, Y. Kuwahara, S. Kurihara, Y. Matsumoto, *J. Phys. Chem. C* **2012**, *116*, 19822–19827.

[129] Y. Matsumoto, M. Koinuma, S. Ida, S. Hayami, T. Taniguchi, K. Hatakeyama, H. Tateishi, Y. Watanabe, S. Amano, *J. Phys. Chem. C* **2011**, *115*, 19280–19286.

[130] Y. H. Ng, A. Iwase, N. J. Bell, A. Kudo, R. Amal, *Catal. Today* **2011**, *164*, 353–357.

[131] O. Akhavan, *Carbon* **2011**, *49*, 11–18.

[132] Q. Guo, C. Zhou, Z. Ma, X. Yang, *Adv. Mater.* **2019**, *31*, 1901997.

[133] J. Schneider, M. Matsuoka, M. Takeuchi, J. Zhang, Y. Horiuchi, M. Anpo, D. W. Bahnemann, *Chem. Rev.* **2014**, *114*, 9919–9986.

[134] Y. Lan, Y. Lu, Z. Ren, *Nano Energy* **2013**, *2*, 1031–1045.

[135] Y. Ma, X. Wang, Y. Jia, X. Chen, H. Han, C. Li, *Chem. Rev.* **2014**, *114*, 9987–10043.

[136] A. Di Paola, M. Bellardita, L. Palmisano, *Catalysts* **2013**, *3*, 36–73.

[137] D. Reyes-Coronado, G. Rodríguez-Gattorno, M. E. Espinosa-Pesqueira, C. Cab, R. De Coss, G. Oskam, *Nanotechnology* **2008**, *19*, 145605.

[138] S. Liu, J. Yu, M. Jaroniec, *Chem. Mater.* **2011**, *23*, 4085–4093.

[139] T. R. Gordon, M. Cargnello, T. Paik, F. Mangolini, R. T. Weber, P. Fornasiero, C. B. Murray, *J. Am. Chem. Soc.* **2012**, *134*, 6751–6761.

[140] T. A. Kandiel, L. Robben, A. Alkaim, D. Bahnemann, *Photochem. Photobiol. Sci.* **2013**, *12*, 602–609.

[141] G. Williams, B. Seger, P. V. Kamat, *ACS Nano* **2008**, *2*, 1487–1491.

[142] X. Zhao, Z. Wang, Y. Xie, H. Xu, J. Zhu, X. Zhang, W. Liu, G. Yang, J. Ma, Y. Liu, *Small* **2018**, *14*, 1801325.

[143] X. Cai, R. Ma, T. C. Ozawa, N. Sakai, A. Funatsu, T. Sasaki, *Nanoscale* **2014**, *6*, 14419–14427.

[144] B. Li, X. Zhang, X. Li, L. Wang, R. Han, B. Liu, W. Zheng, X. Li, Y. Liu, *Chem. Commun.* **2010**, *46*, 3499.

[145] Q. Qu, H. Geng, R. Peng, Q. Cui, X. Gu, F. Li, M. Wang, *Langmuir* **2010**, *26*, 9539–9546.

[146] P. V. Kamat, I. Bedja, S. Hotchandani, *J. Phys. Chem.* **1994**, *98*, 9137–9142.

[147] N. J. Bell, Y. H. Ng, A. Du, H. Coster, S. C. Smith, R. Amal, *J. Phys. Chem. C* **2011**, *115*, 6004–6009.

[148] M. Hada, K. Miyata, S. Ohmura, Y. Arashida, K. Ichiyanagi, I. Katayama, T. Suzuki, W. Chen, S. Mizote, T. Sawa, T. Yokoya, T. Seki, J. Matsuo, T. Tokunaga, C. Itoh, K. Tsuruta, R. Fukaya, S. Nozawa, S.-i. Adachi, J. Takeda, K. Onda, S.-y. Koshihara, Y. Hayashi, Y. Nishina, *ACS Nano* **2019**, *13*, 10103–10112.

[149] H.-B. Yao, L.-H. Wu, C.-H. Cui, H.-Y. Fang, S.-H. Yu, *J. Mater. Chem.* **2010**, *20*, 5190.

[150] G. Panzarasa, G. Soliveri, *Appl. Sci.* **2019**, *9*, 1266.

[151] L. Zhang, S. Diao, Y. Nie, K. Yan, N. Liu, B. Dai, Q. Xie, A. Reina, J. Kong, Z. Liu, *J. Am. Chem. Soc.* **2011**, *133*, 2706–2713.

[152] C. Lv, C. Hu, J. Luo, S. Liu, Y. Qiao, Z. Zhang, J. Song, Y. Shi, J. Cai, A. Watanabe, *Nanomaterials* **2019**, *9*, 422.

[153] R. Liang, A. Luo, Z. Zhang, Z. Li, C. Han, W. Wu, *Sensors* **2020**, *20*, 5601.

[154] F. Fauzi, A. Rianjanu, I. Santoso, K. Triyana, *Sens. Actuator A: Phys.* **2021**, *330*, 112837.

[155] S. Chen, K. Jiang, Z. Lou, D. Chen, G. Shen, *Adv. Mater. Technol.* **2018**, *3*, 1700248.

[156] E. Singh, M. Meyyappan, H. S. Nalwa, *ACS Appl. Mater. Interfaces* **2017**, *9*, 34544–34586.

[157] L. Guo, H.-B. Jiang, R.-Q. Shao, Y.-L. Zhang, S.-Y. Xie, J.-N. Wang, X.-B. Li, F. Jiang, Q.-D. Chen, T. Zhang, H.-B. Sun, *Carbon* **2012**, *50*, 1667–1673.

[158] N. D. K. Tu, J. Choi, C. R. Park, H. Kim, *Chem. Mater.* **2015**, *27*, 7362–7369.

[159] W. Gao, N. Singh, L. Song, Z. Liu, A. L. M. Reddy, L. Ci, R. Vajtai, Q. Zhang, B. Wei, P. M. Ajayan, *Nature Nanotech.* **2011**, *6*, 496–500.

[160] I. Jung, D. Dikin, S. Park, W. Cai, S. L. Mielke, R. S. Ruoff, *J. Phys. Chem. C* **2008**, *112*, 20264–20268.

[161] B.-H. Wee, W.-H. Khoh, A. K. Sarker, C.-H. Lee, J.-D. Hong, *Nanoscale* **2015**, *7*, 17805–17811.

[162] V. I. Popov, D. V. Nikolaev, V. B. Timofeev, S. A. Smagulova, I. V. Antonova, *Nanotechnology* **2017**, *28*, 355501.

[163] C. Anichini, A. Aliprandi, S. M. Gali, F. Liscio, V. Morandi, A. Minoia, D. Beljonne, A. Ciesielski, P. Samorì, *ACS Appl. Mater. Interfaces* **2020**, *12*, 44017–44025.

[164] Y. Wang, L. Zhang, Z. Zhang, P. Sun, H. Chen, *Langmuir* **2020**, *36*, 9443–9448.

[165] K. Hatakeyama, M. R. Karim, C. Ogata, H. Tateishi, A. Funatsu, T. Taniguchi, M. Koinuma, S. Hayami, Y. Matsumoto, *Angew. Chem. Int. Ed.* **2014**, *53*, 6997–7000.

[166] X. Wang, Z. Xiong, Z. Liu, T. Zhang, *Adv. Mater.* **2015**, *27*, 1370–1375.

[167] Q. Fatima, A. A. Haidry, Z. Yao, Y. He, Z. Li, L. Sun, L. Xie, *Nanoscale Adv.* **2019**, *1*, 1319–1330.

[168] A. A. Haidry, Z. Wang, Q. Fatima, A. Zavabeti, L. Xie, H. Zhu, Z. Li, *Appl. Surf. Sci.* **2020**, *531*, 147285.

[169] S. Yang, C. Jiang, S.-h. Wei, *Appl. Phys. Rev.* **2017**, *4*, 021304.

[170] B. Kulyk, B. F. R. Silva, A. F. Carvalho, P. Barbosa, A. V. Girão, J. Deuermeier, A. J. S. Fernandes, F. M. L. Figueiredo, E. Fortunato, F. M. Costa, *Adv. Mater. Technol.* **2022**, *7*, 2101311.

[171] K. Zhou, W. Xu, Y. Yu, W. Zhai, Z. Yuan, K. Dai, G. Zheng, L. Mi, C. Pan, C. Liu, C. Shen, *Small* **2021**, *17*, 2100542.

[172] F. Schedin, A. K. Geim, S. V. Morozov, E. W. Hill, P. Blake, M. I. Katsnelson, K. S. Novoselov, *Nature Mater.* **2007**, *6*, 652–655.

[173] J. T. Robinson, F. K. Perkins, E. S. Snow, Z. Wei, P. E. Sheehan, *Nano Lett.* **2008**, *8*, 3137–3140.

[174] H. Park, H. Ahn, Y. Chung, S. Baek Cho, Y. Soo Yoon, D.-J. Kim, *Mater. Lett.* **2014**, *136*, 164–167.

[175] M. K. Rabchinskii, V. V. Sysoev, O. E. Glukhova, M. Brzhezinskaya, D. Y. Stolyarova, A. S. Varezhnikov, M. A. Solomatin, P. V. Barkov, D. A. Kirilenko, S. I. Pavlov, M. V. Baidakova, V. V. Shnitov, N. S. Struchkov, D. Y. Nefedov, A. O. Antonenko, P. Cai, Z. Liu, P. N. Brunkov, *Adv. Mater. Technol.* **2022**, *7*, 2101250.

[176] E. Lee, D. Lee, J. Yoon, Y. Yin, Y. N. Lee, S. Uprety, Y. S. Yoon, D.-J. Kim, *Sensors* **2018**, *18*, 3334.

[177] Y. Joseph, B. Guse, T. Vossmeyer, A. Yasuda, *J. Phys. Chem. C* **2008**, *112*, 12507–12514.

[178] S. C. Bittinger, MA thesis, University of Hamburg, **2019**.

[179] G. Peng, U. Tisch, O. Adams, M. Hakim, N. Shehada, Y. Y. Broza, S. Billan, R. Abdah-Bortnyak, A. Kuten, H. Haick, *Nat. Nanotechnol.* **2009**, *4*, 669–673.

[180] O. Barash, N. Peled, F. R. Hirsch, H. Haick, *Small* **2009**, *5*, 2618–2624.

[181] J. Wang, L. Kong, Z. Guo, J. Xu, J. Liu, *J. Mater. Chem.* **2010**, *20*, 5271.

[182] M. Haiducu, M. Rahbar, I. G. Foulds, R. W. Johnstone, D. Sameoto, M. Parameswaran, *J. Micromech. Microeng.* **2008**, *18*, 115029.

[183] M. Brust, D. J. Schiffrin, D. Bethell, C. J. Kiely, *Adv. Mater.* **1995**, *7*, 795–797.

[184] H. Schlicke, PhD thesis, University of Hamburg, **2017**.

[185] N. Kahn, O. Lavie, M. Paz, Y. Segev, H. Haick, *Nano Lett.* **2015**, *15*, 7023–7028.

[186] U. Yaqoob, M. I. Younis, *Sensors* **2021**, *21*, 2877.

[187] R. A. Potyrailo, J. Brewer, B. Cheng, M. A. Carpenter, N. Houlihan, A. Kolmakov, *Faraday Discuss.* **2020**, *223*, 161–182.

[188] T. Ung, L. M. Liz-Marzán, P. Mulvaney, *J. Phys. Chem. B* **2001**, *105*, 3441–3452.

[189] N. Olichwer, T. Koschine, A. Meyer, W. Egger, K. Rätzke, T. Vossmeyer, *RSC Adv.* **2016**, *6*, 113163–113172.

[190] H. Rieley, G. K. Kendall, F. W. Zemicael, T. L. Smith, S. Yang, *Langmuir* **1998**, *14*, 5147–5153.

[191] Y. Joseph, B. Guse, G. Nelles, *Chem. Mater.* **2009**, *21*, 1670–1676.

[192] Y. Daskal, S. Rabe, R. Dittrich, C. Oestreich, Y. Joseph in Proceedings, MDPI, **2018**, p. 933.

[193] D. Kou, W. Ma, S. Zhang, B. Tang, *ACS Appl. Polym. Mater.* **2020**, *2*, 2–11.

[194] C. Geiger, J. Reitenbach, L. P. Kreuzer, T. Widmann, P. Wang, R. Cubitt, C. Henschel, A. Laschewsky, C. M. Papadakis, P. Müller-Buschbaum, *Macromolecules* **2021**, *54*, 3517–3530.

[195] F Perrozzi, S Prezioso, L Ottaviano, *J. Phys.: Condens. Matter* **2015**, *27*, 013002.

[196] J. Struck, MA thesis, University of Hamburg, Hamburg, **2021**.

[197] S. Benthien, BA Thesis, University of Hamburg, Hamburg, **2022**.

[198] B. Konkena, S. Vasudevan, *J. Phys. Chem. Lett.* **2012**, *3*, 867–872.

[199] S. Stankovich, R. D. Piner, S. T. Nguyen, R. S. Ruoff, *Carbon* **2006**, *44*, 3342–3347.

[200] ICSD, ICSD Database Entry 364, Brookite, DOI: 10.1002/Zaac.19764200104.

[201] ICSD, ICSD Database Entry 9852, Anatase, DOI: 10.1524/Zkri.1972.136.3-4.273.

[202] R. Buonsanti, V. Grillo, E. Carlino, C. Giannini, T. Kipp, R. Cingolani, P. D. Cozzoli, *J. Am. Chem. Soc.* **2008**, *130*, 11223–11233.

[203] A. Hensel, C. J. Schröter, H. Schlicke, N. Schulz, S. Riekeberg, H. K. Trieu, A. Stierle, H. Noei, H. Weller, T. Vossmeyer, *Nanomaterials* **2019**, *9*, 1230.

[204] A. Mills, S.-K. Lee, A. Lepre, I. P. Parkin, S. A. O'Neill, *Photochem. Photobiol. Sci.* **2002**, *1*, 865–868.

[205] J. I. Paredes, S. Villar-Rodil, A. Martínez-Alonso, J. M. D. Tascón, *Langmuir* **2008**, *24*, 10560–10564.

[206] O. Akhavan, E. Ghaderi, *J. Phys. Chem. C* **2009**, *113*, 20214–20220.

[207] Y. Pellegrin, F. Odobel, *C. R. Chim.*, Artificial Photosynthesis / La Photosynthèse Artificielle **2017**, *20*, 283–295.

[208] H. Yang, H. Amari, L. Liu, C. Zhao, H. Gao, A. He, N. D. Browning, M. A. Little, R. Sebastian Sprick, A. I. Cooper, *Nanoscale* **2020**, *12*, 24488–24494.

[209] Z. Li, S. Cong, X. Xu, *ACS Catal.* **2014**, *4*, 3273–3280.

[210] O. Akhavan, M. Abdolahad, A. Esfandiar, M. Mohatashamifar, *J. Phys. Chem. C* **2010**, *114*, 12955–12959.

[211] E. J. Radich, A. L. Krenselewski, J. Zhu, P. V. Kamat, *Chem. Mater.* **2014**, *26*, 4662–4668.

[212] J. Tian, Z. Zhao, A. Kumar, R. I. Boughton, H. Liu, *Chem. Soc. Rev.* **2014**, *43*, 6920–6937.

[213] J. Zhang, P. Zhou, J. Liu, J. Yu, *Phys. Chem. Chem. Phys.* **2014**, *16*, 20382–20386.

[214] P. K. Dubey, P. Tripathi, R. S. Tiwari, A. S. K. Sinha, O. N. Srivastava, *Int. J. Hydrog. Energy* **2014**, *39*, 16282–16292.

[215] O. O. Kapitanova, G. N. Panin, H. D. Cho, A. N. Baranov, T. W. Kang, *Nanotechnology* **2017**, *28*, 204005.

[216] M.-C. Chen, C.-L. Hsu, T.-J. Hsueh, *IEEE Electron Device Lett.* **2014**, *35*, 590–592.

[217] N. Agmon, *Chem. Phys. Lett.* **1995**, *244*, 456–462.

[218] P. He, J. R. Brent, H. Ding, J. Yang, D. J. Lewis, P. O'Brien, B. Derby, *Nanoscale* **2018**, *10*, 5599–5606.

[219] E. Mansour, R. Vishinkin, S. Rihet, W. Saliba, F. Fish, P. Sarfati, H. Haick, *Sens. Actuator B: Chem.* **2020**, *304*, 127371.

[220] G. Sauerbrey, *Z. Physik* **1959**, *155*, 206–222.

[221] M. Thommes, K. Kaneko, A. V. Neimark, J. P. Olivier, F. Rodriguez-Reinoso, J. Rouquerol, K. S. Sing, *Pure Appl. Chem.* **2015**, *87*, 1051–1069.

[222] J. P. M. Lommerse, S. L. Price, R. Taylor, *J. Comput. Chem.* **1997**, *18*, 757–774.

[223] Y. Wang, Z. Li, C. Tang, H. Ren, Q. Zhang, M. Xue, J. Xiong, D. Wang, Q. Yu, Z. He, F. Wei, J. Jiang, *Environ. Sci.: Nano* **2019**, *6*, 3113–3122.

[224] W. Haiss, N. T. K. Thanh, J. Aveyard, D. G. Fernig, *Anal. Chem.* **2007**, *79*, 4215–4221.

[225] Agilent-Technologies, Agilent E5100A/B Network Analyzer Programming Manual.

[226] Sigma-Aldrich, Safety Data Sheet, Oleylamine Technical Grade, 70% (27.03.2023).

[227] Merck, Microchemicals Safety Data Sheet, AZ MIF 726, Product No. 697333 (27.03.2023), **2023**.

[228] Merck, Microchemicals Safety Data Sheet, ECI 3012, Product No. 211724 (27.03.2023), **2023**.

[229] Merck, Microchemicals Safety Data Sheet, AZ nLOF 2020, Product No. 583503 (27.03.2023), **2023**.

[230] TECHNIC, Safety Data Sheet, TechniStrip NI555, Product No. STD5028 (27.03.2023), **2023**.

A Appendix

A.1 Supplementary Data

A.1.1 DUV Radiation Source

A custom-built deep-UV (DUV) light source was used in different projects of this thesis. The light source consisted of 4 commercial low-pressure mercury vapor UVC fluorescent lamps (OSRAM HNS-L 18 W 2G11 FS1) in a close-packed arrangement with a tilt angle of 60°. Figure A.1 shows a photograph of the lamp and the lamp intensity spectrum with the main emission peak at 254 nm. The distance of the lamps to the thin films during irradiation was ~4 cm. The irradiance of the lamp at 254 nm was measured using a Thorlabs PM100 powermeter, equipped with a Thorlabs S120 UV sensor. The average irradiance was determined as ~520 mW/cm^2, and was recorded over a time period of 5 min, as shown in figure A.2. The irradiance data were kindly provided by Finn Dobschall, M.Sc., research associate and PhD student at University of Hamburg.

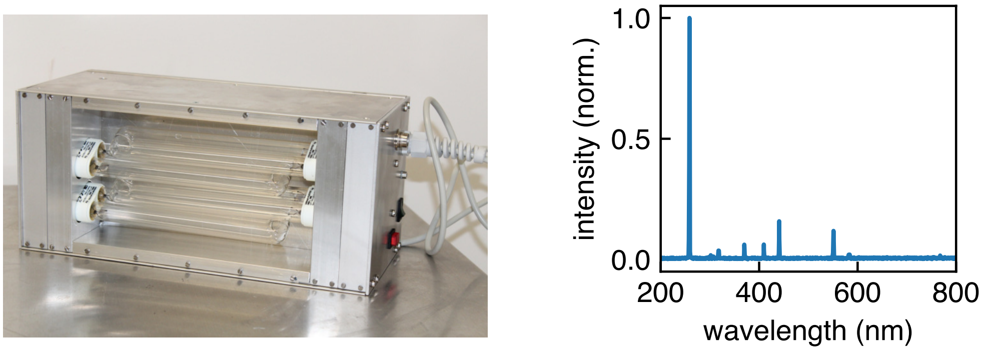

Figure A.1: (Left) Photograph of the custom-built DUV radiation source used for lithography, and for treatment of ADT/GNP- and GO/TNC-, and TNC-thin films for tuning of sensing properties. (Right) Normalized emission spectrum of DUV radiation source with a main emission peak at 254 nm and minor Hg-specific peaks at higher wavelengths.

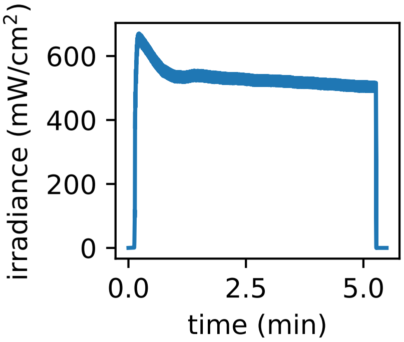

Figure A.2: Measured irradiance (254 nm) of custom-built DUV light source during 5 minutes.

A.1.2 Lithographically Patterned Chemiresistor Array: Timetraces

The following figures depict the baseline-corrected timetraces of the lithographically patterned and refunctionalized chemiresistor array (cf. figure 6.7) towards different analyte vapors at concentrations ranging from 50 to 8000 ppm. All plots are reprinted from the Supporting Information of Ref. [1] (©2021 American Chemical Society).

Water

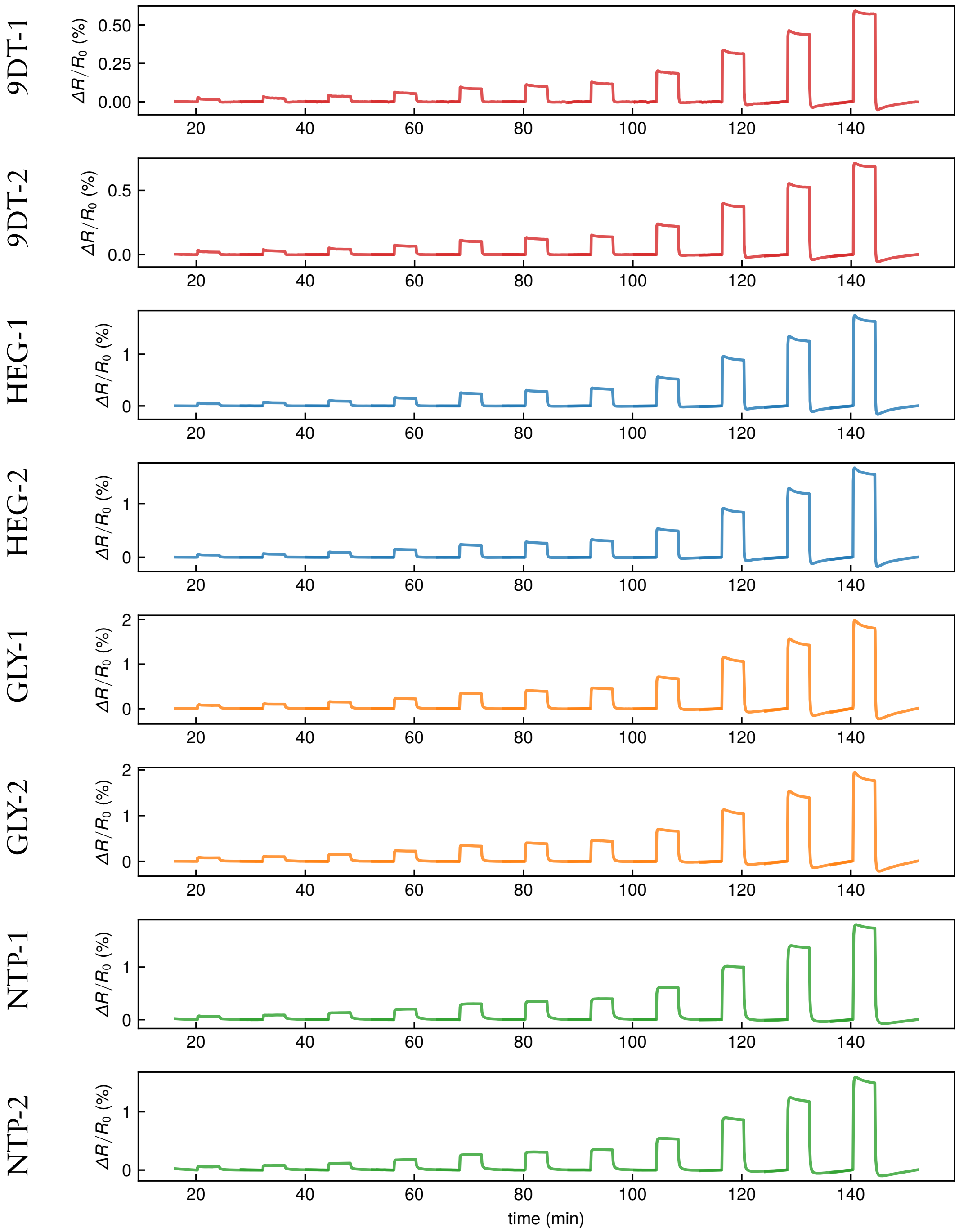

Figure A.3: Baseline corrected responses of the eight GNP chemiresistors to water at concentrations of 50, 100, 200, 400, 600, 800, 1000, 2000, 4000, 6000 and 8000 ppm.

Ethanol

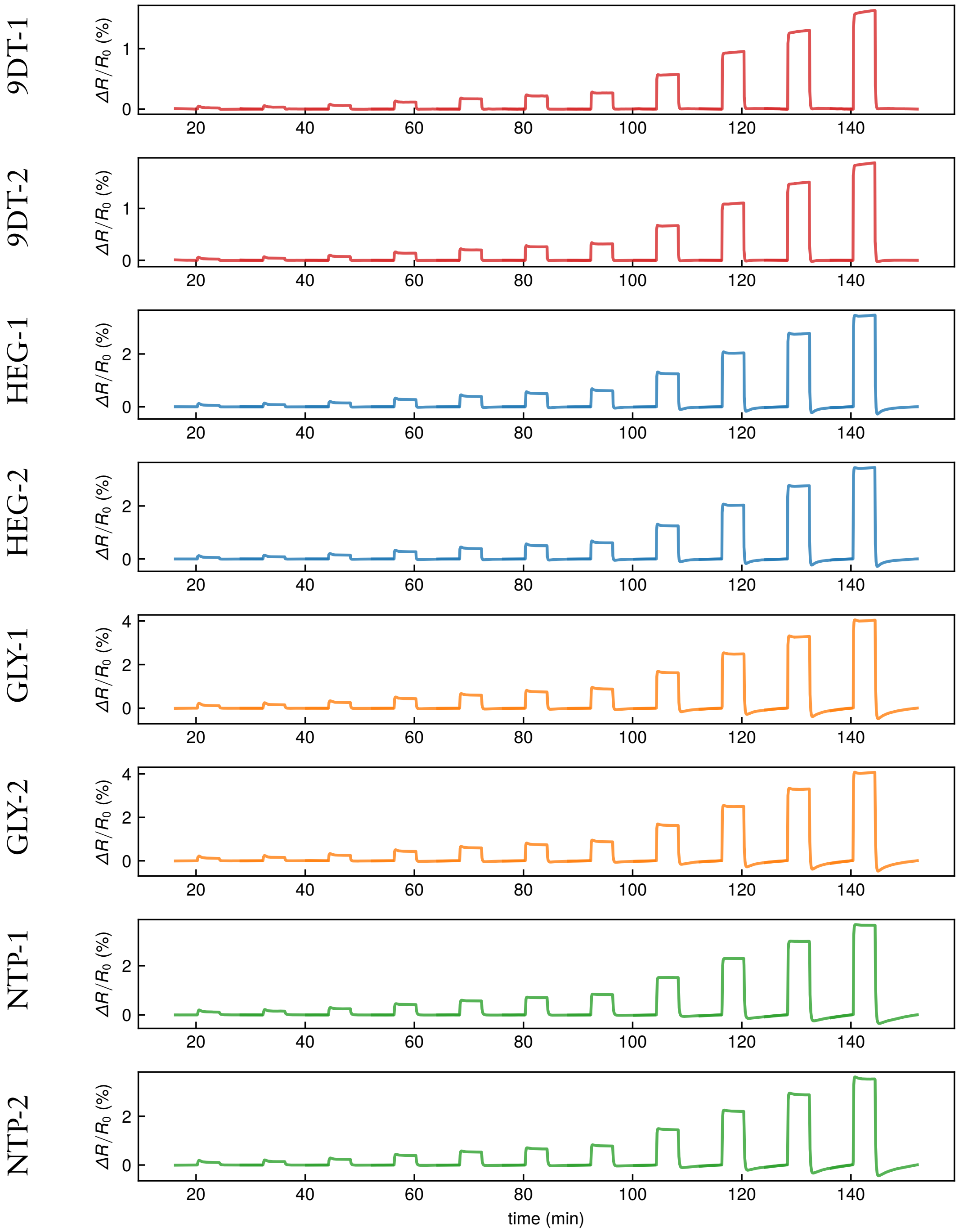

Figure A.4: Baseline corrected responses of the eight GNP chemiresistors to ethanol at concentrations of 50, 100, 200, 400, 600, 800, 1000, 2000, 4000, 6000 and 8000 ppm.

1-Propanol

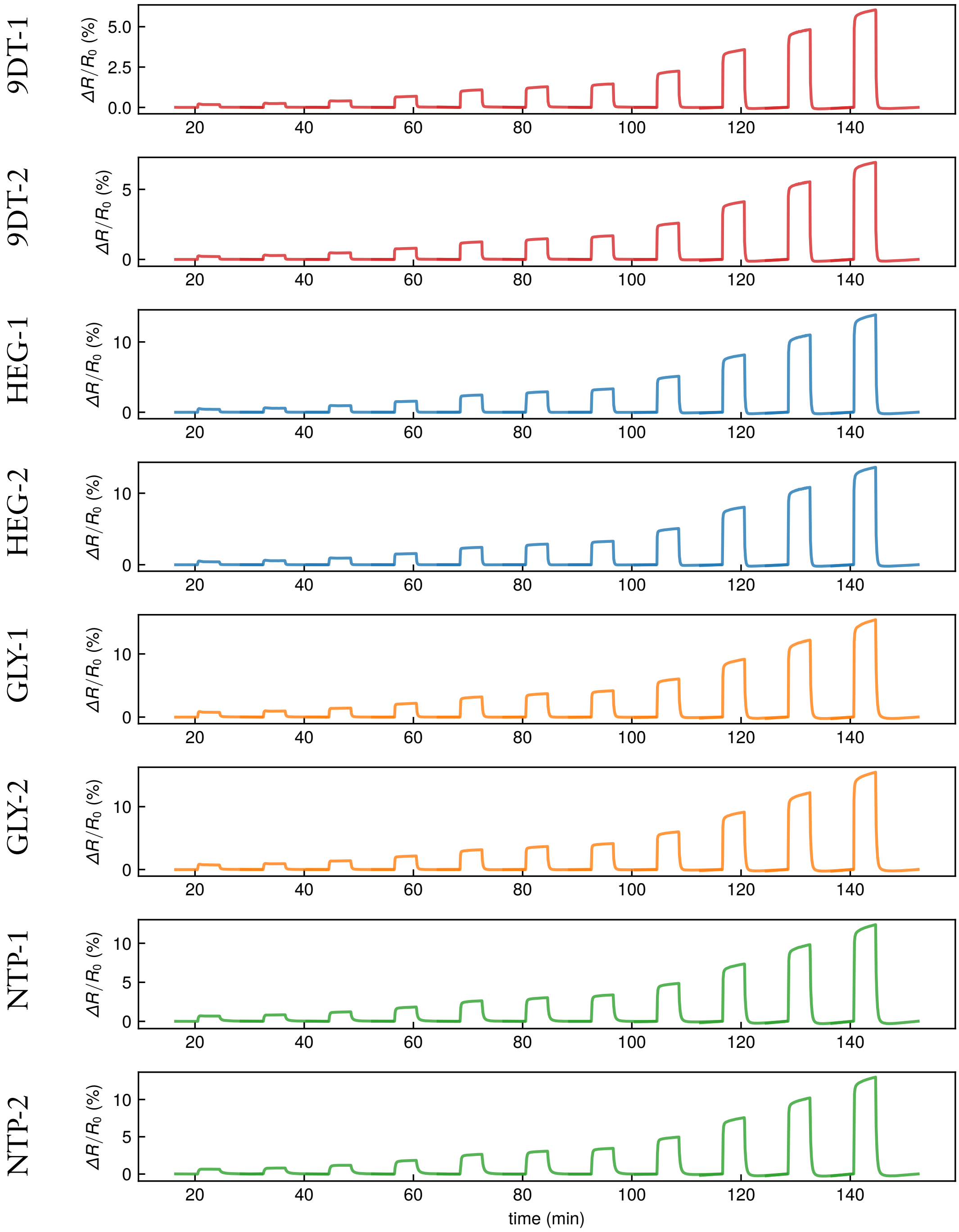

Figure A.5: Baseline corrected responses of the eight GNP chemiresistors to 1-propanol at concentrations of 50, 100, 200, 400, 600, 800, 1000, 2000, 4000, 6000 and 8000 ppm.

1-Butanol

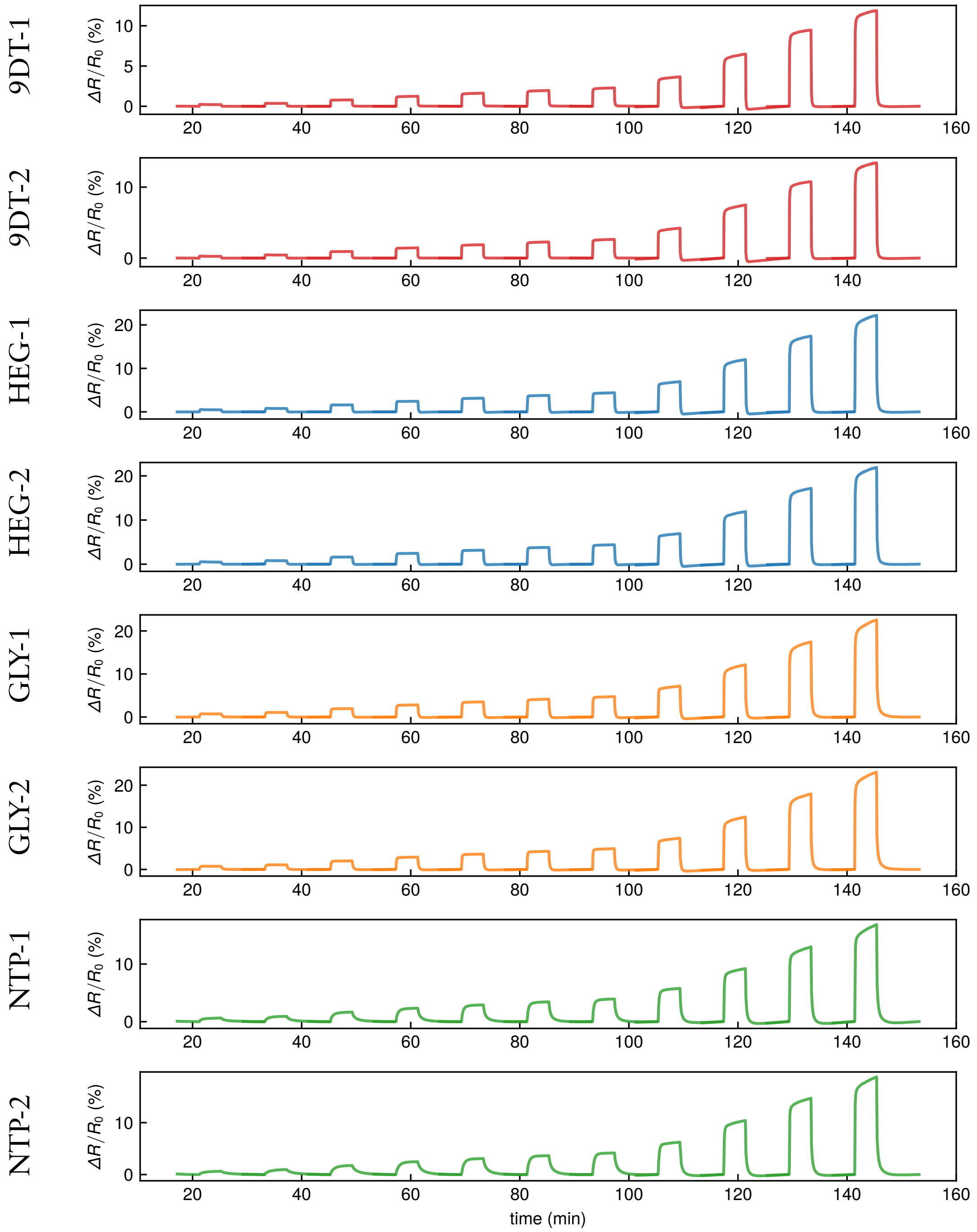

Figure A.6: Baseline corrected responses of the eight GNP chemiresistors to 1-butanol at concentrations of 50, 100, 200, 400, 600, 800, 1000, 2000, 4000, 6000 and 8000 ppm.

Toluene

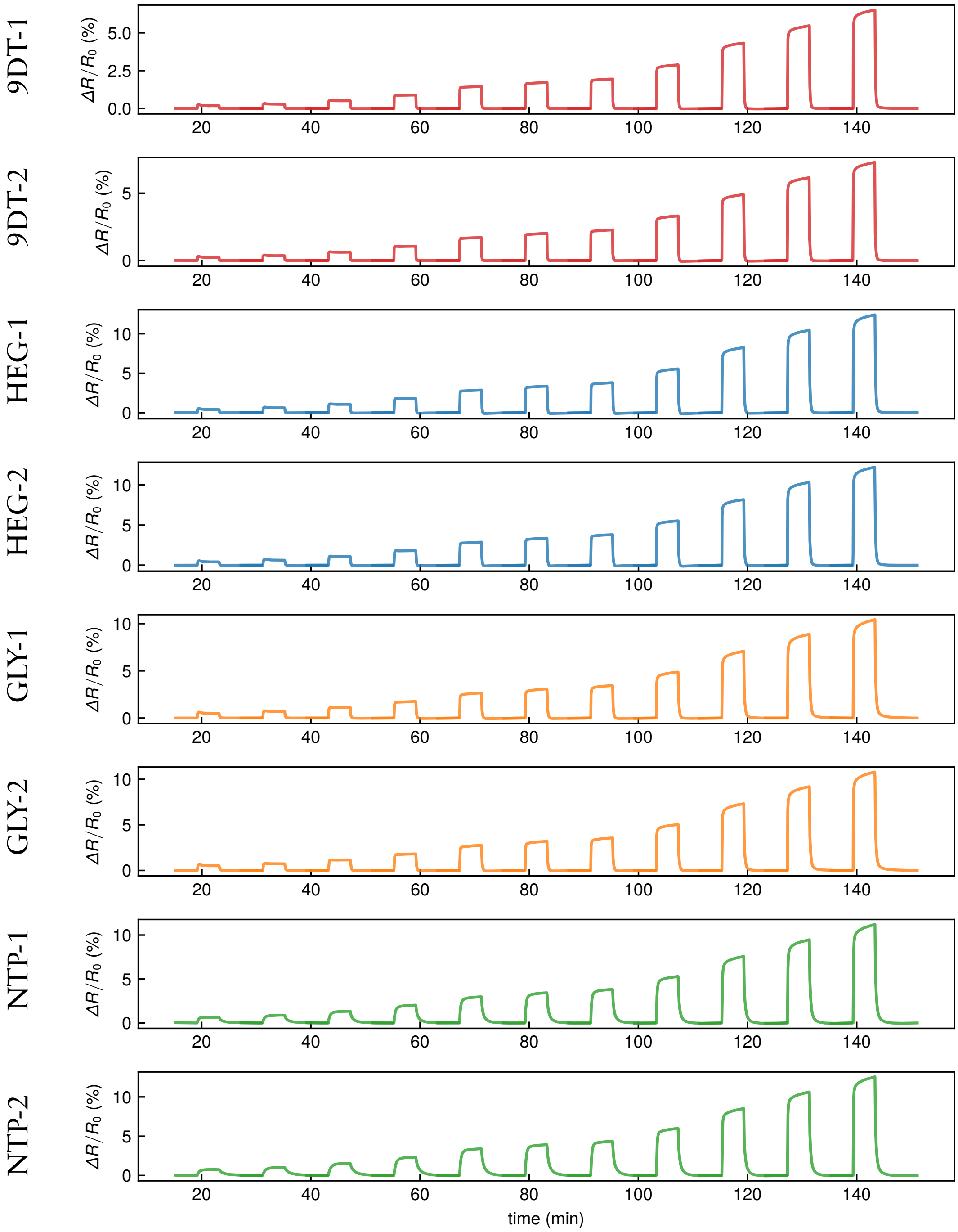

Figure A.7: Baseline corrected responses of the eight GNP chemiresistors to toluene at concentrations of 50, 100, 200, 400, 600, 800, 1000, 2000, 4000, 6000 and 8000 ppm.

MIBK

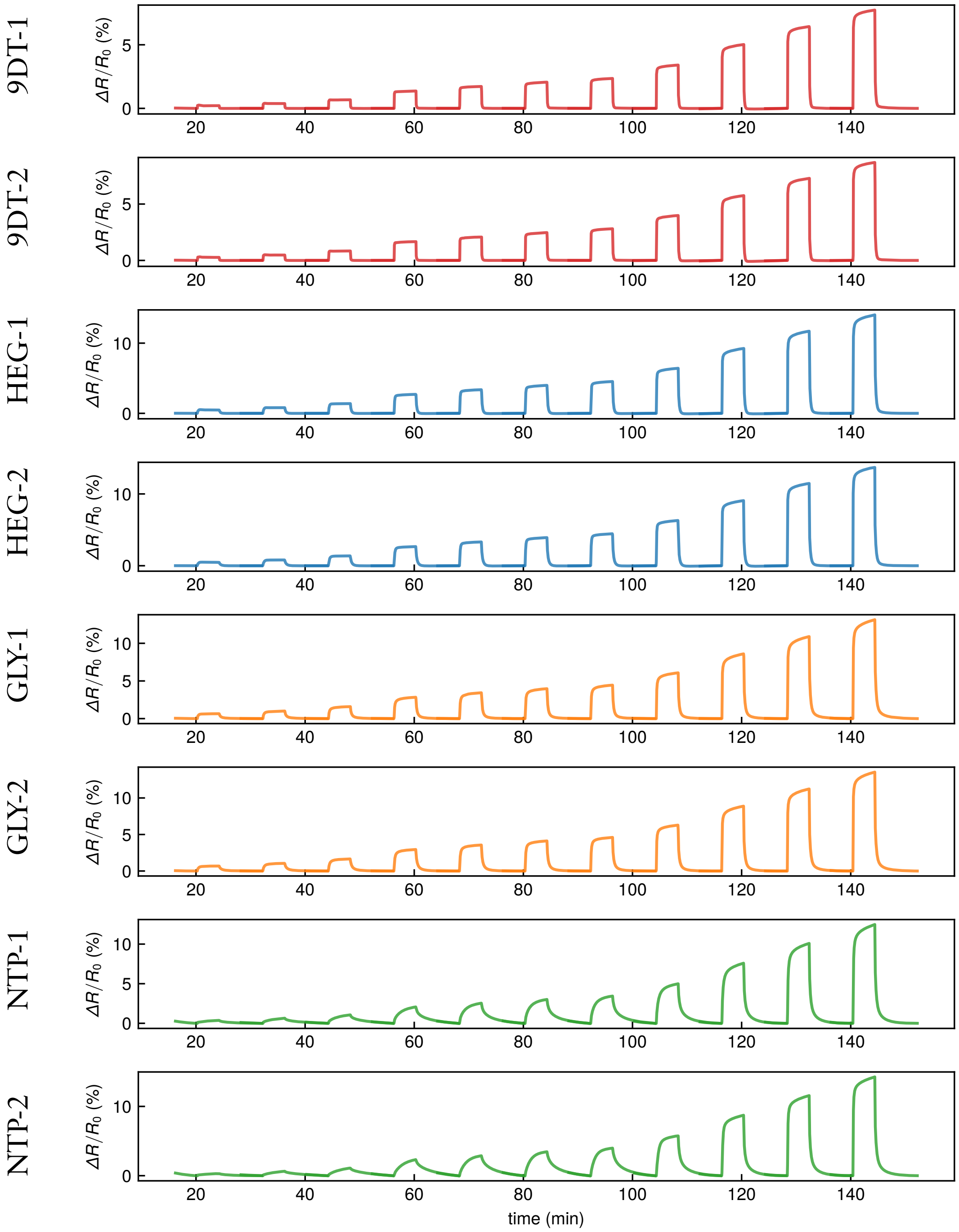

Figure A.8: Baseline corrected responses of the eight GNP chemiresistors to MIBK at concentrations of 50, 100, 200, 400, 600, 800, 1000, 2000, 4000, 6000 and 8000 ppm.

A.1.3 Tuned Response Kinetics: Timetraces

The following figures show all baseline-corrected response transients of the GNP/ADT chemiresistor array with adjusted response times (cf. figure 6.16) toward ten analyte vapors at concentrations of 100, 400, 800, 2000, 4000, 2000, 800, 400, 200, and 100 ppm for toluene, MIBK and 1-propanol, and 400, 800, 2000, 2000, 800, and 400 ppm for all other solvents. It is to note that one heptane exposure of 2000 ppm is missing due to an unexpected interruption of the measurement. All plots are reprinted from the Supporting Information of Ref. [3] (©2021 American Chemical Society).

4DT

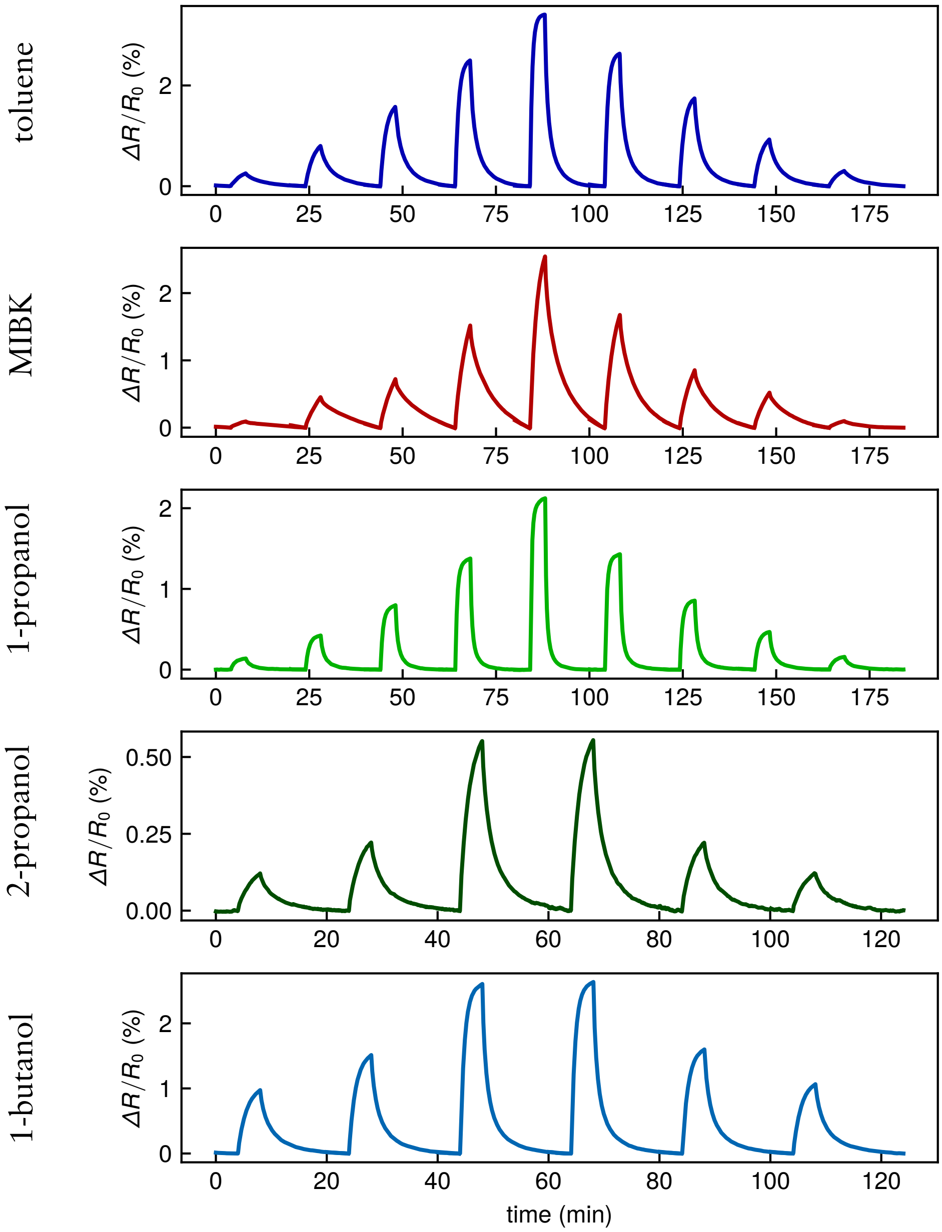

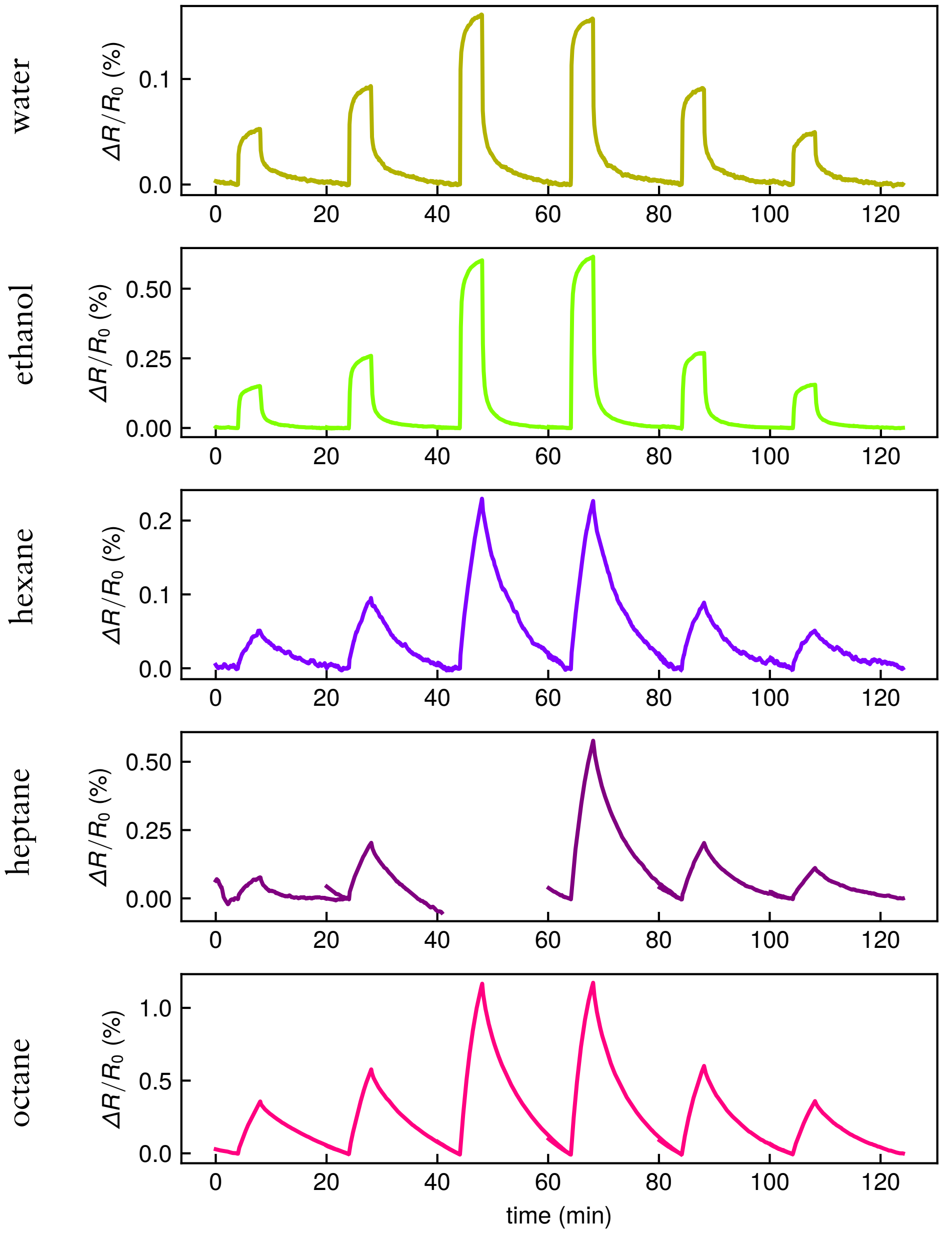

Figure A.9: Baseline corrected responses of a GNP/4DT chemiresistor to 10 different solvent vapors.

6DT

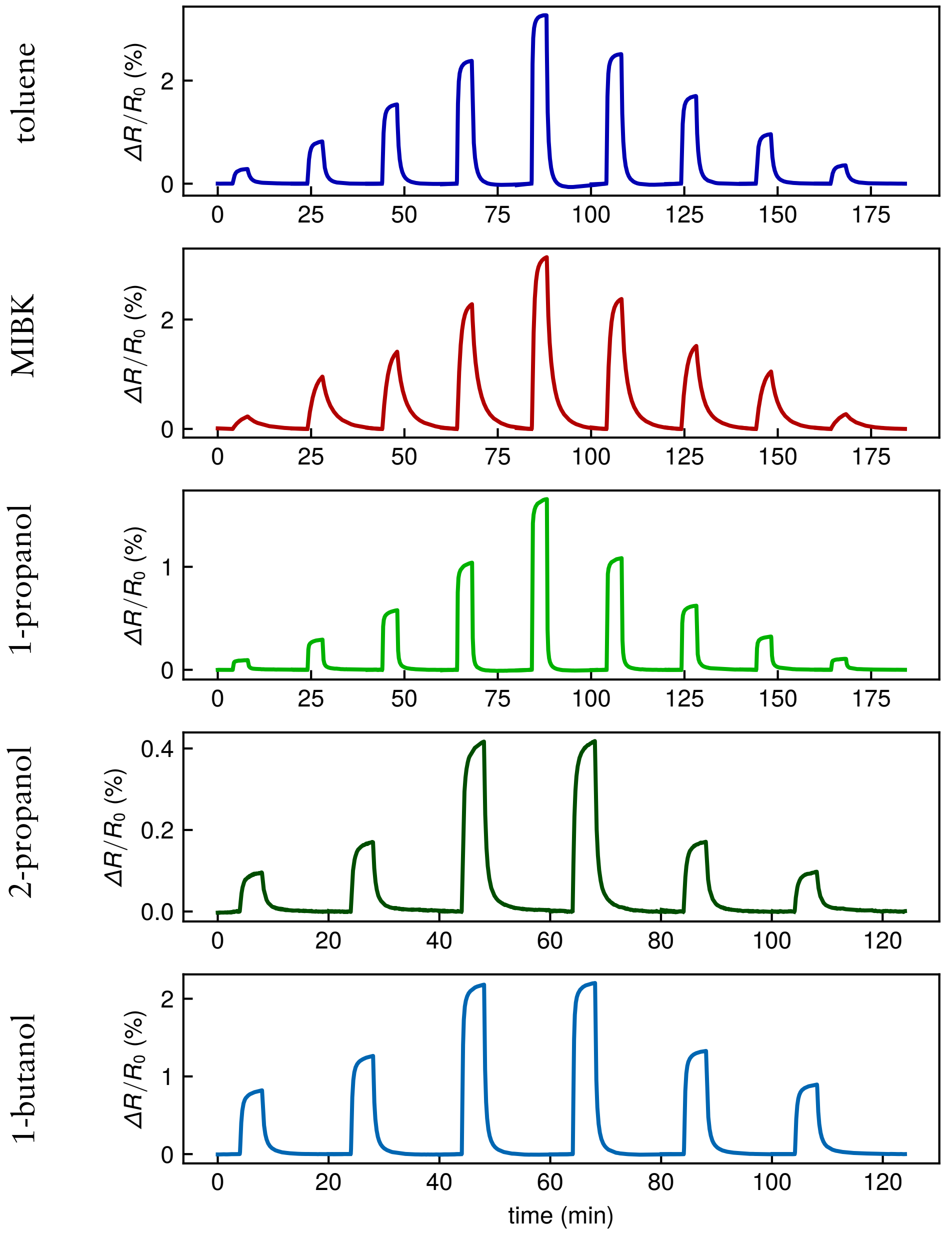
toluene
MIBK
1-propanol
2-propanol
1-butanol
ΔR/R₀ (%)
0
1
2
0.0
0.2
0.4
0
25
50
75
100
125
150
175
0
20
40
60
80
100
120
time (min)

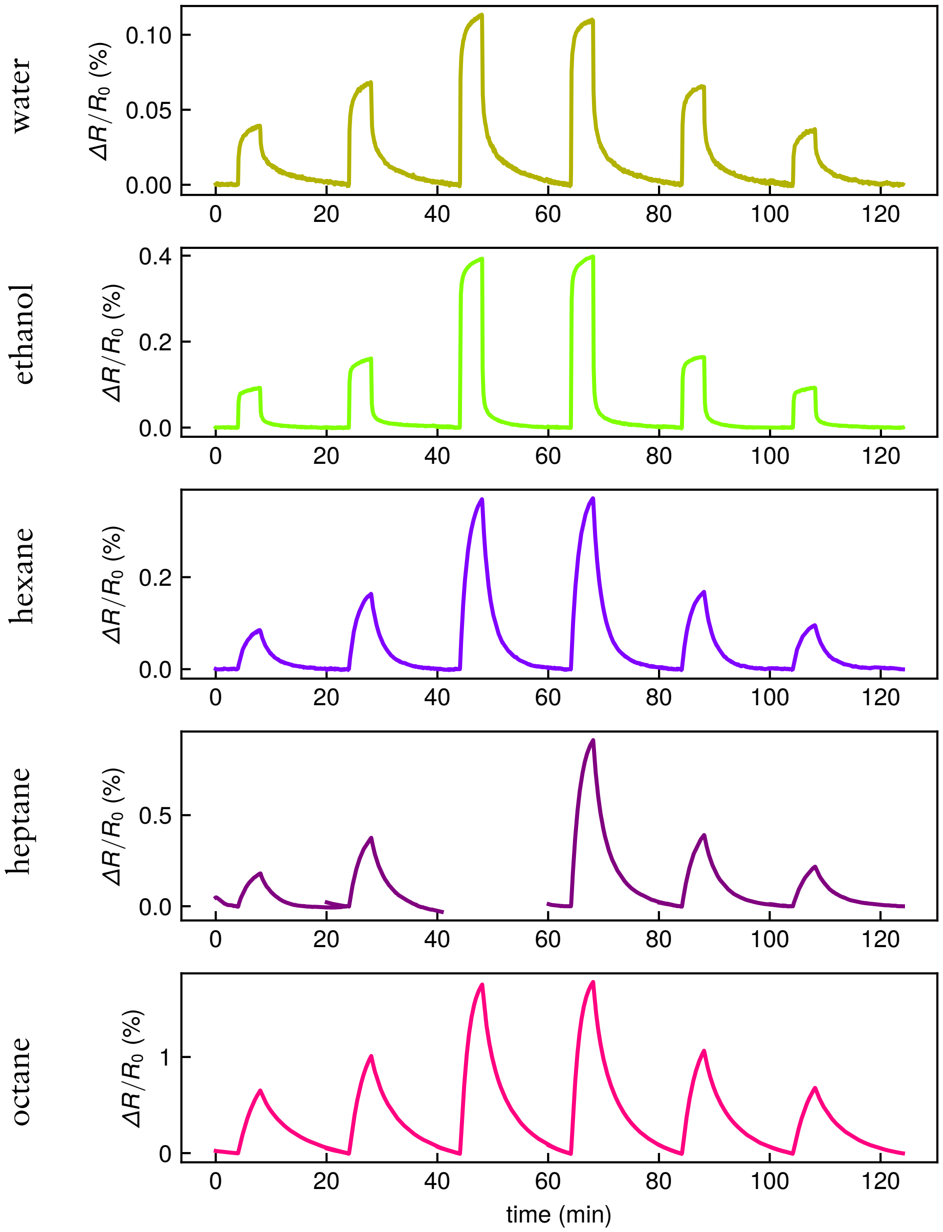

Figure A.10: Baseline corrected responses of a GNP/6DT chemiresistor to 10 different solvent vapors.

8DT

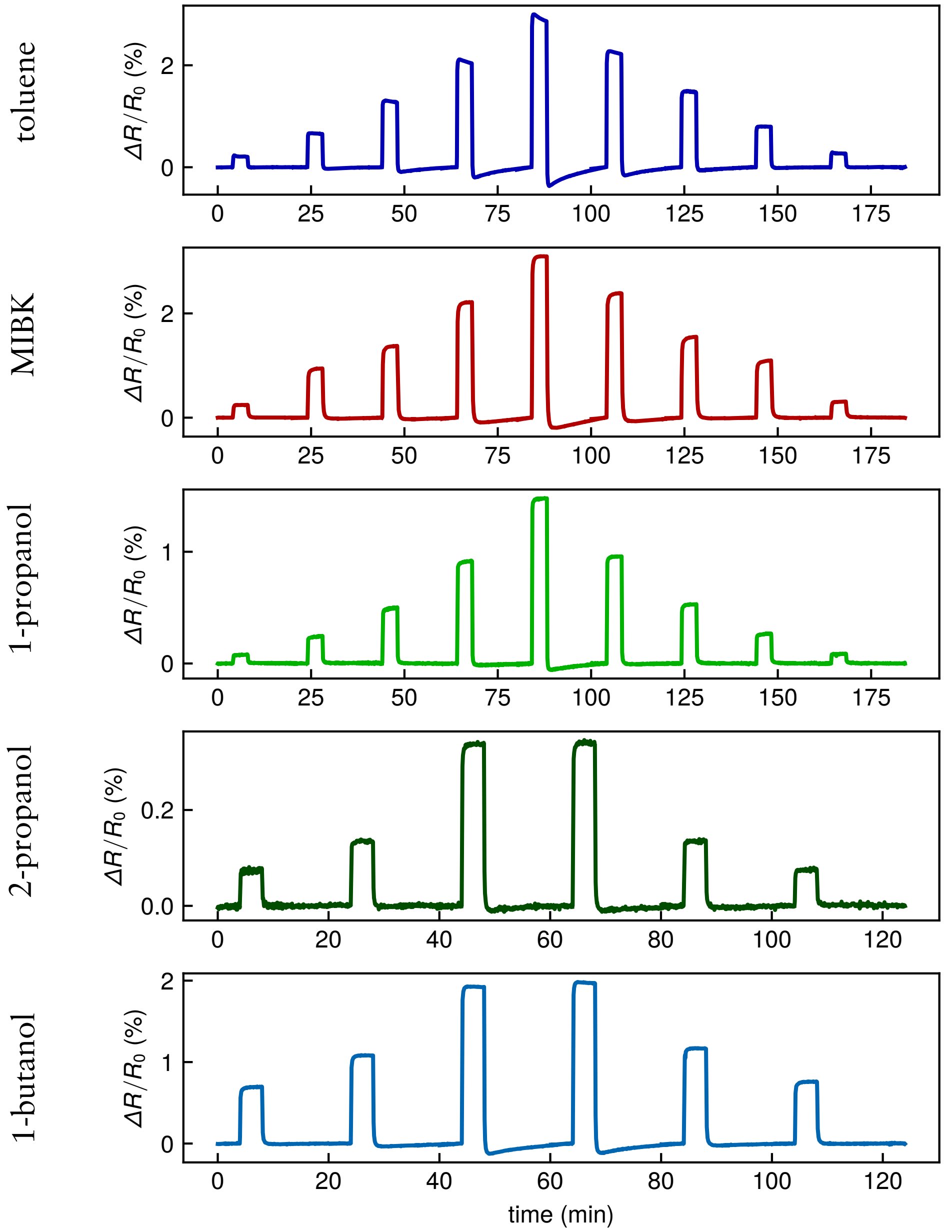
toluene
MIBK
1-propanol
2-propanol
1-butanol
ΔR/R₀ (%)
0
2
1
0.0
0.2
0
25
50
75
100
125
150
175
0
20
40
60
80
100
120
time (min)

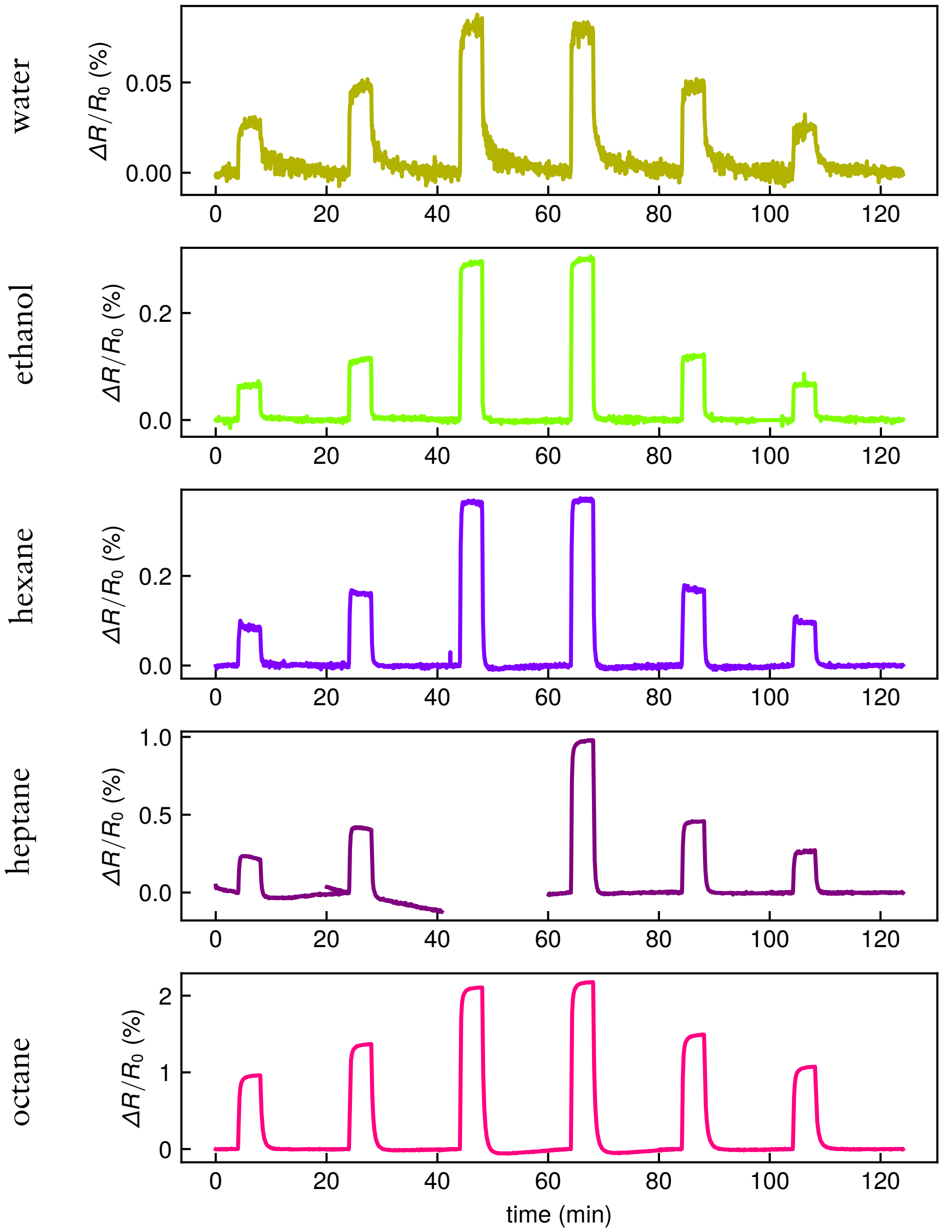

Figure A.11: Baseline corrected responses of a GNP/8DT chemiresistor to 10 different solvent vapors.

9DT-0UV

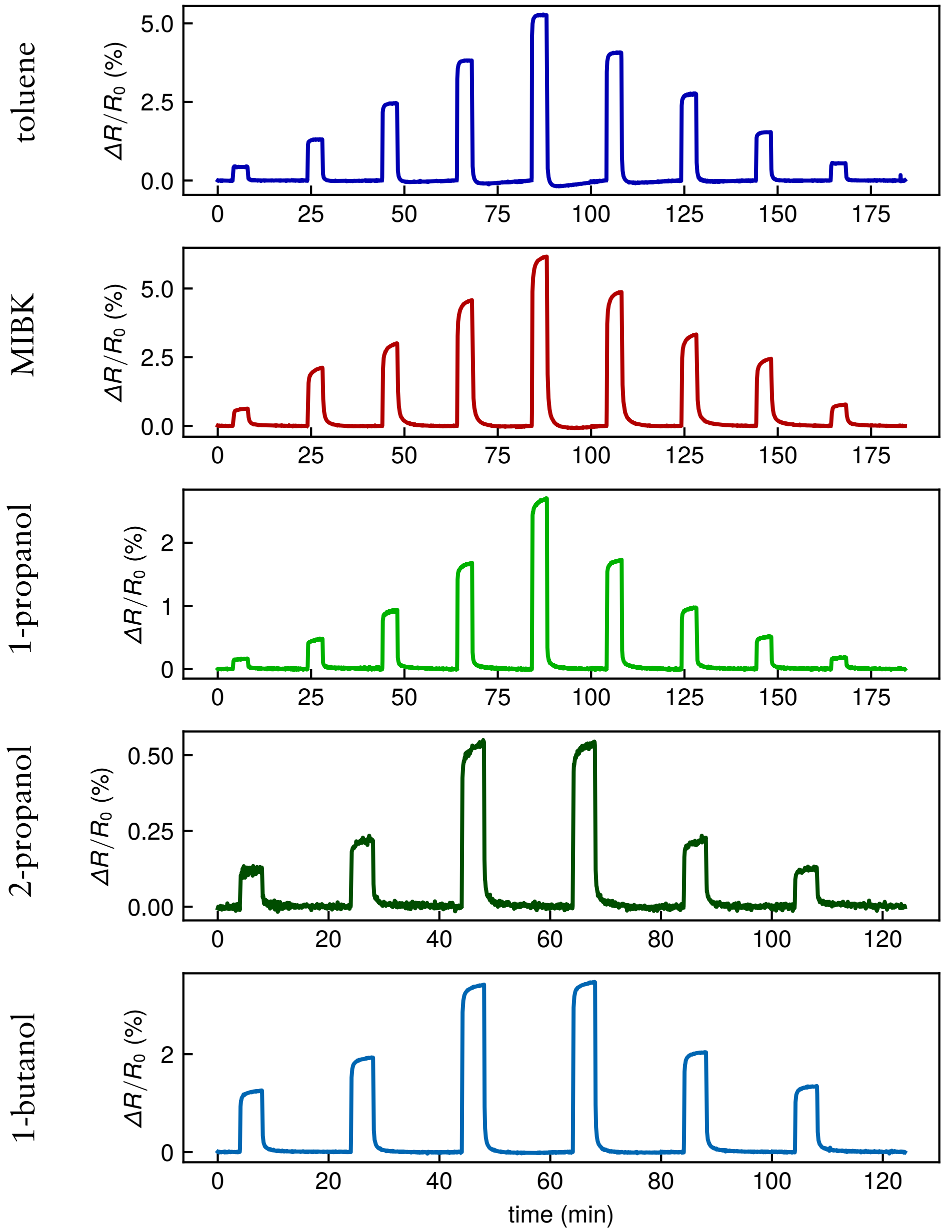
toluene
ΔR/R₀ (%)
5.0
2.5
0.0
0
25
50
75
100
125
150
175
MIBK
ΔR/R₀ (%)
5.0
2.5
0.0
0
25
50
75
100
125
150
175
1-propanol
ΔR/R₀ (%)
2
1
0
0
25
50
75
100
125
150
175
2-propanol
ΔR/R₀ (%)
0.50
0.25
0.00
0
20
40
60
80
100
120
1-butanol
ΔR/R₀ (%)
2
0
0
20
40
60
80
100
120
time (min)

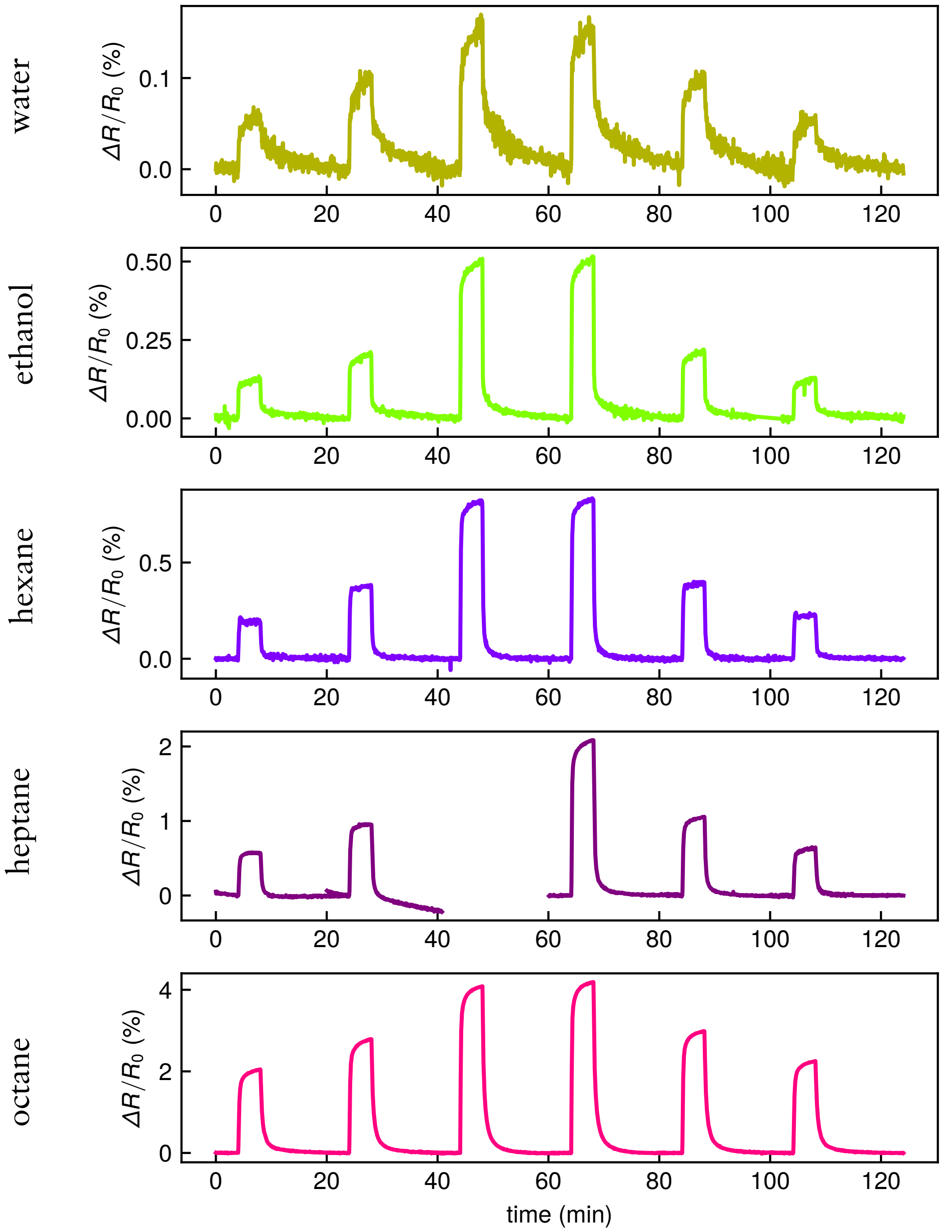

Figure A.12: Baseline corrected responses of a GNP/9DT chemiresistor to 10 different solvent vapors.

9DT-30UV

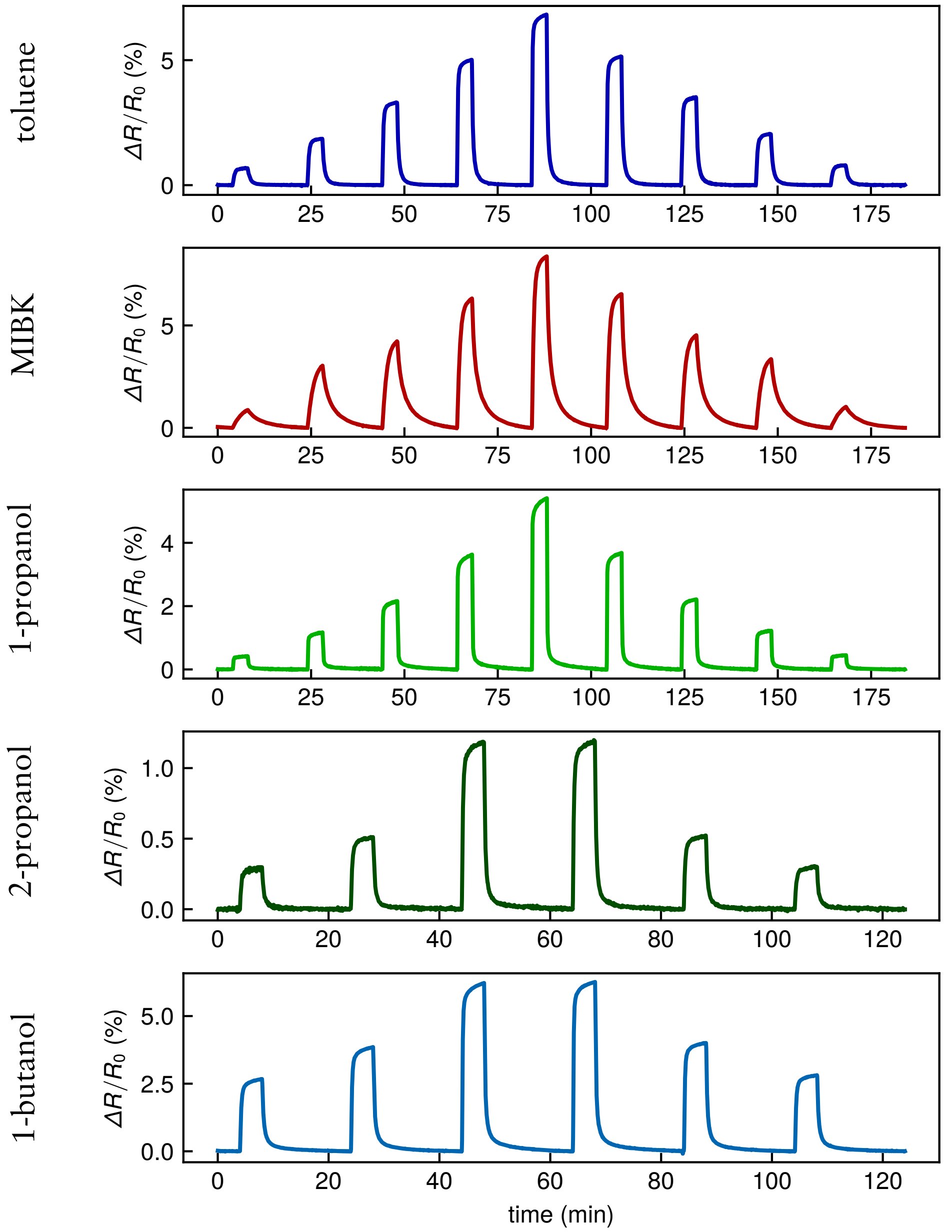
toluene
ΔR/R₀ (%)
0
5
0
25
50
75
100
125
150
175
MIBK
ΔR/R₀ (%)
0
5
0
25
50
75
100
125
150
175
1-propanol
ΔR/R₀ (%)
0
2
4
0
25
50
75
100
125
150
175
2-propanol
ΔR/R₀ (%)
0.0
0.5
1.0
0
20
40
60
80
100
120
1-butanol
ΔR/R₀ (%)
0.0
2.5
5.0
0
20
40
60
80
100
120
time (min)

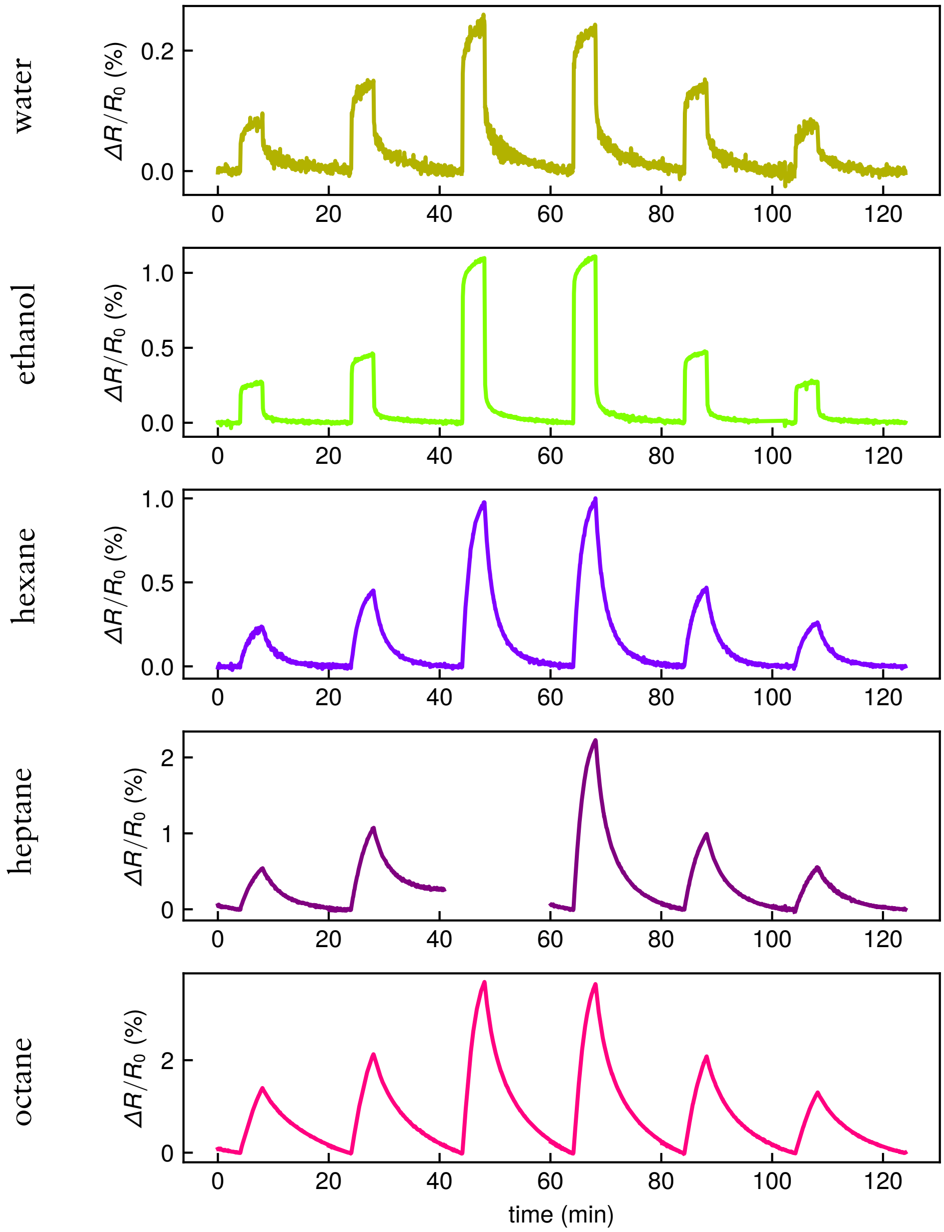

Figure A.13: Baseline corrected responses of a GNP/9DT chemiresistor, exposed to DUV radiation for 30 minutes, to 10 different solvent vapors.

9DT-60UV

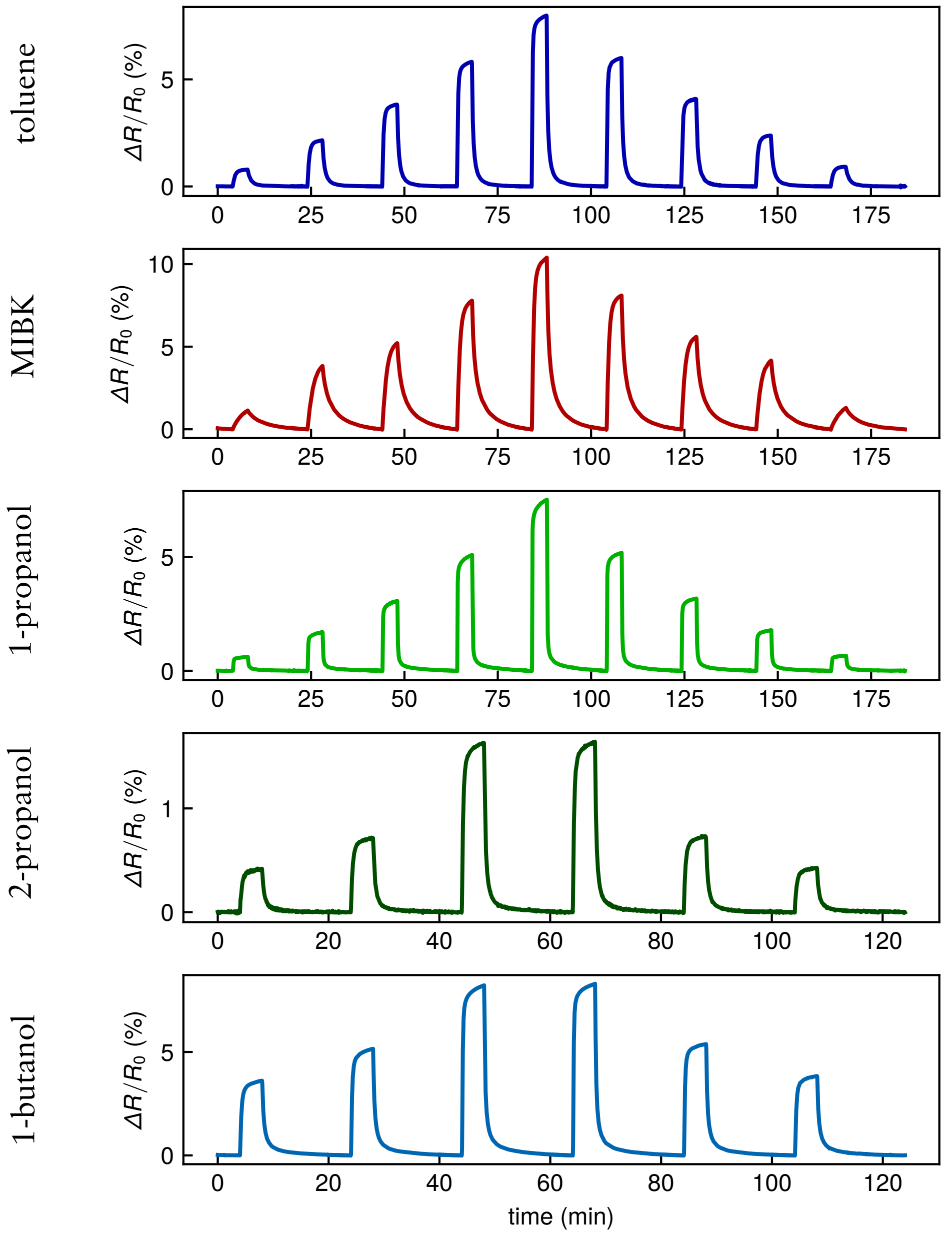
toluene
MIBK
1-propanol
2-propanol
1-butanol
ΔR/R₀ (%)
0
5
10
1
25
50
75
100
125
150
175
20
40
60
80
100
120
time (min)

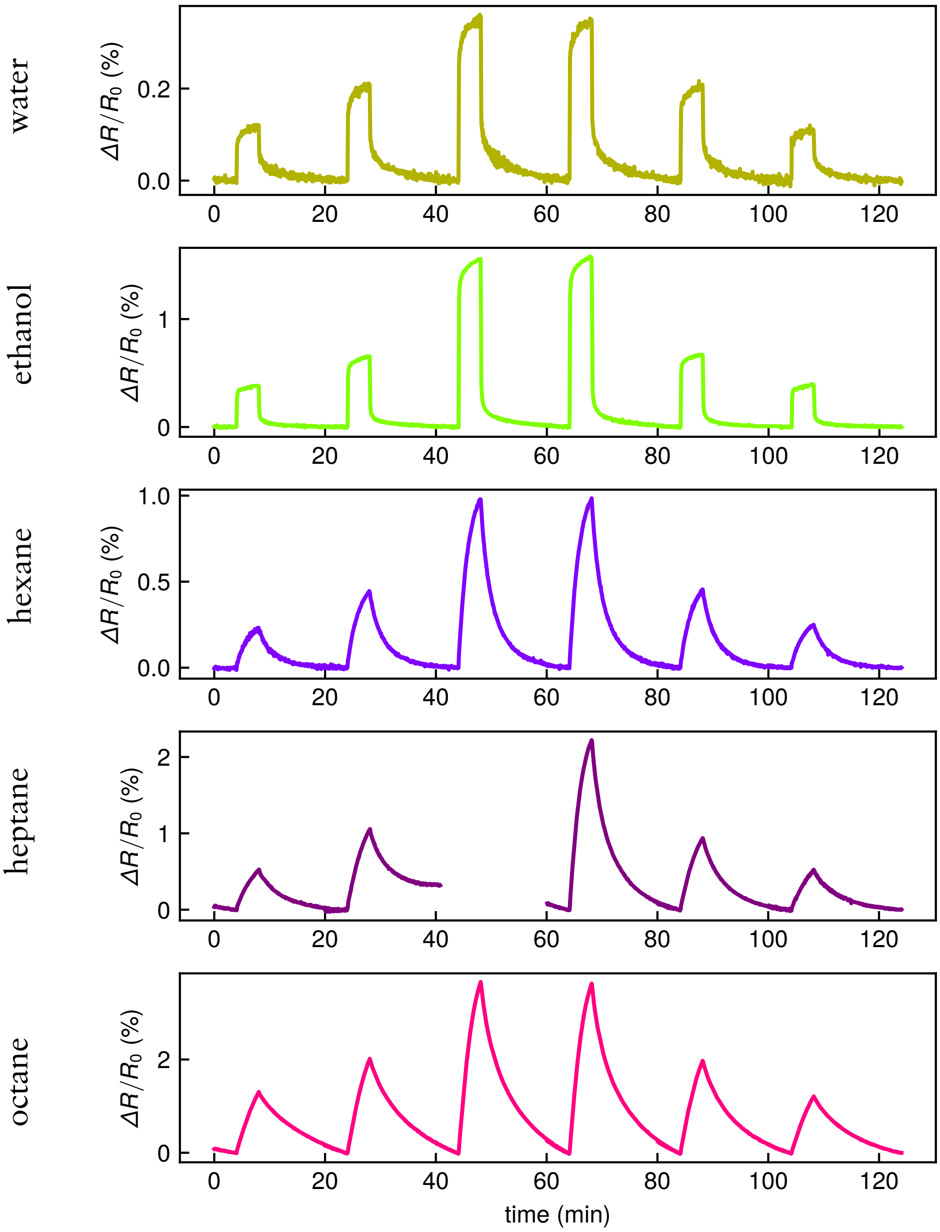

Figure A.14: Baseline corrected responses of a GNP/9DT chemiresistor, exposed to DUV radiation for 60 minutes, to 10 different solvent vapors.

9DT-90UV

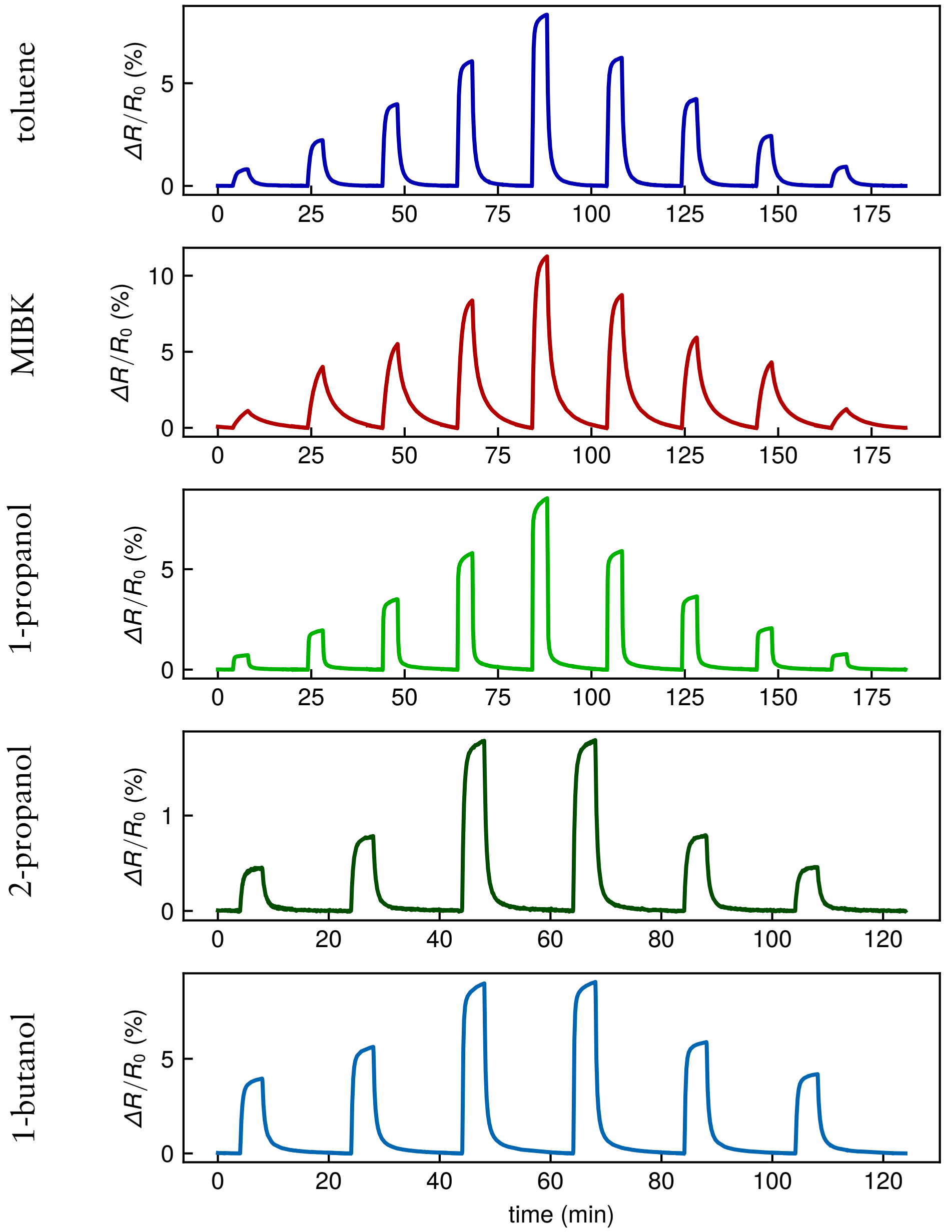
toluene
MIBK
1-propanol
2-propanol
1-butanol
$\Delta R/R_0$ (%)
0
5
10
1
0
25
50
75
100
125
150
175
0
20
40
60
80
100
120
time (min)

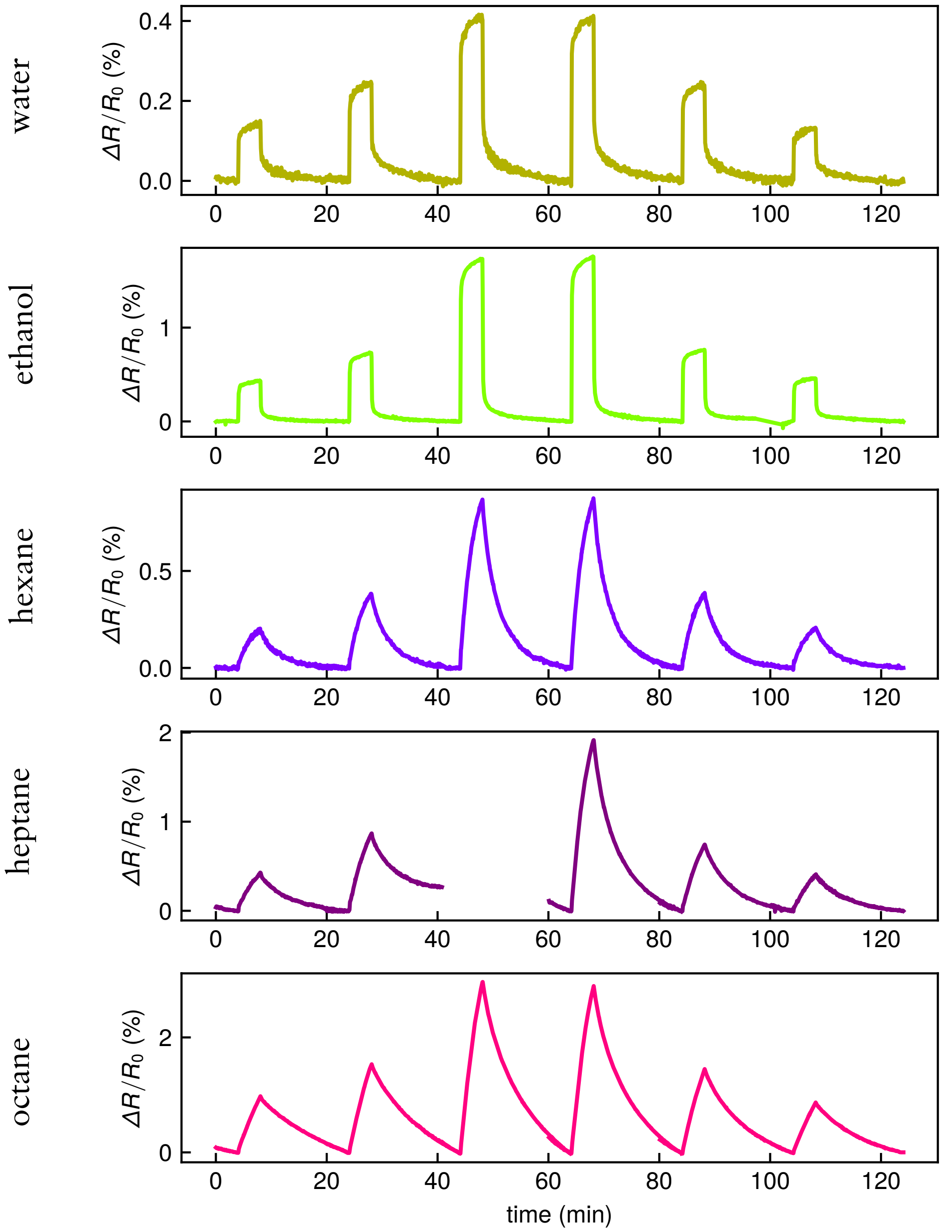

Figure A.15: Baseline corrected responses of a GNP/9DT chemiresistor, exposed to DUV radiation for 90 minutes, to 10 different solvent vapors.

9DT-120UV

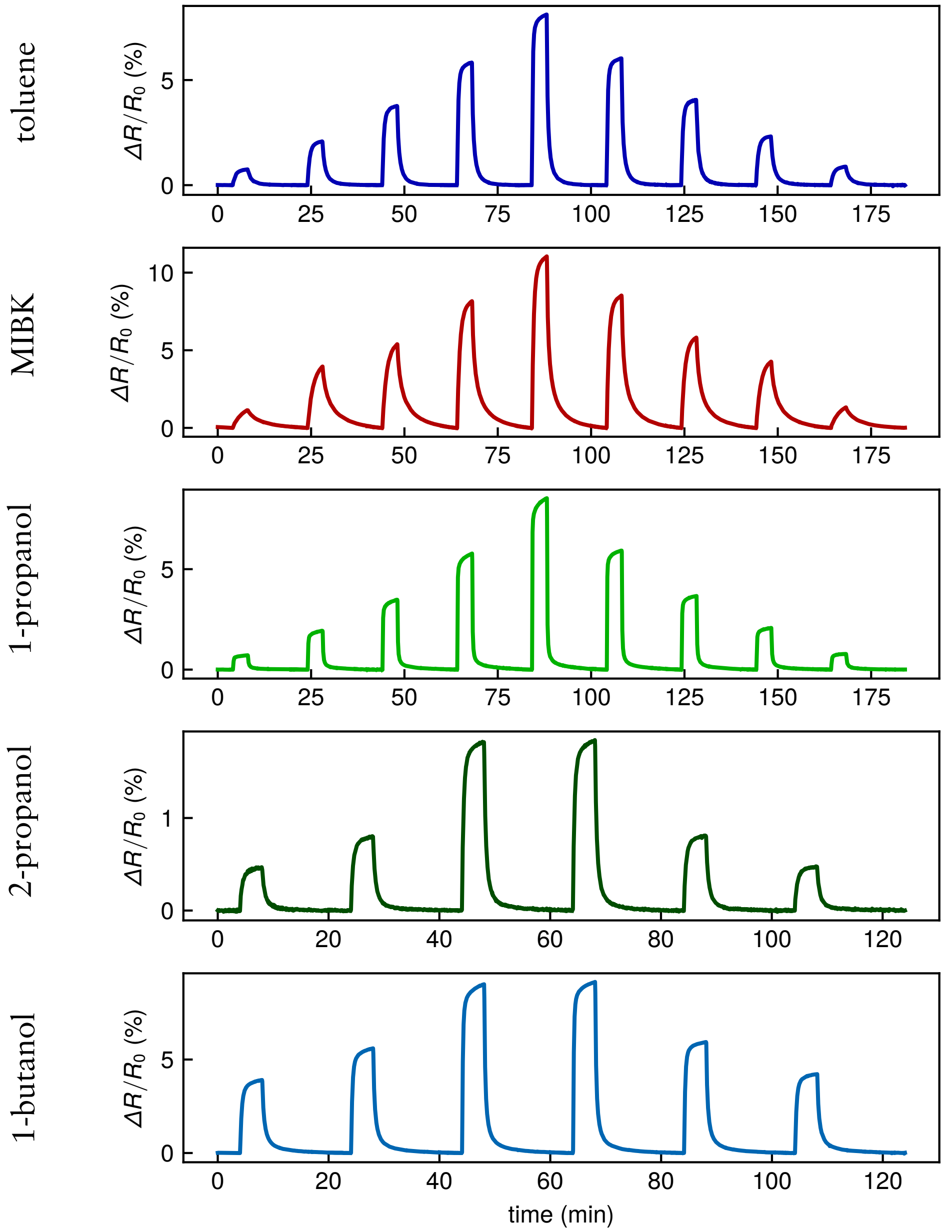
toluene
MIBK
1-propanol
2-propanol
1-butanol
ΔR/R₀ (%)
0
5
10
1
0
25
50
75
100
125
150
175
20
40
60
80
120
time (min)

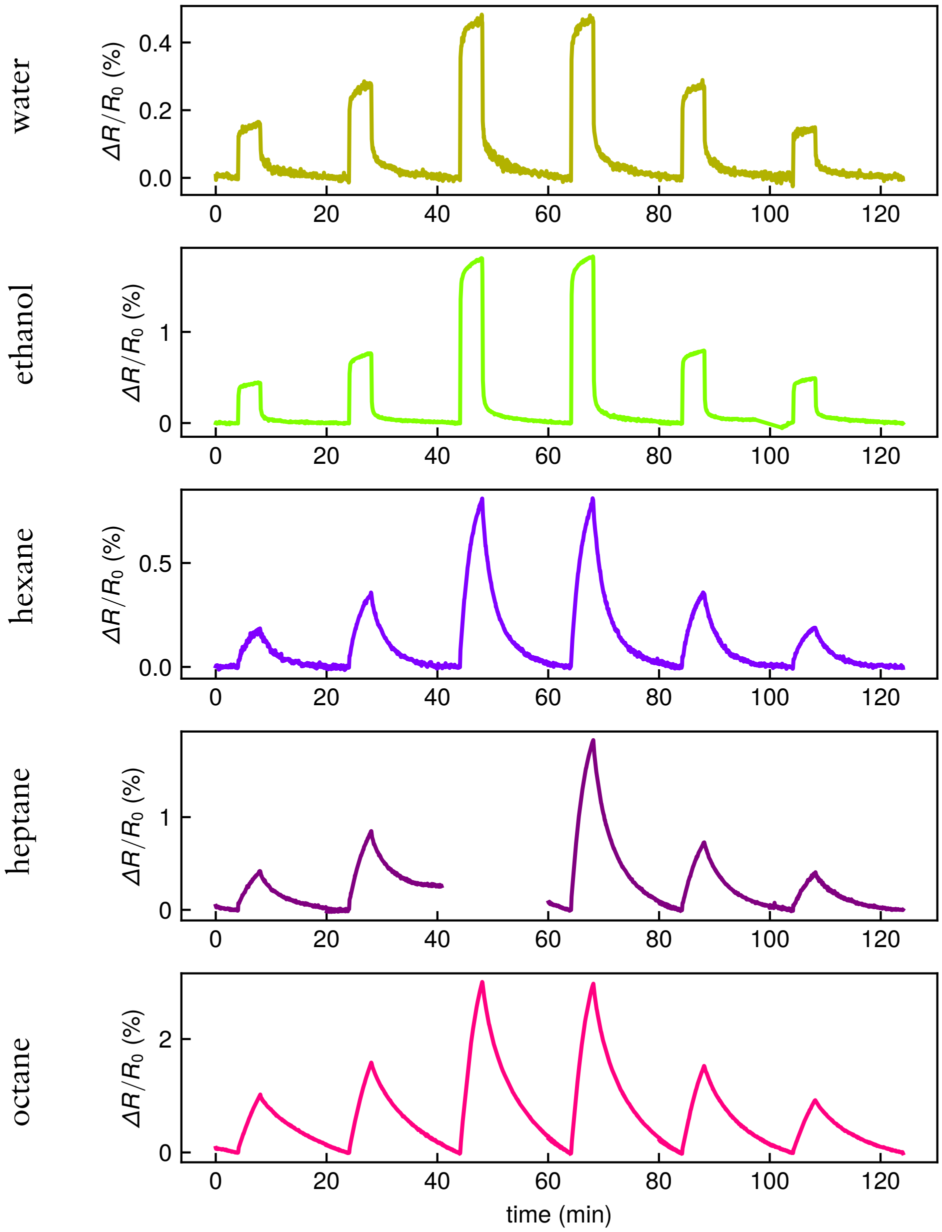

Figure A.16: Baseline corrected responses of a GNP/9DT chemiresistor, exposed to DUV radiation for 120 minutes, to 10 different solvent vapors.

10DT

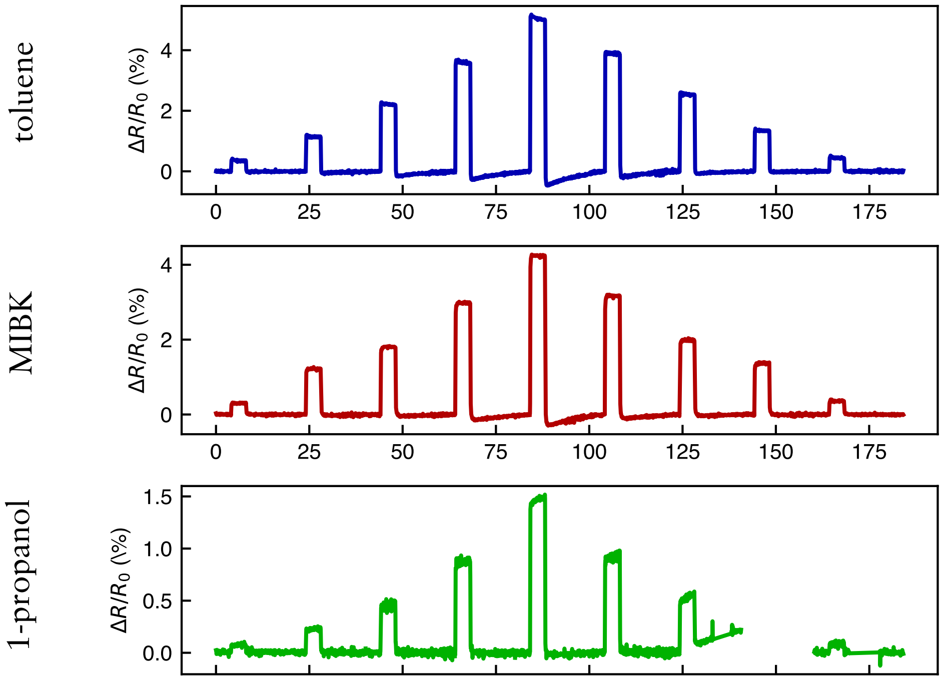

Figure A.17: Baseline corrected responses of a GNP/10DT chemiresistor to toluene, MIBK, and 1-propanol vapors.

A.1.4 Response Times vs. Vapor Pressure

The t_{80} response times for GNP/4DT and GNP/6DT sensors are shown in figure A.18 in dependence of the analyte vapor pressures (at 20 °C). No correlation between the analyte vapor pressure and the extracted response times was found.

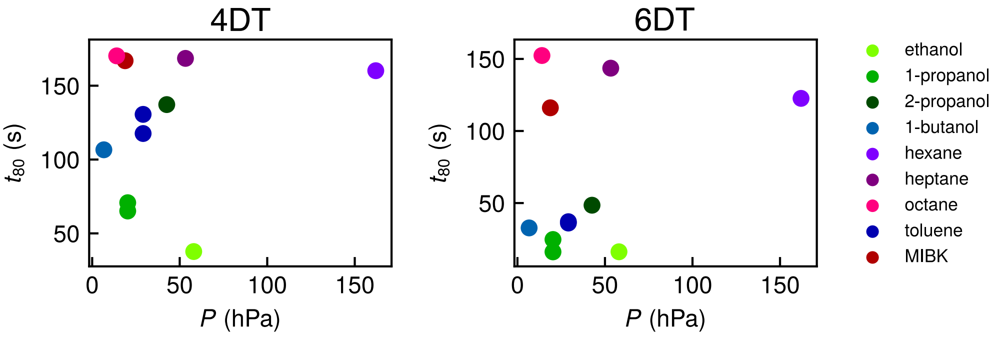

Figure A.18: Response times to various analyte exposures (800 ppm) of a GNP/4DT (left) and GNP/6DT (right) chemiresistors vs. analyte vapor pressures. Reprinted with permission from Ref. [3], ©2021 American Chemical Society.

A.1.5 Investigation of DUV Impact on GNP/9DT Films

Further analysis of the influence of UV exposure on GNP/9DT films was conducted via *IV* measuremets at cryogenic temperatures and optical spectroscopy measurements. For this purpose, a $GNP_{3.6\,nm}$/9DT film ($t_f \sim 66$ nm) was deposited on a glass substrate via LbL SC and then separated into quarters. Two film sections of the glass-supported film were treated with UV light for 1 h, while the other two were used as reference. In analogy to films used as chemiresistors, all film sections were immersed in a methanolic 9DT solution (7.4 mM) for 2 h prior to characterization. UV/vis absorbance spectra were recorded for the composite film directly after film deposition, after 60 min DUV exposure and after restabilization. The respective absorbance spectra are displayed figure A.19. A slight red-shift of $\Delta\lambda \sim 7$ nm of the LSPR band maximum and broadening of the peak, are visible. Immersion into the cross-linker solution after UV exposure does not lead to any significant changes in the recorded spectrum.

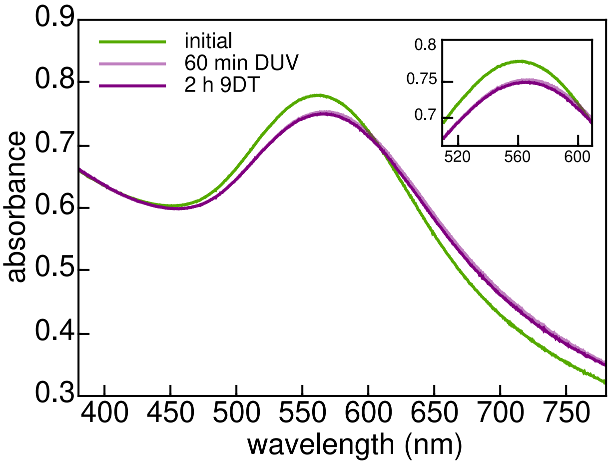

Figure A.19: UV-vis aborbance spectrum of a substrate supported $GNP_{3.6\,nm}$/9DT thin films after film deposition (green), after 60 min UV exposure (pink) and after re-stabilization in a 9DT solution (purple). Inset: zoom-in to the wavelength orange of the LSPR maximum. Adapted and reprinted with permission from Ref. [3], ©2021 American Chemical Society.

In addition, *IV* measurements were conducted at cryogenic temperatures to determine charge transport activation energies according to an Arrhenius activation model. For these measurements, Au electrodes (100 nm) were deposited onto DUV-treated and untreated films section via thermal evaporation. A home-built setup was used for *IV*-measurements at cryogenic temperatures. Here, *IV* curves were recorded at 10 temperatures ranging between 100 K–300 K using a Keithley 2601A sourcemeter. The extracted logarithmic conductivity in dependence of T^{-1} is plotted in figure A.20 for both, the untreated and UV-treated GNP/9DT films. The respective charge transport activation energies were determined as the slopes from linear functions fitted to the data. No signifacnt differences in activation energies were found for the UV treated films compared to the reference films.

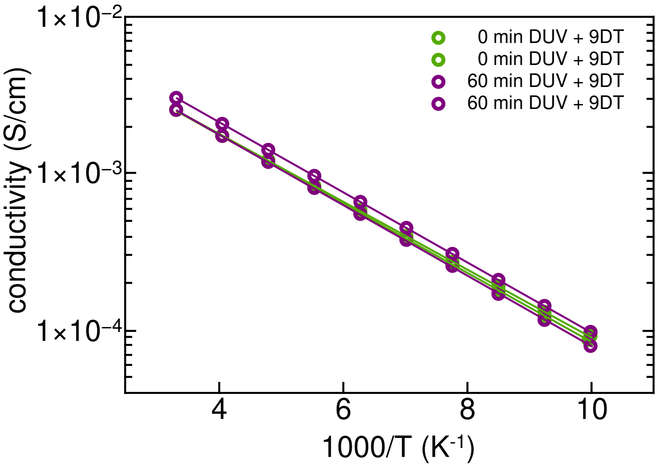

Figure A.20: Arrhenius plots of conductivities. The solid lines represent linear functions fitted to the data according to an Arrhenius model to extract values as activation energies from the slopes. Adapted and reprinted with permission from Ref. [3], ©2021 American Chemical Society.

A.1.6 Linear Discriminant Analysis

Figures A.21–A.22 show linear discriminant analyses (LDAs) with test exposures at a concentration of 400 ppm and 800 ppm, respectively. LDAs were conducted using the `LinearDiscriminantAnalysis` algorithm provided by the `sklearn` (version 0.24.2) python (version 3.9.0) library.

Figure A.23 shows an LDA plot based solely on the resistive response features of the sensors of the sensor array (cf. figure 6.16a) as input. In this LDA, no clearly separated clusters are obtained. Furthermore, the algorithms's analyte prediction fails for some of the test exposures at 800 ppm (as indicated by the crosses and empty circles), confirming the contribution of the kinetic features for successful analyte recognition. Table A.1 shows the the algorithm's analyte predictions for all shown LDAs, where correct prediction are highlighted in green font and incorrect prediction are highlighted in red font. The data labeled as $\mathrm{LDA}_{2000\ \mathrm{ppm}}$ correspond to the LDA plot shown in the Results and Discussion section as a comparison.

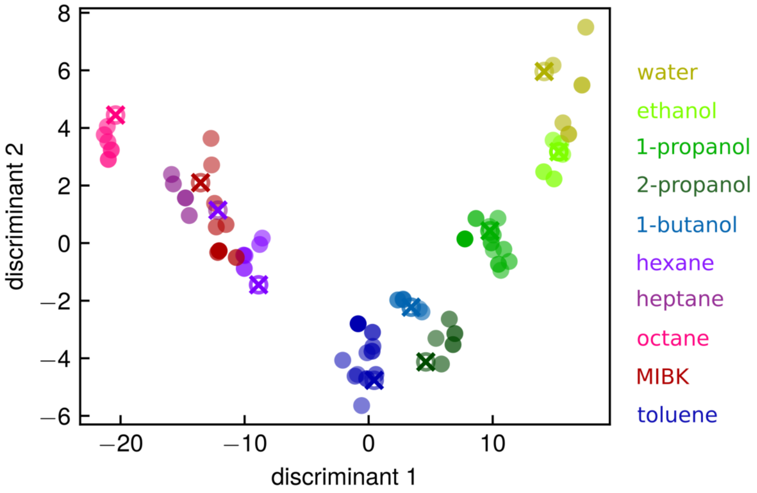

Figure A.21: LDA computed based on the sensor array shown in figure 6.16a). Filled circles represent data points used for computation of the model and empty circles represent test exposures (concentration: 400 ppm) projected to the discriminant coordinate system. The colored crosses represent the respective prediction to the test exposures. Reprinted with permission from Ref. [3], ©2021 American Chemical Society.

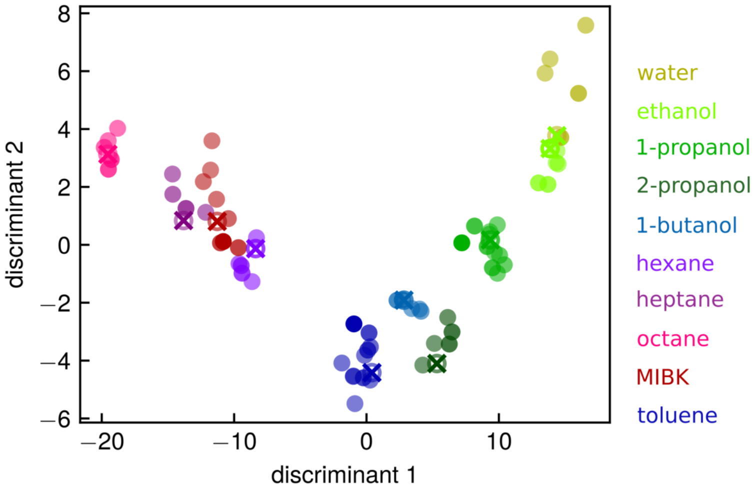

Figure A.22: LDA computed based on the sensor array shown in figure 6.16a). Filled circles represent data points used for computation of the model and empty circles represent test exposures (concentration: 800 ppm) projected to the discriminant coordinate system. The colored crosses represent the respective prediction to the test exposures. Reprinted with permission from Ref. [3], ©2021 American Chemical Society.

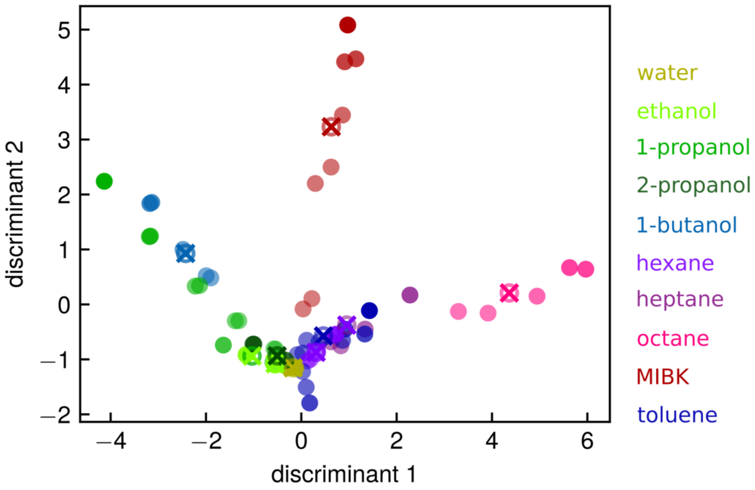

Figure A.23: LDA computed based on the sensor array shown in figure 6.16a) using only resistive response features as input. Filled circles represent data points used for computation of the model and empty circles represent test exposures (concentration: 800 ppm) projected to the discriminant coordinate system. The colored crosses represent the respective prediction to the test exposures. Reprinted with permission from Ref. [3], ©2021 American Chemical Society.

Table A.1: Analyte exposures and corresponding analyte predictions of the LDA algorithms.

test exposure analyte	LDA$_{800\ \mathrm{ppm}}$	LDA$_{400\ \mathrm{ppm}}$	LDA$_{2000\ \mathrm{ppm}}$	LDA$_{800\ \mathrm{ppm},\ \Delta R/R_0}$
toluene	toluene	toluene	toluene	toluene
1-propanol	1-propanol	1-propanol	1-propanol	ethanol
MIBK	MIBK	MIBK	MIBK	MIBK
water	ethanol	water	water	water
heptane	heptane	hexane	heptane	hexane
octane	octane	octane	octane	octane
hexane	hexane	hexane	hexane	hexane
ethanol	ethanol	ethanol	ethanol	ethanol
1-butanol	1-butanol	1-butanol	1-butanol	1-butanol
2-propanol	2-propanol	2-propanol	2-propanol	2-propanol

A.1.7 Binary VOC Mixture Sensing

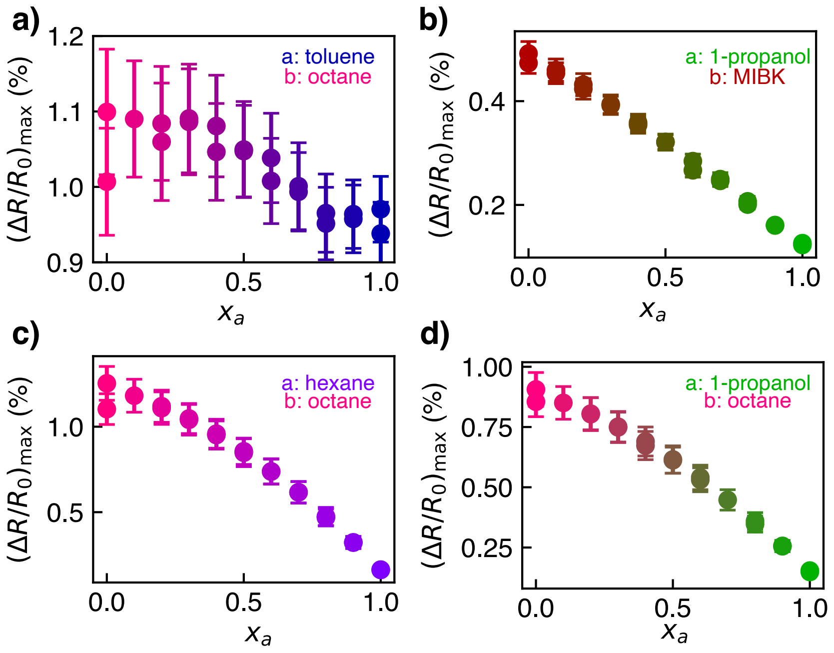

Figure A.24: Correlation of $\left(\frac{\Delta R}{R_0}\right)_{\max}$ and the set analyte fraction x_a in binary VOC mixtures of a) toluene and octane, b) 1-propanol and MIBK, c) hexane and octane, d) 1-propanol and octane. The total vapor concentration was constant at 400 ppm. All mixing ratios were measured twice. The error bars correspond to the standard deviation of values extracted for 13 GNP/6DT chemiresistors.

A.1.8 Binary VOC Mixtures: Timetraces

The following figures show exemplary baseline-corrected response transients of 13 GNP/6DT chemiresistors towards binary VOC mixtures (A-B) at a total analyte concentration of 400 ppm and varying relative analyte fractions.

Toluene-Octane Mixture

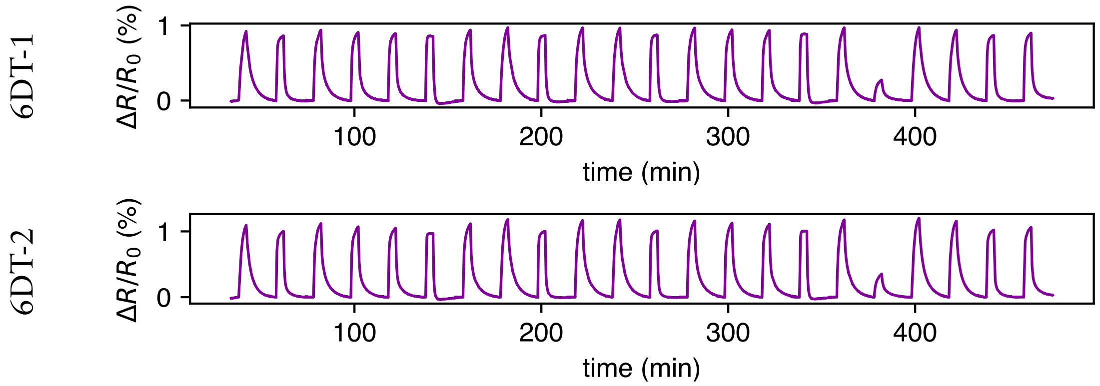

6DT-3

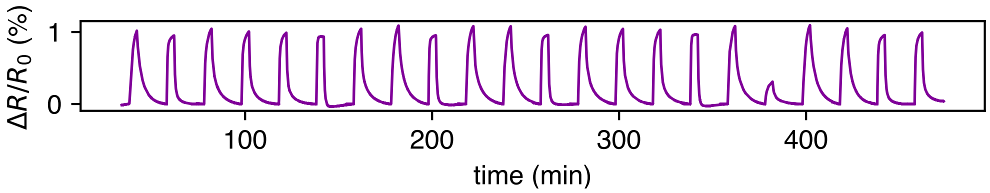

6DT-4

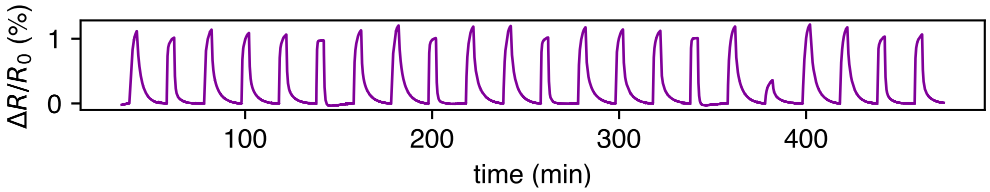

6DT-5

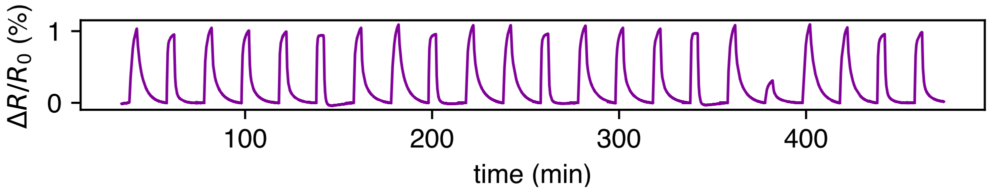

6DT-6

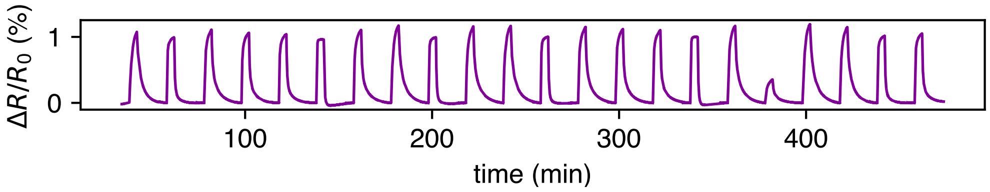

6DT-7

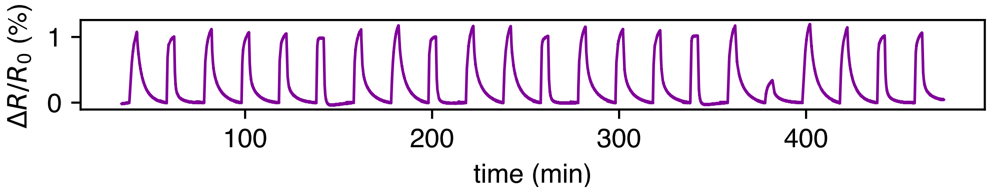

6DT-8

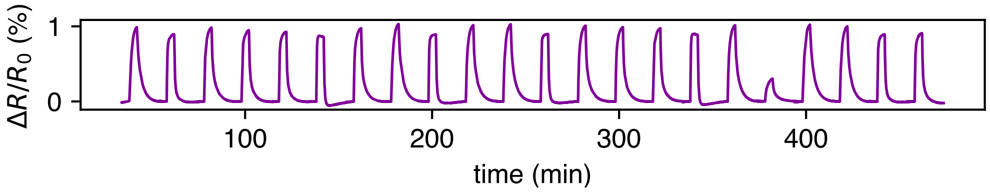

6DT-9

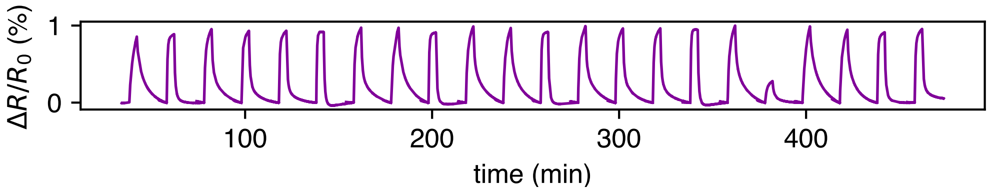

6DT-10

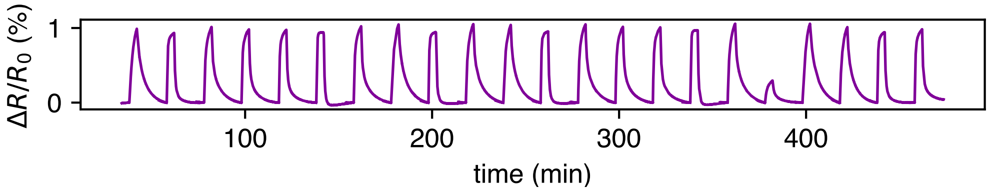

6DT-11

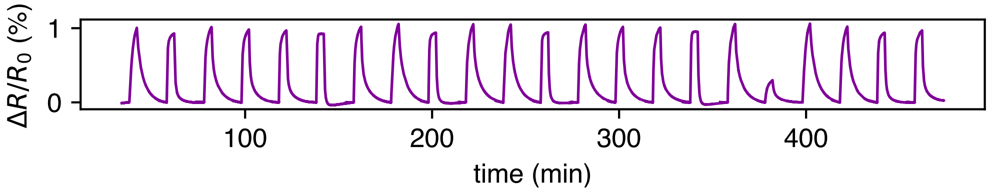

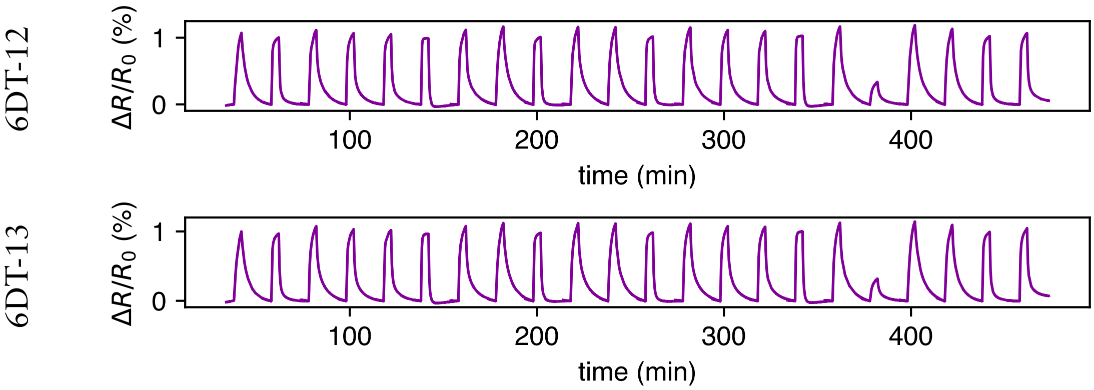

Figure A.25: Examplary baseline corrected responses of 13 GNP/6DT chemiresistor from two arrays to a toluene-octane mixture at different analyte fractions x_a= 0, 0.8, 0.4, 0.6, 0.7, 1, 0.5, 0.1, 0.9, 0.3, 0.2 0.9, 0.4, 0.5, 0.6, 1, 0.3, 0.1, 0, 0.2, 0.8, 0.7. The second set x_a=0.1 transient was excluded from evaluation due to a systematic measurement file error and the resulting lower concentration, as visible from the lower response amplitude.

Hexane-Octane Mixture

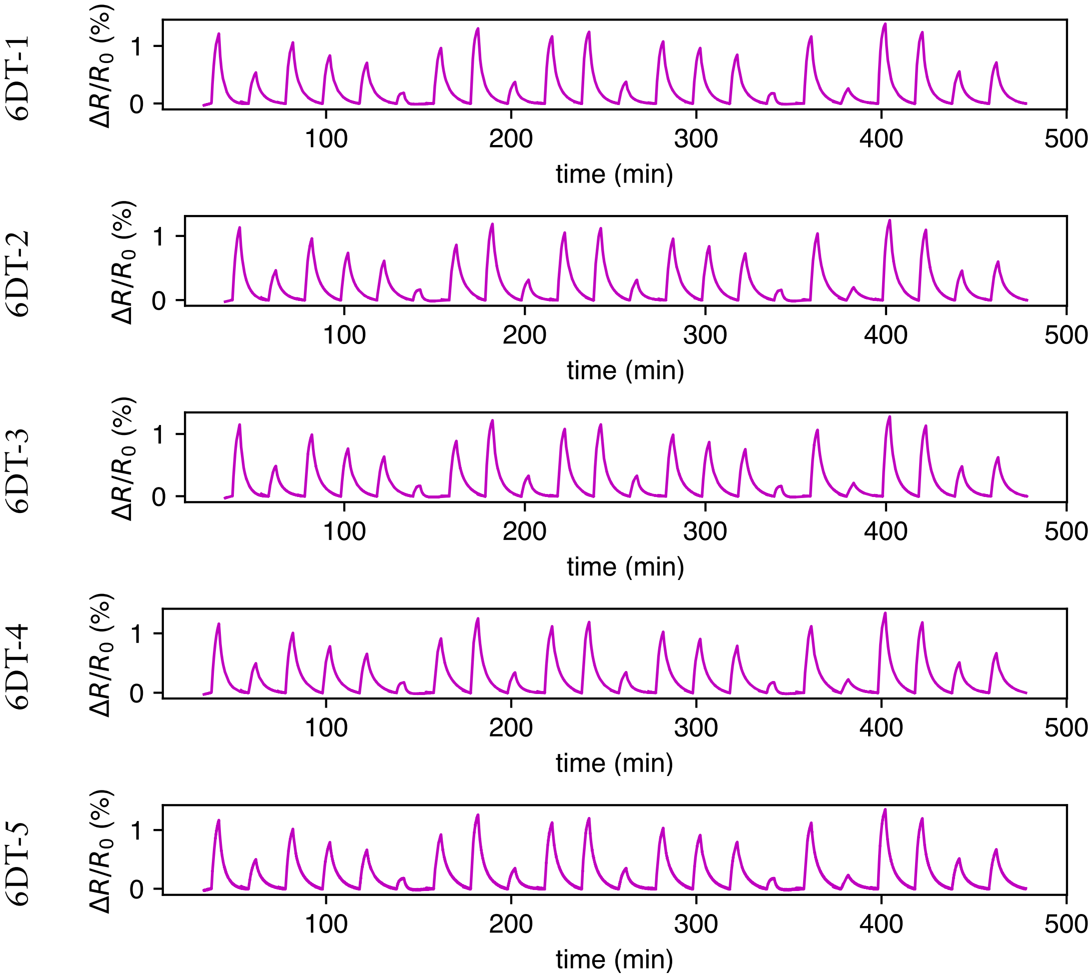

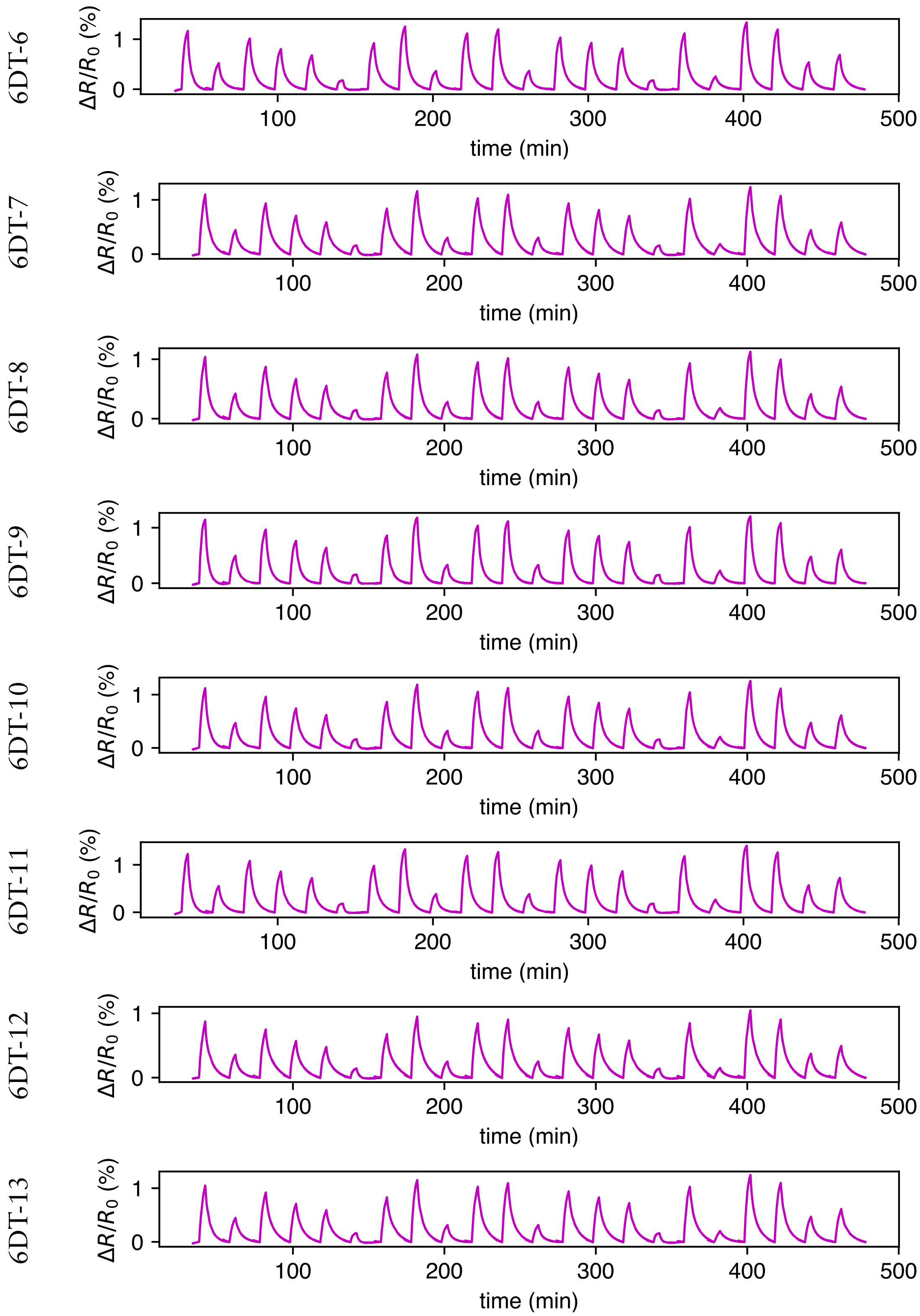

Figure A.26: Examplary baseline corrected responses of 13 GNP/6DT chemiresistor from two arrays to a hexane-octane mixture at different analyte fractions x_a= 0, 0.8, 0.4, 0.6, 0.7, 1, 0.5, 0.1, 0.9, 0.3, 0.2 0.9, 0.4, 0.5, 0.6, 1, 0.3, 0.1, 0, 0.2, 0.8, 0.7. The second set x_a=0.1 transient was excluded from evaluation due to a systematic measurement file error and the resulting lower concentration, as visible from the lower response amplitude.

1-Propanol-MIBK Mixture

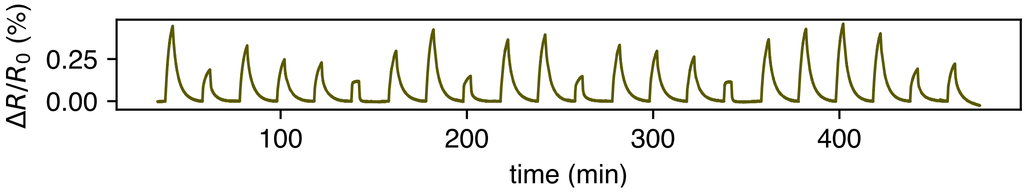

6DT-1

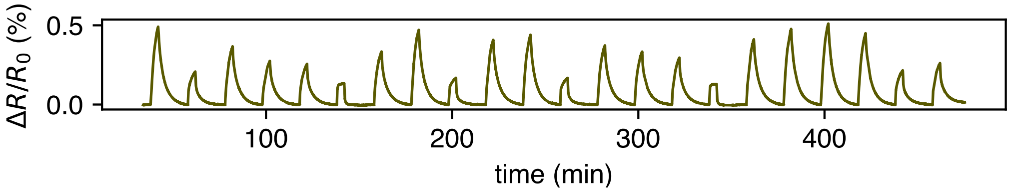

6DT-2

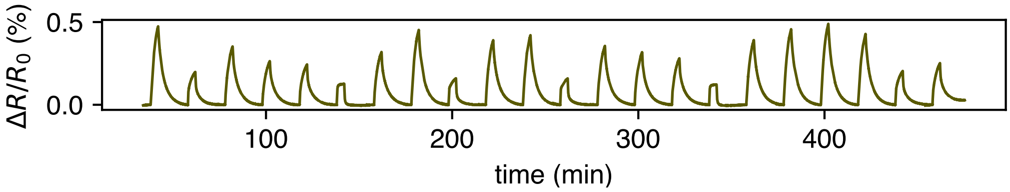

6DT-3

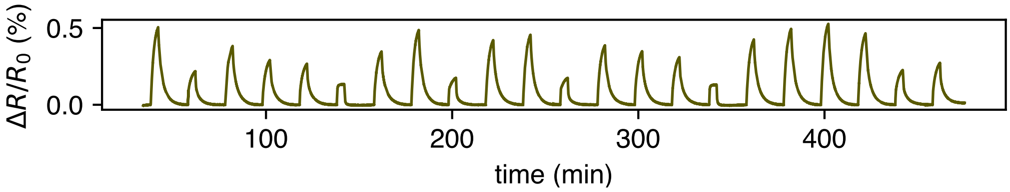

6DT-4

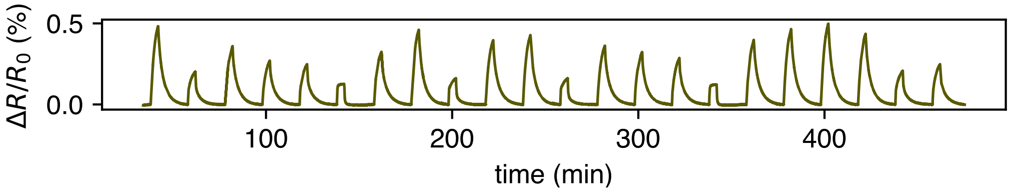

6DT-5

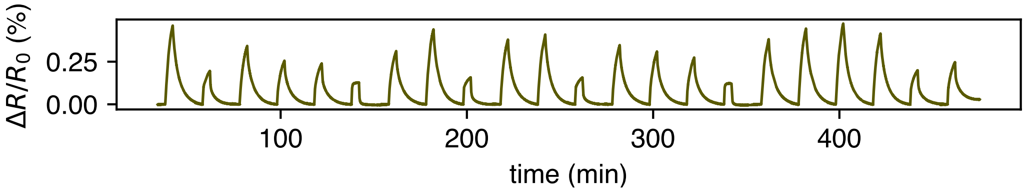

6DT-6

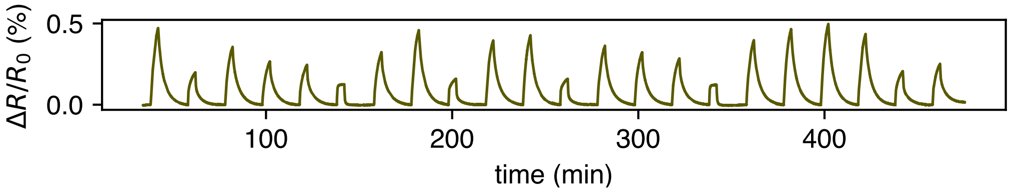

6DT-7

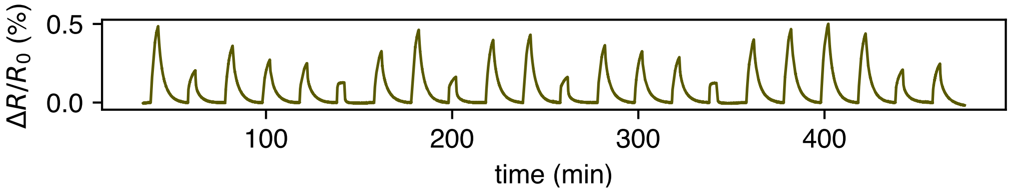

6DT-8

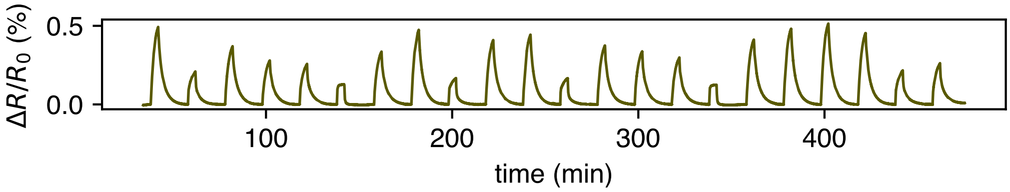

6DT-9

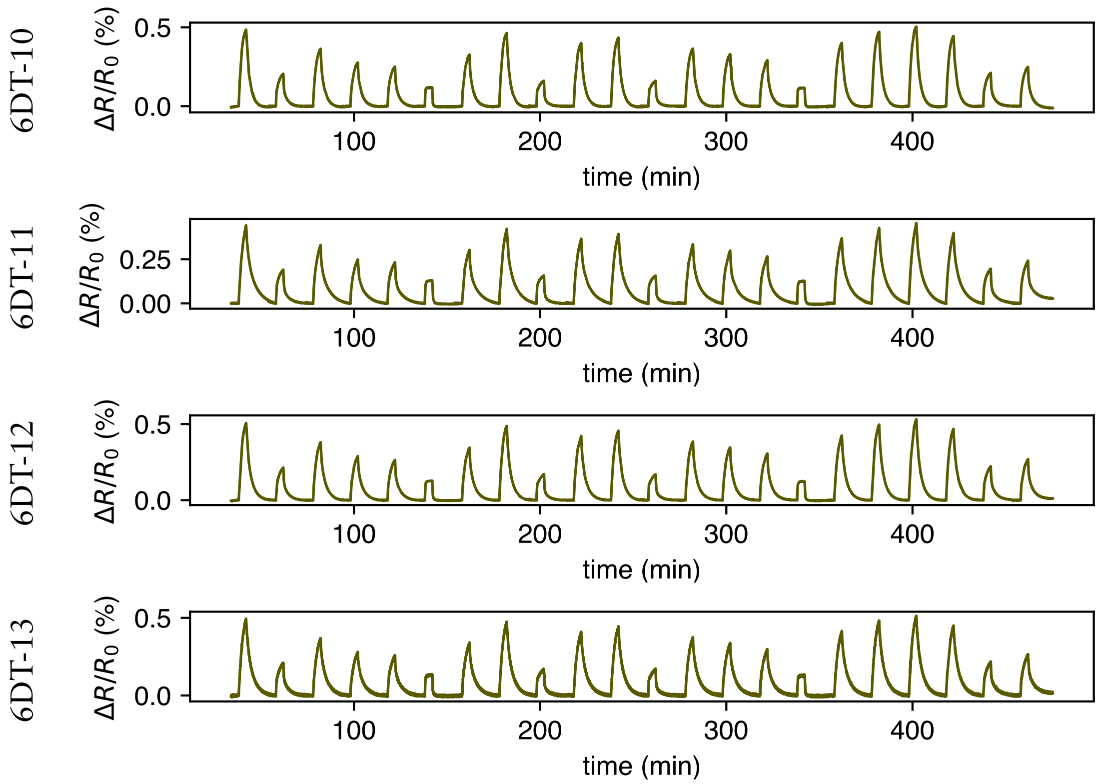

Figure A.27: Examplary baseline corrected responses of 13 GNP/6DT chemiresistor from two arrays to a 1-propanol-MIBK mixture at different analyte fractions x_a= 0, 0.8, 0.4, 0.6, 0.7, 1, 0.5, 0.1, 0.9, 0.3, 0.2 0.9, 0.4, 0.5, 0.6, 1, 0.3, 0.1, 0, 0.2, 0.8, 0.7.

1-Propanol-Octane Mixture

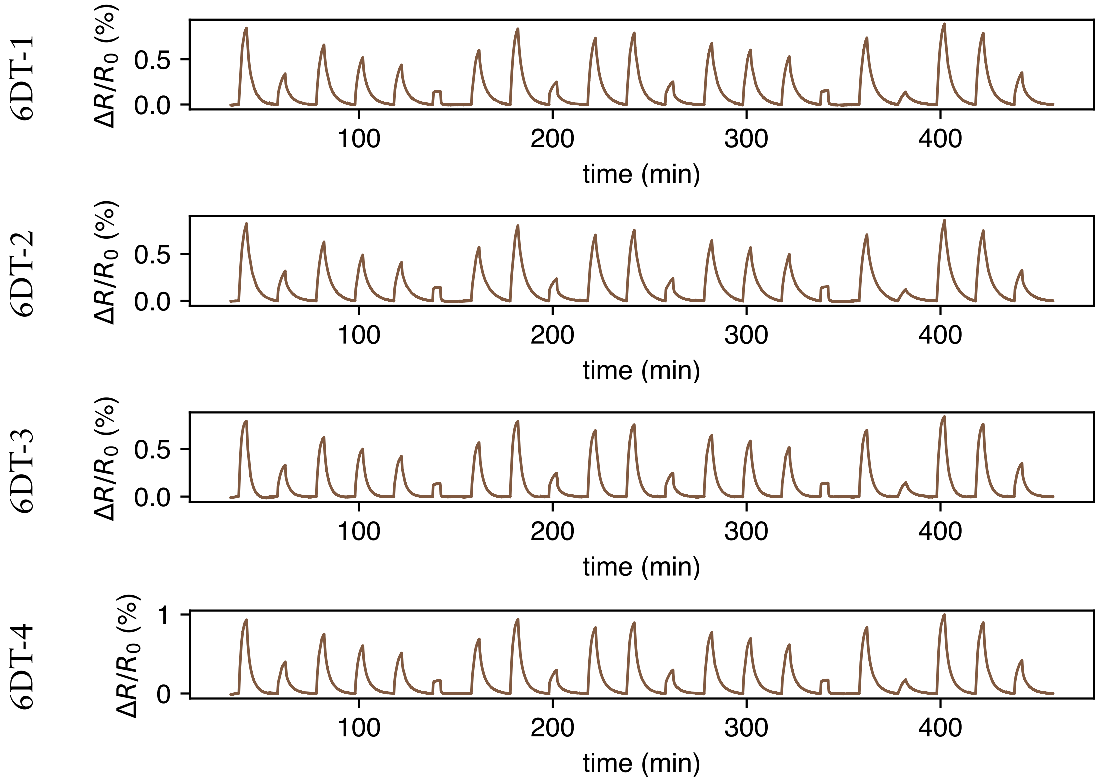

6DT-5

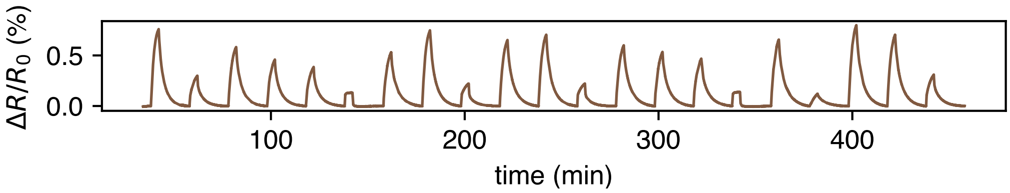

6DT-6

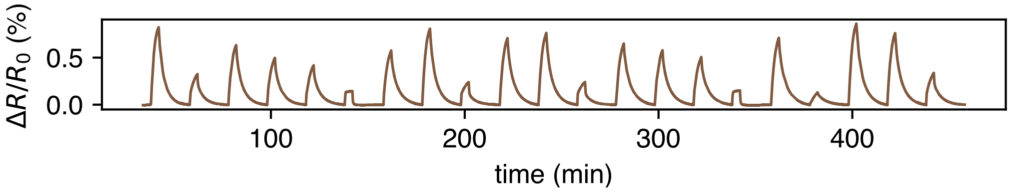

6DT-7

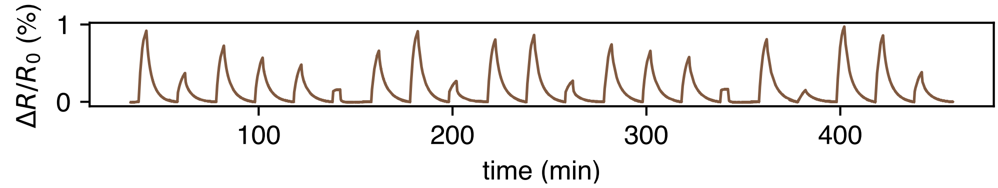

6DT-8

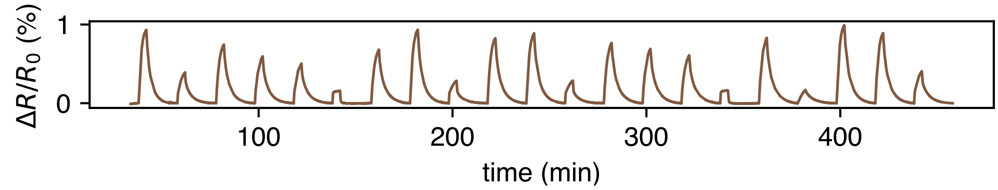

6DT-9

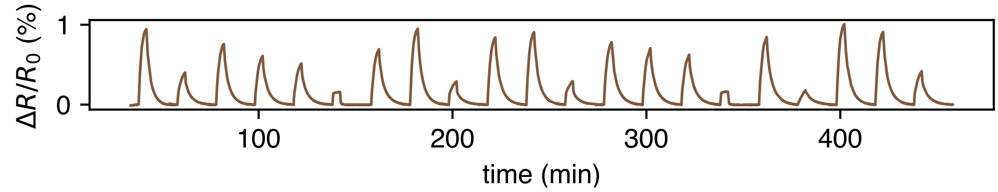

6DT-10

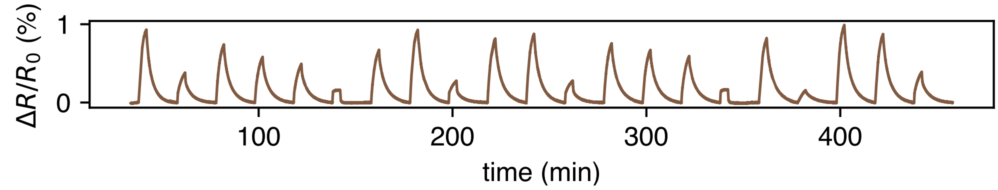

6DT-11

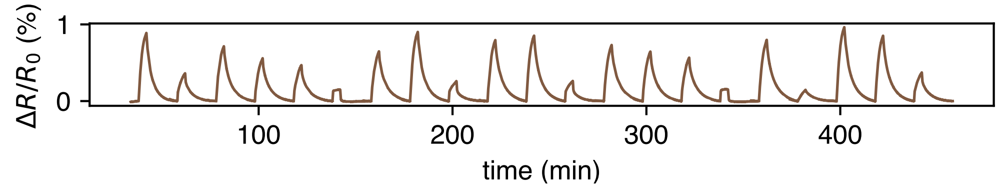

6DT-12

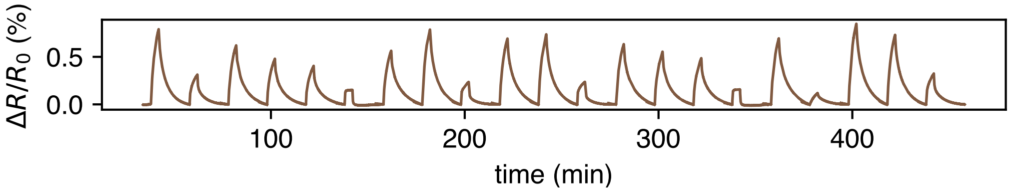

6DT-13

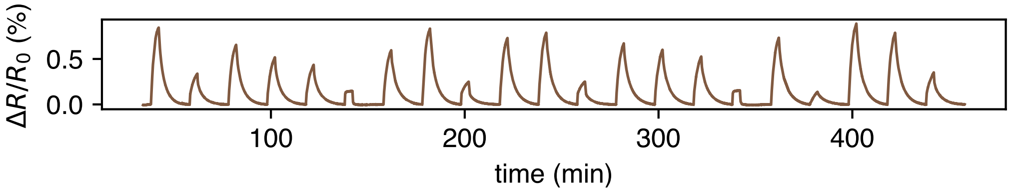

Figure A.28: Examplary baseline corrected responses of 13 GNP/6DT chemiresistor from two arrays to a 1-propanol-octane mixture at different analyte fractions x_a = 0, 0.8, 0.4, 0.6, 0.7, 1, 0.5, 0.1, 0.9, 0.3, 0.2 0.9, 0.4, 0.5, 0.6, 1, 0.3, 0.1, 0, 0.2, 0.8. The second set x_a=0.1 transient was excluded from evaluation due to a systematic measurement file error and the resulting lower concentration, as visible from the lower response amplitude.

A.1.9 Thermogravimetric Analysis

As-synthesized titania nanoplates (TNPs) and titania nanorods (TNRs) were characterized using thermogravimetric analysis (TGA) to determine the organic content, as well as the total mass concentration of the samples. Details on the experimental procedure are described in the Experimental Section 7.2. Figure A.29 shows the change of mass vs. temperature. Both curves show a steep decrease in mass between 350–400 °C corresponding to oleylamine (boiling point: 348 – 350 °C)[226] and demonstrate that the TNRs had a higher organic content (OC) (39.3 %), compared to the TNPs (28.5 %).

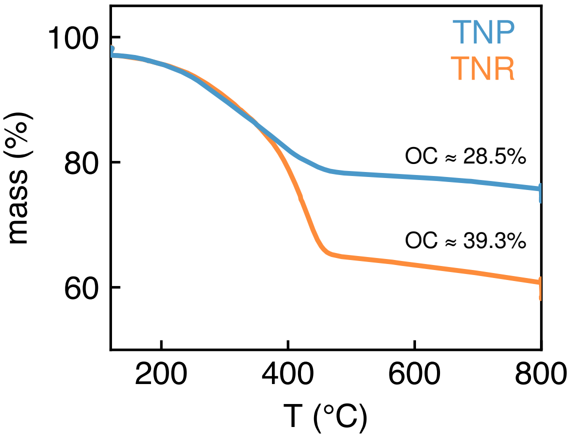

Figure A.29: TGA of oleylamine-stabilized TNPs (blue) and TNRs (orange) used for GO/TNC thin film fabrication and photocatalytic GO reduction.

A.1.10 Method to Determine GO/TiO_2 Hybrid Film Composition

Based on the absorbance spectra, the TNC volume fraction within the hybrid film was estimated. The estimation was based on the postulation that the absorbance spectrum of a hybrid film can be described as a linear combination of the absorbance spectra of the respective single components, according to equation 18.

$$A_{\mathrm{hybrid}}(\lambda) = A \cdot A_{\mathrm{GO}}(\lambda) + B \cdot A_{\mathrm{TNC}}(\lambda) \tag{18}$$

To this end, the factors A and B were extracted from fit parameters that were computed using a custom-written python program that fitted a hybrid film absorbance spectrum to the measured hybrid spectrum, by taking the single components' absorbance spectra as input. Figures A.30a-c) show the fitted absorbance spectra for all GO/TNC films (gray) and the absorbance for the hybrid film after one deposition cycle, as well as the respective weighted TNC and GO spectra (cf. eq. 18). The fit functions show a satisfactory approximation to the measured data, however, some deviations at lower wavelengths, especially for the GO/TNP film (figure A.30 b) are visible. To estimate the volume fraction of TNCs within the hybrid films, the absorbance at 250 nm was extracted from the simulated, weighted TNC spectrum and, according to Lambert's law, the thickness t_{TNC} of the TNC component was calculated using equation 19, by taking into account the decadic attenuation coefficient α_λ for the respective TNCs, that were determined in our group in an earlier study. The attenuation coefficients for each TNC species were determined as 1.50×10^5 cm^{-1}, 1.63×10^5 cm^{-1} and 1.58×10^5 cm^{-1} for TNRs, TNPs, and TNDs, respectively.[203] Under consideration of the hybrid film thickness t_{f} that was determined via AFM, the volume fraction of the TNC component was calculated. The resulting TNC volume fractions are summarized in table A.6. Although all hybrid films show a similar maximal absorbance of ~0.25 and thicknesses of ~20 nm, the spectrum decomposition reveals different relative amounts of TNCs in the films, ranging from 15–44 %. It is to note, that these variations, especially in the case of the GO/TNP sample might be due to an over-weighting of the GO component, as can be seen from the gray fit function. This procedure was not well-suited for thicker films, since the fitted spectra did not describe the measured composite films' spectra well.

$$t_{\mathrm{TNC}} = \frac{A_{\mathrm{TNC,250\,nm}}}{\alpha_{\lambda,\mathrm{TNC}}} \tag{19}$$

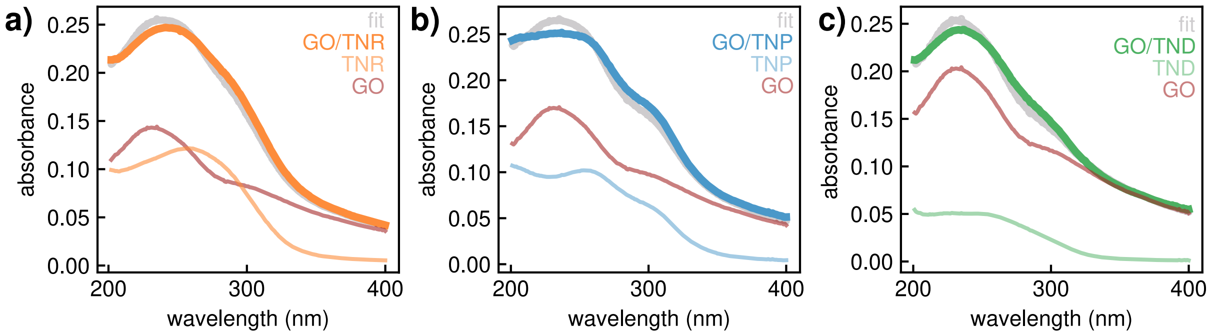

Figure A.30: Simulated UV-vis absorbance spectra (gray) for GO/TNC hybrid films fabricated using a) TNRs, b) TNPs, and c) TNDs. The respective weighted GO spectrum is shown in light red, and the weighted TNC spectra in a) light orange, b) light blue, and c) light green.

Table A.6: Estimation of TNC volume fraction within GO/TNC hybrid films by UV-vis spectroscopy analysis.

film composition	$A_{250\ \mathrm{nm}}$	t_{TNC} (nm)	t_{f} (nm)	v/v (%)
GO/TNR	0.12	8.0	18 ± 1	44
GO/TNP	0.10	6.1	17 ± 2	39
GO/TND	0.05	3.2	21 ± 2	15

Figure A.31 shows exemplary AFM scans of TNC/GO hybrid films fabricated on silicon wafers using TNPs and TNRs and varying number of spin-coating deposition cycles (1 and 4). The scans were recorded at scratch edges between film and substrate. Since the measured thickness for the 4L TNR-based film varied from two scans, two scans are provided. The herein determined film thicknesses were also assumed as estimated thicknesses for hybrid films deposited on other types of substrates.

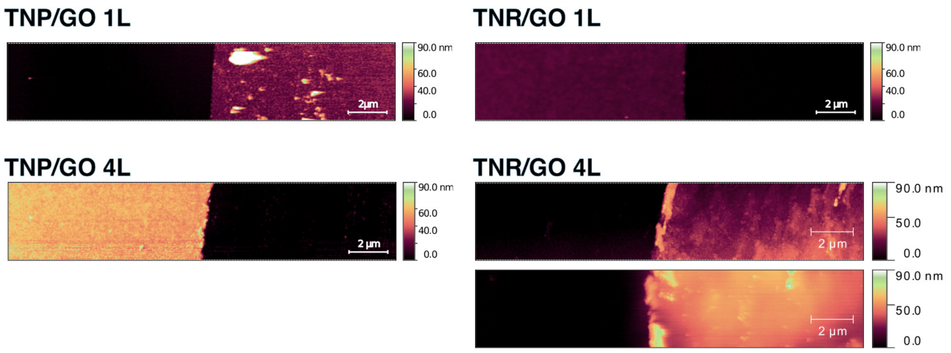

Figure A.31: Exemplary AFM scans for hybrid TNR- and TNP/GO hybrid films fabricated using 1 (top) and 4 (bottom) spin-coating deposition cycles.

A.1.11 Photocatalytic Reduction of GO with Varying TNC Amount

Figure A.32 shows the evolution of conductance of films fabricated using different concentrations of TNC solutions (0.5 mg/mL–4 mg/mL) for hybrid film fabrication (GO: 0.05 *wt*%, 1 spin-coating deposition cycle). Higher TNC concentration resulted in higher conductances and faster conversion of GO to a conductive material. Additional reference experiments using titania nanodots (TNDs) as photocatalyst were performed. TNDs were synthesized in aqueous solution by a method from Fraunhofer Center of Applied Nanotechnology. Before thin film deposition, a post-synthetic surface modification using OLAM as ligand was conducted to transfer the TNDs to an organic solvent, as described in the literature.[203] Thorough characterization of the GO/rGO/TND films during photocatalytic reduction, and preliminary humidity sensing experiments showed similar results to the films fabricated using TNRs. Consequently, further projects focused on TNR- and TNP-based samples, since the use of TNDs involved time-consuming post-synthetic surface modification steps.

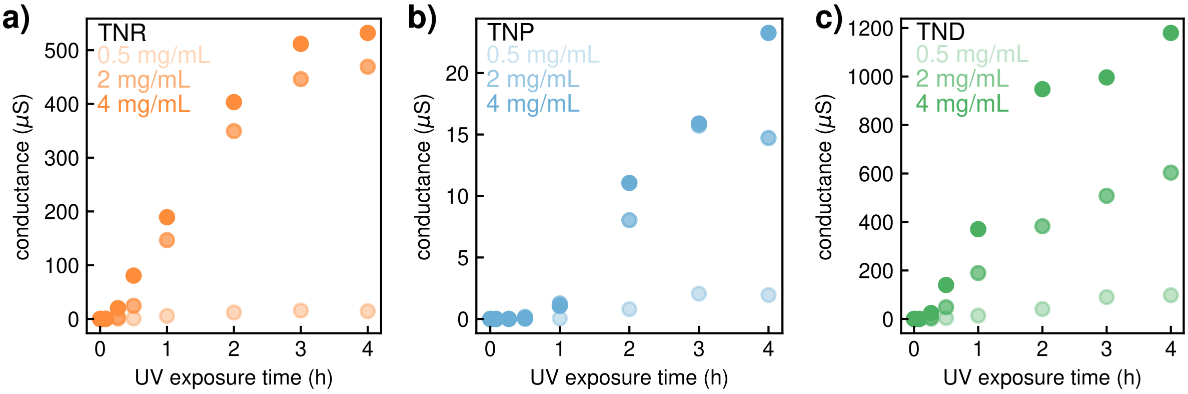

Figure A.32: Conductances obtained for GO/rGO/TNR, b) GO/rGO/TNP, and c) GO/rGO/TND films fabricated using TNC solutions of varying concentrations for UV exposures of up to 4 h.

A.1.12 Phototreatmet of Pure TNR- and GO Films

UV Exposure of TNRs

The impact of UV light on the OLAM-stabilized TNRs was investigated using FTIR spectroscopy. Here, TNRs were drop-casted from their stock solution onto a siliconw afer and exposed to UV light (254 nm) for 0–60 minutes. Figure A.33 shows the evolution of the spectra with increasing UV illumination times. The initial film (0 min UV) shows the characteristic CH_2 band around 2900 cm^{-1} corresponding to the amine ligand, and a pronounced peak around 800 cm^{-1}, that can be assigned to Ti-O-Ti vibrations. After only 5 minutes, the CH_2 band is not visible, suggesting that for this fim, the UV-induced degradation of OLAM is accomplished within the first hour of UV illumination.

UV Exposure of GO Films

GO films were illuminated with UV light (254 nm) without the incorporation of a TNC photocatalyst to compare the photoreduction process and -rates. For this purpose, the GO solution was deposited onto electrode structures and silicon substrates via spin-coating, and drop-casted onto silicon wafers for electrical-, AFM-, and FTIR spectroscopy measurements, respectively. Figure A.34 a-b) shows the evolution of the film conductance extracted from current-voltage (IV) curves of two GO films fabricated using varying amounts spin-coating deposition cycles with increasing UV illumination times. The amount of deposited GO, for the plot shown in figure A.34a), (4 × 25 µL), corresponds to the same

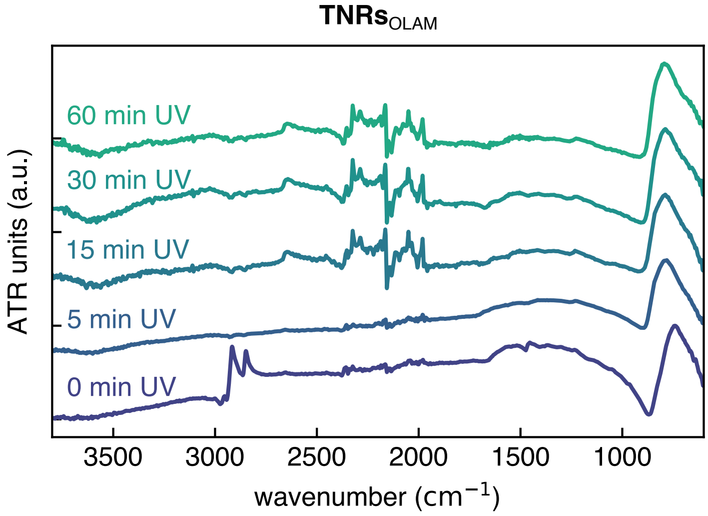

Figure A.33: ATR-FTIR spectra of a drop-casted pure TNR film for different UV exposure times.

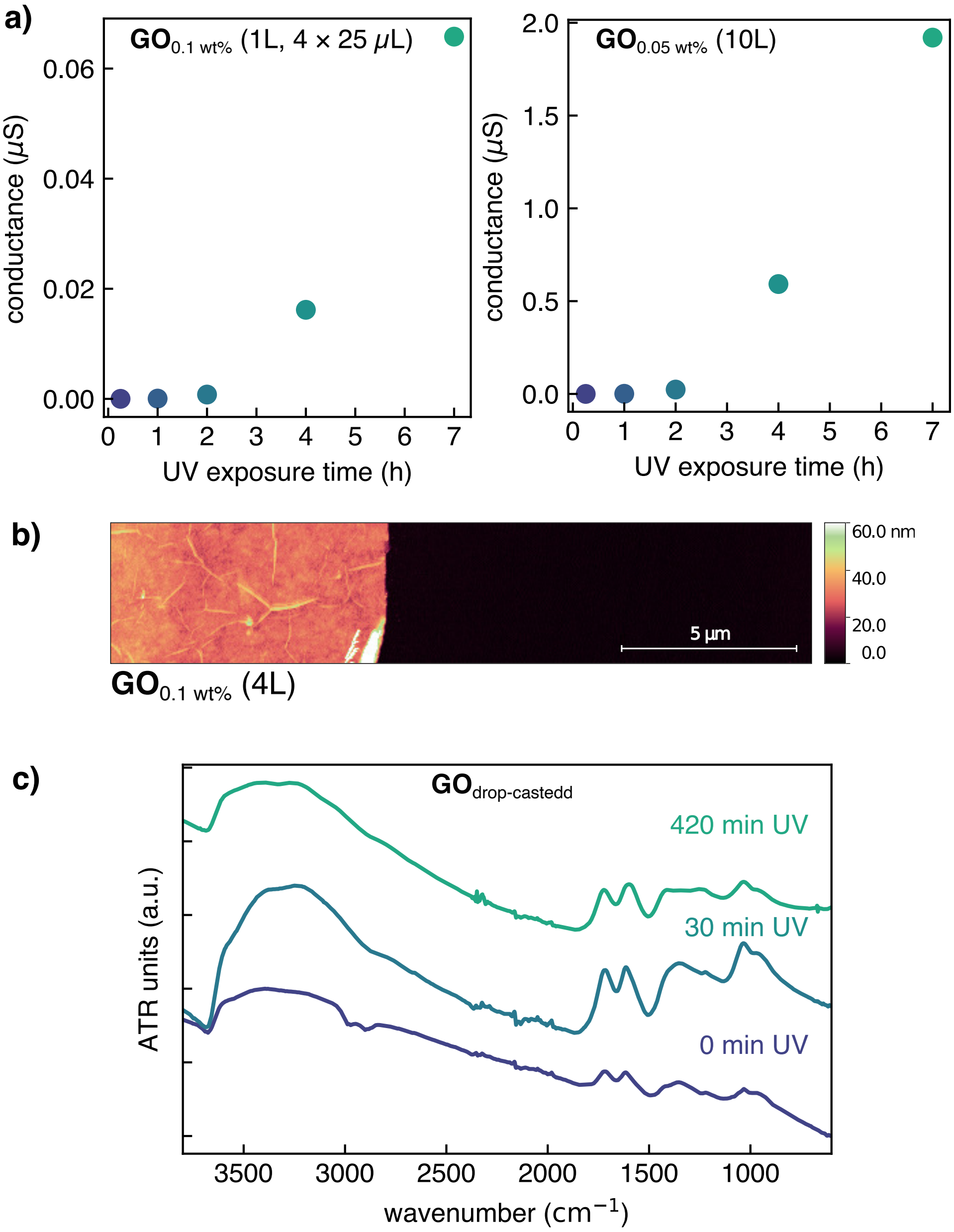

Figure A.34: Plot of the conductance vs. UV illumination time for pure GO films fabricated using (left) 1 spin-coating deposition cycle, and (right) 10 spin-coating deposition cycles. b) Topographic AFM image showing a scratched region between a GO film and a silicon substrate. The film was fabricated applying 4 spin-coating deposition cycles (10 L). c) ATR-FTIR spectra of drop-casted GO film for 0, 30, and 420 min UV illumination.

amount used for 1 layered GO/TNC hybrid films. Obviously, the onset of reduction (assessed by the material's conductance), is delayed compared to the GO/TNC composite films upon illumination, and much lower overall conductances are obtained, even after 7 h UV exposure.

Figure A.34b) shows an exemplary AFM scan of a GO film deposited on a Si wafer after 10 spin-coating steps. An average film thickness of 27.4 ± 0.5 nm was determined by averaging 10 height profiles from two AFM scans. Finally, figure A.34c) shows the evolution of the FTIR spectra of a drop-casted GO film on a silicon wafer after 0, 30, and 420 min UV exposure. The shown spectra show no pronounced changes compared to the GO/TNC films, supporting the assumption that reduction occurs at a lower rate in the absence of TNCs.

A.1.13 Monitoring Relative Humidity with a Commercial Sensor

The set relative humidity (r.h.) levels using the gas calibration system were monitored using a commercial gas sensor (BME680, Bosch SensorTec). Figures A.35-A.36 show the obtained r.h. timetraces for two representative measurements with a set baseline humidity of 30 %, and transient increase in r.h. of 40, 50, 60, 70, 80, 60, 50, and 40 %. Figure A.37 shows the obtained r.h. timetrace during a measurement with a set baseline r.h. of 0 % (dry purified air), and varying set water vapor concentrations (100 ppm, 400 ppm, 800 ppm, 2000 ppm, 4000 ppm, 8000 ppm, 30 %, 40 %, 50 %, 60 %, 70 %, 80 %). The obtained values are listed in table A.7.

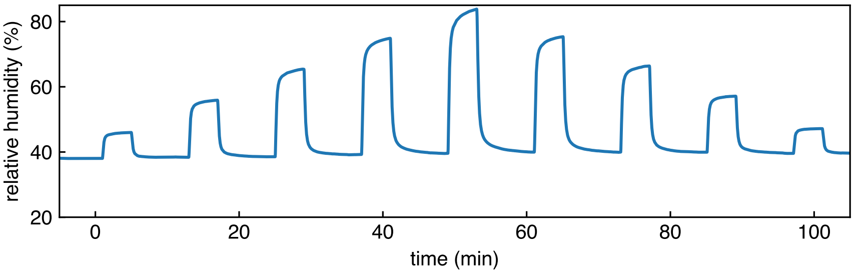

Figure A.35: Relative humidity timetrace measured using a commercial sensor for 4 min r.h. transients and humidified zero gas (purified air).

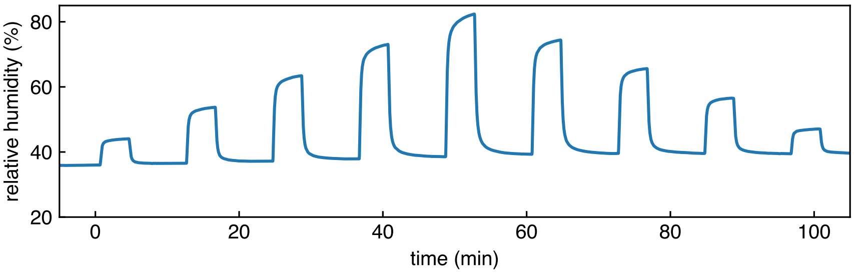

Figure A.36: Relative humidity timetrace measured using a commercial sensor for 4 min r.h. transients and humidified zero gas (purified air).

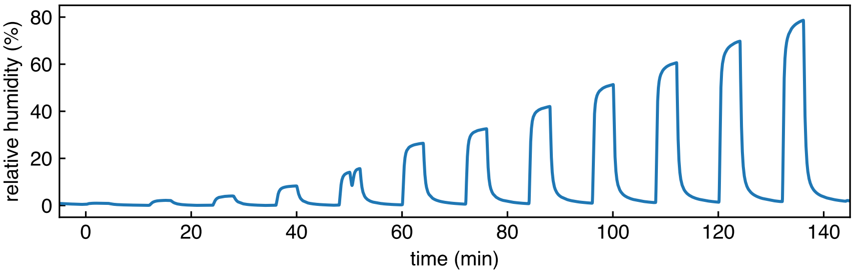

Figure A.37: Relative humidity timetrace measured using a commercial sensor for 4 min r.h. transients and dry zero gas (purified air).

Table A.7: R.h. values determined with a commercial humidity sensor.

set vapor concentration	**r.h. (%)**
100 ppm	0.95
400 ppm	2.2
800 ppm	4.0
2000 ppm	8.3
4000 ppm	16
8000 ppm	27
30 % r.h.	33
40 % r.h.	42
50 % r.h.	51
60 % r.h.	61
70 % r.h.	70
80 % r.h.	79

A.1.14 Humidity Sensing – Comparative Measurements

1-Layered Hybrid Films.

Resistive humidity measurements correlated with quartz crystal microbalance (QCM) gravimetric measuremets were also conducted using thinner films of GO/rGO/TNP films deposited on PI foil and QCMs, respectively. The films were fabricated using 1 spin-coating (SC) deposition cycle (estimated thickness: 15–20 nm, based on AFM measurements on silicon wafers). The sensing performance was studied for the range of 0–30 % r.h. The findings are summarized in the following two figures. Figure A.38 shows the response transients for both types of sensors. The frequency shifts show fast and reversible sorption of water vapor with shifts of down to 30 Hz for the less reduced GO/rGO/TNP-20 sample (fig. A.38a). Figure A.38c-d) show the corresponding relative conductance changes. The less reduced sample (figure A.38c) shows positive relative conductance changes for all tested r.h. levels, while only negative responses were obtained for the GO/rGO/TNP-120 sample. These trends are in agreement with the results discussed in the main section. Figure A.39 show the resistive response isotherms, as well as the relative mass uptake, calculated from the estimated film mass and the frequency shifts. Different from the results shown for the thicker films, a pronounced difference is visible for both degrees of reduction. Here, an approximately 4 times higher relative

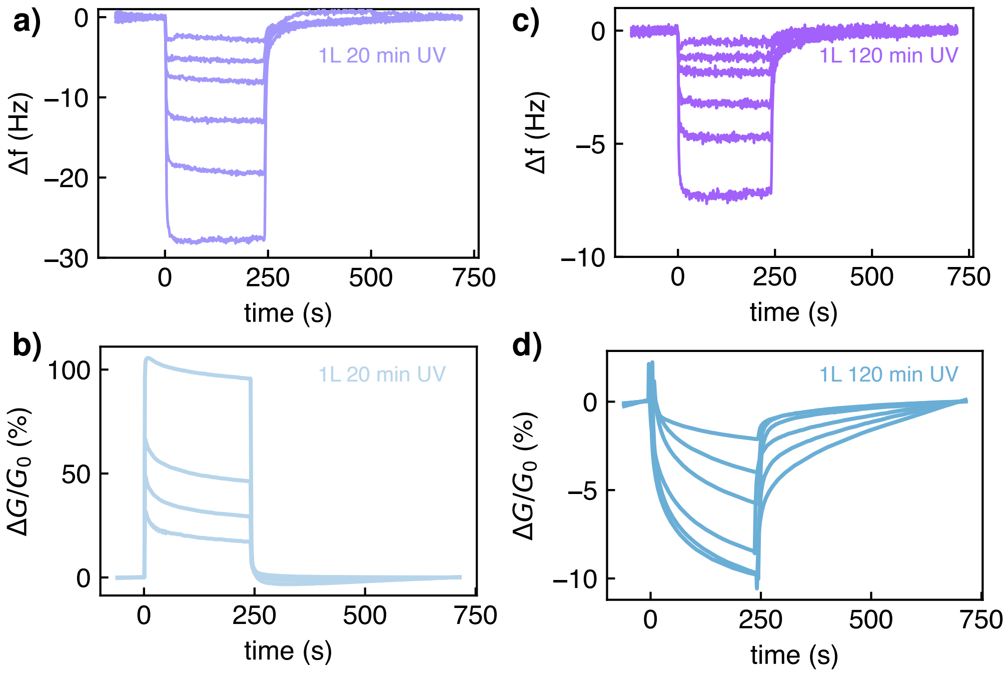

Figure A.38: Relative frequency shifts of GO/rGO/TNP-coated QCMs illuminated to UV light for a) 20 min and b) 120 min, upon exposure to water vapor up to 30 % r.h. c-d) Corresponding relative conductance changes of analogous chemiresistors.

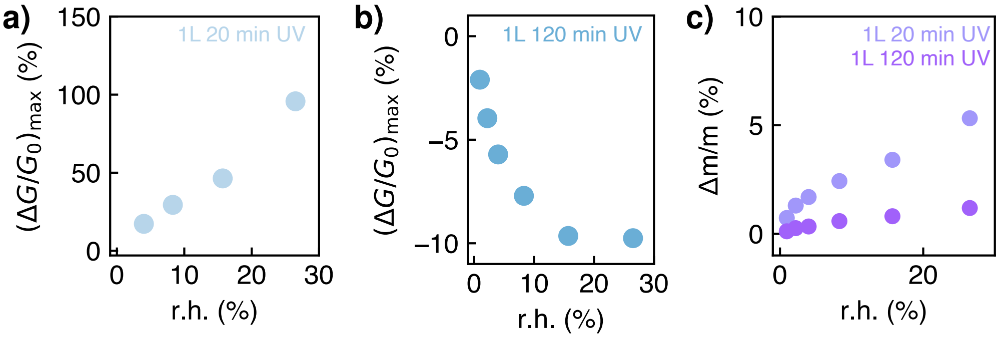

Figure A.39: a-b) Resistive response isotherms of GO/rGO/TNP chemiresistors (1 SC deposition cycle) exposed to UV light for a) 20 min and b) 120 min to Δr.h. up to 30 %. c) Sorption isotherms of two QCM samples coated with GO/rGO/TNP films (1 SC deposition cycle) with varying degree of reductions for r.h. levels ranging from 0.95 – 79 %.

mass uptake was calculated for the GO-rich film, compared to the film after longer UV exposure.

TNR/GO/rGO Films.

Reference experiments were also performed with hybrid films that were fabricated using TNRs (4 SC deposition cycles). The films were deposited on QCM substrates, as well as on PI substrates, and illuminated with UV light for 5, 20, 120, and 240 minutes. The sensing performance over a r.h. range between 0–80 % was investigated. Figure A.40 shows

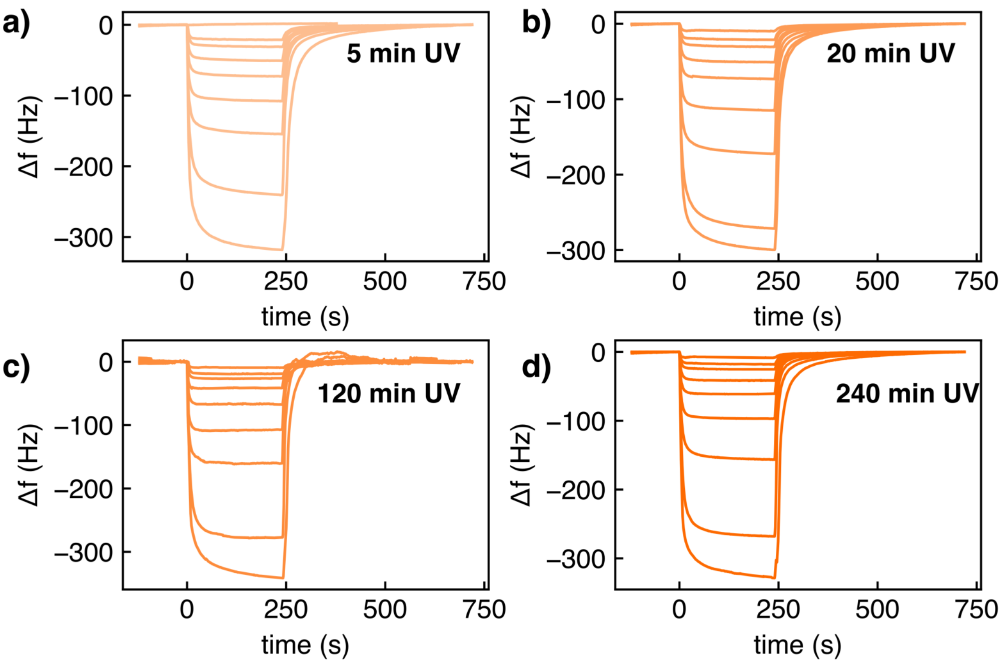

Figure A.40: Resonance frequency shifts of GO/rGO/TNR-coated QCMs to Δr.h. between ~1–80 %. The coated QCMs were exposed to UV light for different times ranging from 5–240 minutes to adjust the coatings' degrees of reduction.

the relative frequency shifts of the coated QCM sensors. All samples exhibitted similar frequency shifts upon water sorption of ~-300 Hz. Figure A.41 shows the corresponding sorption isotherms of the chemiresistors. The raw data of the chemiresistor measurements is provided in the following section A.1.15.

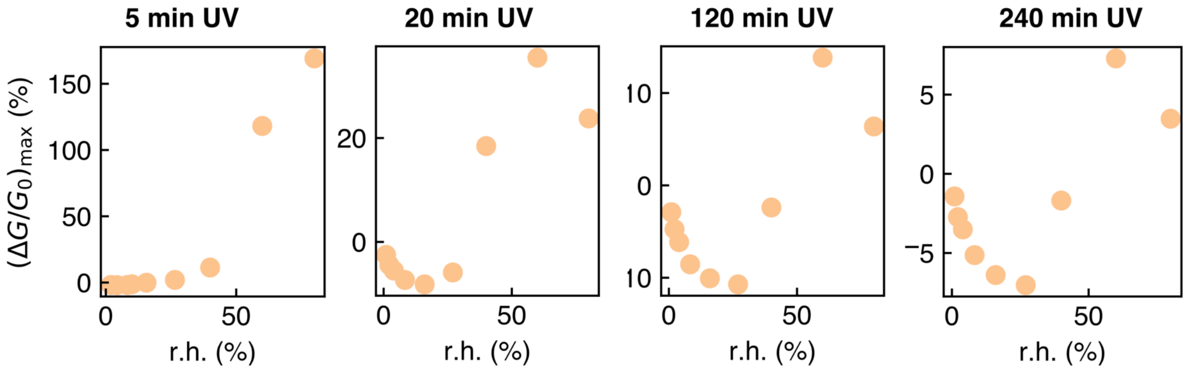

Figure A.41: Resistive response isotherms of GO/rGO/TNR chemiresistors (4 SC deposition cycles) exposed to UV light for different durations to Δr.h. up to ~80 %.

A.1.15 Humidity Sensing: Timetraces

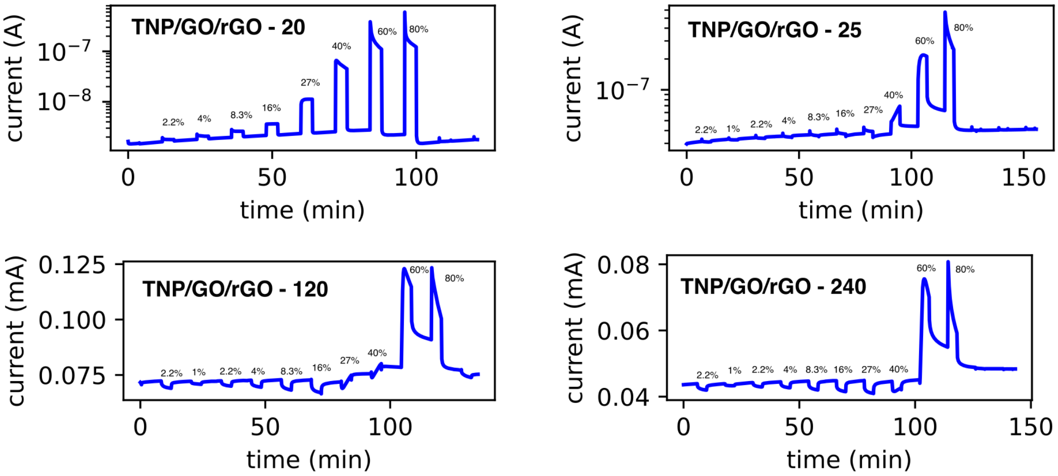

Figure A.42: Timetraces of GO/rGO/TNP-chemiresistors of different degrees of reduction to relative humidity changes over a range of 0–80 % r.h. at room temperature. The respective r.h. levels are annotated to the transients.

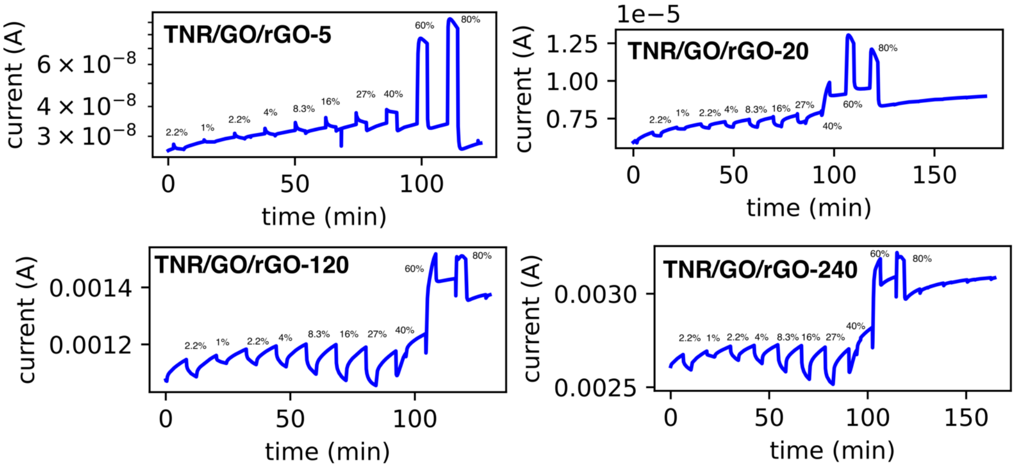

Figure A.43: Timetraces of GO/rGO/TNR-chemiresistors of different degrees of reduction to relative humidity changes over a range of 0–80 % r.h. at room temperature. The respective r.h. levels are annotated to the transients.

A.1.16 GO/rGO/TNC Chemiresistors

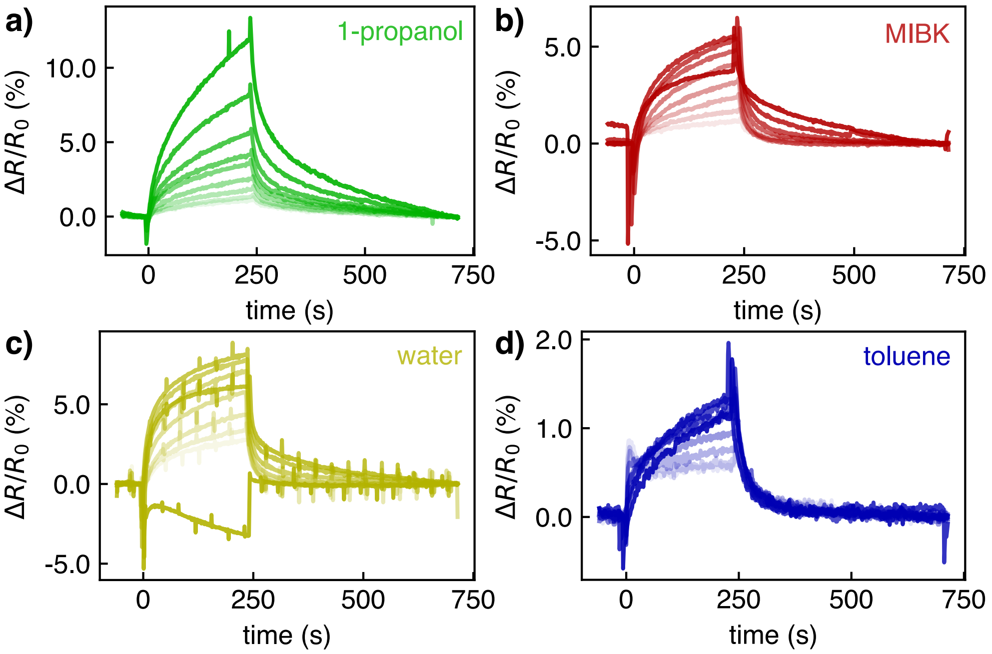

Figure A.44: Response transients of a GO/rGO/TNR thin film (UV illumination time: 15 min) to a) 1-propanol, b) MIBK, c) water, and d) toluene vapor at varying concentrations, as indicated by the intensity of the color.

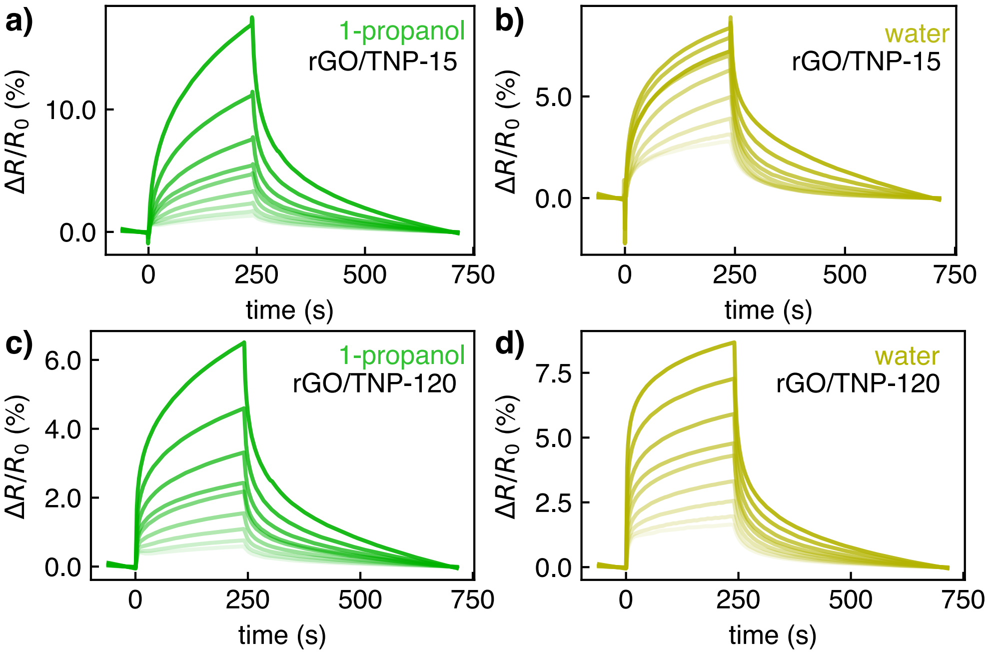

Figure A.45: Response transients of a a-b) GO/rGO/TNP thin film (UV illumination time: 15 min) to a) 1-propanol, b) water, and c-d) GO/rGO/TNP thin film (UV illumination time: 120 min) to c) 1-propanol and d) water, at varying concentrations, as indicated by the intensity of the color.

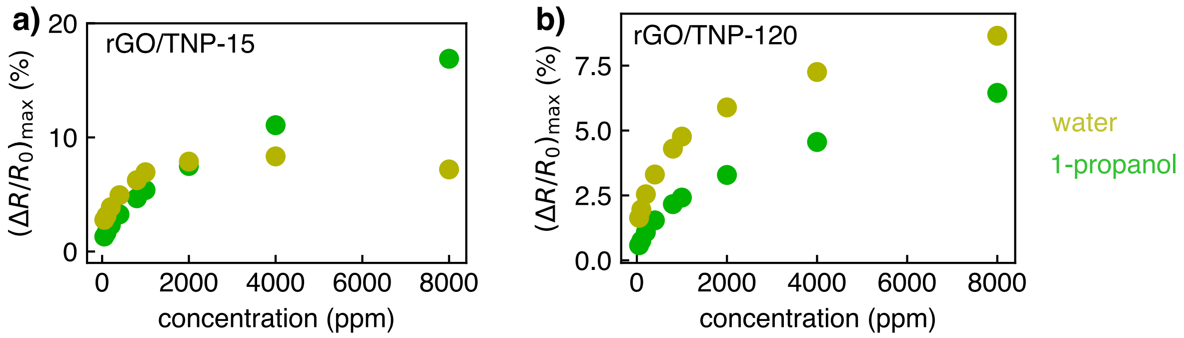

Figure A.46: Response isotherms of the a) GO/rGO/TNP-15 and b) GO/rGO/TNP-120 sensors for water (yellow) and 1-propanol (green) in a nitrogen atmosphere.

A.2 Safety

A.2.1 Chemicals

All chemicals used in this work are listed in table A.8 with their respective GHS symbols and hazardous and precautionary statements.

Table A.8: Used chemicals with respective GHS symbols, hazardous and precautionary statements.

Substance	GHS symbol	Hazardous statements	Precautionary statements
Acetone	02, 07	225, 319, 336	210, 233, 305+351+338
AZ 726 MIF[227]	05, 06, 08	290, 302, 311, 314, 371, 373	260, 280, 301+330+331, 303+361+353, 304+340+310, 305+351+338
AZ ECI 3012[228]	02, 07	226, 318, 336, 218, 280	305+351+338, 313
AZ nLOF 2020[229]	02, 07	226, 336	210
Borane tert-butylamine complex	06, 09	301+311, 315, 319, 411	264, 273, 301+310, 302+352+312 305+351+338
Chlorobenzene	02, 07, 09	226, 332, 315, 411	260, 262, 273, 403
Chloroform	06, 07	302, 315, 319, 331, 336, 351, 361d, 373	202, 301+312, 302+352, 304+340+311, 305+351+338, 308+313
Chromium Etchant	05	314, 318	260, 280, 305+351+338, 370+378
Diethylene glycol	07	302	264, 270, 301+312, 501
1-Dodecylamine	05, 07, 08, 09	304, 314, 335, 373, 410	261, 273, 280, 301+310, 305+351+338
Ethanol	02, 07	225, 319	210, 280, 310
Graphite flakes	–	–	–
Heptane	02, 07, 08, 09	225, 304, 315, 336, 410	210, 261, 273, 310+301, 331, 501
Hexane	02, 07, 08, 09	225, 304, 315, 361f, 373, 336, 411	210, 240, 273, 310+301, 331, 302+352, 403+235

Table A.8: Used chemicals with respective GHS symbols, hazardous and precautionary statements.

Substance	GHS symbol	Hazardous statements	Precautionary statements
1, 6-Hexaethylenegycoldithiol	07	315, 319, 335	261, 264, 271, 280+302+352, 305+351+338
1, 6-Hexanedithiol	07	227, 303	210, 280, 312, 370+378, 403+235, 501
Hydrogen peroxide	03, 05, 07	302+332, 315, 318, 335	280, 305+338+351, 310
Iodine	07, 08, 09	312+332, 315, 319, 335, 372, 400	261, 273, 280, 305+351+338, 314
Methanol	02, 06, 08	225, 317	210, 260, 280, 301+310, 311
4-Methy-2-pentanone	02, 07	225, 332, 335, 319	210, 305+351+338, 304+340
4-Nitrothiophenol	07	315, 319, 335	261, 305+351+338
1,9-Nonanedithiol	07	315, 319, 335	261, 305+351+338
1-Octadecene	08	304	301+310, 331
Oleic acid	–	–	–
Oleylamine	05, 07, 08, 09	302, 304, 314, 335, 373, 410	260, 280, 301+310, 303+361+353, 304+310+340, 305+351+338
Octane	02, 07, 08, 09	225, 304, 315, 336, 410	210, 273, 301+330+331, 302+352
1,8-Octanedithiol	07	302	–
Potassium iodide	–	–	–
Potassium permanganate	03, 05, 07, 08, 09	272, 302, 314, 361d, 373, 410	201, 260, 273, 280, 303+361+353, 305+351+338
PMMA	–	–	–
1-Propanol	02, 05, 07	225, 318, 336	210, 233, 240, 280, 303+361+353, 310, 305+351+338, 370+378, 501
2-Propanol	02, 07	225, 319, 336	201, 261, 305+351+338

Table A.8: Used chemicals with respective GHS symbols, hazardous and precautionary statements.

Substance	GHS symbol	Hazardous statements	Precautionary statements
Sodium hydroxide	05	290, 314	280, 301+330+331, 305+351+338, 308+310
Tetrachloroauric(III) acid trihydrate	05, 07, 08, 09	290, 302, 314, 373, 411	260, 273, 280, 303+361+353, 305+351+338, 314
Technistrip NI555[230]	07	302, 312	-
Titanium(IV) chloride	05, 06	314, 330, 335	260, 271, 280, 303+361+353, 304+340+310, 305+351+338
Titanium(IV) fluoride	05, 07	302, 312, 332, 314	260, 280, 301+312, 303+361+353, 304+340+310, 305+351+338
Toluene	02, 07, 08	225, 361D, 304, 373, 315, 336	210, 240, 301+330+310, 302+352, 308+313, 314, 403+233
Triammonium citrate	07	315, 319, 335	261, 305+351+338

A.2.2 CMR Substances

See attached document.

A.2.3 GHS Symbols

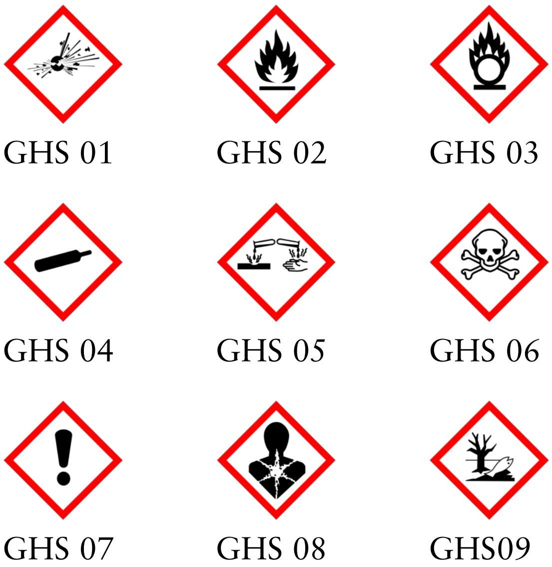
GHS 01 GHS 02 GHS 03
GHS 04 GHS 05 GHS 06
GHS 07 GHS 08 GHS09

Figure A.47: GHS hazard pictograms 01 - 09.

B Danksagung

Ich möchte mich an erster Stelle bei Dr. Tobias Vossmeyer und Prof. Dr. Horst Weller für die Aufnahme in die Arbeitsgruppe bedanken.

Ganz besonders danke ich Dr. Tobias Vossmeyer für die hervorragende Betreuung während meines Promotionsprojektes, sowie für viele Diskussionen und für Deine Unterstützung. Prof. Dr. Alf Mews danke ich für die Übernahme des Zweitgutachtens meiner Arbeit.

Auch ganz besonders bedanke ich mich bei Dr. Hendrik Schlicke, der einen Großteil der Projekte co-betreut hat, immer sehr hilfsbereit war, und immer Zeit gefunden hat, um mir bei Fragen zu helfen. Die Zusammenarbeit mit Dir hat mir viel Spaß gemacht und hat mich immer motiviert – danke, dass du seit meiner Bachelorarbeit so ein toller Mentor warst.

Auch bei allen Mitgliedern der Sensorgruppe: Dr. Hendrik Schlicke, Chi-Yin Liu, Dr. Bendix Ketelsen, Finn Dobschall, Svenja Kunze, Hauke Hartmann, Ahir Bose, Shi-Da Wu, Jana Struck und Clemens Schröter möchte ich mich für die gute Zusammenarbeit, Hilfsbereitschaft und schöne Zeit im Labor bedanken. Besonders danke an Clemens, Bendix und Hauke, die mich zu Beginn meiner Arbeit in Synthesen und Setups eingearbeitet haben. Außerdem möchte ich mich bei den Studierenden und Auszubildenden bedanken, die im Rahmen ihrer Abschlussarbeiten und Praktika zu dieser Arbeit beigetragen haben: Bri Dobson, Jana Struck, Jonathan Brandt, Sophie Benthien und Jan-Niklas Beyer.

Bei allen Mitgliedern des Graduiertenkollegs GRK Nanohybrid bedanke ich mich für interessante Meetings, Workshops, Gespräche, Diskussionen und Kollaborationen. Hierbei möchte ich mich besonders bei Prof. Dr. Dorota Koziej, die im Rahmen des Graduiertenkollegs meine Co-Betreuerin war, für viele Anregungen und für ihre Unterstützung bedanken. Auch danke an Andreas Kolditz für die Hilfe bei allen organisatorischen Abläufen im GRK.

Robert Schön und Dr. Charlotte Ruhmlieb danke ich für die Durchführung von SEM-Messungen, und Stefan Werner danke ich für die Durchführung von TEM- und XRD-Messungen. Almut Barck und Nina Schober danke ich ebenfalls für die Durchführung von XRD Messungen. Dr. Heshmat Noei und Dr. Mona Kohantorabi (DESY) danke ich für die Durchführung der XPS-Messungen, Roman Kusterer danke ich für die Messung von Raman-Spektren.

Der Forschungswerkstatt des Instituts für Physikalische Chemie und der Elektronikwerkstatt danke ich für die Anfertigung vieler Messzellen, UV-Lampen, Platinen, sowie ihrer Hilfe bezüglich Fragen zu verschiedenen Geräten oder Aufbauten.

Meinen Bürokolleg:innen in 253 und 347 möchte ich für die good times im Büro danken: Finn Dobschall, Ahir Bose, Elena Felgenhauer, Jan-Niklas Beyer, Svenja Kunze, Dr. Maik Finsel, Clemens Schröter und Dr. Gregor Dahl. Außerdem auch dem ganzen AK Weller für die schöne Zeit! Bei Dr. Skadi Kull und ihrem Team möchte ich mich für die tolle Zeit und interessante Zusammenarbeit bei Molecules & Schools im letzten Jahr bedanken.

Für die Durchsicht dieser Arbeit danke ich Finn Dobschall, Benito Pflüger und Dr. Bendix Ketelsen.

Bei Marion Manin und Sigrid Zeckert möchte ich mich für ihre Hilfsbereitschaft bei allen organisatorischen Fragestellungen bedanken.

Auch bei den Mitarbeiterinnen vom Café Grindel möchte ich mich für die vielen Kaffees während meiner Zeit als Doktorandin bedanken.

Schließlich möchte ich von ganzem Herzen meiner Familie in Marburg, Hamburg, Paraguay und überall sonst, für ihre Liebe und Unterstützung danken: Lili Fricke, Robin, Marlen, Marvin, Margit und Georg Pflüger, und ganz besonders: Benito Pflüger und Abla-Dog, meiner Mutter Maria Persano, meinen Schwestern Helene und Marianne Bittinger, meinem Neffen Vincent José, und meinem Papa, der im Herzen immer bei mir ist – todo lo que hago es gracias a ustedes y es para ustedes: les quiero muchísimo!

C Eidesstattliche Versicherung

Hiermit versichere ich an Eides statt, die vorliegende Dissertation selbst verfasst und keine anderen als die angegebenen Hilfsmittel benutzt zu haben.

November 2, 2023

Sophia Caroline Bittinger